DE GRUYTER

Edward Yu. Bormashenko

WETTING OF REAL SURFACES

2ND EDITION

STUDIES IN MATHEMATICAL PHYSICS 19

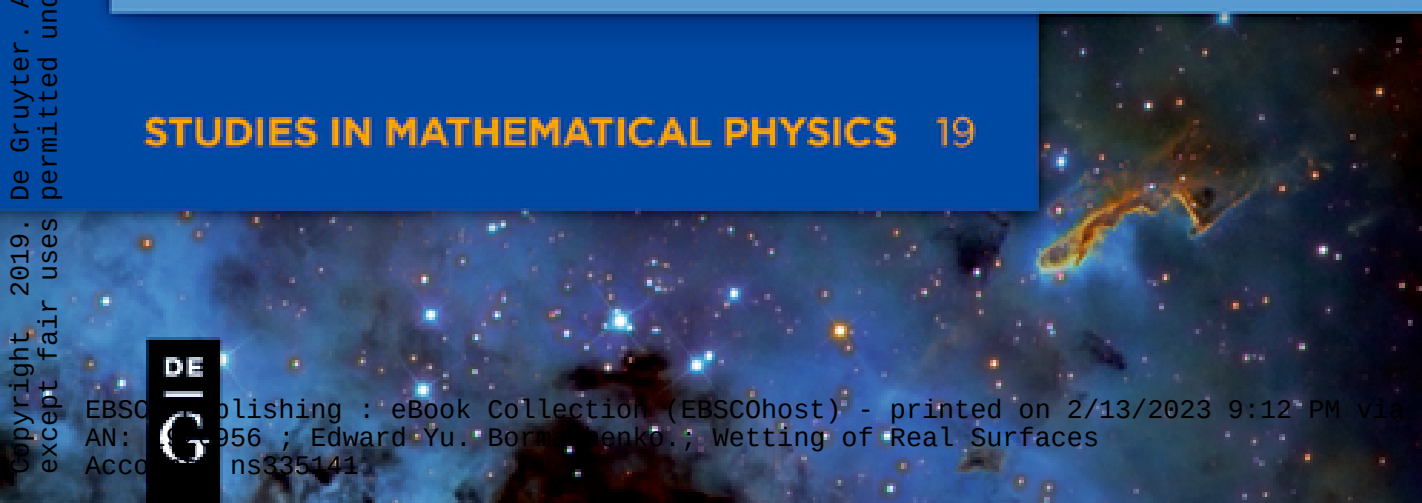

Edward Yu. Bormashenko

Wetting of Real Surfaces

De Gruyter Studies in Mathematical Physics

Volume 19

Edward Yu. Bormashenko

Wetting of Real Surfaces

2nd Edition

DE GRUYTER

Physics and Astronomy Classification Scheme 2010
68.08.-p, 68.03.Cd, 68.08.Bc, 68.35.Ct, 68.08.De, 68.35.Md, 02.30.Xx, 47.55.D-.

Author
Prof. Dr. Edward Yu. Bormashenko
Ariel University,
Faculty of Engineering
Department of Chemical Engineering, Biotechnology and Materials
Laboratory of Interface Science
P.O. Box 3
40700 ARIEL
Israel
edward@ariel.ac.il

ISBN 978-3-11-058106-5
e-ISBN (PDF) 978-3-11-058314-4
e-ISBN (EPUB) 978-3-11-058118-8
ISSN 2194-3532

Library of Congress Control Number: 2018951017

Bibliographic information published by the Deutsche Nationalbibliothek
The Deutsche Nationalbibliothek lists this publication in the Deutsche Nationalbibliografie; detailed bibliographic data are available on the Internet at http://dnb.dnb.de.

Typesetting: le-tex publishing services GmbH, Leipzig
Printing and binding: CPI books GmbH, Leck

www.degruyter.com

בסייד
To my parents

Preface to the second edition

In the second edition, the author has adhered to the general framework of the first edition of the book: the variational approach to the problems of wetting is implemented, exploiting the transversality conditions of a variational problem with free endpoints. At the same time, the principle of locality is emphasized: contact angles depend on physical and chemical events occurring in the vicinity of the triple (three-phase) line. Along with these, the second edition surveys the latest achievements in the field of wetting of real surfaces, including new chapters devoted to the wetting of lubricated and gradient surfaces and reactive wetting, which have seen rapid progress in the last decade. Additional reading, surveying the progress across the entire field of wetting of real surfaces, is suggested to the reader.

Ariel, Israel, Ariel University, September 2018 Edward Yu. Bormashenko

https://doi.org/10.1515/9783110583144-201

Preface to the first edition

Immanuel Kant said: "Two things fill the mind with ever new and increasing admiration and awe, the more often and steadily reflection is occupied with them: the starry heaven above me and the moral law within me." In my student days, two small-scale miracles likewise filled my mind with admiration: the power of the variational principles of physics, and the fascinating behavior of water droplets demonstrating an amazing variety of physical phenomena. This book is devoted to the applications of those variational principles to wetting problems. Exploiting variational principles allows natural construction of a general umbrella enclosing a broad variety of wetting effects. This book demonstrates that the well-known Young, Boruvka–Neumann, Cassie–Baxter, and Wenzel equations are actually the boundary transversality conditions for the appropriate problem of wetting.

My interest in wetting was stimulated by the book "Droplet," written by my scientific mentor, Professor Yakov Evseevitch Gegusin in the 1980s. Regrettably, this book, which remains one of the best published in the field of interface science, remains unknown to a broad readership, because it has not been translated into English. I take this opportunity to honor the memory of Professor Gegusin, a brilliant scientist and teacher.

The field of wetting remained unattractive to young scientists for a long time, and this is in spite of the fact that Einstein, Schrödinger, and Bohr devoted their research activity to this class of effects. It has been latently supposed that only the physics of particles and phenomena occurring in a micro-world deserve the attention of inquisitive minds. Several factors, however, have revived an interest in wetting and wettability. The first of these was the discovery of the "lotus" effect (or superhydrophobicity) by Barthlott and Neinhuis in 1997. The second factor was the rapid progress achieved in the field of wetting by the scientific school led by P. G. de Gennes. It is noteworthy that the main notions of the modern theory of wetting (such as disjoining pressure, superhydrophobicity, contact angle hysteresis, and wetting transitions) are younger than the basic ideas of relativity and quantum mechanics. Hence, the study of wetting phenomena is a rapidly developing field of modern physics, full of exciting physical insights.

It is reasonable to ask: why one more book on wetting? Two excellent books summarizing the state of the art in the field have been published recently: *Capillarity and Wetting Phenomena* by P. G. de Gennes, F. Brochard-Wyart, and D. Quéré; and *Surface Chemistry of Solid and Liquid Interfaces* by H. Y. Erbil, which are strongly recommended to the reader. However, the rapid progress in the understanding of the wetting of *real*, i.e., *rough*, and *chemically heterogeneous* surfaces achieved in the last decade calls for the review carried out in this book. A special chapter is devoted to the physical origin of contact angle hysteresis, as it was recently studied intensively. The attention was devoted to superhydrophobicity and wetting transitions on rough surfaces. The

https://doi.org/10.1515/9783110583144-202

book also deals with the electrowetting phenomenon and so-called nonstick droplets (including Leidenfrost droplets and liquid marbles), which have been studied intensively in the past decade. The book generally maintains a macroscopic approach; however, intermolecular forces were naturally involved in the clarification of the notion of surface tension.

The book is intended for MSc and PhD students studying physics, chemical engineering, and materials and interface science, and of course for researchers working in the field of interface phenomena. Fluency in the use of the mathematical apparatus of calculation of variations is desirable for the reader. An excellent textbook, *Calculus of Variations* by Gelfand and Fomin is strongly recommended for the reader to acquire skill in the calculation of variations, one of the most exciting fields of calculus.

The author is indebted to Professor Whyman for his longstanding fruitful cooperation in the study of wetting phenomena. His critique and numerous remarks definitely improved the text. I am thankful to Professor R. Pogreb for his contribution in understanding the diversity of wetting phenomena. I am grateful to Dr. T. Stein for his cooperation in the field of superhydrophobicity. I want to thank my numerous MSc and PhD students for their research activity and allegiance to the spirit of scientific research. I am grateful to Dr. I. Legchenkova and Dr. A. Musin for their kind help in editing the book. I am thankful to Professor Haim Taitelbaum for useful discussions on the effect of reactive wetting. I am especially indebted to my wife, Yelena Bormashenko, for her inestimable help in preparing this book. I am greatly thankful to Mrs. Hannah Weiss for her valuable help in the English editing of this book.

Symbol Index

a	contact radius of a droplet
$\tilde{a}$	characteristic length describing precursor films in dynamic wetting (Section 4.3)
A	Hamaker constant
b, c, h	geometrical parameters of rough surfaces
$\tilde{b}$	root mean square width of the triple line (Section 3.10.3)
$\hat{b}$	width of a precursor film (Section 4.3)
h_{m}	limiting height (scale)
$\tilde{h}$	thickness of the liquid film in the "drag-out" problem (Section 4.10)
C	capacitance
$\check{C}$	specific capacitance
$\hat{C}$	curvature
$\tilde{d}$	characteristic thickness in the drag-out problem (Section 4.10)
d_{m}	molecular diameter, atomic scale
e	thickness of the insulating vapor layer, thickness of the liquid layer
$\hat{e}$	eccentricity of the spheroidal droplet (Section 2.9)
E	electric field
f_{i}	fraction in the substrate surface
f_{s}	fraction in the wetted substrate surface
F_{c}	critical force for wetting transitions (Section 7.7)
g	gravity acceleration
$\tilde{g}$	geometrical factor
G	free energy
$\hat{G}$	specific free energy
G_{r}	energy of chemical reaction (Section 11.2)
H	capillary rise
I	ionization potential
J	moment of inertia
k	wavenumber
$\hat{k} = 2.1 \cdot 10^{-7} \frac{\mathrm{J}}{\mathrm{mol}^{2/3}\mathrm{K}}$	the Eötvös constant
$k_{\mathrm{B}} = 1.38 \cdot 10^{-23} \frac{\mathrm{J}}{\mathrm{K}}$	the Boltzmann constant
l	the length of the column of liquid in the capillary (Section 4.9)
l_{stop}	stopping distance of "liquid marbles" (Section 9.3.6)

https://doi.org/10.1515/9783110583144-203

$\widetilde{l}$	wavelength of a potential comb (Section 4.6), period of a rough relief (Section 7.4.1)
$\widetilde{m}$	mass of the unit length of a two-dimensional drop (Appendix 3A to Chapter 3)
M_{W}	molar mass
p	pressure
p_{c}	critical pressure of wetting transition (Section 7.5)
p_0	atmospheric pressure
p_{L}	Laplace pressure
p_{S}	pressure of the saturated vapor
p_{vap}	pressure of the vapor
p_{liq}	pressure in the liquid
$\widetilde{p}$	dipole moment
$\overline{p}$	perimeter (Sections 2.14, 7.6)
r	radius of the capillary tube, pore, etc.
r_0	characteristic size of the defect (Section 3.10.1)
$\widetilde{r}$	roughness of a surface
R	radius of a droplet
R_{eq}	the radius of the equivalent spherical drop
$\widetilde{R} = 8.31\ \frac{\mathrm{J}}{\mathrm{mol\,K}}$	the gas constant
S	area
t	time
t_{st}	"stick" time (Section 3.4)
T	temperature
Q	energy of evaporation
U	potential energy
$U_{\mathrm{int}}^{\mathrm{total}}$	total energy of the interaction of one particular molecule with all the other molecules
$\hat{U}$	voltage
v	velocity
v_{cm}	velocity of center mass
v_{p}	pulling speed in the drag-out problem (Section 4.10)
v_{p}^*	critical pulling speed in the drag-out problem (Section 4.10)
V	volume, volume of a droplet
V_{ML}	molar volume of a liquid
V_{MS}	molar volume of a solid
W	energy, work
W_{diss}	energy of dissipation (Section 4.4)
W_{line}	energy related to line tension
$\widetilde{W}$	energy per unit length of the triple line
W_{tr}	energy of wetting transition, energy barrier separating the Cassie and Wenzel states

α polarizability of the molecule
$\tilde{\alpha}_L$ specific volume polarizability of liquid
$\tilde{\alpha}_S$ specific volume polarizability of solid
$\hat{\alpha}$ specific heat exponent, determining the order of the wetting transition, scaling exponent (Section 3.10.3)
$\hat{\beta}$ kinetic coefficient in the Vedantam and Panchagnula model of contact angle hysteresis (Section 3.9)
Γ line tension
δ scaling dimensionless parameter δ relating contributions of surface tension and elastic terms (Section 3.11)
$\hat{\delta} = \Gamma/\hat{\psi}$ parameter in the Vedantam and Panchagnula model of contact angle hysteresis (Section 3.9)
ζ vertical displacement of a solid substrate (Section 3.11)
γ surface tension
γ_C critical surface tension (Appendix 2B to Chapter 2)
γ_{eff} effective surface tension
γ_{SA} solid–air interfacial tension
γ_{SL} solid–liquid interfacial tension
γ_{12} interfacial tension between liquids
ε dielectric constant
ε_0 dielectric constant of a vacuum
$\tilde{\varepsilon}$ the coefficient of slip
η viscosity
$\hat{\eta}$ dimensionless order parameter in the Vedantam and Panchagnula model of contact angle hysteresis (Section 3.9)
θ_A advancing contact angle
θ_C Cassie contact angle
θ_D dynamic contact angle
θ_{el} electrowetting contact angle
θ_m microscopic contact angle
θ_R receding contact angle
θ_{rw} reactive wetting contact angle
θ_Y Young contact angle
θ_W Wenzel contact angle
κ thermal conductivity
Λ parameter of macroscopic dissipation (Section 4.5).
λ Lagrange multiplier
$\tilde{\lambda}$ volumetric heat of evaporation
$\hat{\lambda}$ mass heat of evaporation
μ elastic (shear) modulus of the solid
ν frequency
Π disjoining pressure

ρ density
$\tilde{\rho}$ number density
τ characteristic time
τ_0 microscopic time for a single molecule jump (Section 4.6)
χ inverse characteristic length in the expression for disjoining pressure due to electric double layers
ϖ a constant in the expression relating the Hamaker constant A to specific volume polarizabilities of liquid and solid
Ψ spreading parameter
$\hat{\psi}$ gradient coefficient in the Vedantam and Panchagnula model of contact angle hysteresis (Section 3.9)
ϵ cutoff length (Section 3.11)

Contents

1 What is surface tension?

1.1 Surface tension and its definition

Surface tension is one of the most fundamental properties of liquid and solid phases. Surface tension governs a diversity of natural or technological effects, including floating of a steel needle, capillary rise, walking of water striders on the water surface, washing, and painting. It governs many phenomena in climate formation, plant biology, and medicine. Surface tension is exactly what it says: the tension on a surface and the reality of its existence is demonstrated in Figure 1.1, presenting a metallic needle and water strider supported by a water surface.

Imagine a rectangular metallic frame closed by a mobile piece of wire, as depicted in Figure 1.2. If one deposits a soap film within the rectangle, the film will want to diminish its surface area. Thus, it acts perpendicularly and uniformly on the mobile wire, as shown in Figure 1.2. The surface tension $\vec{\gamma}$ could be defined as a force per unit length of the wire.

The surface tension defined in this way is a tensor that acts perpendicularly to a line on the surface. Surface tension is often identified as specific surface free energy. Indeed, when the mobile rod in Figure 1.2 moves by a distance $\mathrm{d}x$, the work $2\gamma l\,\mathrm{d}x$ is done (the factor of 2 reflects the presence of the upper and lower interfaces). Thus, the

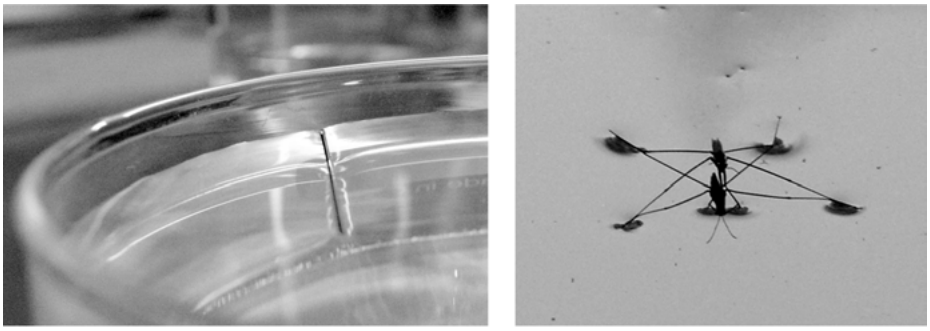

(a) (b)

Fig. 1.1: Manifestation of surface tension: steel needle (a) and water strider (b) supported by water surface.

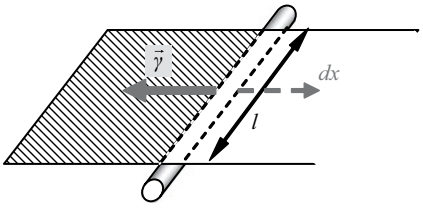

Fig. 1.2: The definition of surface tension: force normal to the line (rod).

https://doi.org/10.1515/9783110583144-001

surface tension γ could be identified with the energy supplied to increase the surface area by one unit. This identification may give rise to misinterpretations: the surface tension defined as force per unit length of a line in the surface is a *tensor*, whereas specific surface free energy is a *scalar* thermodynamic property of an area of the surface without directional attributes [7]. However, for liquids at a constant temperature and pressure and in equilibrium, the surface tension is numerically equal and physically equivalent to the specific surface free energy [7]. Let us start from this simplest situation, i.e., the surface tension of liquids in equilibrium.

1.2 Physical origin of the surface tension of liquids

Liquid is a condensed phase in which molecules interact. The origin of surface tension is related to the unusual energetic state of the surface molecule, which misses half its interactions (Figure 1.3). The energy states of molecules in the bulk and at the surface of the liquid are not the same owing to the difference in the nearest surrounding of a given molecule. Each molecule in the bulk is surrounded by others on every side, whereas, for the molecule located at the liquid/vapor interface, there are very few molecules outside, as shown in Figure 1.3.

Here, a widespread misinterpretation should be avoided; the resulting force acting on the molecule in the bulk and at the interface equals zero (both "bulk" and "interface" molecules are in mechanical equilibrium). For example, we can read: "the unbalanced force on a molecule is directed inward" [1]. If this is the case, the molecule according to the 2nd Newton's Law has to move toward the bulk, and all the liquid has to flow instantaneously in obvious conflict with the energy conservation. This common misinterpretation was revealed and analyzed in Moore et al. [13]. Figure 1.4, depicting an "instantaneous photo" of the potential relief, describing the interaction of a molecule of liquid with its surrounding, clarifies the situation. If all molecules are supposed to be fixed, the potential energy of a molecule changes, as shown schematically in Figure 1.4. Obviously, the force acting on a molecule in equilibrium is zero.

However, an increase in the liquid/vapor surface causes a rise in the quantity of "interface" molecules and a consequent growth in the surface energy. Liquids tend to diminish the number of interface molecules to decrease surface energy. Thus, the

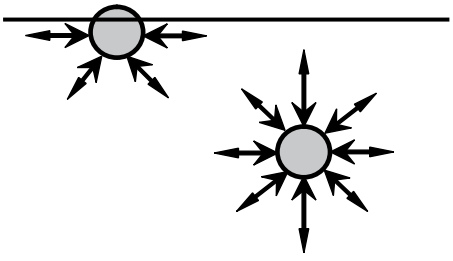

Fig. 1.3: A molecule at the surface misses about half its interactions.

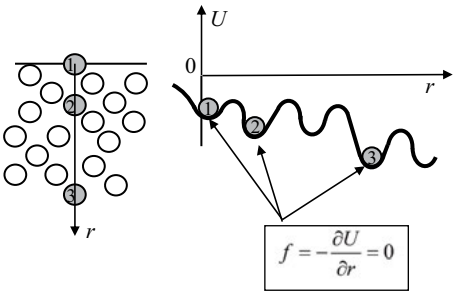

Fig. 1.4: A potential relief describing the interaction of a molecule of liquid with its surrounding. Molecules labeled "1," "2," and "3" are in equilibrium. The force acting on these molecules is zero.

surface free energy of the material is the work that should be supplied to bring the molecules from the interior bulk phase to its surface to create a new surface with a unit area. Let the potential describing the pair intermolecular interaction in the liquid be $U(r)$. The surface tension γ could be estimated as:

$$\gamma = f_{\mathrm{m}} \frac{1}{d_{\mathrm{m}}} \cong \frac{N}{2} \frac{|U(d_{\mathrm{m}})|}{d_{\mathrm{m}}} \frac{1}{d_{\mathrm{m}}} = \frac{N}{2} \frac{|U(d_{\mathrm{m}})|}{d_{\mathrm{m}}^2}, \tag{1.1}$$

where f_{m} is the force necessary to bring a molecule to the surface, which could be roughly estimated as $f_{\mathrm{m}} \cong N/2|U(d_{\mathrm{m}})|/d_{\mathrm{m}}$, where d_{m} is the diameter of the molecule, N is the number of nearest neighbor molecules (the multiplier 1/2 is due to the absence of molecules "outside," i.e., in the vapor phase), and $1/d_{\mathrm{m}}$ is the number of molecules per unit length of the liquid surface. It is seen from (1.1) that the surface tension in liquids is defined by the pair intermolecular interaction $U(r)$, the diameter of the molecule d_{m}, and the number N. Now, let us cast a glance at Table 1.1, supplying surface tensions of a number of liquids. The similar values of surface tensions of liquids, summarized in Table 1.1, which are very different in their physical and chemical nature, catch the eye. Indeed, the values of surface tension of most organic liquids are located within the narrow range 20–65 mJ/m^2. This is in striking contrast to other mechanical properties of liquids, such as viscosity. For example, the viscosity of ethyl alcohol

Tab. 1.1: Surface tension, enthalpy of vaporization, and dipole moment of some organic molecules.

Liquid	Surface tension, γ, mJ/m^2	Enthalpy of vaporization, ΔH, kJ/mol	Dipole moment, $\tilde{p}$, D^*
Glycerol, $C_3H_8O_3$	64.7	91.7	2.56
Formamide, CH_3ON	55.5	60.0	3.7
CCl_4	25.7	32.54	0
Chloroform, $CHCl_3$	26.2	31.4	1.04
Dichloromethane, CH_2Cl_2	31	28.6	1.60
Toluene, C_7H_8	28.5	38.06	0.36
Ethyl alcohol, C_2H_6O	22	38.56	1.7
Acetone, C_3H_6O	24	31.3	2.9

* The unit of a dipole moment is Debye: 1 D = $3.3 \cdot 10^{-30}$ C · m.

at ambient conditions equals $1.2 \cdot 10^{-3}$ kg/m · s, whereas the viscosity of glycerol is 1.5 kg/m · s, while at the same time, the surface tensions of alcohol and glycerol are of the same order of magnitude. The more striking example is honey, the viscosity of which may be very high; however, its surface tension is 50–60 mJ/m^2. A reasonable question is: why is the range of values of surface tension so narrow? This range obviously depends on the intermolecular potential $U(r)$. In general, there are three main types of intermolecular interactions:

1. The attractive interaction between identical dipolar molecules, given by the Keesom formula:
$$U_{\mathrm{K}}(r) = -\frac{\tilde{p}^4}{3(4\pi\varepsilon_0)^2 k_{\mathrm{B}} T}\frac{1}{r^6}\,, \tag{1.2}$$
where $\tilde{p}$ is the dipole moment of the molecule, k_{B} is the Boltzmann constant, T is the temperature, ε_0 is the vacuum permeability, and r is the distance between molecules [4, 9].
2. The Debye attractive interaction between dipolar molecules and induced dipolar molecules is:
$$U_{\mathrm{D}}(r) = -\frac{2\tilde{p}^2\alpha}{(4\pi\varepsilon_0)^2}\frac{1}{r^6}\,, \tag{1.3}$$
where α is the polarizability of the molecule [4, 9].
3. The London dispersion interactions, which are of a pure quantum mechanical nature. The London dispersion force is an attractive force that results when the electrons in two adjacent atoms occupy positions that make the atoms form temporary dipoles; its potential is given by:
$$U_{\mathrm{L}}(r) = -\frac{3\alpha^2 I}{4(4\pi\varepsilon_0)^2}\frac{1}{r^6}\,, \tag{1.4}$$
where I is the ionization potential of the molecule [4, 9]. All attractive intermolecular interactions given by formulae (1.2)–(1.4) decrease as $1/r^6$. The importance of the power law index −6 is discussed in Appendix 1A at the end of this chapter.

The Keesom, Debye, and London interactions are collectively termed *van der Waals interactions*. It should be stressed that the London dispersion forces given by formula (1.4) govern intermolecular van der Waals interactions in most organic liquids. They are several orders of magnitude larger than the dipole–dipole Keesom and Debye forces described by expressions (1.2) and (1.3) [2, 4, 9]. Taking this into account, we obtain using formulae (1.1) and (1.4) a very simple (and crude) estimation of the surface tension of liquids (for details see Bormashenko [2]):

$$\gamma \cong \frac{3N}{2^{10}}\frac{I}{d_{\mathrm{m}}^2}\,. \tag{1.5}$$

Formula (1.5) answers the question: why do surface tensions of most organic liquids demonstrate close values? Indeed, it is seen from (1.5) that the surface tension of a broad variety of organic liquids depends on the potential of the ionization and the

diameter of the molecule only. These parameters vary slightly for all organic liquids. Formula (1.5) predicts for simple liquids a surface tension that is roughly close to the values displayed in Table 1.1 [2]. Moreover, formula (1.5) predicts $\gamma \approx \text{const}/d_{\text{m}}^2$; this dependence actually takes place for *n*-alkanes [17].

Moreover, enthalpies of vaporization (supplied in Table 1.1) and tensile strengths of most liquids (which are also governed by intermolecular forces) are of the same order of magnitude.

The London dispersion force dictates the surface tension of a liquid when hydrogen or metallic (mercury) bonds acting between molecules could be neglected. When hydrogen or metallic bonds are not negligible, it was supposed that the surface tension of liquids could be presented in an additive way:

$$\gamma = \gamma^{\text{d}} + \gamma^{\text{h}}; \quad \gamma = \gamma^{\text{d}} + \gamma^{\text{met}} , \tag{1.6}$$

where the first term represents the dispersion London force contribution and the second term represents the hydrogen or metallic bonding [5]. However, the concept of additivity of surface tension components was criticized by several groups, and it was shown that liquids exist for which equation (1.6) becomes problematic [18].

1.3 Temperature dependence of the surface tension

When the temperature is increased, the kinetic agitation of the molecules increases. Thus, the molecular interactions become weaker and weaker compared with the kinetic energy of the molecular motion. Hence, it is quite expectable that the surface tension will decrease with the temperature. The temperature dependence of the surface tension is well described by the Eötvös equation (Eötvös rule):

$$(V_{\text{ML}})^{2/3}\gamma = \hat{k}(T_{\text{c}} - T) , \tag{1.7}$$

where V_{ML} is the molar volume of the liquid, $V_{\text{ML}} = M_{\text{W}}/\rho_{\text{L}}$, M_{W} and ρ_{L} are the molar mass and the liquid density respectively, T_{c} is the critical temperature of a liquid, and $\hat{k}$ is a constant valid for all liquids. The Eötvös constant has a value of: $\hat{k} = 2.1 \cdot 10^{-7}\,\text{J/mol}^{2/3}\text{K}$. An abundance of modifications of the Eötvös formula (1.7) have been proposed; however, for practical purposes the linear dependence of the surface tension could be supposed [1, 4].

1.4 Surfactants

Surface tension of liquids could be modified not only physically but also chemically by introducing surfactants. A surfactant is a molecule that has two parts with different affinities. One of these parts has an affinity to nonpolar media and the second part has

an affinity to polar media such as water. The energetically most favorable orientation for these molecules may be attained at surfaces or interfaces, so that each part of the molecule can reside in an environment for which it has the greatest affinity.

In most cases, the hydrophobic part is formed by one (or more) aliphatic chains $CH_3(CH_2)_n$. The hydrophilic part can be an ion (either anion or cation) that forms a "polar head." The polar head has an affinity to liquids with a high dielectric constant such as water. Surfactants modifying the spreading of liquids on surfaces are of primary importance in various fields of industry, and much literature is devoted to them [16]. They also govern a diversity of phenomena related to the wetting of real surfaces, such as superspreading, which is discussed further (see Section 4.8).

1.5 The Laplace pressure

Surface tension leads to the important and widespread phenomenon of overpressure existing in the interior of drops and bubbles [11]. Consider two media (they may be liquids or a liquid and its vapor), separated by a curved interface. Let us displace the interface infinitesimally. The length of the vector of the normal built in every place of the interface we denote $\delta\varsigma$. Thus, a volume confined between two surfaces is $\delta\varsigma\,\mathrm{d}S$, where $\mathrm{d}S$ is the element of the surface. Let p_1 and p_2 be pressures in media 1 and 2 respectively, and let $\delta\varsigma$ be positive when displacement occurs toward medium 2 (Figure 1.5). The work necessary for the volume change $\delta\varsigma\,\mathrm{d}S$ is:

$$\int(-p_1 + p_2)\delta\varsigma\,\mathrm{d}S\,. \tag{1.8}$$

Total work δW for the displacement of the surface includes the work $\gamma\delta S$ necessary for the change of the interface (γ is the interfacial tension). Hence, the total work equals:

$$\delta W = -\int(p_1 - p_2)\delta\varsigma\,\mathrm{d}S + \gamma\delta S\,. \tag{1.9}$$

The thermodynamic equilibrium is attained when the requirement $\delta W = 0$ is satisfied. Now let R_1 and R_2 be the main radii of curvature of the surface at a certain point (R_1

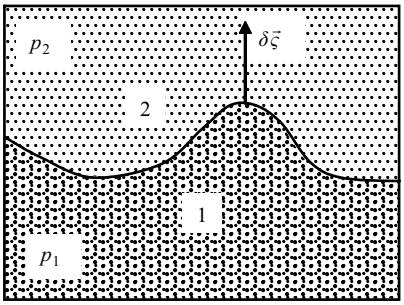

Fig. 1.5: A curved interface characterized by a normal vector $\delta\vec{\varsigma}$ separates Media 1 and 2.

and R_2 are positive when they are oriented toward the first medium). The linear elements $\mathrm{d}l_1$ and $\mathrm{d}l_2$ built in the planes of the main cross-sections obtain under infinitesimal displacement of the surface the increments given by $\delta\varsigma_1/R_1\,\mathrm{d}l_1$ and $\delta\varsigma_2/R_2\,\mathrm{d}l_2$. Thus, the element of the interface $\mathrm{d}S = \mathrm{d}l_1\,\mathrm{d}l_2$ is equal after the displacement:

$$\mathrm{d}l_1\left(1+\frac{\delta\varsigma}{R_1}\right)\mathrm{d}l_2\left(1+\frac{\delta\varsigma}{R_2}\right)\approx \mathrm{d}l_1\,\mathrm{d}l_2\left(1+\frac{\delta\varsigma}{R_1}+\frac{\delta\varsigma}{R_2}\right). \tag{1.10}$$

The change of the surface element is given by:

$$\delta\varsigma\,\mathrm{d}S\left(\frac{1}{R_1}+\frac{1}{R_2}\right). \tag{1.11}$$

This yields for the change of the surface:

$$\delta S = \int \delta\varsigma\left(\frac{1}{R_1}+\frac{1}{R_2}\right)\mathrm{d}S\,. \tag{1.12}$$

Substitution of (1.12) into (1.9) yields:

$$\int \delta\varsigma\left[(p_1-p_2)-\gamma\left(\frac{1}{R_1}+\frac{1}{R_2}\right)\right]\mathrm{d}S = 0\,. \tag{1.13}$$

The condition (1.13) is valid under arbitrary $\delta\varsigma$; thus, we eventually obtain:

$$p_1 - p_2 = p_\mathrm{L} = \gamma\left(\frac{1}{R_1}+\frac{1}{R_2}\right). \tag{1.14}$$

Equation (1.14) is the famous Laplace formula defining the surface (Laplace) overpressure p_L. When we have a drop surrounded by vapor it obtains the form $p_\mathrm{liq} - p_\mathrm{vap} = p_\mathrm{L} = \gamma(1/R_1 + 1/R_2)$, where $p_\mathrm{liq}, p_\mathrm{vap}$ are the pressures of a liquid and vapor respectively. The meaning of the main radii of curvature of the surface is illustrated in Figure 1.6, presenting a dumbbell-like body. We look for R_1 and R_2 at a certain point of the surface enclosing the dumbbell and characterized by a normal vector $\vec{\varsigma}$. To calculate R_1 and R_2 we have to cut our surface with two mutually orthogonal planes intersecting each other along $\delta\vec{\varsigma}$ (Figure 1.6). The intersection of these planes with the interface defines two curves, the radii of curvature of which are R_1 and R_2. The radii of curvature could be positive or negative. R is defined as positive if the center of the corresponding circle lies inside the bulk and negative otherwise. The curvature

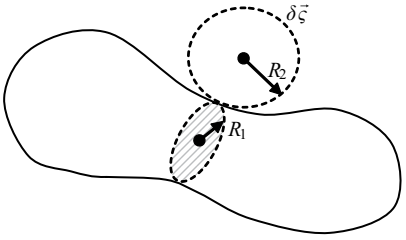

Fig. 1.6: Scheme depicting the main radii of curvature of a dumbbell-like surface.

of the surface $\hat{C} = 1/R_1 + 1/R_2$ is independent on the orientation of the planes. For a *spherical* droplet $R_1 = R_2 = R$ and consequently for the Laplace pressure jump we have $p_1 - p_2 = p_{\text{liq}} - p_{\text{vap}} = p_{\text{L}} = 2\gamma/R$. A derivation of this formula based on simple intuitive arguments is supplied in Appendix 1B.

1.6 Surface tension of solids

Unlike the situation with liquids, the surface tension of solids is not necessarily equal to the surface free energy. We can imagine the process of forming a fresh surface of condensed phase divided into two steps. First, the material is cleaved, keeping the atoms fixed in the same positions that they occupied in the bulk; second, the atoms in the surface region are allowed to rearrange themselves to their final equilibrium positions. In the case of liquid, these two steps occur as one, owing to the high mobility of liquid molecules, but with solids the second step may occur only slowly, owing to the low mobility of molecules constituting the surface region [1, 4]. Thus, it is possible to stretch a surface of a solid without changing the number of atoms in it, but only their distances from one another.

Thus, the surface stretching tension (or surface stress) τ is defined as the external force per unit length that must be applied to retain the atoms or molecules in their initial equilibrium positions (equivalent to the work spent in stretching the solid surface in a two-dimensional plane), whereas a *specific* surface free energy $\hat{G}_{\text{S}}$ is the work spent in forming a unit area of a solid surface. The relation between surface free energy and stretching tension could be derived as follows. For an anisotropic solid, if the area is increased in two directions by $\mathrm{d}S_1$ and $\mathrm{d}S_2$ the relation between τ_1, τ_2 and the free energy per unit area $\hat{G}_{\text{S}}$ is given by:

$$\tau_1 = \hat{G}_{\text{S}} + S_1 \frac{\mathrm{d}\hat{G}_{\text{S}}}{\mathrm{d}S_1}; \quad \tau_2 = \hat{G}_{\text{S}} + S_2 \frac{\mathrm{d}\hat{G}_{\text{S}}}{\mathrm{d}S_2} . \tag{1.15}$$

If the solid surface is isotropic, equation (1.15) reduces to:

$$\tau = \frac{\mathrm{d}(S\hat{G}_{\text{S}})}{\mathrm{d}S} = \hat{G}_{\text{S}} + S\frac{\mathrm{d}\hat{G}_{\text{S}}}{\mathrm{d}S} . \tag{1.16}$$

For liquids, the last term in equation (1.16) is zero, hence $\tau = \hat{G}_{\text{S}} = \gamma$.

1.7 Values of surface tensions of solids

De Gennes et al. proposed to divide all solid surfaces into two large groups [3].

(1) *High-energy surfaces*. These are surfaces possessing the specific surface energy $\hat{G}_{\text{S}} \approx 200–5000\,\text{mJ/m}^2$. High-energy surfaces are inherent for materials built with strong chemical bonds, such as ionic, metallic, or covalent. For a covalent bond-built diamond, the surface energy could be approximately equaled to half of

the energy required to break the total number of covalent bonds passing through a unit of a cross-sectional area of the material [4]. The appropriate calculation supplies the value $5670\,\mathrm{mJ/m^2}$. For ionic and metallic solids, the calculations are more complicated; for the values of surface energies of various solids see Israelachvili [9].

(2) *Low-energy solid surfaces*. These are surfaces possessing the specific surface energy of $10–50\,\mathrm{mJ/m^2}$. Low-energy solid surfaces are inherent for solids based on the relatively weak van der Waals chemical bonds, such as in polymers. As already shown in Section 1.2, the London dispersion force dominates in van der Waals forces. Thus, the estimation $\hat{G}_S \approx \mathrm{const}/d_m^2$ is valid for solids built on the van der Waals forces. Moreover, a straightforward calculation of the energy of the London interaction given by equation (1.4) supplies the value $k_B T$ [9]. Hence, for a rough estimation of the surface energy of this type of solid we can take $\hat{G}_S \approx k_B T/d_m^2$. This formula explains the surprising proximity of specific surface energies of very different solids and liquids, such as plastics and organic solvents. For example, the specific surface energy of polystyrene equals $32–33\,\mathrm{mJ/m^2}$ (compare this value with surface tensions of organic solvents supplied in Table 1.1) [9]. The extended discussion of the minimal possible specific surface energy of solids has been carried out in Nosonovsky and Chen [14].

Additional Reading

Lautrup [12] contains an excellent introduction to the macroscopic approach to surface tension-related problems. Patashinski et al., Granek et al., Guttman et al., and Kimball [6, 8, 10, 15] introduce the exotic notion of a "negative surface tension." Consider the situation when a chemical reaction between two immiscible liquids creates surfactant molecules (see Section 1.4) at the interface between them. In this case, the interfacial surface tension decreases with as the amount of the surfactant increases [15]. The overpopulation of the interface by surfactants can give rise to a negative surface tension, when an interfacial reaction is faster than the time scale of the system's equilibration [15]. Other mechanisms that can render the interfacial tension transiently negative have been discussed in the context of micro-emulsions and spontaneous emulsification [6, 8]. Remarkably the first discussion of the exotic case of "negative surface tension" took place 100 years ago [10].

Appendix 1A. The short-range nature of intermolecular forces

The Keesom, Debye, and London dispersion forces introduced in Section 1.2 all decrease with the distance as $\approx 1/r^6$. All these forces contribute to the so-called *van der Waals forces* acting between molecules. The power law index −6 is of primary importance for constituting bulk and surface properties of condensed phases. Because of

this power law, the total interaction of the molecule with other molecules is defined by neighboring ones, and the contribution of the distant molecules is negligible. Let us discuss a cubic vessel L containing molecules with a diameter d_m attracting through a potential $U(r) = -\widetilde{C}/r^n$, where $\widetilde{C}$ is the constant, and n is an integer. Let us also suppose that the number density of molecules $\widetilde{\rho}$ is constant. Let us estimate the total energy of interaction of *one particular molecule* with all the other molecules in the vessel $U_\mathrm{int}^\mathrm{total}$:

$$U_\mathrm{int}^\mathrm{total} = \int_{d_\mathrm{m}}^{\mathrm{L}} U(r)\widetilde{\rho}4\pi r^2\,\mathrm{d}r = -4\pi\widetilde{C}\widetilde{\rho}\int_{d_\mathrm{m}}^{\mathrm{L}} r^{2-n}\,\mathrm{d}r = -\frac{4\pi\widetilde{C}\widetilde{\rho}}{(n-3){d_\mathrm{m}}^{n-3}}\left[1-\left(\frac{d_\mathrm{m}}{L}\right)^{n-3}\right]. \tag{1.17}$$

Taking into account $d_\mathrm{m}/L < 1$, we recognize that long-range contributions from distant molecules disappear only for $n > 3$. When $d_\mathrm{m}/L \ll 1$, $n > 3$ we obtain:

$$U_\mathrm{int}^\mathrm{total} = -\frac{4\pi\widetilde{C}\widetilde{\rho}}{(n-3){d_\mathrm{m}}^{n-3}}. \tag{1.18}$$

But for $n < 3$, we have $(d/L)^{n-3}$ greater than unity, and for $L \gg d_\mathrm{m}$ the contribution from distant molecules dominates over neighboring ones (for $n = 3$ formula (1.17) gives $U_\mathrm{int}^\mathrm{total} \approx \log(d_\mathrm{m}/L)$, which is usually considered to be long-ranged). When $n > 3$, the size of the system should not be taken into account, and some of the thermodynamic properties such as pressure and temperature turn out to be *intensive*. Thus, we see that the power index $n = 6$ turns out to be of primary importance, allowing us to neglect distant interactions between molecules. However, we see later that in certain cases the range of intermolecular forces between liquid layers can extend out to 100 nm.

Appendix 1B. The Laplace pressure from simple reasoning

Let us consider a drop of liquid 1 placed in liquid 2 (Figure 1.7). The drop is supposed to be in equilibrium. The minimal surface energy of a drop corresponds to its spherical shape of radius R. Assume that the pressure in the drop is p_1 and the pressure outside the drop is p_2. If the interface between liquids is displaced by an amount of $\mathrm{d}R$ (Figure 1.7), according to the principle of virtual works the total work $\delta W = 0$. The total work is given by:

$$\delta W = p_1\,\mathrm{d}V_1 + p_2\,\mathrm{d}V_2 - \gamma\,\mathrm{d}S, \tag{1.19}$$

where γ is the surface tension at the interface between liquids. Considering $\mathrm{d}V_1 = -\mathrm{d}V_2 = 4\pi R^2\,\mathrm{d}R$, $\mathrm{d}S = 8\pi R\,\mathrm{d}R$ immediately yields:

$$p_1 - p_2 = p_\mathrm{L} = \frac{2\gamma}{R}. \tag{1.20}$$

The well-known simplified Laplace formula is recognized.

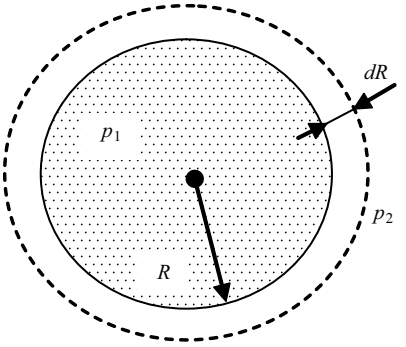

Fig. 1.7: A droplet of liquid 1 of the radius R is in equilibrium with the surrounding liquid 2.

Bullets

- Surface tension is a tension in a surface due to the unusual energetic state of the surface molecules.
- For liquids at a constant temperature and pressure and in equilibrium, the surface tension is physically equivalent to the specific surface free energy.
- The surface tension of solids is not necessarily equal to the surface free energy.
- Surface tension is stipulated by the London dispersion forces and metallic or hydrogen bonds (when they are present).
- The surface tension of most liquids at room temperature is within $20–70\,\mathrm{mJ/m^2}$.
- The exotic case of the "negative surface tension" is possible [6, 8, 10, 15].
- Surface tension is temperature-dependent.
- Surface tension leads to the Laplace overpressure existing in the interior of drops and bubbles, $p_\mathrm{L} = p_1 - p_2 = \gamma(1/R_1 + 1/R_2)$.

References

[1] A. W. Adamson, and A. P. Gast, *Physical Chemistry of Surfaces*, 6th edn., Wiley-Interscience Publishers, New York, 1990.
[2] E. Bormashenko, Why are the values of the surface tension of most organic liquids similar? *Am. J. Phys*. **78** (2010), 1309–1311.
[3] P. de Gennes, F. Brochard-Wyart, and D. Quéré, *Capillarity and Wetting Phenomena*, Springer, Berlin, 2003.
[4] H. Y. Erbil, *Surface Chemistry of Solid and Liquid Interfaces*, Blackwell, Oxford, 2006.
[5] F. M. Fowkes, Additivity of intermolecular forces at interfaces, *J. Phys. Chem*. **67** (1962), 2538–2541.
[6] R. Granek, R. C. Ball, and M. E. Cates, Dynamics of spontaneous emulsification, *J. Phys. II France* **3**(6) (1993) 829–849.
[7] V. R. Gray, Surface aspects of wetting and adhesion, *Chemistry & Industry* **23** (1965), 969–978.
[8] S. Guttman, Z. Sapir, M. Schultz, A. V. Butenko, B. M. Ocko, M. Deutsch, and E. Sloutskin, How faceted liquid droplets grow tails, *PNAS*, **113** (2016) 493–496.
[9] J. N. Israelachvili, *Intermolecular and Surface Forces*, 3rd edn., Elsevier, Amsterdam, 2011.

[10] A. L. Kimball, Negative surface tension, *Science*, **45** (1917) 85–87.
[11] L. Landau and E. Lifshitz, *Fluid Mechanics*, 2nd edn., Butterworth-Heinemann, Oxford, UK, 1987.
[12] B. Lautrup, *Physics of Continuous Matter: Exotic and Everyday Phenomena in the Macroscopic World*, 2nd edn., CRS Press, Boca Raton, FL, 2011.
[13] J. C. Moore, A. Kazachkov, A. G. Anders, and C. Willis, *The Danger of misrepresentations in science education*, in: G. Planinsic and A. Mohoric (eds), Informal Learning and Public Understanding of Physics, 3rd International GIREP Seminar 2005, Selected Contributions, 399–404, University of Ljubljana, Ljubljana, Slovenia, 2005.
[14] M. Nosonovsky and Z. Chen, Revisiting lowest possible surface energy of a solid, *Surf. Topogr. Metrol. Prop.* **5** (2017) 045001.
[15] A. Z. Patashinski, R. Orlik, K. Paclawski, M. A. Ratner, and B. A. Grzybowski, The unstable and expanding interface between reacting liquids: theoretical interpretation of negative surface tension, *Soft Matter*, **8** (2012) 1601–1608.
[16] L. L. Schramm, *Emulsions, Foams and Suspensions, Fundamentals and Applications*, Wiley, Weinheim, 2005.
[17] Y.-Z. Su and R. W. Flumerfelt, A continuum approach to microscopic surface tension for the *n*-alkanes, *Ind. Eng. Chem. Res.* **35** (1996), 3399–3402.
[18] C. J. Van Oss, R. J. Good, and M. K. Chaudhury, Additive and nonadditive surface tension components and the interpretation of contact angles, *Langmuir* **4** (1988), 884–891.

2 Wetting of ideal surfaces

2.1 What is wetting? The spreading parameter

Wetting is the ability of a liquid to maintain contact with a solid surface, resulting from intermolecular interactions when the two are brought together. The idea that wetting of solids depends on the interaction between particles constituting a solid substrate and liquid has been expressed explicitly in the famous essay by Thomas Young [48]. When a liquid drop is placed on the solid substrate, two main *static* scenarios are possible: either liquid spreads completely, or it sticks to the surface and forms a cap as shown in Figure 2.1a (a solid surface may be flat or rough, homogenous or heterogeneous). The precise definition of the contact angle θ, shown schematically in Figure 2.1a, is given later (actually it is the apparent contact angle); at this stage, we only require that the radius of the droplet should be much larger than the characteristic scale of the surface roughness. The observed wetting scenario is dictated by a spreading parameter:

$$\Psi = \hat{G}^*_{\mathrm{SA}} - (\hat{G}^*_{\mathrm{SL}} + \hat{G}_{\mathrm{LA}}) \,, \tag{2.1}$$

where $\hat{G}^*_{\mathrm{SA}}$ and $\hat{G}^*_{\mathrm{SL}}$ are the *specific* surface energies at the rough solid/air and solid liquid interfaces (the asterisk reminds us that $\hat{G}^*_{\mathrm{SA}}$ and $\hat{G}^*_{\mathrm{SL}}$ do not coincide with the specific surface energies of smooth surfaces $\hat{G}_{\mathrm{SA}}$, $\hat{G}_{\mathrm{SL}}$), and $\hat{G}_{\mathrm{LA}} = \gamma$ is the specific energy of the liquid/air interface. When $\Psi > 0$, total wetting is observed, depicted in Figure 2.1b. The liquid spreads completely to lower its surface energy ($\theta = 0$). When $\Psi < 0$, the droplet does not spread, but forms a cap resting on a substrate with a contact angle θ, as shown in Figure 2.1a. This case is called *partial wetting*. When the liquid is water, surfaces demonstrating $\theta < \pi/2$ are called *hydrophilic*, whereas surfaces characterized by $\theta > \pi/2$ are referred to as *hydrophobic*. One more extreme situation is possible, when $\cos\theta = -1$, as depicted in Figure 2.1c. This is the situa-

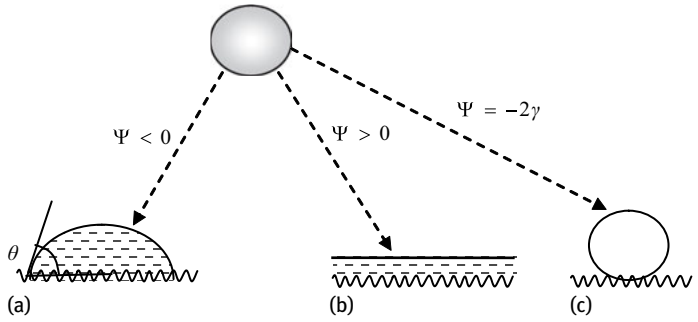

Fig. 2.1: The three wetting scenarios for sessile drops. a: partial wetting; b: complete wetting; c: complete dewetting.

https://doi.org/10.1515/9783110583144-002

tion of *complete dewetting* or *superhydrophobicity*, which is discussed in Chapter 6. When the solid surface is atomically flat, chemically homogeneous, isotropic, insoluble, nonreactive, and nonstretched (thus, there is no difference between the specific surface energy and surface tension, as explained in Section 1.5), the spreading parameter obtains its convenient form:

$$\Psi = \gamma_{SA} - (\gamma_{SL} + \gamma) \,, \tag{2.2}$$

where $\gamma_{SA}, \gamma_{SL}, \gamma$ are the surface tensions at the solid/air (vapor), solid/liquid, and liquid/air interfaces respectively [17]. When the droplet forms a cap, the line at which solid, liquid, and gaseous phases meet is called the *triple* or (three phase) *line*.

2.2 The Young equation

We will start from wetting of an *ideal*, i.e., atomically flat, chemically homogeneous, isotropic, insoluble, nonreactive, and nondeformed, solid surface in the situation when $\Psi < 0$. When a droplet is deposited on such an ideal substrate, described in Figure 2.2, its free energy G could be written as:

$$G\,[h(x,y)] = \iint\limits_{S} \left[\gamma\sqrt{(1+(\nabla h)^2} + (\gamma_{SL} - \gamma_{SA})\right] \mathrm{d}x\,\mathrm{d}y \,, \tag{2.3}$$

where $h(x, y)$ is the local height of the liquid surface above the point (x, y) of the substrate (it is supposed latently that there is no difference between surface tensions and surface energies for γ_{SL}, γ_{SA}), and the integral is extended over the substrate area. The first term of the integrand presents the capillary energy of the liquid cap and the second term describes the change in the energy of the solid substrate covered by liquid.

Now we want to complicate the situation and expose our droplet to an external field. We restrict ourselves with an axially symmetrical situation depicted in Figure 2.2, and thus the interaction of the droplet with the field is described by the linear density $U(x, h(x))$ of the additional energy with the dimension of (J/m)

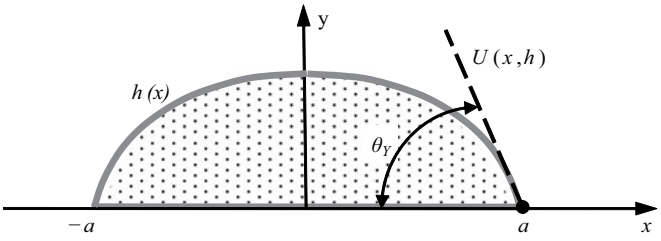

Fig. 2.2: A cross-section of the spherically symmetrical droplet deposited on the ideal solid substrate and exposed to an external field $U(x, h)$.

$U(x, h(x)) = \int_0^{h(x)} 2\pi x w(x, y)\,\mathrm{d}y$, where $w(x, y)$ is the volume energy density of the droplet in the external field. The functions $w(x, y)$ and $U(h(x), x)$ are dictated by the external field and are supposed to be known (for example, for a uniform gravity field $w = \rho g y/2$, $U(x, h(x)) = x/2\pi\rho g h^2(x)$, where ρ is the density of the liquid). Finally, the free energy of the droplet is given by:

$$G(h, h') = \int_0^a \left[2\pi\gamma x\sqrt{1 + h'^2} + 2\pi x(\gamma_{SL} - \gamma_{SA}) + U(x, h)\right]\mathrm{d}x\,, \tag{2.4}$$

where $h' = \mathrm{d}h/\mathrm{d}x$. We also suppose that the droplet does not evaporate; thus, the condition of the constant volume V should be considered:

$$V = \int_0^a 2\pi x h(x)\,\mathrm{d}x = \text{const}\,. \tag{2.5}$$

If we want to calculate the shape of the droplet, equations (2.4) and (2.5) reduce the problem to minimization of the functional:

$$G(h, h') = \int_0^a \widetilde{G}(h, h', x)\,\mathrm{d}x\,, \tag{2.6}$$

$$\widetilde{G}(h, h', x) = 2\pi\gamma x\sqrt{1 + h'^2} + 2\pi x(\gamma_{SL} - \gamma_{SA}) + U(x, h) + 2\pi\lambda x h\,, \tag{2.7}$$

where λ is the Lagrange multiplier to be deduced from equation (2.5). For a calculation of the droplet's shape we would have to solve the appropriate Euler–Lagrange equations. However, we do not focus on the calculation of the droplet's shape, as our interest is the contact angle θ corresponding to the equilibrium of the droplet. Now we make one of the main assumptions of our treatment: *we suppose that the boundary (the triple line) of the droplet is free to slip along the x-axis*. It has to be emphasized that we solve the variational problem with *free endpoints*. Thus, the conditions of transversality of the variational problem should be considered [21]. The use of the transversality conditions of variational problems is explained in detail in Appendix 2A at the end of this chapter. The transversality condition at the endpoint a yields:

$$(\widetilde{G} - h'\widetilde{G}'_{h'})_{x=a} = 0\,, \tag{2.8}$$

where $\widetilde{G}'_{h'}$ denotes the h' derivative of $\widetilde{G}$. Substitution of formula (2.7) into the transversality condition (2.8), and taking into account $h(a) = 0$, $U(x = a, h = 0) = 0$ gives rise to:

$$\left(\gamma\sqrt{1 + h'^2} + \gamma_{SL} - \gamma_{SA} - \frac{\gamma h'^2}{\sqrt{1 + h'^2}}\right)_{x=a} = 0\,. \tag{2.9}$$

Simple transformations yield:

$$\left(\frac{1}{\sqrt{1 + h'^2}}\right)_{x=a} = \frac{\gamma_{SA} - \gamma_{SL}}{\gamma}\,. \tag{2.10}$$

Taking into account $h'(x = a) = -\tan\theta_Y$, where θ_Y is the equilibrium (Young) contact angle immediately yields:

$$\cos\theta_Y = \frac{\gamma_{SA} - \gamma_{SL}}{\gamma} . \tag{2.11}$$

Expression (2.11) presents the well-known *Young equation*. It asserts that the contact angle θ is unambiguously defined by the triad of surface tensions: γ, γ_{SL}, γ_{SA}, as was first stated by Sir Thomas Young: "For each combination of a solid and a fluid, there is an appropriate angle of contact between the surfaces of the fluid, exposed to the air, and to the solid" [48]. The *Young contact angle* θ_Y is supplied by equation (2.11). The *Young contact angle* is the *equilibrium* contact angle that a liquid makes with an *ideal* solid surface [32]. It is shown later that for droplets or surfaces with very small radii of curvature deposited on the *ideal* surfaces, the equilibrium contact angle may be different owing to line tension. Equation (2.11) tells us that the *Young angle* depends only on the physicochemical nature of the three phases and that it is *independent of the droplet shape volume and external field U* under very general assumptions about U, i.e., $U = U(x, h(x))$. The external field may deform the droplet, but it has no influence on the Young angle θ_Y.

In this section, we developed the main mathematical tool of our approach, which turns out to be extremely powerful for solving wetting problems, i.e., the use of transversality conditions of the variational problem of wetting (for details see the Appendix 2A at the end of this chapter). We also introduced one of the key notions of our book, i.e., the *Young contact angle* [8, 31, 32]. The use of transversality conditions form the general framework of our book, allowing general and accurate solving of wetting problems that are very different in nature.

The traditional way of deriving the Young equation is by equating the capillary forces acting on the triple line, as shown in Figure 2.3. When normalized to a unit length of the triple line, these forces are the interfacial tensions γ, γ_{SL}, γ_{SA}. Projecting these forces on the horizontal plane immediately yields:

$$\gamma\cos\theta_Y = \gamma_{SA} - \gamma_{SL} . \tag{2.12}$$

Comparing equation (2.12) with equation (2.2) supplies the useful formula:

$$\Psi = \gamma(\cos\theta_Y - 1) . \tag{2.13}$$

It could be recognized that in the situation of *complete dewetting* or *superhydrophobicity*, shown in Figure 2.1c, $\Psi = -2\gamma$. This result is intuitively clear: indeed, in the situation of complete dewetting, there is no actual contact of a droplet with a solid

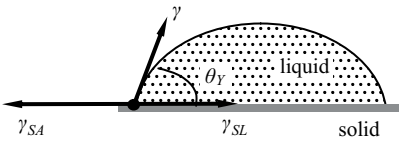

Fig. 2.3: Scheme illustrating the Young equation.

surface, and the spreading parameter is totally defined by the liquid/air surface specific energy γ. Actually, this situation is unachievable on *flat* surfaces, but it exists on *rough* surfaces, as shown in Chapter 6.

There are also other simple ways of proving the Young equation by exploiting the principle of virtual works or other convenient methods of mathematical physics [5, 22]. However, we preferred the variational approach for two reasons: (1) it demonstrated the independence of the equilibrium contact angle from the external fields (this fact is not so intuitively clear), and (2) the variational approach supplies a key to much more complicated problems.

2.3 Wetting of flat, homogeneous, curved surfaces

For the sake of simplicity, we start with a 2D wetting problem, where a cylindrical drop extended uniformly in the y direction is under discussion (Figure 2.4 depicts the cross-section of such a drop). We consider the liquid drop that is symmetrical around the z-axis deposited on the curved solid substrate described by the given function $f(x)$ and exposed to some external field that is symmetrical around the z-axis. The interaction of the droplet with the field gives rise to the linear energy density $U(x, h(x))$, as was shown in the previous section. The free energy of the droplet is supplied by:

$$G(h, h') = \int_{-a}^{a} \left[\gamma \sqrt{1 + h'^2} + (\gamma_{SL} - \gamma_{SA}) \sqrt{1 + f'^2} + U(x, h(x)) \right] \mathrm{d}x \,, \tag{2.14}$$

where $h(x)$ is the local height of the liquid surface above the point x of the substrate (the profile of the droplet $h(x)$ is assumed to be a single-valued and even function). Condition (2.15) of the constant area S also has to be taken into account:

$$S = \int_{-a}^{a} [h(x) - f(x)] \, \mathrm{d}x = \text{const} \,. \tag{2.15}$$

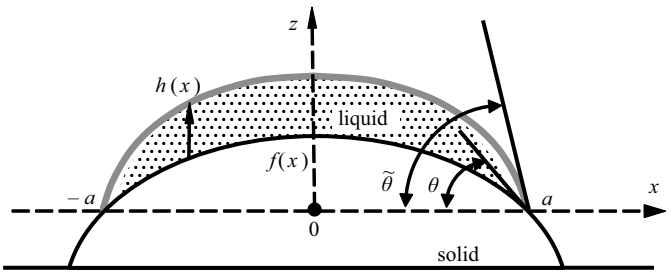

Fig. 2.4: Scheme of the section of a cylindrical drop deposited on a flat homogeneous curved substrate.

Note that this is equivalent to the constant volume requirement in the case of cylindrical "drops" (extended in the y direction; h is independent of y).

Equations (2.14) and (2.15) reduce the problem to minimization of the functional:

$$G(h, h') = \int_{-a}^{a} \widetilde{G}(h, h', x)\,\mathrm{d}x\,, \tag{2.16}$$

$$\widetilde{G}(h, h', x) = \gamma\sqrt{1 + h'^2} + (\gamma_{\mathrm{SL}} - \gamma_{\mathrm{SA}})\sqrt{1 + f'^2} + U(x, h) + \lambda(h - f)\,, \tag{2.17}$$

where λ is the Lagrange multiplier to be deduced from equation (2.15). The constant terms in equation (2.17) could be omitted when the functional $\widetilde{G}$ is minimized; however, they turn out to be important for the analysis of the situation at the boundary. As mentioned above, we focus on the calculation of θ and ignore the calculation of the droplet's shape. As for flat surfaces, the variational problem with *free endpoints* is solved, i.e., it is suggested now that the endpoints of the drop $x = \pm a$ are not fixed and are free to move along the line $f(x)$. Without the loss of generality, we suggest that the curve $f(x)$ and the entire problem are symmetrical around the vertical axis. Thus, the transversality condition in this case obtains the form [21]:

$$\left[\widetilde{G} + \widetilde{G}'_{h'}(f' - h')\right]_{x=a} = 0\,, \tag{2.18}$$

where $\widetilde{G}'_{h'}$ denotes the h' derivative of $\widetilde{G}$. Substitution of formula (2.17) into the transversality condition (2.18), and considering $h(a) = f(a)$, $U(a, h(a)) = 0$, gives rise to:

$$\left[\gamma\sqrt{1 + h'^2} + (\gamma_{\mathrm{SL}} - \gamma_{\mathrm{SA}})\sqrt{1 + f'^2} + \frac{\gamma h'(f' - h')}{\sqrt{1 + h'^2}}\right]_{x=a} = 0\,. \tag{2.19}$$

Simple transformations yield:

$$\left[\gamma\frac{1 + h'f'}{\sqrt{1 + h'^2}} + (\gamma_{\mathrm{SL}} - \gamma_{SA})\sqrt{1 + f'^2}\right]_{x=a} = 0\,. \tag{2.20}$$

Taking into account $h'(x = a) = -\tan\theta$, where θ is the slope of the liquid–air interface at $x = a$, and $f'(x = a) = -\tan\widetilde{\theta}$, where $-\tan\widetilde{\theta}$ is the slope of the solid substrate in $x = a$, $(\widetilde{\theta} < \pi/2)$ immediately gives:

$$\cos(\widetilde{\theta} - \theta) = \frac{\gamma_{\mathrm{SA}} - \gamma_{\mathrm{SL}}}{\gamma}\,. \tag{2.21}$$

The Young equation (compare with equation (2.11)) is recognized. It is reasonable to define the equilibrium (Young) contact angle as $\widetilde{\theta} - \theta$. The redefined Young angle is insensitive to an external field, meeting the conditions $U = U(x, h)$, $U \neq U(h')$, $U(a, h(a)) = 0$.

Three-dimensional flat, homogeneous, axially symmetrical surfaces are treated in a similar way. The free energy functional G supplying the free energy of the droplet assumes the form $G(h, h') = \int_0^a \widetilde{G}(h, h', x)\,\mathrm{d}x$, where

$$\widetilde{G}(h, h', x) = 2\pi\gamma x\sqrt{1 + h'^2} + 2\pi x\sqrt{1 + f'^2}(\gamma_{\mathrm{SL}} - \gamma_{\mathrm{SA}}) + U(x, h) + 2\pi\lambda x(h - f) \tag{2.22}$$

(λ is the Lagrange multiplier). We leave it to the reader to carry out the challenging exercise of the substitution of formula (2.22) into the transversality condition (2.18) and obtaining the Young equation (2.21).

2.4 Line tension

Surface tension is due to the special energy state of the molecules at a solid or liquid surface. Molecules located at the triple (three-phase) line, where solid, liquid, and gaseous phases meet, are also in an unusual energy state. The notion of line tension has been introduced by Gibbs. Gibbs stated: "These (triple) lines might be treated in a manner entirely analogous to that in which we have treated surfaces of discontinuity. We might recognize linear densities of energy, of entropy, and of several substances which occur about the line, also a certain linear tension" [2]. In spite of the fact that the concept of line tension is intuitively clear, it remains one of the most obscure and disputable notions of the surface science [2]. Researchers disagree not only on the value of the line tension, but even on its sign. Experimental values of a line tension Γ in the range of 10^{-5}–10^{-11} N were reported [2]. Very few methods allowing experimental measurement of line tension were developed [15, 36]. Marmur estimated a line tension as $\Gamma \cong 4d_{\mathrm{m}}\sqrt{\gamma_{\mathrm{SA}}\gamma}\cot\theta_{\mathrm{Y}}$, where d_{m} is the molecular dimension, γ_{SA}, γ are surface energies of solid and liquid correspondingly, and θ_{Y} is the Young angle. Marmur concluded that the magnitude of the line tension is less than $5 \cdot 10^{-9}$ N, and that it is positive for acute and negative for obtuse Young angles [30]. However, researchers reported negative values of line tension for hydrophilic surfaces [36]. As for the magnitude of line tension, the values in the range 10^{-9}–10^{-12} N look realistic. Large values of Γ reported in the literature are most likely due to contaminations of the solid surfaces [17].

Let us estimate the characteristic length scale l at which the effect of line tension becomes important by equating surface and "line" energies: $l \cong \Gamma/\gamma = 1-100$ nm. It is clear that the effects related to line tension can be important for nano-scaled droplets or for nano-scaled rough surfaces.

Let us estimate the influence of line tension on the contact angle of an axisymmetric droplet. The free energy functional supplying its free energy, while also considering line tension, is given by $G(h, h') = \int_0^a \widetilde{G}(h, h', x)\,\mathrm{d}x$, where

$$\widetilde{G}(h, h', x) = 2\pi\gamma x\sqrt{1 + h'^2} + 2\pi x(\gamma_{\mathrm{SL}} - \gamma_{\mathrm{SA}}) + U(h, x) + 2\pi\lambda x h + 2\pi\Gamma\,. \tag{2.23}$$

For the sake of simplicity, Γ is anticipated as constant. Substitution of formula (2.23) into the transversality condition (2.8) yields:

$$\cos\theta = \frac{\gamma_{\mathrm{SA}} - \gamma_{\mathrm{SL}}}{\gamma} - \frac{\Gamma}{\gamma a}\,, \tag{2.24}$$

where a is the contact radius of the droplet. Equation (2.24) represents the well-known Boruvka–Neumann formula considering the effect of line tension [2].

2.5 Disjoining pressure

Now we want to study very thin liquid films deposited on ideal solid surfaces. If we place a film of thickness e (Figure 2.5) on an ideal solid substrate, its specific surface energy is $\gamma_{SL} + \gamma$. However, if the thickness e tends toward zero, we return to a bare solid with a specific surface energy of γ_{SA} [17]. It is reasonable to present the specific surface energy of the film $\hat{G} = G/S$ (S is area) as:

$$\hat{G}(e) = \gamma_{SL} + \gamma + \Omega(e) \,, \tag{2.25}$$

where $\Omega(e)$ is a function of the film defined in such a way that $\lim_{e\to\infty} \Omega(e) = 0$ and $\lim_{e\to 0} \Omega(e) = \Psi = \gamma_{SA} - \gamma_{SL} - \gamma$ [17]. It could be shown that when the molecules of solid and liquid interact via the van der Waals interaction (see Section 1.2), $\Omega(e)$ obtains the form:

$$\Omega(e) = \frac{A}{12\pi e^2} \,, \tag{2.26}$$

where A is the so-called Hamaker constant, which is in the range of $A \cong 10^{-19} \div 10^{-20}$ J [17, 19, 25]. The Hamaker constant could be expressed as:

$$A = \pi^2 \varpi \tilde{\alpha} L(\tilde{\alpha}_S - \tilde{\alpha}_L) \,, \tag{2.27}$$

where $\tilde{\alpha}_L$, $\tilde{\alpha}_S$ are specific volume polarizabilities of liquid and solid substrate respectively, and ϖ is a constant that depends very little on the nature of solid and liquid [17].

It could be seen from equation (2.27) that the Hamaker constant can be positive or negative. It is positive when the solid has higher polarizability than the liquid ($\tilde{\alpha}_S > \tilde{\alpha}_L$). This situation can happen on high-energy surfaces (see Section 1.6); the opposite occurs on low-energy surfaces ($\tilde{\alpha}_S < \tilde{\alpha}_L$). It could be seen from equation (2.25) that when $\Omega(e) < 0$, it diminishes the specific surface energy of the solid/thin liquid film system; thus, the van der Waals interaction thins the film, trying to cover as large a surface of the substrate as possible.

The negative derivative of $\Omega(e)$ is called the disjoining pressure:

$$\Pi(e) = -\frac{\mathrm{d}\Omega}{\mathrm{d}e} = \frac{A}{6\pi e^3} \,, \tag{2.28}$$

Fig. 2.5: Scheme illustrating the origination of the disjoining pressure.

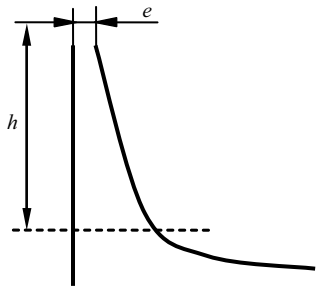

Fig. 2.6: Film of liquid helium climbing upward owing to the disjoining pressure.

introduced into surface science by B. V. Derjaguin [16]. The disjoining pressure given by equation (2.28) is mainly due the London dispersion forces introduced in Section 1.2. The disjoining pressure plays a primary role in the theory of thin liquid films deposited on solid surfaces; however, one of the most amazing examples is discovered when liquid helium is deposited on a solid surface. The polarizability of liquid helium is lower than that of any solid substrate; thus, the Hamaker constant given by formula (2.27) is positive (this corresponds to the repulsive van der Waals film force across an adsorbed helium film), and the disjoining pressure thickens the film to lower its energy. Let us discuss the liquid helium film climbing a smooth vertical wall, depicted in Figure 2.6, and derive the profile of the film $e(z)$. The components of the free energy of the unit area of the film depending on its thickness are supplied by (see equation (2.26)):

$$\hat{G}(e) = \frac{A}{12\pi e^2} + \rho g h e \,. \tag{2.29}$$

The equilibrium corresponds to $\partial \hat{G}/\partial e = 0$, which yields the thickness profile:

$$e(h) = \left(\frac{A}{6\pi\rho g h}\right)^{1/3} . \tag{2.30}$$

Considering that the disjoining pressure becomes important for very thin angstrom-scaled films, when the liquid is water, the range of the effects promoted by the disjoining pressure could be as large as 100 Ångstroms, owing to the Helmholtz-charged double layer [17, 25]. The electrical double layers give rise to the disjoining pressure described by an expression different from (2.28), i.e.,

$$\Pi_{\mathrm{EDL}}(e) = D \exp(-\chi e) \,, \tag{2.31}$$

where $1/\chi \approx 100\,\mathrm{nm}$, and D is the characteristic parameter of the system, which can be either positive or negative [44]. Yet another component of the disjoining pressure Π_{S} is the so-called structural component caused by orientation of water molecules in the vicinity of the solid surface or at the aqueous solution/vapor interface [16, 44]. Only a semi-empirical equation resembling equation (2.31) exists:

$$\Pi_{\mathrm{S}} = \Lambda \exp(-\nu e) \,, \tag{2.32}$$

where Λ and ν are constants, $1/\nu \approx 10\text{–}15$ Å [16, 44].

2.6 Wetting of an ideal surface: influence of absorbed liquid layers and the liquid vapor

Up to this point, we have neglected two important factors: layers of absorbed liquid molecules that may be present on the solid substrate (still supposed to be ideal), and the impact of the gaseous phase. Consideration of these factors was recently carried out by Starov and Velarde [44]. They imposed three obvious conditions of the thermodynamic equilibrium of a droplet/substrate/vapor system. When the drop is in equilibrium, the chemical potentials of the liquid molecules in the ambient vapor phase and the liquid inside the droplet should be equal. The latter results in Kelvin's equation inside the drop:

$$p_{\mathrm{L}} = \frac{\tilde{R}T}{V_{\mathrm{ML}}} \ln \frac{p}{p_{\mathrm{S}}} , \tag{2.33}$$

where $p_{\mathrm{L}} = p_{\mathrm{liq}} - p_{\mathrm{vap}}$, p_{vap}, p_{liq} are the pressures in the vapor and the liquid phases respectively, p_{L} is the Laplace pressure (see Section 1.5), V_{ML} is the molar volume of the liquid (see Section 1.3), p_{S} is the pressure of the saturated vapor at the temperature T above the flat liquid surface, $\tilde{R}$ is the gas constant, and p is the vapor pressure, which is in equilibrium with the drop (for a detailed derivation and explanation of Kelvin's equation see Erbil [19]. Equation (2.33) was the first requirement imposed by the authors [44]. Starov and Velarde also suggested that the solid substrate is covered by a thin layer of a thickness e of absorbed liquid molecules (Figure 2.7). The thermodynamic equilibrium requires equality of chemical potentials of molecules in the vapor phase and in the adsorbed layer. This was the second condition. The third condition was a minimum of the excess free energy of a droplet. These conditions, combined with use of the apparatus of transversality conditions of the variational problem of wetting lead to the following equation defining the contact angle θ:

$$\cos\theta \approx 1 + \frac{1}{\gamma} \int_{\mathrm{e}}^{\infty} \Pi(e)\, \mathrm{d}e , \tag{2.34}$$

where $\Pi(e)$ is the disjoining pressure introduced in the previous paragraph. Emergence of $\Pi(e)$ in equation (2.34) predicting the contact angle is natural, the thickness of the adsorbed liquid layer is supposed to be nano-scaled [44]. It should be stressed that the contact angle θ needs redefinition, because the droplet cap does not touch the solid substrate, as shown in Figure 2.7. Starov and Velarde define the contact angle in this case as an angle between the horizontal axis and the tangent to the droplet cap profile at the point where it touches the absorbed layer of molecules (which is also called the *precursor film*) [44].

Let us estimate the disjoining pressure in the absorbed layer according to $\Pi(e) = A/6\pi e^3$. If we assume $A \approx 10^{-19} \div 10^{-20}$ J, $e = 1$ nm, we obtain giant values for the disjoining pressure: $\Pi(e) \cong 5 \cdot 10^4 \div 5 \cdot 10^5$ Pa. For $e = 10$ nm we obtain much more reasonable values of the disjoining pressure: $\Pi(e) \cong 50 \div 5 \cdot 10^2$ Pa; however, they are still larger or comparable with the Laplace pressure in the drop. For $r \approx 1$ mm, we have $p = 2\gamma/r \cong 140$ Pa. How is the mechanical equilibrium possible in this case? Perhaps

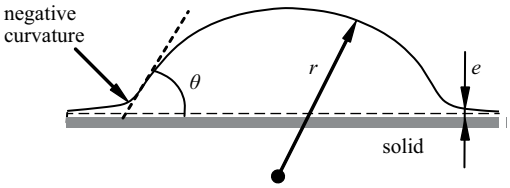

Fig. 2.7: Droplet of the radius r surrounded by the thin layer of liquid of the thickness e governed by the disjoining pressure.

it is due to the negative curvature of the droplet at the area where the cap touches the absorbed layer, as shown in Figure 2.7. Moreover, if we take for the disjoining pressure equation (2.28) we obtain from equation (2.34) $\cos\theta \approx 1 + 1/\gamma \int_e^\infty \Pi(e)\,\mathrm{d}e = 1 + A/12\pi\gamma e^2 > 1$, which corresponds to complete wetting [44]. The latter condition implies that at oversaturation, no solution exists for an equilibrium liquid film thickness e outside the drop. If we take $A < 0$, there is a solution for an equilibrium liquid film thickness e, but such an equilibrium state is unstable [44].

To understand how the partial wetting is possible in this case, Starov and Velarde discussed more complicated forms of disjoining pressure isotherms, comprising the London–van der Waals, double layer, and structural contributions given by formulae (2.28), (2.31), and (2.32). They considered more complicated disjoining pressure isotherms, such as those depicted in Figure 2.8 (curve 2). The development of formula (2.24) yielded:

$$\cos\theta \approx 1 + \frac{1}{\gamma}\int_e^\infty \Pi(e)\,\mathrm{d}e \approx 1 - \frac{S_- - S_+}{\gamma}\,, \tag{2.35}$$

where S_- and S_+ are the areas depicted in Figure 2.8. Obviously (see Starov and Velarde [44]), the partial wetting is possible when $S_- > S_+$. Thus, when a droplet is surrounded by a thin layer of liquid, the possibility of partial wetting depends according to Starov and Velarde on the particular form of the Derjaguin isotherm [44].

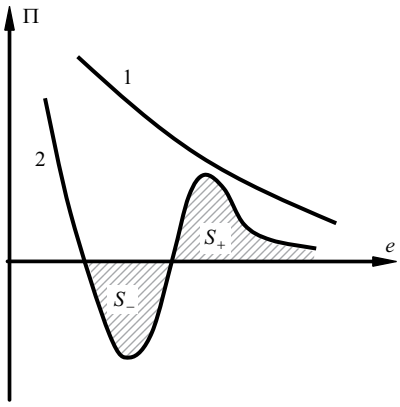

Fig. 2.8: Disjoining pressure (Derjaguin isotherms): 1. isotherm corresponding to the complete wetting, only the London–van der Waals component is considered; 2. isotherm comprising London, double-layer, and structural contributions and corresponding to the partial wetting.

2.7 Gravity and wetting of ideal surfaces: a droplet shape and liquid puddles

Gravity does not influence the Young contact angle, as shown in Section 2.1, but it does deform the droplet shape. The interrelation between gravity and surface tension is described by the Bond number (also known as the Eötvös number):

$$Bo = \frac{\rho g L^2}{\gamma}\,, \tag{2.36}$$

where L is the characteristic length scale, which in the case of the droplet deposited on the solid substrate obviously equals the radius of the droplet r; hence, $Bo = \rho g r^2/\gamma$. When $Bo \ll 1$, the effects due to gravity are negligible, and the shape of the droplet is dictated by the surface tension. There exists an alternative way of thinking about the interrelation between gravity and surface tension, namely introducing the notion of the so-called capillary length. The hydrostatic pressure in a droplet is of the order of magnitude $\rho g 2r$, whereas the Laplace pressure is $2\gamma/r$. Equating these pressures supplies a characteristic length scale:

$$r = l_{\mathrm{ca}} = \sqrt{\frac{\gamma}{\rho g}}\,, \tag{2.37}$$

which is called *the capillary length* [17]. Comparing (2.36) and (2.37) shows that formula (2.37) actually rephrases expression (2.36). The value of l_{ca} is of the order of magnitude of a few millimeters for the vast majority of liquids and even for mercury, for which both ρ and γ are large. For clean water, the capillary length equals 2.7 mm. When $r \ll l_{\mathrm{ca}}$, the effects due to gravity are negligible, and the drop deposited on the solid substrate keeps the shape of a spherical cap, as shown in Figure 2.9a.

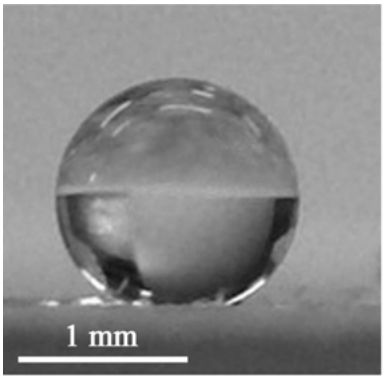

(a)

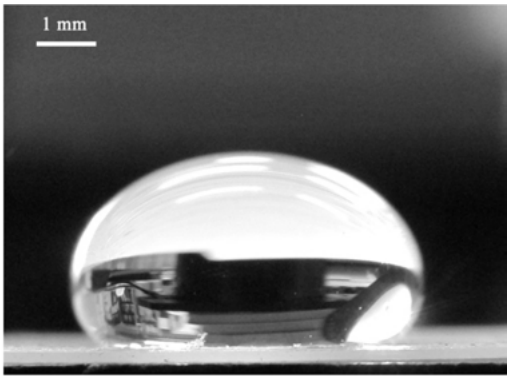

(b)

Fig. 2.9: a: a 10–µl water droplet maintains the form of a spherical cap. The radius of the droplet is less than the capillary length l_{ca}; b: a 200-µl droplet deformed by gravity.

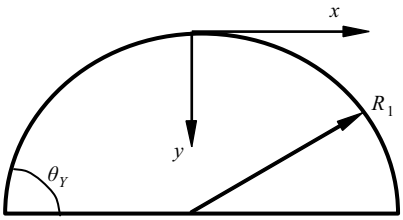

Fig. 2.10: Frame used for the calculation of the shape of a "heavy" droplet deformed by gravity.

The most complicated case occurs when $r \approx l_{ca}$. In this situation, where both gravity- and surface tension-related effects are essential, the Laplace equation is used for the calculation of the droplet shape, as depicted in Figure 2.9b. Application of expression (1.14) while considering gravity yields:

$$\frac{2\gamma}{b} = \gamma\left(\frac{1}{R_1} + \frac{1}{R_2}\right) - \rho g y \,, \tag{2.38}$$

where b is the radius of the curvature at the drop apex, R_1 is the radius of the curvature in the plane of the paper, R_2 is the radius of curvature in the plane normal to the plane of the paper, and y is the vertical distance from the drop apex (Figure 2.10). Simple mathematical considerations supplied in Chatterjee [14] transform equation (2.38) to the following dimensionless equation:

$$2Y''_{x,y=0} = \frac{Y'}{X\sqrt{1+Y'^2}} + \frac{Y''}{(1+Y'^2)^{3/2}} - Bo \cdot Y \,, \tag{2.39}$$

where Y and X are dimensionless coordinates divided by R_{eq}, which is the radius of the curvature of the drop apex of the spherical drop of the same volume, $Bo = \rho g R/\gamma$ (see equation (2.36)) [14]. The numerical solutions of equation (2.39) are supplied in [14]. However, it was shown that for practical purposes the shape of a gravity-deformed droplet could be well approximated by an oblate spheroid [29, 47]. It is important that the use of the oblate spheroid model keeps the contact angle practically constant with the volume growth (the equilibrium contact angle is not influenced by gravity, as demonstrated in Section 2.1).

Now let us discuss the situation when the characteristic length of the droplet is much larger than the capillary length l_{ca}. In this case, gravity flattens the droplet and it forms a "liquid puddle," depicted in Figure 2.11a. The thickness h of this puddle results from the competition between the capillary forces (per unit length) and gravity [17]. Consider the balance of force acting on the shaded part of the puddle (Figure 2.11b). The force acting on the unit length of the puddle resulting from gravity (hydrostatic pressure) equals $\widetilde{f} = \int_0^h \rho g(h-z)\,\mathrm{d}z = 1/2\rho g h^2$. The equilibrium of forces per unit length of the triple line yields:

$$\frac{1}{2}\rho g h^2 + \gamma_{SA} - (\gamma + \gamma_{SL}) = 0 \,, \tag{2.40}$$

which leads to:

$$\Psi = -\frac{1}{2}\rho g h^2 \,, \tag{2.41}$$

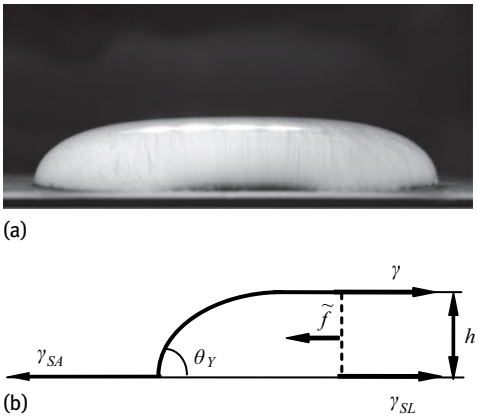

Fig. 2.11: a: liquid "puddle" flattened by gravity placed on the polymer substrate; b: balance of forces acting on the unit length of the triple line of the "puddle.".

where Ψ is a spreading parameter that was introduced in Section 2.1. As was shown, gravity does not influence the contact angle; hence, the Young equation takes place: $\gamma_{SA} - (\gamma \cos\theta_Y + \gamma_{SL}) = 0$. Combining the Young equation with equation (2.40) gives

$$\frac{1}{2}\rho g h^2 = \gamma(1 - \cos\theta_Y) \,. \tag{2.42}$$

Finally, we obtain for the equilibrium thickness of the puddle:

$$h = 2l_{ca} \sin\frac{\theta_Y}{2} \,. \tag{2.43}$$

This surprising result predicts that the height of a liquid puddle is entirely defined by the Young angle of the liquid on a given substrate and the capillary length inherent to the liquid. Actually, the experimental situation is much more complicated, owing to the phenomenon of contact angle hysteresis, which is discussed later [3]. The "transient area" between heavy droplets and liquid puddles was recently treated by Extrand and Moon [20].

2.8 The shape of the droplet and the disjoining pressure

The droplet is distorted not only by the gravity, but also by long-range surface forces resulting in the *disjoining pressure* (see Section 2.3). Minimization of the free energy of the 2D cylindrical droplet gives rise to the Euler equation:

$$\frac{\gamma h''}{(1 + h'^2)^{3/2}} + \Pi(h) = -p_L \,, \tag{2.44}$$

where $h(x)$ is the unknown profile of the cylindrical droplet, $\Pi(h)$ is the disjoining pressure, $p_L = p_{liq} - p_{vap}$, p_{vap}, p_{liq} are the pressures in the vapor and the liquid phases (see Sections 1.5, 2.3, 2.4) [44]. Equation (2.44) is also called the Laplace–Derjaguin equation. For the numerical solutions to equation (2.44) see Ruckenstein and Berim [40].

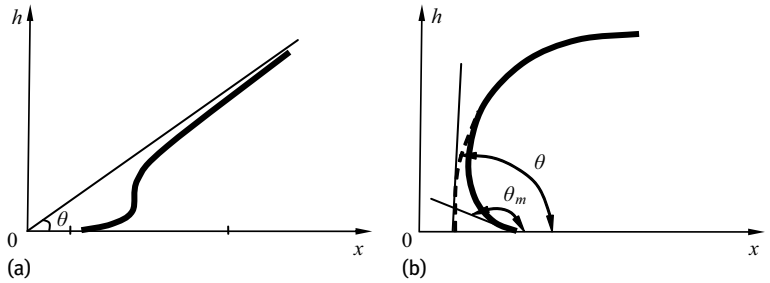

Fig. 2.12: Fine structure of the triple line defined by the disjoining pressure. a: scenario discussed in de Gennes et al. [17]. Micro-contact angle is zero; b: scenario discussed in Ruckenstein and Berim [40]. Micro-contact angle is θ_m and macroscopic (apparent) contact angle is θ. The latter angle is defined by extrapolating the circular part of the drop profile up to the surface.

One of the qualitative peculiarities of the solution of the Laplace–Derjaguin equation (2.44) should be underlined. In the vicinity of the solid surface, the profile of a liquid drop on a solid substrate exhibits a rapid variation of curvature in a small region (~ 10–30 Å) near the surface, owing to the rapid variation of the interactions between the molecules of liquid and those of the solid [40]. Therefore, an additional micro-contact angle θ_m can be considered along with the Young contact angle (Figure 2.12). Various scenarios of distorting the triple line by surface forces were discussed, as shown in Figure 2.12 [17, 40, 44]. However, because of its small size, the region of distortion and, in particular, the micro-contact angle θ_m (Figure 2.12) are practically undetectable by macroscopic experiments.

Ruckenstein and Berim also discussed the alternative approach to considering interaction of the droplet with the surface, based on a nonlocal density functional theory (DFT), which accounts for the heterogeneity of the liquid density and temperature effects (features that are missing in the macroscopic approach) [40]. They concluded that the long-range surface forces govern the fine structure of the triple line, which is expected to be complicated. Lack of experimental data related to the fine structure of the triple line should be taken into account.

2.9 Distortion of droplets by an electric field

The shape of the droplet could be distorted by an external field such as an electric field. The deformation of the droplet by electric field was studied in Bormashenko et al. [9]. The 15-μl water droplet deposited on the nonstick surface was introduced into vertical homogenous electric field $E = 1 - 8 \cdot 10^5$ V/m, as shown in Figure 2.13. The drop has been deformed, as depicted in Figure 2.14.

Nayyar and Murty, following the method developed by Chandrasekhar and Fermi, have shown that the shape of the electrically deformed *dielectric* droplet could be ap-

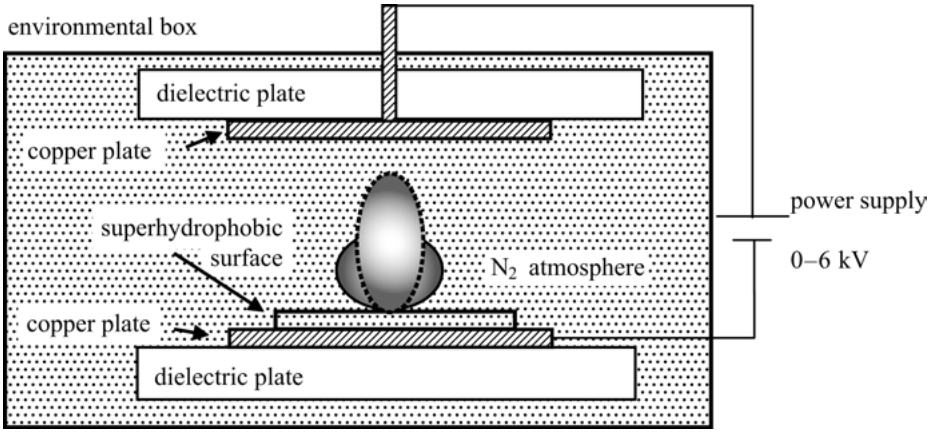

Fig. 2.13: Experimental set used for study of the deformation of water droplets exposed to an electric field.

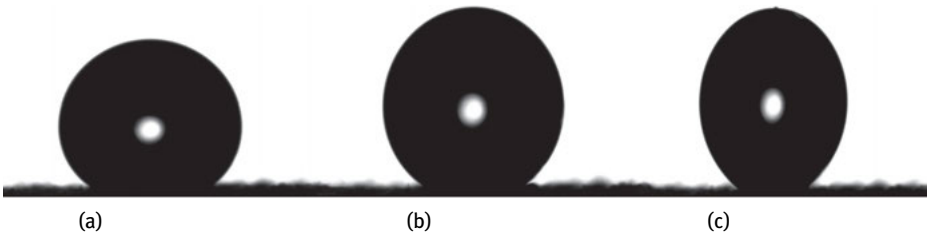

Fig. 2.14: Deformation of a 15-µl water droplet under the influence of an electric field.
a: $E = 0$; b: $E = 0.65 \cdot 10^6$ V/m; c: $E = 0.84 \cdot 10^6$ V/m.

proximated by a prolate spheroid [13, 35]. The eccentricity $\hat{e}$ of the spheroidal droplet in the presence of the homogeneous electric field E is expressed in this case as:

$$\hat{e} = \kappa E\,, \qquad \kappa = \frac{3}{2}\frac{(\varepsilon_1 - \varepsilon_2)}{(\varepsilon_1 + 2\varepsilon_2)}\sqrt{\frac{\varepsilon_0 \varepsilon_2 R_{\text{eq}}}{\gamma}}\,, \tag{2.45}$$

where R_{eq} is the radius of the spherical droplet of the same volume [9, 13]. The SI unit system is used in equation (2.45): ε_0 is the vacuum permeability, ε_1 and ε_2 are dielectric constants of liquid and air respectively, and γ is the surface tension of the liquid. The experiments reported in Bormashenko et al. [9] confirmed the linear dependence of the drop eccentricity on the value of the applied electric field. It should be stressed that the switch in the direction of the electric field does not change the effect of the droplet deformation, i.e., the electric field always stretches the droplet and does not compress it. This could be understood if we consider the contact of the droplet with the solid substrate and the double electrical layer formed in the contact area; hence, the droplet has a nonzero dipole moment even in the absence of an external field (Figure 2.15). Switch in the direction of the external field leads to a change of polarity in

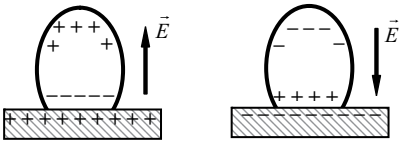

Fig. 2.15: Liquid droplet deposited on a solid substrate in the presence of an external electric field. Switching the field direction switches the polarity of both substrate and droplet.

both the substrate and the droplet; thus, obviously, the droplet can only be stretched by the external field.

It is noteworthy that for nonstick droplets or so-called "liquid marbles," the dependence of the drop eccentricity on the value of the applied electric field is nonlinear, and it is described by a rather complicated function [10]. This is due to the fact that "liquid marbles" are disconnected from the solid substrate and possess zero dipole moment in the absence of an external electric field (see Section 9.3.7) [10].

2.10 Capillary rise

One of the most important and widespread wetting phenomena is the rise of liquid in capillary tubes, illustrated in Figure 2.16a–c. When a narrow tube is brought into contact with a liquid, some liquids (water in a glass tube) rise and some (mercury in a glass tube) descend in the tube. Capillary rise is abundant in nature and technology. What is the physical reason for capillary rise? Let us consider an ideal (smooth, nondeformable, nonreactive) capillary tube wetted by a liquid. In tubes with an inner radius smaller than the capillary length l_{ca}, the meniscus within a tube is a portion of a sphere. The radius of this sphere equals $R = r/\cos\theta_Y$, where r is the radius of the capil-

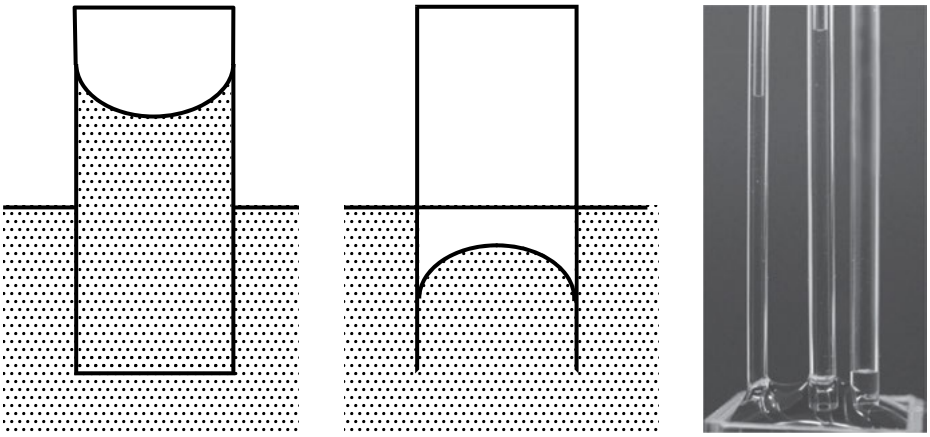

Fig. 2.16: a: capillary rise: water in the glass tube; b: capillary descent, mercury in the capillary tube; c: water rise in glass capillary tubes.

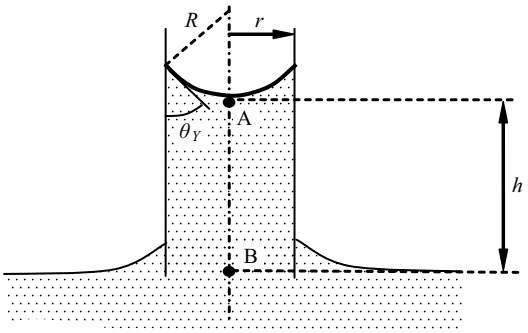

Fig. 2.17: Capillary rise in a cylindrical tube: the Young contact angle is θ_Y.

lary tube (Figure 2.17), θ_Y is the contact angle of the *ideal* tube/liquid pair. The pressure in Point A (immediately underneath the meniscus) is given by $p_A = p_0 - 2\gamma \cos\theta_Y / r$, where p_0 is atmospheric pressure. The pressure in Point B ($z = 0$) equals p_0. On the other hand, $p_B - p_A = \rho g H$ (Figure 2.17). Substituting p_B and p_A yields the well-known Jurin's law:

$$H = \frac{2\gamma \cos\theta_Y}{\rho g r} \,. \tag{2.46}$$

Grounding of Jurin's law with energetic reasoning is supplied in [17]. It is useful to rewrite expression (2.46) in the following form:

$$H = \frac{2l_{ca}^2}{r} \cos\theta_Y \,, \tag{2.47}$$

strengthening the importance of the capillary length in problems where the physics is defined by the interplay of surface tension and gravity.

When deriving Jurin's law we neglected the weight of the liquid above the bottom of the small meniscus in the capillary tube. It was shown by Richards and Carver [37] that the correction of Jurin's law for small capillary tubes is given by:

$$H = H_0 + \frac{r}{3} \,, \tag{2.48}$$

where H is the true corrected height of the capillary column, H_0 is the observed height of the column to the bottom of the meniscus, and r is the radius of the tube. For more a sophisticated correction of Jurin's law see Richards and Carver [37].

Capillary rise is responsible for plenty of natural and technological phenomena; however, it is usually illustrated by an effect to which it is not related. It is a widespread myth that capillarity is responsible for the sap rise in tree capillaries. Let us estimate the maximal capillary rise according to equation (2.46) if the complete wetting of capillary vessels is assumed, i.e., $\cos\theta_Y = 1$. The characteristic radius of capillary vessels in trees is close to 10 μm [26]. Substituting $\gamma \cong 70\,\mathrm{mJ/m^2}$, $\rho \cong 10^3\,\mathrm{kg/m^3}$, $r \cong 10^{-5}\,\mathrm{m}$ into equation (2.46), we obtain, for the most optimistic estimation of the maximal water rise in tree capillary vessels $H \cong 1.4\,\mathrm{m}$. At the same time, water is transported even

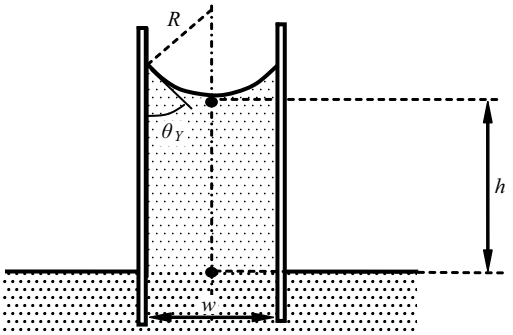

Fig. 2.18: Capillary rise between two vertical ideal plates. The separation between plates is w.

to redwood trees 100 m tall. The mechanism of water rise in trees is still not understood fully today; however, it is generally accepted that water is pulled from the roots to the leaves by a pressure gradient arising from evaporation of water from the leaves. Negative pressures as high as −100 atm were registered in plants [41].

Capillary rise can be also observed when liquid is confined between two vertical planes separated by a distance w, as shown in Figure 2.18. In the case of *ideal planes* the Laplace pressure is given by $p_{\mathrm{L}} = \gamma/R = 2\gamma/w \cos\theta_{\mathrm{Y}}$ (the shape of the meniscus is supposed to be cylindrical). The Laplace pressure for the cylindrical surface is given by equation (1.14), i.e., $p_{\mathrm{L}} = \gamma(1/R_1 + 1/R_2) = \gamma/R = 2\gamma\cos\theta_{\mathrm{Y}}/w$, owing to $R_2 = \infty$, $R_1 = R = w/2\cos\theta_{\mathrm{Y}}$. Considerations akin to those leading to equation (2.46) yield:

$$H = \frac{2\gamma\cos\theta_{\mathrm{Y}}}{\rho g w} = 2\frac{l_{\mathrm{ca}}^2}{w}\cos\theta_{\mathrm{Y}}\,. \tag{2.49}$$

The corrections to expression (2.49) are supplied in Bullard and Garboczi [11]. When the separation between plates becomes micrometrically scaled, the effect of the disjoining pressure on the capillary height should be considered [12, 28].

Capillary rise could be used for the experimental establishment of surface tension. For a detailed discussion of the advantages and shortcomings of the capillary rise method, and also for the surface tensions established with this method, see Erbil [19].

2.11 The shape of a droplet wetting a fiber

Wetting of fibers is important for textile and other industrial applications. If the characteristic size of the droplet is much less than the capillary length, gravity can be neglected. Thus, for the equilibrium drop, the Laplace overpressure into the droplet should be constant $p_{\mathrm{L}} = \gamma(1/R_1 + 1/R_2) = \mathrm{const}$; this leads to the equation:

$$\frac{1}{R_1} + \frac{1}{R_2} = \mathrm{const} = \frac{p_{\mathrm{L}}}{\gamma}\,. \tag{2.50}$$

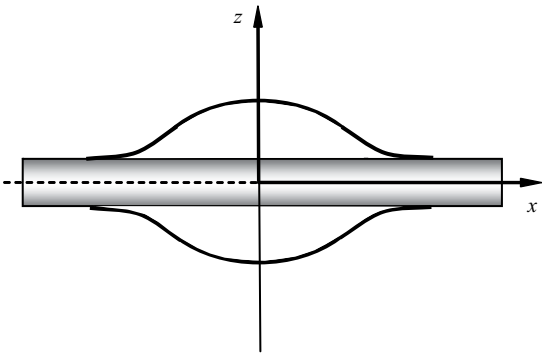

Fig. 2.19: Drop deposited on a cylindrical fiber.

The mathematical transformations supplied in de Gennes et al. [17] lead to the equation defining the shape of the droplet (Figure 2.19):

$$-\frac{z''}{(1+z'^2)^{3/2}}+\frac{1}{z(1+z'^2)^{1/2}}=\frac{p_{\mathrm{L}}}{\gamma}\,, \tag{2.51}$$

where $z'=\mathrm{d}z/\mathrm{d}x$. Equation (2.51) could be solved numerically. Somewhat surprisingly the problem of wetting a thin vertical fiber of the radius r, depicted in Figure 2.20, has an analytical solution. In this case, if the gravity is neglected ($r \ll l_{\mathrm{ca}}$), we have $p_{\mathrm{L}}=0$, because the meniscus is connected to the flat surface of the liquid bath. Thus, for a thin vertical fiber equation (2.50) becomes:

$$\frac{1}{R_1}+\frac{1}{R_2}=0\,, \tag{2.52}$$

which defines a surface with zero curvature. The profile of a meniscus is given by a catenary curve (which is the profile of a hanging cord):

$$z=r\cos\mathrm{h}\frac{x}{r}\,. \tag{2.53}$$

Considering that gravity leads to the equation:

$$\gamma\left(\frac{1}{R_1}+\frac{1}{R_2}\right)=-\rho g z\,. \tag{2.54}$$

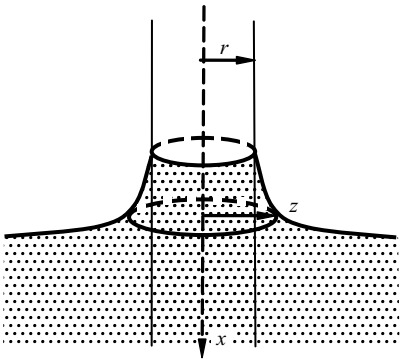

Fig. 2.20: Liquid wetting the vertical fiber.

In the nearest vicinity of the triple line at the distances $x \ll l_{ca}$ from the fiber, the effects due to gravity are negligible and the shape of the meniscus is governed by capillary forces only; thus, in this region we return to the surface of a zero curvature described by equation (2.52). The solution of this equation yields:

$$z = r \cos h \frac{x - h}{r} , \tag{2.55}$$

where h is the height of the meniscus (the meniscus adopts the form of a catenary curve) [17]. The height of the meniscus could be estimated as $h \approx r \ln(2l_{ca}/r)$. For the calculation of the precise shape of the meniscus, we have to solve equation (2.54) numerically [17].

2.12 Wetting and adhesion: the Young–Dupré equation

Let us estimate the specific energy (per unit area of the solid substrate) necessary for disconnection of the droplet W_{ad} from the solid substrate illustrated in Figure 2.21. This energy could be calculated as:

$$W_{ad} = \gamma_{SA} + \gamma - \gamma_{SL} . \tag{2.56}$$

Considering the Young equation (equation (2.11)) we obtain $\gamma_{SA} - \gamma_{SL} = \gamma \cos \theta_Y$. Substituting this expression in equation (2.56) supplies W_{ad}, which is called "the energy of adhesion" in the form:

$$W_{ad} = \gamma(1 + \cos \theta_Y) , \tag{2.57}$$

which is called the Young–Dupré equation. It is noteworthy that our derivation of the Young–Dupré equation implies conservation of the droplet shape after disconnection from the solid substrate, as depicted in Figure 2.21. This approach has been criticized by Schrader [42]. Schrader suggested that the droplet detached from the substrate obtains its natural spherical shape and supplied the corrected equation for the net energy of the droplet adhesion [42].

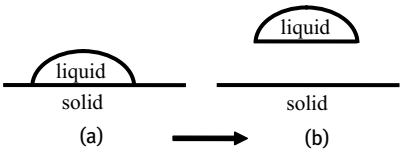

Fig. 2.21: Disconnection of the droplet from the solid substrate. a: droplet on the solid substrate; b: droplet detached from the substrate.

2.13 Wetting transitions on ideal surfaces

The surface tension of liquids is temperature-sensitive, as discussed in Section 1.3. γ_{SA} and γ_{SL} are also temperature-sensitive. What is observed when both the droplet and

the substrate are heated? At a certain point, it may be that the sum of the solid–liquid and the liquid–air (vapor) surface tensions becomes equal to the solid–air (vapor) interfacial tension; then, the spreading parameter $\Psi = \gamma_{SA} - (\gamma_{SL} + \gamma)$ is equal to zero, and the transition from partial wetting to complete wetting occurs (Figure 2.1). The wetting transition is the transition between a partial and a complete wetting state [7]. The temperature of transition is called the *wetting temperature*, T_W. The *order* of the wetting transition is determined – in the same manner as for a bulk phase transition – by the discontinuities of the surface free energy. If a discontinuity occurs in the first derivative of the free energy, the transition is said to be of the first order and takes place in a discontinuous way. If the first derivative of the free energy is continuous at a phase transition point, then this indicates that it is a higher-order phase transition. For the wetting of a liquid drop on a substrate, the relevant free energy is the surface tension of the substrate–air (vapor) interface γ_{SA}. Let us rewrite the Young equation in this way:

$$\gamma_{SA} = (\gamma_{SL} + \gamma) - \gamma(1 - \cos\theta_Y) \,. \tag{2.58}$$

As the term proportional to $\gamma(1 - \cos\theta_Y)$ is the part that is going to zero at the wetting transition to complete wetting, it is the critical part of the specific free energy to be examined to determine the critical exponents. According to the definition of the critical exponent, this part of the specific free energy approaches zero following $(1-\cos\theta_Y) \infty (T_W - T)^{2-\hat{\alpha}}$, where $\hat{\alpha}$ is the specific heat exponent, determining the order of the wetting transition. For $\hat{\alpha} = 1$, the first derivative of $\cos\theta_Y$, and therefore the first derivative of the specific surface free energy, is discontinuous with respect to temperature ($\cos\theta_Y = 1$, for $T \geq T_W$); thus the wetting transition is of the first order [7].

The accumulated experimental data and much theoretical work carried out in the field confirm the fact that wetting transitions are generally of the first order, as shown in Figure 2.22. In this case, if one measures the thickness of the absorbed film beside the droplet, at the wetting transition, a discontinuous jump in film thickness occurs from a microscopically thin to a thick film [7]. This is true for a broad range of liquid/solid pairs ranging from liquid helium to room temperature binary liquids and high temperature metallic systems. There were also several exceptions reported, for which

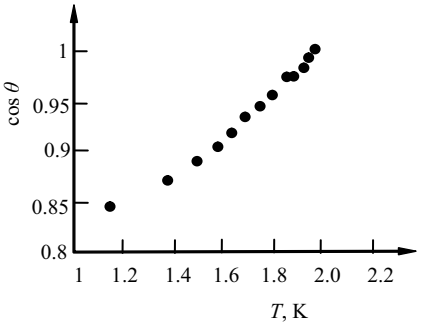

Fig. 2.22: Typical dependence of the cosine of the contact angle on the temperature, illustrating wetting transitions on flat substrates, as established for liquid helium on cesium substrate; cos θ goes linearly to unity at the temperature of transition, indicating that the wetting transition is of the first order (Adapted with permission from Bonn and Ross [7]). Copyright 2001 IOP Publishing.

a discontinuity in a higher derivative of the specific surface free energy was observed. Such a behavior was reported for liquid/air pairs governed by the long-range van der Waals interactions (see Section 2.5) [7].

2.14 How is the surface tension measured?

2.14.1 The Du Noüy ring and the Wilhelmy plate methods

Now we are ready to discuss experimental procedures allowing measurement of surface tension. Historically, the first methods leading to the establishment of surface tension were the "Du Noüy ring" and the "Wilhelmy plate" methods, based on the immersion of solids in liquid, followed by pulling them from the liquid with a balance. The Du Noüy ring method depicted in Figure 2.23 utilizes a platinum or platinum/iridium alloy wire with a radius of 2–3 cm. The radius of the wire ranges from 1/30 to 1/60 of that of the ring. The platinum ring is a high-surface-energy object; hence, the adhesion of liquid to the ring is greater than the cohesion with the liquid. It is also supposed that the contact angle between a liquid and the ring is zero. Thus, when a ring is pulled from the liquid, it entrains the liquid, as shown in Figure 2.23, the force F necessary for detachment is that of cohesion rather than adhesion. Under the suggestions mentioned above, the detachment takes place when:

$$F = mg + 2\overline{p}\gamma \,, \tag{2.59}$$

where m is the mass of the ring, $\overline{p}$ is its mean perimeter, the perimeter of the ring is multiplied by 2 because of the presence of two surfaces, created on both sides of the ring; obviously, $\overline{p} = 2\pi r_{\text{mean}} = 2\pi r_{\text{ext}} + r_{\text{min}}/2 = \pi(r_{\text{ext}} + r_{\text{min}})$ (Figure 2.23); substituting $\overline{p}$ into (2.59) and measurement of F with a balance allows calculation of the surface tension γ.

A similar method utilizes a vertical platinum or platinum/iridium alloy plate (the so-called Wilhelmy plate) immersed in a liquid and pulled from it as shown in Fig-

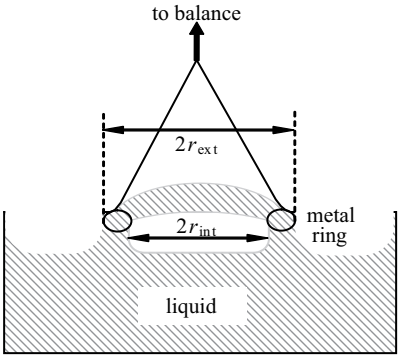

Fig. 2.23: Measurement of surface tension with the Du Noüy ring.

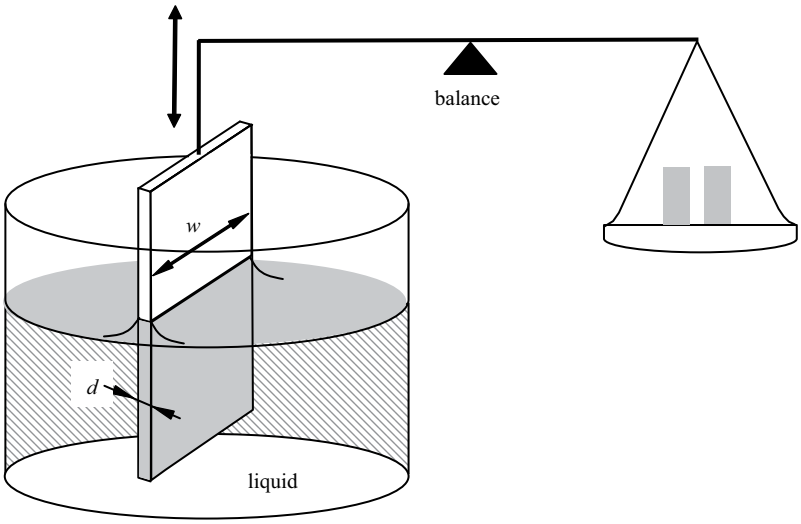

Fig. 2.24: Measurement of surface tension using a Wilhelmy plate.

ure 2.24. If the contact angle is zero, the force necessary for detachment of the Wilhelmy plate is given by:

$$F = mg + p\gamma = mg + 2(w + d)\gamma \,, \tag{2.60}$$

where $p = 2(w + d)$ is the perimeter of the Wilhelmy plate. If the contact angle is not zero, equation (2.60) looks like:

$$F = mg + 2(w + d)\gamma \cos\theta \,. \tag{2.61}$$

Measurement of F and θ allows calculation of the surface tension according to formula (2.61). Shortcomings of the Du Noüy ring and the Wilhelmy plate methods are discussed in detail in Adamson and Gast, and Erbil [1, 19].

2.14.2 The pendant drop method

The pendant drop method is one of the most precise and commonly used methods of measurement of the surface tension of liquids. When a liquid is suspended from the tip of a thin tube with an inner radius R, as shown in Figure 2.25, its shape results from a balance between capillarity and gravitational forces. The equilibrium of pressures yields:

$$\gamma\left(\frac{1}{R_1} + \frac{1}{R_2}\right) = \rho g z \,, \tag{2.62}$$

where R_1 and R_2 are the main radii of curvature of the pendant droplet surface (equation (1.14) and Figure 2.25). Defining $r' = \mathrm{d}r/\mathrm{d}z$, $r'' = \mathrm{d}^2 r/\mathrm{d}z^2$, we obtain the following

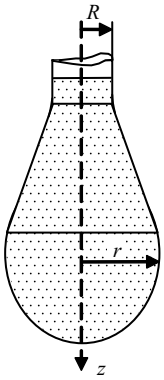

Fig. 2.25: Scheme illustrating the pendant drop method of measurement of surface tension.

equation [17]:

$$\gamma\left(\frac{1}{r(1+r'^2)}+\frac{r''}{(1+r'^2)^{3/2}}\right)=\rho g z\,, \tag{2.63}$$

which could be solved numerically. The pendant drop is imaged and γ is considered to be a fitting parameter. The surface tension γ is adjusted until the solution of equation (2.63) agrees with experimental results, obtained with droplet imaging [17, 19, 39].

The "negative" of the pendant droplet method is the "sessile air bubble" method, when an air bubble trapped by a liquid is digitally imaged, and the surface tension γ is calculated numerically from the bubble shape. Surface tension could also be derived from the shape of sessile drops, as described in detail in Rotenberg et al. [39].

2.14.3 Maximum bubble pressure method

One of the pioneers of the "maximum bubble pressure" method displayed in Figure 2.26 was Erwin Schrödinger [43]. It is pertinent to note that Albert Einstein also started his scientific career from an investigation devoted to capillary phenomena [18]. Moreover, Niels Bohr also expended effort in the experimental establishment of the surface tension of liquids [6]. Thus, a triad of founders of modern physics took the problems of capillarity seriously, and it could definitely be recommended for a young scientist to enter this exciting field of exact sciences, which is rich in ideas and which remains attractive for investigators (this is well-illustrated by brilliant results obtained recently by de Gennes and his school [17]).

When the surface tension is measured by the maximum bubble pressure method, air is blown into a thin capillary tube, as shown in Figure 2.26. The pressure measured at the end of the tube is given by:

$$p(R)=p_0+\rho g h+\frac{2\gamma}{R}\,, \tag{2.64}$$

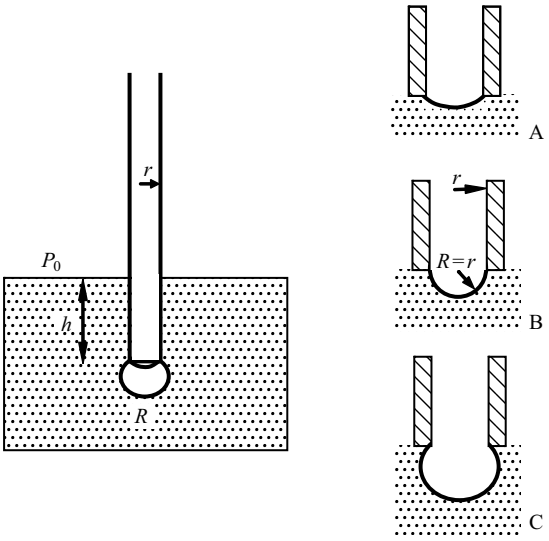

Fig. 2.26: The maximum bubble pressure method: when air is blown into the capillary tube, the radius of the bubble R is decreased (stage A), passes through the minimum (stage B, $R = r$), and afterward increases (stage C).

where p_0 is the atmospheric pressure, and R is the radius of the air bubble blown at the end of the capillary tube. Let us follow the evolution of the radius, R: early in the development of the bubble, R is decreased, passes through the minimum when $R = r$ (r is the inner radius of the tube; if the tube is wetted by liquid, at this point the pressure is maximal) and afterward increases. The idea of the method lies in the experimental establishment of the maximal pressure, allowing the deduction of γ with formula (2.64). For analysis of the accuracy of the maximum bubble pressure method, see Mysels [34].

2.14.4 Dynamic methods of the measurement of surface tension

Novel methods exploiting vibrations or rotation of droplets to establish their surface tension have recently been reported. One of these methods uses bulk (Rayleigh) modes excited in spherical droplets of a radius R [33]. In this method a droplet is placed between two specially prepared needles facing each other, as shown in Figure 2.27. Next, the needles are moved backward very quickly, and the excited oscillations of a droplet are imaged digitally. For a rough estimation of the n-th bulk eigenfrequency, ω_n, of the droplet ($n = 2, 3 \ldots$), the well-known Rayleigh formula can be used:

$$\omega_n^2 = \frac{n(n-1)(n+2)\gamma}{\rho R^3}\,, \tag{2.65}$$

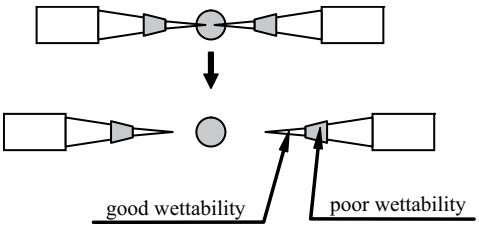

Fig. 2.27: Dynamic measurement of surface tension using the oscillating droplet method [33]. The design of specially prepared needles holding the droplet is shown. Needles are pushed apart rapidly and the droplet starts to oscillate.

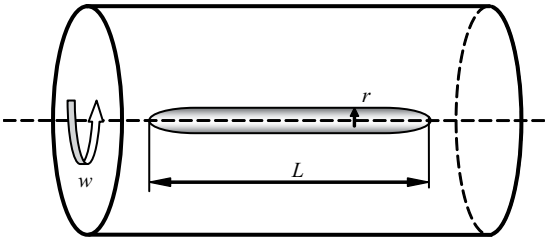

Fig. 2.28: Measurement of the interfacial tension between two liquids with a spinning droplet [27].

where γ and ρ are the surface tension and density of the liquid respectively [27]. Thus, the surface tension is calculated from the eigenfrequencies of a droplet established experimentally [33].

Another method of measuring surface tension is based on the spinning of a drop placed in a horizontal transparent drum (tube) filled with another immiscible and denser liquid (Figure 2.28) [17, 46]. The drum is rotated with a frequency, ω, of a few thousand revolutions per minute. As the density of the drop is less than that of the surrounding liquid it locates itself close to the axis of the drum. The drop elongates when rotated and obtains a cylinder-like shape (Figure 2.28). The energy of a spinning droplet, W, could be written as:

$$W = \frac{1}{2} J\omega^2 + \gamma_{12} 2\pi r L \,, \tag{2.66}$$

where J is the moment of inertia of a spinning droplet, r and L are the radius and the length of the cylinder respectively (the contributions of extremities of the droplet are neglected), and γ_{12} is the interfacial tension between liquids. Taking into account $J = (1/2)(\Delta\rho V)r^2 = (1/2)\Delta\rho L r^4$, where $\Delta\rho$ is the difference between the densities of the liquids, and substituting J into expression (2.66) yields:

$$W = \frac{1}{4}\pi\Delta\rho\omega^2 L r^4 + \gamma_{12} 2\pi r L \,. \tag{2.67}$$

It seems from expression (2.67) that W is a monotonously growing function of r; however, the condition of the conservation of the droplet volume should be considered:

$V = \pi r^2 L$. Substituting V into expression (2.67) results in:

$$W = \frac{1}{4}\Delta\rho\omega^2 V r^2 + \gamma_{12} 2\frac{V}{r} \,. \tag{2.68}$$

In equilibrium, $\mathrm{d}W/\mathrm{d}r = 0$; hence, we obtain an equation allowing calculation of the interfacial tension:

$$\gamma_{12} = \frac{1}{4} r^3 \Delta\rho w^2 = \frac{1}{4\pi^{3/2}}\Delta\rho\omega^2 \left(\frac{V}{L}\right)^{3/2} \,. \tag{2.69}$$

Formula (2.69) contains parameters that could be easily established experimentally with high accuracy, i.e., the length of the spinning droplet, L, its volume, V, and the difference between the densities of the liquids. This method turns out to be extremely suitable for measurement of low interfacial tensions that occur in water/oil systems in the presence of surfactants. Its additional advantage is the absence of contact with a solid. The method can also exploit a bubble instead of a liquid; thus liquid/vapor interfacial tension could be established [46].

A method of measurement of surface tension by the jet vibration method has been proposed and successfully tested by Bohr [6].

2.15 Measurement of the surface tension of solids

Estimation of the surface tension of solids is a much more challenging experimental task than that of liquids. When the spreading parameter, Ψ, is negative and we deal with the partial wetting, the surface tension of a solid could be estimated from the Young contact angle. Good and Girifalco supposed that the relation between interfacial tensions is given by:

$$\gamma_{SL} = \gamma_{SA} + \gamma - 2\Phi(\gamma_{SA}\gamma)^{1/2} \,, \tag{2.70}$$

where $\Phi = 4(V_{MS}V_{ML})^{1/3}/(V_{MS}^{1/3} + V_{ML}^{1/3})^2$, and V_{MS}, V_{ML} are the molar volumes of solid and liquid respectively [23, 24]. Combining equation (2.70) with the Young equation $\gamma_{SA} - \gamma_{SL} = \gamma\cos\theta_Y$ yields:

$$\gamma_{SA} \cong \gamma\frac{(1+\cos\theta_Y)^2}{4\Phi^2} \,. \tag{2.71}$$

Thus, measurement of the Young contact angle allows calculation of the surface tension of solids according to equation (2.71). Calculation of γ_{SA} for polymers with equation (2.71) supplied values of γ_{SA} in the range of 19–47 mJ/m^2 in satisfactory agreement with the values of the surface tension established using other experimental techniques (see Section 1.7, where such surfaces were classified as "low-energy"). We shall later see that the precise measurement of the Young contact angle is not a simple task, owing to the phenomenon of the contact angle hysteresis. This fact decreases the accuracy of estimation of the surface energy of solids with expression (2.71).

One more method for the estimation of surface tension of solid polymers was proposed by Roe [38]. This method is based on the reasonable suggestion that the difference between solid and melted amorphous polymers is not dramatic, and that the melting of these polymers is not accompanied by the phase transition (melting in this case manifests mainly in the decrease in viscosity of the polymer melt). Thus, the surface tension of amorphous polymers could be obtained by the extrapolation of surface tension data of polymer melts to room temperature. Roe measured the surface tension of polymer melt using the pendant drop method introduced in Section 2.14.2 [38]. For polystyrene at room temperature, the extrapolation procedure supplied the value of $\gamma_{SA} = 40.7\ \mathrm{mJ/m^2}$, which is rather close to the surface tension derived from the measurement of the contact angle with expression (2.71), which was $42\ \mathrm{mJ/m^2}$. Satisfactory agreement of the Good and Girifalco and Roe methods has also been reported for poly(methyl methacrylate) and polyethylene [44–46]. For a review of other semi-empirical methods of the establishment of the surface tension of polymers see Whyman and Bormashenko [47]. In the following chapter we discuss the possibility of establishing the surface tension of solids from the contact angle hysteresis data (see Section 3.14).

Additional Reading

In our treatment we kept a macroscopic, physical approach. Chemical aspects of the wetting of surfaces are well summarized in Joud and Barthes-Labrousse [50].

Appendix 2A. Transversality conditions

In this volume, we shall broadly use the mathematical apparatus of transversality conditions of the appropriate variational problem of wetting. Let us acquaint ourselves with this fascinating mathematical tool more closely. Consider the functional (see Arfken and Weber [4]):

$$J(y) = \int_{x_0}^{x_1} F\left(x, y, y'\right) \mathrm{d}x\,, \tag{2.72}$$

defined on smooth curves, the ends of which are located on two given curves $\phi(x)$ and $\varphi(x)$ (Figure 2.29). We seek the extremum of this functional by variation of the function $y(x)$. A typical problem of this kind is the calculation of the distance between two curves. It is demonstrated by Gelfand and Fomin [21] that a function $y(x)$ supplying an extremum to the functional given by expression (2.72), the ends of which are free to slip along curves $\phi(x)$ and $\varphi(x)$ has to satisfy the following boundary conditions:

$$F + F_{y'}(\varphi' - y')_{x=x_1} = 0 \tag{2.73a}$$

$$F + F_{y'}(\phi' - y')_{x=x_0} = 0 \tag{2.73b}$$

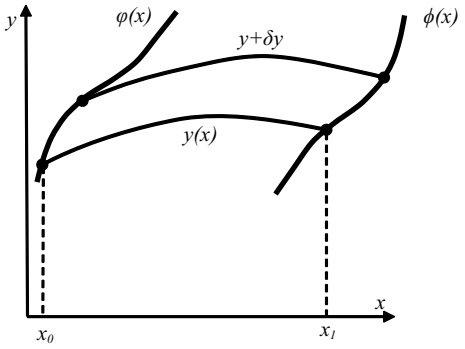

Fig. 2.29: Sketch illustrating the transversality conditions of the variational problem. Ends of the function $y(x)$ are free to slip along the curves $\phi(x)$ and $\varphi(x)$.

where $F_{y'}$ denotes the y' derivative of F. These boundary conditions are called the *transversality conditions*. The function $y(x)$ satisfying conditions (2.73a, b) is called *transversal* to functions $\phi(x)$ and $\varphi(x)$.

Appendix 2B. Zisman plot

A liquid totally wets a solid surface when the spreading parameter $\Psi = \gamma_{SA} - (\gamma_{SL} + \gamma)$ is positive (see Section 2.1), i.e., $\gamma < \gamma_{SA} - \gamma_{SL}$. However, Zisman developed the empirical criterion that says that total wetting occurs when $\gamma < \gamma_C$, where γ_C is the so-called critical surface tension [49]. Zisman measured θ for a series of nonpolar liquids on the same solid sample and plotted versus γ for the test liquids, obtaining graphs similar to that represented in Figure 2.30. Zisman revealed that the majority of experimental points concentrate in a vicinity of a straight line. This straight line approaches $\cos\theta = 1$ (corresponding to complete wetting) at a given value of γ, which Zisman called "the critical surface tension" of a solid γ_C. It turned out that γ_C is independent of the liquid. This is really strange, because total wetting is dictated by a single parameter γ_C and not by the pair γ_{SA}, γ_{SL} resulting from the spreading parameter based approach. Thus,

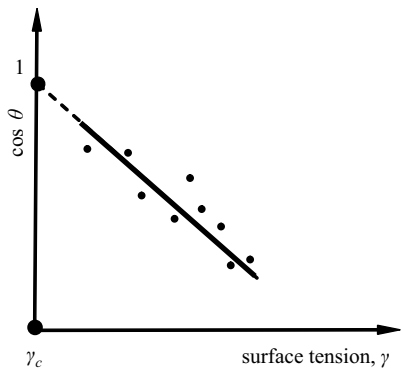

Fig. 2.30: Typical Zisman plot.

total spreading is defined by γ_C of a solid alone, which is independent of the liquid. P. G. de Gennes explained the Zisman rule as follows. A liquid spreads completely if it is less polarizable than the solid; this corresponds to the situation $\gamma < \gamma_C$; the wetting is partial when $\gamma > \gamma_C$ [17].

The approach developed by Zisman has given rise to certain objections. It works well for low-energy surfaces (Teflon, polyethylene) and nonpolar liquids. The value of γ_C may be uncertain because of extrapolation that is too long, and it should be stressed that γ_C is an empirical parameter, and $\gamma_{SA} \neq \gamma_C$! Nevertheless, it is generally accepted that Zisman's approach works well for liquids governed by the van der Waals forces deposited on polymer surfaces. For the values of γ_C established for different solids see de Gennes et al., Erbil, and Zisman [17, 19, 49].

Appendix 2C. Antonoff's rule

The measurement of the interface tension at solid–liquid interfaces (appearing in the Young equation [2.11]) presents serious experimental difficulties. Antonoff suggested that the solid–liquid interface tension at the interface is the absolute value of the difference between the surface energies of liquid and solid in the equilibrium state:

$$\gamma_{SL} = |\gamma_{SA} - \gamma| \tag{2.74}$$

The physical reasoning behind Antonoff's rule is that the surface energy is due to missing bonds of atoms/molecules at the surface [51]. When two materials come into contact, they form new bonds and one with lower energy (fewer bonds available) partially compensates for missing bonds in the other material. For two surfaces of the same material, all bonds are filled and the interfacial energy is zero. The extended discussion of the validity of Antonoff's rule and Good and Girifalco approaches [23, 24], proposed for the calculation of γ_{SL} and γ_{SA}, may be found in Nosonovsky and Chen [52].

Bullets

- An atomically flat, chemically homogeneous, isotropic, insoluble, nonreactive, and nonstretched substrate is called an ideal surface.
- The spreading parameter $\Psi = \gamma_{SA} - (\gamma_{SL} + \gamma)$ governs the wetting regime, when $\Psi < 0$, wetting is partial, when $\Psi > 0$, wetting is complete.
- The contact angle established on the ideal surface is called the Young contact angle θ_Y, and it is given by the Young equation: $\cos\theta_Y = \gamma_{SA} - \gamma_{SL}/\gamma$.
- Actually, the Young equation is the transversality condition for the variational problem of wetting.
- The Young contact angle is independent of the droplet shape and external fields.

- Line tension. Γ, arises from the unusual energetic state of molecules located at the triple line. There is no currently general agreement concerning either the value of line tension or its sign.
- The contact angle is modified by the line tension according to the Neumann–Boruvka equation: $\cos\theta = \gamma_{SA} - \gamma_{SL}/\gamma - \Gamma/\gamma a$.
- Wetting of very thin liquid layers is governed to a large extent by disjoining pressure. Wetting situations where a droplet sits on a dry substrate should be distinguished from those where it finds itself on a layer of absorbed molecules of liquid.
- Droplets with characteristic dimensions much less than $l_{ca} = \sqrt{\gamma/\rho g}$ (the capillary length) keep their spherical shape; larger drops are distorted by gravity.
- When droplet and substrate are heated, the transition from partial wetting to complete wetting occurs, which is called the "wetting transition."
- The energy necessary for disconnection of the droplet is called the "adhesion energy," W_{ad}. It is given by the Young–Dupré equation: $W_{ad} = \gamma(1 + \cos\theta_Y)$.

References

[1] A. W. Adamson and A. P. Gast, *Physical Chemistry of Surfaces*, 6th edn., Wiley Interscience Publishers, New York, 1990.

[2] A. Amirfazli and A. W. Neumann, Status of the three-phase line tension, *Adv. Colloid & Interface Sci.* **110** (2004), 121–141.

[3] C. Andrieu, C. Sykes, and F. Brochard, Average spreading parameter on heterogenous surfaces, *Langmuir* **10** (1994), 2077–2080.

[4] G. B. Arfken and H. J. Weber, *Mathematical Methods for Physicists*, Harcourt/Academic Press, San Diego, 2001.

[5] J. Bico, U. Thiele, and D. Quéré, Wetting of textured surfaces. *Colloids & Surf. A* **206** (2002), 41–46.

[6] N. Bohr, Determination of the Surface-Tension of Water by the Method of Jet Vibration, *Phil. Trans. R. Soc. Lond. A* **209** (1909), 281–317.

[7] D. Bonn and D. Ross, Wetting transitions, *Rep. Prog. Phys.* **64** (2001), 1085–1163.

[8] E. Bormashenko, Young, Boruvka–Neumann, Wenzel, and Cassie–Baxter equations as the transversality conditions for the variational problem of wetting, *Colloids & Surf. A*, **345** (2009), 163–165.

[9] E. Bormashenko, R. Pogreb, T. Stein, G. Whyman, and M. Hakham-Itzhaq, Electrostatically driven droplets deposited on superhydrophobic surfaces, *Applied Phys. Lett.* **95** (2009), 264102.

[10] E. Bormashenko, R. Pogreb, T. Stein, G. Whyman, M. Schiffer, and D. Aurbach, Electrically deformable liquid marbles, *J. Adhesion Sci. & Technology* **25** (2011), 1371–1377.

[11] J. W. Bullard, E. J. Garboczi, Capillary rise between planar surfaces, *Phys. Rev. E* **79** (2009), 011604.

[12] F. Caupin, M. W. Cole, S. Balibar, and J. Treiner, Absolute limit for the capillary rise of a fluid, *Europhys. Lett.* **82** (2008), 56004.

[13] S. Chandrasekhar and E. Fermi, Problems of gravitational stability in the presence of a magnetic field, *Astrophys. J.* **118** (1953), 113.

[14] J. Chatterjee, Limiting conditions for applying the spherical section assumption in contact angle estimation, *J. Colloid & Interface Sci.* **259** (2003), 139–147.
[15] A. Checco and P. Guenoun, Nonlinear dependence of the contact angle of nanodroplets on contact line curvature, *Phys. Rev. Lett.* **91**(18) (2003), 186101.
[16] B. V. Derjaguin and N. V. Churaev, Structural component of disjoining pressure, *J. Colloid & Interface Sci.* **49** (1974), 249–255.
[17] P. G. de Gennes, Brochard-Wyart, and D. Quéré, *Capillarity and Wetting Phenomena*, Springer, Berlin, 2003.
[18] A. Einstein, Folgerungen aus den Capillaritätserscheinungen, *Annalen der Physik* **309**(3) (1901), 513–523.
[19] H. Y. Erbil, *Surface Chemistry of Solid and Liquid Interfaces*, Blackwell, Oxford, 2006.
[20] C. W. Extrand and S. I. Moon, When sessile drops are no longer small: transitions from spherical to fully flattened, *Langmuir* **26** (2010), 11,815–11,822.
[21] I. M. Gelfand and S. V. Fomin, *Calculus of Variations*, Dover, 2000.
[22] R. J. Good, A thermodynamic derivation of Wenzel's modification of Young's equation for contact angles; together with a theory of hysteresis, *J. Am. Chem. Soc.* **74** (1952), 5041–5042.
[23] R. J. Good and L. A. Girifalco, A theory for estimation of surface and interfacial energies I. Derivation and application to interfacial tension, *J. Phys. Chem.* **61**(7) (1957), 904–909.
[24] R. J. Good and L. A. Girifalco, A theory for estimation of surface and interfacial energies III. Estimation of surface energies of solids from contact angle data, *J. Phys. Chem.* **64**(5) (1960), 561–565.
[25] J. N. Israelachvili. *Intermolecular and Surface Forces*, 3rd edn., Elsevier, Amsterdam, 2011.
[26] M. M. Kohonen, Engineered wettability in tree capillaries, *Langmuir* **22** (2006), 3148–3153.
[27] L. Landau and E. Lifshitz, *Fluid Mechanics*, 2nd edn., Butterworth-Heinemann, Oxford, UK, 1987.
[28] B. Legait and P. G, de Gennes, Capillary rise between closely spaced plates: Effects of Van der Waals forces, *Le Journal de Physique – Lett.* **45** (1984), L647–L652.
[29] V. A. Lubarda and K. A. Talke, Analysis of the equilibrium droplet shape based on an ellipsoidal droplet model, *Langmuir* **27** (2011), 10,705–10,713.
[30] A. Marmur, Line tension and the intrinsic contact angle in solid-liquid-fluid systems, *J. Colloid & Interface Sci.* **186** (1997), 462–466.
[31] A. Marmur, Line tension effect on contact angles: Axisymmetric and cylindrical systems with rough or heterogeneous solid surfaces, *Colloids & Surf. A* **136** (1998), 81–88.
[32] A. Marmur, A guide to the equilibrium contact angles maze, in: K. L. Mittal (ed(s).) Contact Angle Wettability and Adhesion, 6, 3–18, VSP, Leiden, 2009.
[33] T. Matsumoto, T. Nakano, T. H. Fujii, M. Kamai, and K. Nogi, Precise measurement of liquid viscosity and surface tension with an improved oscillating drop method, *Phys. Rev. E* **65** (2002), 031201.
[34] K. J. Mysels, The maximum bubble pressure method of measuring surface tension, revisited, *Colloids & Surfaces* **43** (1990), 241–262.
[35] N. K. Nayyar and G. S. Murty, The flattening of dielectric liquid drop in a uniform electric field, *Proceedings of the National Institute of Science of India A* **25**(6), (1959), 373–379.
[36] T. Pompe, A. Fery, and S. Herminghaus, Measurement of contact line tension by analysis of the three-phase boundary with nanometer resolution, in: J. Drelich, J. S. Laskowski, and K. L. Mittal (eds.) Apparent and Microscopic Contact Angles, 3–12, VSP, Utrecht, 2000.
[37] T. W. Richards and E. K. Carver, A Critical study of the capillary rise method of determining surface tension, *J. Am. Chem. Soc.* **43** (1921), 827–847.
[38] R.-J. Roe, Surface tension of polymer liquids, *J. Phys. Chem*. **72**(6) (1968), 2013–2017.

[39] Y. Rotenberg, L. Boruvka, and A. W. Neumann, Determination of surface tension and contact angle from the shapes of axisymmetric fluid interfaces, *J. Colloid & Interface Sci.* **93** (1983), 169–183.
[40] E. Ruckenstein and G. O. Berim, Microscopic description of a drop on a solid surface, *Advances in Colloid and Interface Sci.* **157** (2010), 1–33.
[41] P. F. Scholander, H. T. Hammel, E. D. Bradstreet, and E. A. Hemmingsen, Pressure in Vascular Plants, *Science* **148** 1965), 339–346.
[42] M. Schrader, Young–Dupre revisited, *Langmuir* **11** 1995), 3585–3589.
[43] E. Schrödinger, Notiz über den Kapillardruck in Gasblasen, *Annalen der Physik* **351**(3) (1915), 413–418.
[44] V. M. Starov and M. G. Velarde, Surface forces and wetting phenomena, *J. Phys: Condens. Matter* **21** (2009), 464121.
[45] D. W. Van Krevelen, Properties of polymers, 3rd edn., Elsevier, Amsterdam, 2003.
[46] B. Vonnegut B., Rotating bubble method for determination of surface and interfacial tensions, *Review of scientific Instruments*, 1942, **13**, 6–9.
[47] G. Whyman and E. Bormashenko, Oblate spheroid model for calculation of the shape and contact angles of heavy droplets, *J. Colloid & Interface Sci.* **331** (2009), 174–177.
[48] T. Young, An Essay on the cohesion of liquids, *Phil. Trans. Royal Society of London* **95** (1805), 65–87.
[49] W. Zisman, Contact angle, in: F. Fowkes (ed(s).), Wettability and Adhesion, 43, Advances in Chemistry, Washington, D. C., 1964.

Additional Reading

[50] J. C. Joud, M-G. Barthes-Labrousse, Physical Chemistry and Acid-Base Properties of Surfaces, Wiley Interscience Publishers, New York, 2015.
[51] G. Antonoff, On the validity of Antonoff's rule, *J. Phys. Chem*. **46** (1942), 497–499.
[52] M. Nosonovsky and Z. Chen, Revisiting lowest possible surface energy of a solid, *Surf. Topogr. Metrol. Prop*. **5** (2017), 045001.

3 Contact angle hysteresis

3.1 Contact angle hysteresis: its sources and manifestations

The Young equation derived in Section 2.2, i.e., $\cos\theta_Y = (\gamma_{SA} - \gamma_{SL})/\gamma$ predicts a sole value of the contact angle for a given ideal solid/liquid pair. In reality, however, the situation is much more complicated. Let us deposit a droplet onto an inclined plane, as described in Figure 3.1 in the situation of partial wetting (the spreading parameter $\Psi < 0$). The inclined plane is supposed to be ideal, i.e., atomically flat, chemically homogeneous, isotropic, insoluble, nonreactive, and nondeformed. We nevertheless recognize different contact angles, θ_1, θ_2, as shown in Figure 3.1. This experimental observation definitely contradicts the predictions of the Young equation. Moreover, a droplet on an inclined plane could be in equilibrium only when the contact angles θ_1, θ_2 are different [8, 25]. If we increase the inclination angle α, the contact angles θ_1, θ_2 change, and at some critical angle, α, the droplet starts to slip. This critical contact angle is called the *sliding angle*. We conclude that a variety of contact angles can be observed for the same ideal solid substrate/liquid pair.

Let us perform one more simple experiment. When a droplet is inflated with a syringe as shown in Figure 3.2, we observe the following picture: the triple line is pinned to the substrate up to a certain volume of the droplet. When the triple line is pinned the contact angle increases up to a certain threshold value, θ_A, beyond which the triple line moves. The contact angle θ_A is called the *advancing contact angle* [11]. When a droplet is deflated as depicted in Figure 3.2b, its volume can be decreased to a certain limiting value; in parallel, the contact angle decreases to a threshold value, θ_R, known as the *receding contact angle* [11]. When $\theta = \theta_R$, the triple line suddenly moves. Both θ_A and θ_R are equilibrium, despite metastable contact angles [31]. The difference between θ_A and θ_R is called *contact angle hysteresis*. The Young, receding and advancing contact angles are essentially macroscopic notions; the same is obviously true for the contact angle hysteresis.

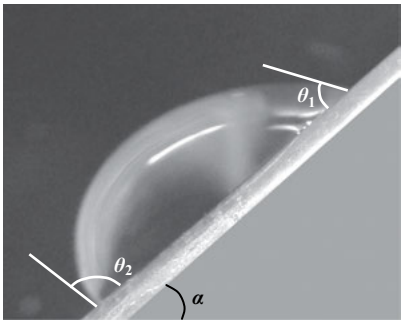

Fig. 3.1: Drop on the inclined plane. Difference between contact angles θ_1 and θ_2 prevents the droplet sliding. α is the inclination angle.

https://doi.org/10.1515/9783110583144-003

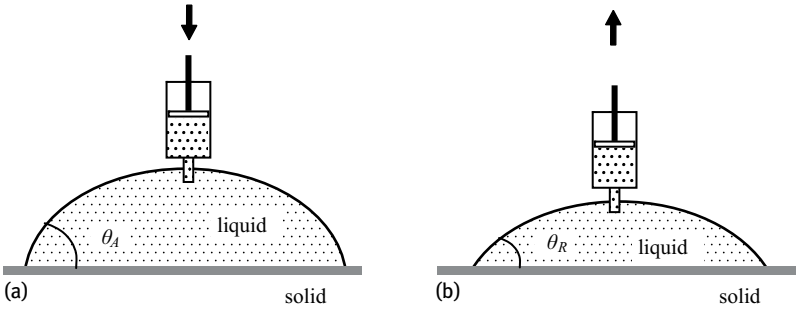

Fig. 3.2: Inflating and deflating of a droplet. a: Advancing θ_A; b: receding contact angles θ_R are shown.

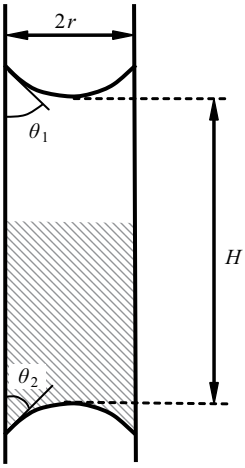

Fig. 3.3: Manifestation of contact angle hysteresis in the capillary tube: the column of liquid is retained by contact angle hysteresis.

One more manifestation of contact angle hysteresis is presented in Figure 3.3. Actually, this effect is well-known to most people: a vertical column of liquid placed into a vertical tube does not fall, but is retained by molecular interaction between the molecules of the tube and those of the liquid, giving rise to deformation of the liquid surface and resulting in capillary menisci. The difference between the contact angle at the lower and upper menisci makes the balance of forces possible:

$$\frac{2\gamma}{r}(\cos\theta_1 - \cos\theta_2) = \rho g H \,. \tag{3.1}$$

The maximal height of the liquid column $H_{\max}$ that could be retained by the capillary tube is given by:

$$\frac{2\gamma}{r}(\cos\theta_R - \cos\theta_A) = \rho g H_{\max} \,, \tag{3.2}$$

where θ_A and θ_R are the receding and advancing contact angles respectively.

Both measurement and understanding of the phenomenon of contact angle hysteresis remain challenging experimental and theoretical tasks. It is customary to at-

tribute the phenomenon of contact angle hysteresis to physical or chemical heterogeneities of the substrate [22]; however, even the ideal substrates discussed in the previous chapter demonstrate significant contact angle hysteresis. We begin our discussion with the physical reasons of contact angle hysteresis on ideal substrates.

3.2 Contact angle hysteresis on smooth homogeneous substrates

Contact angle hysteresis has been registered, even for silicon wafers, which are regarded as atomically flat rigid substrates, and are considered very close to being ideal ones. Extrand and Kumagai studied contact angle hysteresis of various liquids, including water, ethylene glycol, methylene iodide, acetophenone, and formamide, deposited on silicon wafers using a tilted plane method [15]. Contact angle hysteresis (defined as $\theta_A - \theta_R$) as high as 14° was established for the water/silicon wafer and methylene iodide/silicon wafer pairs. It should be mentioned that contact angle hysteresis on the order of magnitude of 5–10° has been reported for other silicon wafer/liquid pairs [15]. High contact angle hysteresis has also been observed for atomically smooth polymer substrates. Lam et al. used polymer-coated silicon wafers for studying contact angle hysteresis and reported the values of contact angle hysteresis on the order of tens of degrees [26]. The question is: how is such dispersion of contact angles possible, in contradiction to the predictions of the Young equation?

The explanation of contact angle hysteresis observed on smooth surfaces becomes possible if we consider the effect of the *pinning of the triple line*. The intermolecular forces acting between molecules of solid and those of liquid, which pin the triple line to the substrate, are responsible for contact angle hysteresis. Yaminsky developed an extremely useful analogy between the phenomena occurring at the triple line with the static friction [45]:

> … for a droplet on a solid surface there is a static resistance to shear. It occurs *not over the entire solid–liquid interface, but only at the three-phase line* …This paradox is easily resolved once one realizes that the liquid–solid interaction is in fact not involved in the process of overflow of liquids above solid surfaces. A boundary condition of zero shear velocity typically occurs even for liquid–liquid contacts … But even given that the strong binding condition does apply to solid–liquid interfaces, this does not prevent the upper layer of the liquid from flowing above the "stagnant layer" of a gradient velocity. The movement of the liquid over the wetted areas occurs in the absence of static resistance. Interaction in a manner of dry friction occurs only at the three-phase line [45].

Thus, contact angle hysteresis on ideal surfaces is caused by the intermolecular interaction between molecules constituting a solid substrate and a liquid; this interaction pins the triple line and gives rise to a diversity of experimentally observed contact angles.

3.3 Strongly and weakly pinning surfaces

In Section 1.7, we already classified solid substrates as "high energy" and "low energy". Recall that high-energy surfaces are inherent for materials built with strong chemical bonds such as ionic, metallic, or covalent (see Section 1.7). Thus, a water droplet deposited on a well-polished metallic surface is expected to show complete wetting ($\Psi > 0$), and it should spread forming a thin film corresponding to a zero contact angle. We placed 10-μl water droplets on thoroughly prepared (degreased and polished) stainless steel and aluminum surfaces [7]. Large "as placed" angles (in the notions proposed in [42]) for steel, as high as 70°, attracted our attention and definitely contradicted the expected complete wetting. Large contact angles observed on nonoxidized and oxidized metallic surfaces were also reported by other groups for iron, gold, and stainless steel [1, 21, 44]. Of course, the oxide film covering the metallic surfaces is also involved in the formation of large "as placed" angles; however, the presence of this film does not convert the surface to a "low-energy" one: it remains a high-energy surface. Bewig and Zisman supposed that high contact angles observed on metallic surfaces are due to organic contaminants, and "in order to rid these metal surfaces of adsorbed hydrophobic contaminants, it is necessary to heat them to white-hot temperatures in flowing streams of high purity gases" [2].

A diversity of factors besides organic contamination could be responsible for high "as placed" contact angles observed on metallic surfaces. To understand the situation properly we *evaporated* the droplets deposited on the metallic (steel and aluminum) surfaces [7]. At the first stage of evaporation, a droplet remains pinned to the substrate and the contact angle is decreased from about 70° to 20°, demonstrating the giant hysteresis of the contact angle. Further evaporation is followed by a de-pinning of the three-phase line. The radius of the contact area a (shown in Figure 3.4) decreases, and the contact angle continues to fall to values of about 5°, as depicted in Figure 3.5a, b.

High values of "as placed" angles may be explained by organic contamination of metallic surfaces, but it definitely does not explain the giant contact angle hysteresis observed on polished and degreased metals. We suggest that the true physical reason explaining both the high values of contact angles and the giant hysteresis registered on high-energy surfaces is the effect of the pinning of the triple (three-phase) line discussed in the previous section (see also Yaminsky [45]). A zero contact angle, which is thermodynamically favorable, remains unattainable owing to a potential barrier produced by the pinning of the triple line to the substrate.

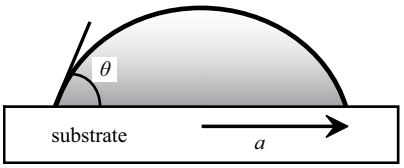

Fig. 3.4: The contact angle and contact radius of a droplet, a.

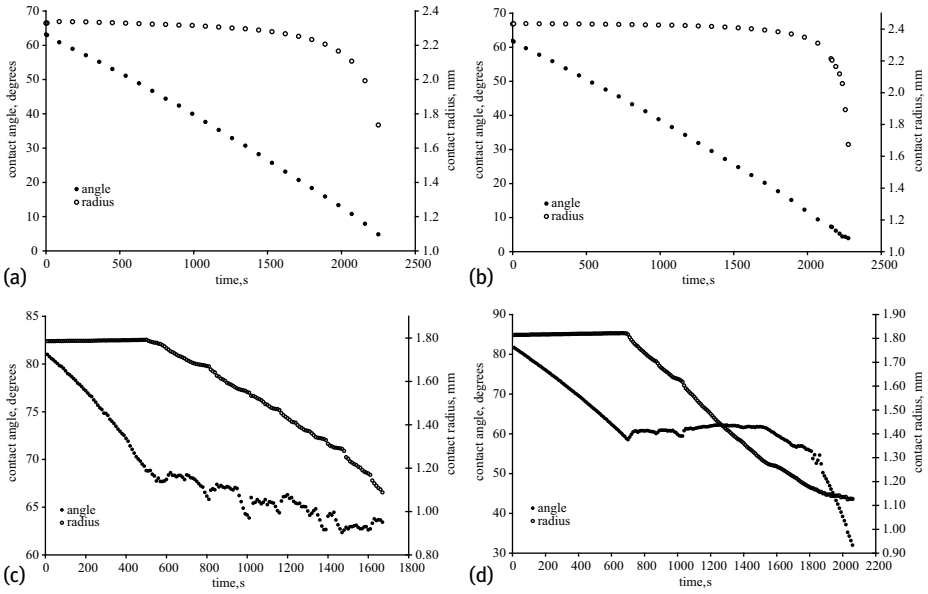

Fig. 3.5: The changes in the contact angle and the contact radius of the water droplet during evaporation on a: steel; b: Al; c: polysulfone; d: polypropylene surfaces.

Now compare the evaporation of droplets deposited on metallic, as opposed to polymer surfaces. Figure 3.5c and d depict changes in the contact angle and the contact radius of a water droplet with the same volume of 10 µl during evaporation on the low-energy polymer (polysulfone and polypropylene) surfaces. Initially, a triple line is pinned, as on high-energy substrates, and the contact angle decreases from about 80° to 65°. But this stage is followed by a stick–slip motion of the triple line when the contact radius jumps to smaller values, and the contact angle may increase again to some extent.

Actually, high-energy (metallic) surfaces demonstrate "as placed" contact angles close to values inherent to low-energy (polymer) substrates. The reasonable question is: what is the actual difference in the wetting behavior of low- and high-energy surfaces? To answer this question, we have to compare graphs describing the dependence of the contact angle on the radius of the contact area (Figure 3.6). Two distinct portions of the curve can be recognized for high-energy substrates: (1) evaporation of a droplet when the three-phase line is pinned (the radius of the contact area is constant), accompanied by a decrease in the contact angle, and (2) fast decrease of a contact radius, accompanied by a slower decrease in the contact angle.

The same portions of curves are also seen in the curves obtained with various polymeric substrates. However, the low-energy surfaces demonstrate somewhat more complicated behavior. The graphs for low-energy substrates include a step with a pinned triple line as observed for high-energy surfaces, but this is followed by a

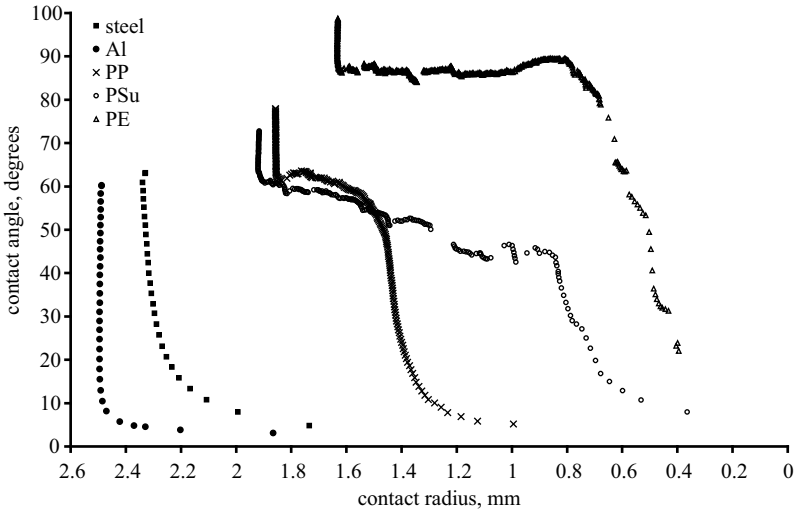

Fig. 3.6: Dependence of the contact angle on the radius of the contact area for a water droplet deposited on various substrates. *PP* polypropylene, *PSu* polysulfone, *PE* polyethylene.

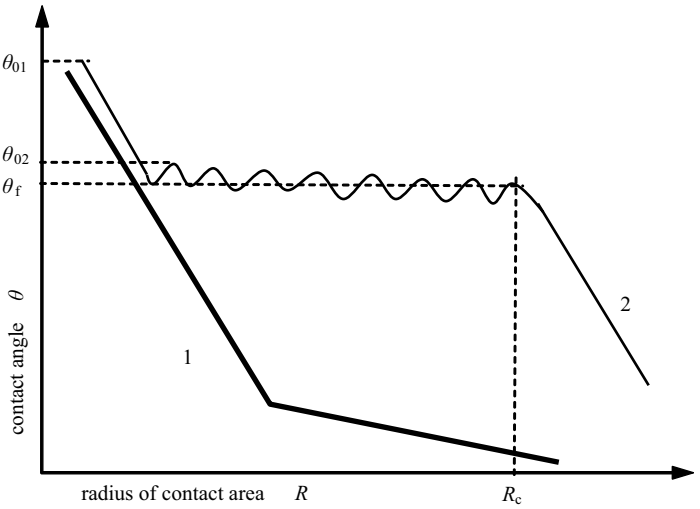

Fig. 3.7: Two types of triple line motion during evaporation on (1) metal, strongly pinning, and (2) nonmetal (polymer), weakly pinning surfaces. Contact radius decreases from left to right as in Figure 3.6.

stick–slip behavior once the contact radius decreases, steadily or with jumps, and the contact angle oscillates around a specific value, as shown schematically in Figure 3.7. These oscillations may be more or less pronounced. This stage was also observed by other investigators [35, 37]. The stick–slip motion of evaporating drops occurring

under a constant contact angle was observed for various polymers, including polytetrafluoroethylene (Teflon), polyethylene, polypropylene, polyethylene terephthalate, and polysulfone [6, 7]. This kind of motion could be related to the weak interaction of a droplet with a polymer substrate, resulting in low pinning of the triple line and promoting sliding of the droplet. At the final stage of evaporation, when the contact radius decreases to the critical value a_c, the contact angle does not oscillate but decreases steadily, starting from the value labeled θ_f, as shown in Figure 3.7.

Thus, we suppose that a new classification of surfaces should be introduced according to the dynamics of a triple line under the evaporation of a drop. It is reasonable to sort solid surfaces into *strongly pinning* (metal) and *weakly pinning* (polymer) surfaces.

3.4 Qualitative characterization of the pinning of the triple line

Figures 3.5 and 3.6 demonstrate that a diversity of contact angles is possible on smooth polymer substrates, providing a manifestation of the phenomenon of contact angle hysteresis. The as-placed contact angle θ_{01} is very different from the angle just after the first slip of the contact line θ_{02} (Figure 3.7), which is supposed to be the second equilibrium contact angle [37]. Study of the stick–slip motion of the evaporated droplets allowed qualitative characterization of the pinning of the triple line. The main parameters that were extracted from the analysis of this motion are the stick time, i.e., the time till the first jump of the contact line, and the energy barrier to be surmounted for the displacement of the triple line. The volume evaporation rate may be calculated as [37]:

$$\frac{\mathrm{d}V}{\mathrm{d}t} = \frac{\mathrm{d}V}{\mathrm{d}\theta}\frac{\mathrm{d}\theta}{\mathrm{d}t} = \frac{\pi a^3}{(1+\cos\theta)^2}\frac{\mathrm{d}\theta}{\mathrm{d}t} \tag{3.3}$$

(a is the radius of the contact area). After integrating equation (3.3) between $\theta = \theta_0$ and $\theta = \theta_t$ the stick time t_{st} is given by:

$$t_{st} = -\frac{\pi a^3 \delta\theta}{(1+\cos\theta_0)^2\,\mathrm{d}V/\mathrm{d}t}\,, \tag{3.4}$$

where $\delta\theta = \theta_0 - \theta_t$. The volume evaporation rate $\mathrm{d}V/\mathrm{d}t$ is negative and may be extracted from the experiments, as well as θ_0, θ_t, and $\delta\theta$. Table 3.1 presents the times of pinning (stick times) until the first jump of the triple line for six different polymer substrates. Two values are included – calculated according to equation (3.4) and measured directly on the graph. Taking into account the variability of the evaporation data measured on the same substrate at different points, the matching of calculated and measured values is quite convincing (with, perhaps, the sole exception of Teflon).

The more important qualitative parameter characterizing the pinning of the triple line is the value of the potential barrier to be surpassed for the displacement of the

Tab. 3.1: Stick times for different polymer substrates.

Polymer	Stick time, s	
	Calculated	Experimental
PE	1108	970
PP	984	730
PVDF (Kynar)	868	850
PET	774	880
PSu	689	570
Teflon	2650	1200

PE polyethylene, *PP* polypropylene, *PVDF* polyvinylidene fluoride, *PET* polyethylene terephthalate, *PSu* polysulfone

droplet. The free surface energy G can be evaluated as [37]:

$$G(a,\theta) = \gamma\pi a^2 \left[\frac{2}{1+\cos\theta} - \cos\theta_0\right] . \tag{3.5}$$

After a slip, the droplet is in a new equilibrium state with a contact radius a_1 and a contact angle θ_1. In the pinned state, before the slip, a droplet with a contact radius a and contact angle θ had a free energy excess equal to the energy barrier to be surmounted for the slip motion $U = 2\pi a\widetilde{U}$, where $\widetilde{U}$ is the potential barrier per unit length of the triple line

$$\gamma\pi\left\{a^2\left[\frac{2}{(1+\cos\theta)} - \cos\theta_0\right] - a_1^2\left[\frac{2}{(1+\cos\theta_1)} - \cos\theta_0\right]\right\} = 2\pi a\widetilde{U} . \tag{3.6}$$

The values of $\widetilde{U}$ calculated from experimental data for different polymers are presented in Table 3.2; the characteristic value of $\widetilde{U}$ are on the order of 10^{-6}–10^{-7} J/m [6, 7, 37]. This value is also close to the upper limit of the reported values of line tension (see Section 2.4); however, it remains disputable whether $\widetilde{U}$ could be identified with line tension [37]. The final stage of evaporation starting from the critical radius a_c (Figure 3.7) was discussed in Bormashenko et al. and Shanahan and Sefiane [6, 37]. It was suggested by these authors that the stick–slip motion of a droplet does not occur at this stage owing to insufficiency of the excess capillary free energy to overcome the potential barrier to be surmounted under stick–slip displacement of the triple line.

Tab. 3.2: The values of potential barrier per unit length of the triple line $\widetilde{U}$.

Polymer	$\widetilde{U}$, J/m
PE	$3.8 \cdot 10^{-7}$
PP	$4.5 \cdot 10^{-7}$
PVDF (Kynar)	$3.5 \cdot 10^{-7}$
PET	$4.4 \cdot 10^{-7}$
PSu	$4.5 \cdot 10^{-7}$
Teflon	$8.7 \cdot 10^{-7}$

3.5 The zero eventual contact angle of evaporated droplets and its explanation

One of the most striking manifestations of contact angle hysteresis is the zero eventual contact angle observed for droplets evaporated on various polymer substrates (Figure 3.6). The explanation of the zero eventual contact angle registered for evaporated sessile droplets is provided by the recent theory developed by Starov and Velarde and discussed in Section 2.6. They suggested that a droplet deposited on a solid substrate may be surrounded by a precursor film, as shown in Figure 2.7. This idea had already been put forward by Shanahan and Sefiane, who suggested that after the first slip of the triple (three-phase) line, the surface surrounding a droplet is already wetted and therefore differs from the original dry one [37]. In this situation, the contact angle is given by equation (2.35):

$$\cos\theta \approx 1 + \frac{1}{\gamma}\int_{e}^{\infty} \Pi(e)\,\mathrm{d}e \approx 1 - \frac{S_- - S_+}{\gamma}\,,$$

where S_- and S_+ are areas depicted in Figure 2.8. Obviously, partial wetting is possible when $S_- > S_+$. Actually, the complete wetting (a zero contact angle) is observed at the final stage of evaporation of sessile droplets, which means that the opposite relation ($S_+ > S_-$) takes place. Thus, we conclude that considering the specific form of the disjoining isotherm reasonably explains the complete wetting observed in the final stage of evaporation of droplets deposited on polymer substrates. Thus, we came to a very important conclusion: two very different regimes of wetting of solid surfaces are possible. In the first, the droplet is surrounded by a dry substrate and the advancing and receding contact angles can be measured. The second wetting regime corresponds to the situation where the droplet is surrounded by a wetted solid substrate. This occurs in the course of evaporation of sessile droplets. In this case, the experimentally observed apparent contact angle tends to zero (corresponding to complete wetting). This could be explained by the peculiarities of the Derjaguin isotherm (see Figure 2.8), stipulating the zero eventual contact angle observed for evaporated sessile droplets. In this case, neither the receding nor the Young contact angles turn out to be unmeasurable physical values.

3.6 Contact angle hysteresis and line tension

When a droplet is surrounded by a wet area, both the Young and the receding contact angles are unattainable. But what do we observe in the opposite situation? When a droplet is placed on a dry solid substrate, we do not observe the Young contact angle either, owing to contact angle hysteresis; in fact, we observe the so-called “as-placed” contact angle, which may be very different from the Young contact angle. The Young

contact angle is the important theoretical construction appearing in equation (2.57) defining the adhesion work and also in expression (2.71) proposed for the calculation of the solid/air surface energy. Thus, the value of the Young angle is essential for the characterization of the wetting situation. Let advancing θ_A and receding θ_R angles be measured experimentally. The question is: how can the Young contact angle be deduced from these data? Two "naive" formulae have been proposed for the calculation of the Young contact angle:

$$\theta_Y = \frac{\theta_A + \theta_R}{2} \tag{3.7}$$

and

$$\cos\theta_Y = \frac{\cos\theta_A + \cos\theta_R}{2}\,. \tag{3.8}$$

It is noteworthy that the "naive" formulae (3.7) and (3.8) are empirical and are not rooted in any fundamental theory [31]. Tadmor proposed the approach that allows calculation of the Young angle from the advancing and receding angles. He related the origin of contact angle hysteresis on smooth substrates to the line tension [39], introduced in Section 2.4. According to Tadmor, the effects of the pinning of the triple line and the line tension are interrelated, and the line energy contribution "opposes the progress toward an equilibrium contact angle" [39]. When a droplet is located on a smooth dry solid substrate, the line tension prevents the displacement of the triple line whenever the droplet is inflated or deflated, as depicted in Figure 3.2. Also according to Tadmor [39], the Young contact angle could be calculated from the receding and advancing angles as:

$$\theta_Y = \arccos\frac{\Gamma_A\cos\theta_A + \Gamma_R\cos\theta_R}{\Gamma_A + \Gamma_R}\,, \tag{3.9}$$

where

$$\Gamma_R = \left(\frac{\sin^3\theta_R}{2 - 3\cos\theta_R + \cos^3\theta_R}\right)^{1/3}\quad;\quad \Gamma_A = \left(\frac{\sin^3\theta_A}{2 - 3\cos\theta_A + \cos^3\theta_A}\right)^{1/3}\,.$$

It is quite reasonable to relate the origin of contact angle hysteresis to the line tension for small micrometrically scaled droplets when the contact angle is governed by the Boruvka–Neumann equation (2.24) [20]. However, expression (3.9) was applied in [39] for the analysis of experimental data obtained with large millimeter-sized droplets. Identification of the line tension with the effect of pinning of the triple line remains highly disputable for large droplets and much experimental and theoretical effort is still necessary to clarify the situation.

3.7 More physical reasons for contact angle hysteresis on smooth ideal surfaces

Let us extend our discussion of contact angle hysteresis to the microlevel. Neumann et al. studied contact angles of 21 liquids from two homologous series (*n*-alkanes and 1-

alkyl alcohols) on fluorocarbons-coated silicon wafers [26]. They found that the receding contact angles decreased with time [26]. Contact angle hysteresis and the receding contact angles also decreased with increasing chain length of the liquid molecules for both the alkane and alcohol series [26]. These results achieve a reasonable explanation in terms of liquid sorption by the solid surface: very large molecules are unlikely to penetrate into the solid substrate. Thus, contact angle hysteresis turned out to be a *time-dependent effect*. Neumann et al. related contact angle hysteresis to the liquid penetration and surface swelling. The receding angles θ_R turned out to be very sensitive to the surface swelling; thus, θ_R does not represent a property of the solid alone. Neumann et al. came to the radical conclusion of disregarding contact angles as a characteristic of the wetting situation and considering only the advancing angles in the study of the surface energetics of solids [26].

Tadmor, in his recent works, also reported the pronounced *time-dependent* character of contact angle hysteresis [40, 41]. He related his observations to the *molecular reorientation of the solid surface* molecules resulting in a higher intermolecular force [40, 41].

3.8 Contact angle hysteresis on chemically heterogeneous smooth surfaces: the phenomenological approach. Acquaintance with the apparent contact angle

Neumann, Good, and Marmur proposed simple phenomenological models explaining contact angle hysteresis on chemically heterogeneous smooth surfaces [29, 32]. We focus on the more simple model introduced by Marmur for 2D cylindrical droplets [29]. He supposed that the local contact angle θ_l of the droplet/surface pair oscillates owing to the chemical heterogeneities inherent to the surface according to the law:

$$\cos\theta_l(x) = \cos\theta_0 + \phi\cos\left(\frac{2\pi x}{l} - \vartheta\right), \tag{3.10}$$

where θ_0 is the average local (intrinsic) contact angle, and ϕ, l, ϑ are the amplitude, wavelength, and phase shift of heterogeneity respectively. Marmur calculated the free energy of the droplet as a function of an apparent contact angle, θ^*. Now we have to acquaint ourselves with one of the most important notions of the wetting of real surfaces: the *apparent contact angle*. The apparent contact angle is an equilibrium contact angle measured macroscopically on a solid surface that may be rough or chemically heterogeneous [31]. The detailed microscopic topography of a rough or chemically heterogeneous surface cannot be viewed with regular optical means; therefore, this contact angle is defined as the angle between the tangent to the liquid–vapor interface and the apparent solid surface, as macroscopically observed [31].

Minimizing the free energy of the droplet $G = G(\theta^*)$ for the chemically heterogeneous surface described by equation (3.10) yielded for the apparent contact angle:

$$\cos\theta^* = \frac{1}{2}\left[\cos\theta_1(x = -a) + \cos\theta_1(x = a)\right] , \tag{3.11}$$

where a is the radius of the contact area. For the symmetrical case ($\vartheta = 0$), the apparent contact angle equals the intrinsic local contact angle θ_1; however, for asymmetrical situations, the apparent contact angle is an average of contact angles at the two edges of the drop, and it is different from the intrinsic (local) contact angle.

The model proposed by Marmur successfully predicts other important features of contact angle hysteresis. Figure 3.8 depicts the typical dimensionless free energy of a droplet as a function of the apparent contact angle. Multiple minima of the dependence are clearly seen. And this is the most important feature of this curve explaining (at least phenomenologically) the effect of contact angle hysteresis, i.e., multiple equilibrium contact angles become possible [24, 29]. The minimum points of the curve presented in Figure 3.8 correspond to various equilibrium positions, and the maximum points are shown to present the energy barriers between successive equilibrium states [29]. It should be stressed that the barriers increase as the global minimum is approached. This prediction coincides with the observation made earlier by Neumann and Good [32].

The model proposed by Marmur also treats the experimentally observed *dependence of contact angle hysteresis on the droplet volume* [29]. According to Marmur, the energy barriers shown in Figure 3.8 do not depend on the droplet volume; on the other hand, the number and location of these barriers do depend on the drop volume. The dependence of the highest and lowest possible contact angles on the volume is described by an oscillatory curve [29]. These oscillations stem from the dependence of the number and locations of the energy barriers on the drop volume. It should be

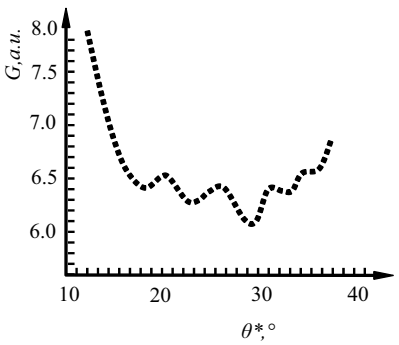

Fig. 3.8: Dimensionless free energy of a droplet as a function of the apparent contact angle. The model developed in Marmur [29] predicts only maxima and minima points of the curve. Local maxima and minima are connected with a dashed line to indicate that the points in between are thermodynamically meaningless. (Reprinted from Marmur [29], with permission from Elsevier.).

stressed that the highest possible contact angle does not necessarily equal the highest local contact angle. The lowest possible contact angle is higher than the lowest intrinsic contact angle [29]. It should be concluded that, despite its simplicity, the phenomenological model proposed by Marmur represents the main features of the static contact angle hysteresis observed on smooth, chemically heterogeneous surfaces.

Now the similarity of contact angle hysteresis to other types of hysteresis becomes clear. *The unifying concept is that hysteresis requires a large number of metastable states that are accessible to the system* [24].

3.9 The phenomenological approach to the hysteresis of the contact angle developed by Vedantam and Panchagnula

Vedantam and Panchagnula developed the phenomenological approach to contact angle hysteresis based on the Ginzburg–Landau theory. They treated the motion of the sessile drop as causing a "phase" transition between wetted and nonwetted "phases" [43]. The theory consists of two essential features: a free energy functional and an evolution equation for the phase field variable. The free energy functional is composed of a coarse grained free energy function and a gradient energy term. The coarse grained energy accounts for the surface energy contributions of the solid–liquid, liquid–vapor, and solid–vapor interfaces [43]. The gradient term accounts for the three-phase contact-line region. The total free energy of the droplet in the phase-field model is given by

$$G = \int_S \left(f(\hat{\eta}) + \frac{1}{2}\hat{\psi} \left|\nabla\hat{\eta}\right|^2 \right) \mathrm{d}S \,, \tag{3.12}$$

where integration is performed over the contact area, and $\hat{\eta}(x, y)$ is the order parameter, selected in such a manner that $\hat{\eta} = 0$ for nonwetted regions, $\hat{\eta} = 1$ for wetted regions, and $0 < \hat{\eta} < 1$ for partially wetted regions. $f(\hat{\eta})$ is an energy function that is built in such a way that $\int_S f(\hat{\eta})\,\mathrm{d}S$ gives the free energy of the droplet without contributions supplied by the contact line (line tension). The gradient coefficient $\hat{\psi}$ is related to the three-phase (line) tension.

The kinetic equation is given in the form:

$$\hat{\beta}\dot{\hat{\eta}} = -\frac{\mathrm{d}G}{\mathrm{d}\hat{\eta}} = \lambda\nabla^2\hat{\eta} - \frac{\partial f}{\partial\hat{\eta}} \,, \tag{3.13}$$

where $\hat{\beta} > 0$ is the kinetic coefficient. Vedantam and Panchagnula showed that in the simplest case of $\hat{\beta} = \text{const}$ for an axisymmetric drop advancing with a velocity v and receding with velocity $-v$ equation (3.13) leads to:

$$\cos\theta_A - \cos\theta_R = 2\hat{\delta}\hat{\beta}v \,, \tag{3.14}$$

where $\hat{\delta} = \Gamma/\hat{\psi}$ and Γ is the line tension (see Section 2.4). It is seen from equation (3.14) that contact angle hysteresis vanishes for $v \to 0$. However, as we discussed in Sec-

tion 3.2, contact angle hysteresis is nonzero for negligibly small contact angle velocities. To explain this discrepancy, Vedantam and Panchagnula sought more complicated forms of the kinetic coefficient, $\hat{\beta}$ [43].

3.10 The macroscopic approach to contact angle hysteresis, the model of Joanny and de Gennes

3.10.1 Elasticity of the triple line

One of the first macroscopic approaches to contact angle hysteresis was developed by Joanny and de Gennes [11, 22]. They related the phenomenon to the pinning of the triple line by surface irregularities, which could be surface roughness or chemical contaminations, that pin and deform the triple line. The natural question is: what is the form of such a distorted triple line? In the simplified model presented by Joanny and de Gennes [22], the authors considered the particular case where the contact angle is 90°, and they calculated the distortion energy of the triple line when the distortion has small sinusoidal amplitude, characterized by a wavenumber k (Figure 3.9).

The surface of a nonperturbed droplet is vertical at the contact with the solid and it coincides with the (YOZ) plane. Joanny and de Gennes considered the case where the triple line is perturbed by a displacement $u(y) = u_k \cos ky$ along the x-axis. The surface of the droplet is now distorted, with a local displacement $\varsigma(y, z)$. Joanny and de Gennes neglected gravity; thus, the Laplace pressure inside the droplet is zero. Hence, the liquid–air interface possesses a zero curvature, which implies:

$$\frac{\partial^2 \varsigma}{\partial y^2} + \frac{\partial^2 \varsigma}{\partial z^2} = 0 \,. \tag{3.15}$$

The solution of this equation is:

$$\varsigma(y, z) = u_k e^{-kz} \cos ky \,. \tag{3.16}$$

It could be seen from the solution (3.16) that the distortion of a liquid's surface extends only over a characteristic height k^{-1} (Figure 3.9); beyond this height, the surface re-

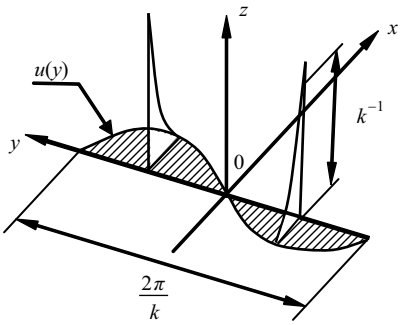

Fig. 3.9: The contact angle is 90° (the surface of the droplet is normal to the XOY plane). The triple line is distorted by a sinusoidal perturbation of a wavenumber, k; a deformation is significant up to a height k^{-1}.

turns to a vertical plane [11, 22]. The energy of distortion of the triple line per unit length along the y direction F is given by:

$$\widetilde{W} = \int \frac{1}{2}\gamma \left[\left(\frac{\partial \varsigma}{\partial z} \right)^2 + \left(\frac{\partial \varsigma}{\partial y} \right)^2 \right] \mathrm{d}z = \frac{1}{4}\gamma k \left| u_{\mathrm{k}} \right|^2 \ . \tag{3.17}$$

De Gennes et al. emphasized that the energy is proportional to k rather than to squared k [11, 22]. Distortion energies $\sim (\nabla \varsigma(y, z))^2$ vary as k^2, but they contribute only up to a fringe height, which scales as k^{-1}. This explains why $\widetilde{W}$ scales as k. De Gennes et al. called this effect the fringe elasticity of the triple line, and stressed that this effect is often misinterpreted as the line tension (see Section 2.4). The energy W_{line} associated with the line tension Γ is given by:

$$W_{\mathrm{line}} = \frac{1}{4}\Gamma k^2 \left| u_{\mathrm{k}} \right|^2 \ , \tag{3.18}$$

and it scales as k^2 (see [11]). The ratio of these energies is:

$$\frac{\widetilde{W}}{W_{\mathrm{line}}} \approx k\frac{\Gamma}{\gamma} \approx k d_{\mathrm{m}} \ , \tag{3.19}$$

where d_{m} is a molecular length. For optically observable distortions of the triple line $k d_{\mathrm{m}} \ll 1$; hence, according to de Gennes, the effects related to the line tension are negligible. Thus, the situation looks like this: the irregularities of the relief pin and distort the triple line, but the energy stored by the triple line is stipulated by its "fringe elasticity," and not by the line tension, as it could be supposed. De Gennes et al. also calculated the precise shape of the triple line pinned by the "point defect," as depicted in Figure 3.10. The precise form of the triple line in this case is given by:

$$u(y) = \frac{f}{\pi\gamma} \ln \frac{y}{r_0} \ , \tag{3.20}$$

where f and r_0 are the "strength" and characteristic size of the defect (see de Gennes et al. [11] and Figure 3.10). It is seen that the triple line pinned by the point defect obtains a logarithmic shape, which is quite different from the shape predicted for a line under tension. The analysis of the elasticity of the triple line relating to contact angles different from 90° is supplied in Joanny and de Gennes [22].

3.10.2 Contact angle hysteresis in the case of a dilute system of defects

Joanny and de Gennes discussed contact angle hysteresis on a surface comprising an ensemble of identical defects distributed randomly over the surface, with a number of defects per unit area denoted as n [11, 22]. They obtained a very general relationship between the advancing and receding angles and the total energy W, dissipated by one defect around a hysteretic cycle:

$$\gamma(\cos\theta_{\mathrm{R}} - \cos\theta_{\mathrm{A}}) = nW \ . \tag{3.21}$$

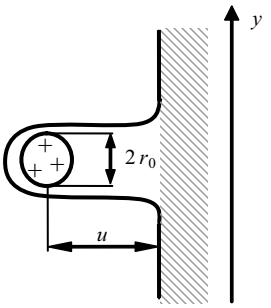

Fig. 3.10: Pinning of the triple line by a point defect with a characteristic dimension of r_0. The shaded regions represent the liquid.

For the strong point defects capable of pinning the triple line, shown in Figure 3.10, and Young contact angles of 90°, expression (3.21) obtains the form:

$$\gamma(\cos\theta_{\mathrm{R}} - \cos\theta_{\mathrm{A}}) = n\frac{f_{\mathrm{m}}^2 \ln\frac{L}{r_0}}{2\pi\gamma}\,, \tag{3.22}$$

where f_{m} is the maximum force that the defect can exert on the triple line before it jumps, and L is the average distance between adjacent anchor defects [11]. It is seen that the hysteresis is proportional to the density of defects n and to the squared maximum pinning force f_{m}. For general expressions considering various contact angles the reader should see Joanny and de Gennes [22]. The lack of experimental data validating the predictions of expression (3.22) should be stressed.

3.10.3 Surfaces with dense defects and the fine structure of the triple line

Consider a surface comprising dense chemical heterogeneities (blemishes). In this case, the triple line is already not smooth, but meanders as shown in Figure 3.11. The quantitative characteristic of meandering is the root mean square (rms) width $\tilde{b}$, defined in Decker and Garoff [10]. The contact line roughness calculation averages over segments of size L as shown in Figure 3.11; thus, treatment of experimental data al-

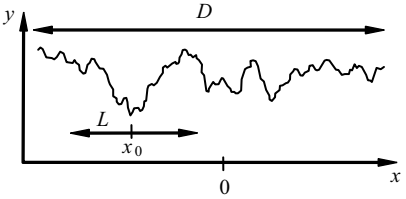

Fig. 3.11: The triple line is presented as a function $y(x)$. The contact line roughness calculation averages over segments of size L, centered at x_0, and varies the position of x_0 over a contact line of a length D [10]. (Adapted with permission from Decker and Garoff [10]. Copyright 1997 American Chemical Society.).

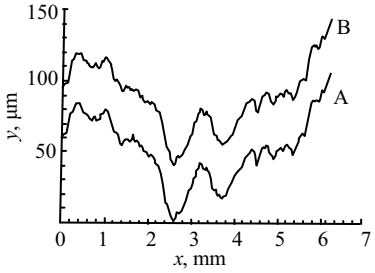

Fig. 3.12: Slowly relaxing the contact line from the recede condition observed by Decker and Garoff [10]. No smoothening of the triple line under receding was observed. (Adapted with permission from Decker and Garoff [10]. Copyright 1997 American Chemical Society).

lows a dependence $\tilde{b}(L)$ to be extracted. It was supposed that this dependence could be described by the scaling law $\tilde{b}(L) \approx L^{\hat{\alpha}}$, where $\hat{\alpha}$ is the scaling exponent [10, 34].

The study of such heterogeneous surfaces involves serious experimental difficulties, and experimental data related to this situation are scarce. Decker and Garoff studied the fine structure of the triple line of chemically heterogeneous surfaces coated by organic monolayers [10]. The characteristic scale of heterogeneity was ~ 100 Å. They reported values of $\hat{\alpha}$, which were slightly less than 1, whereas values $\hat{\alpha} = 1/2$ and $\hat{\alpha} = 1/3$ were predicted, depending on the dimension of heterogeneity [11, 34]. The lack of experimental data in the field should be noted (see also Additional Reading to Section 5).

Decker and Garoff also studied the relaxing of the triple line pinned by dense chemical heterogeneities from the recede conditions illustrated in Figure 3.12. One might expect smoothening of the triple line under receding; however, Decker and Garoff reported that contact line roughness is not influenced by the relaxation of the macroscopic contact angles [10]. It is noteworthy that in spite of the fact that individual defects were 100 Å-scaled, the overall pattern of the triple line suggests blemishes of 100–500 μm, as shown in Figure 3.12. The explanation of this discrepancy was proposed in [11]; however, study of the fine structure of the triple line definitely calls for new experimental and theoretical efforts. Direct environmental scanning electron microscopy (ESEM) observation of the meandering of the triple line has been reported recently for droplets placed on microporous polymer substrates, as illustrated in Figure 3.13 [3, 4].

3.11 Deformation of the substrate as an additional source of contact angle hysteresis

Let us take a closer look at the Young equation (2.11) and Figure 2.3. The Young equation could be interpreted as the balance of horizontal projections of forces acting on the triple line. However, the vertical balance is still neglected. The component of the liquid surface tension $\gamma \sin\theta$ perpendicular to the plane of the solid (Figure 3.14) must be equilibrated, and this leads necessarily to some distortion of the substrate near the

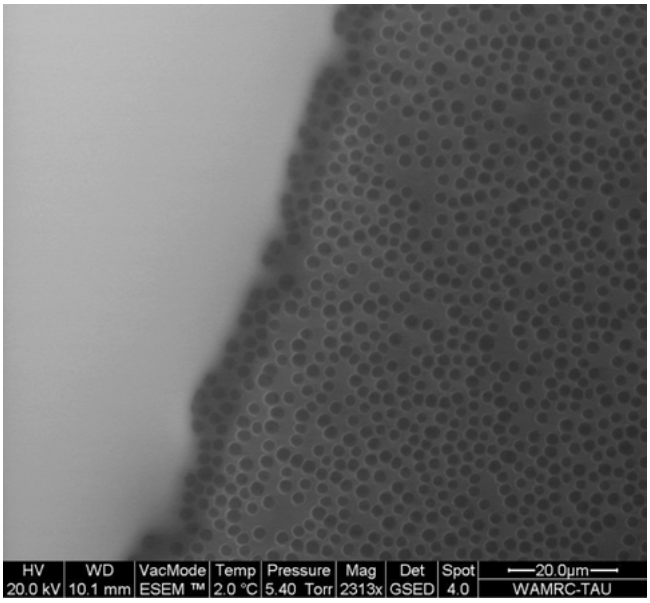

Fig. 3.13: Environmental scanning electron microscopy image of a water droplet (white field) deposited on a micro-porous polystyrene substrate. Meandering of the triple line is clearly seen. Scale bar is 20 µm.

triple line, called the "wetting ridge" [27, 36]. This distortion is negligible for rigid substrates such as glass or steel, but it should be considered for soft substrates such as rubbers (elastomers) [33]. This wetting ridge (depicted in Figure 3.14) leads to additional pinning of the triple line and strengthens contact angle hysteresis.

The problem of elastic deformation of a substrate by a droplet was treated in Long et al. and Shanahan and Carre [27, 36]. The scaling dimensionless parameter δ, relating contributions of surface tension and elastic terms, could be introduced according to:

$$\delta = \frac{\gamma_{SA}}{\mu d} , \tag{3.23}$$

where μ is the elastic (shear) modulus of the solid, and d is the depth (thickness of the substrate) [27]. For distances much larger than the thickness d, the vertical displacement ζ (Figure 3.14) decays exponentially:

$$\zeta \cong \frac{\gamma \sin\theta}{\mu} \sin\frac{|x|}{\kappa} \exp\left(-\frac{|x|}{k'}\right) , \tag{3.24a}$$

where x is a distance measured from the triple line parallel to the undisturbed surface (Figure 3.14), and κ, k' are characteristic lengths of the order d [27]. At intermediate distances $\delta d < x < d$ the deformation ζ is given by:

$$\zeta \cong \frac{\gamma \sin\theta}{2\pi\mu} \ln\frac{d}{|x|} . \tag{3.24b}$$

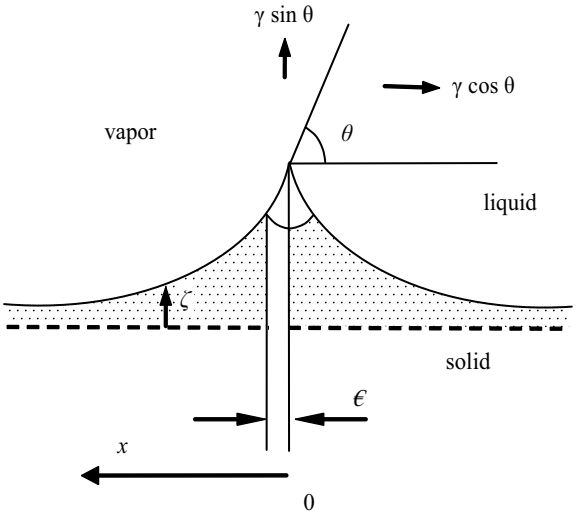

Fig. 3.14: Scheme of the wetting ridge. ζ is the vertical displacement caused by the vertical component of surface tension, $\gamma \sin\theta$. ϵ is the cutoff distance for linear elastic behavior.

Formula (3.24b) is true for $|x| > \epsilon$, where ϵ is a cutoff length, below which the solid no longer behaves in a linearly elastic manner (typically on the order of a few nanometers for an elastomer) [36]. At short distances ($x < \delta d$), the vertical displacement ζ is estimated as:

$$\zeta \cong \frac{1}{2\pi} \frac{\gamma \sin\theta}{\mu} \ln \frac{1}{\delta} . \tag{3.24c}$$

For details of the solution of a problem of distortion of a soft substrate by a droplet see Long et al., Pericet-Camara et al., and Shanahan and Carre [27, 33, 36]. Anyway, this distortion is not negligible for soft materials such as elastomers and it makes an essential contribution to contact angle hysteresis.

3.12 How contact angle hysteresis can be measured

Contact angle hysteresis can be established by different experimental techniques, i.e., *the needle-syringe method* when a droplet is "inflated" by additional quantities of water, as shown in Figure 3.2a. The threshold maximal value of the contact angle, before the triple line jumps corresponds to θ_A. The minimal value of the contact angle (when the droplet is deflated as shown in Figure 3.2b) corresponds to θ_R. The mirror image of the needle-syringe method is the so-called *captive bubble method*, represented in Figure 3.15a. In this method, a fluid bubble touches the sample surface as shown in Figure 3.15a. The size of the bubble is enlarged or reduced with a micro-pump to cre-

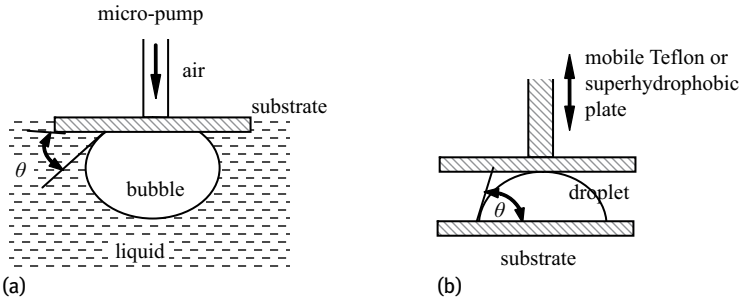

Fig. 3.15: a: Scheme of the captive bubble method for the measurement of contact angle hysteresis. b: Scheme of the study of contact angle hysteresis with deformed droplets (for details see Bormashenko et al. [5]).

ate advancing or receding conditions for the triple line [12]. The interpretation of the results obtained with the needle-syringe and captive bubble methods requires great care to be taken. Marmur demonstrated that a drop and a captive bubble show very different behavior during contact angle hysteresis measurements [30]. The stick–slip behavior of droplets and bubbles, discussed in the Section 3.4, is quite different. Both advancing and receding contact angles depend on the size of the droplet (bubble), but these dependences are different [19, 30]. Thus, we see that advancing and receding contact angles are sensitive not only to the volume of the drop (bubble), but also to the experimental technique used to establish them. This should be emphasized for receding contact angles, when even zero eventual contact angles are observed under the evaporation of sessile droplets, as discussed in Section 3.5.

Advancing and receding contact angles can also be established under the deformation of a droplet, as shown in Figure 3.15b [5]. This method has certain advantages, because contact angle hysteresis is measured under a constant volume of the deformed droplet (for details, see Bormashenko et al. [5]). Contact angle hysteresis is often established using the *tilted plane method*, as illustrated in Figure 3.1. The shortcomings of this method are discussed in Appendix 3A at the end of this chapter.

3.13 Roughness of the substrate and contact angle hysteresis

Systematic study of the impact exerted by the roughness of the substrate on contact angle hysteresis was performed by Johnson and Dettre [23]. They studied advancing and receding contact angles of water drops placed on wax surfaces. Johnson and Dettre plotted advancing and receding angles as functions of roughness, defined as the ratio of the real surface area to its projected value [31]. They demonstrated that roughness influences both θ_R and θ_A, and thus it influences contact angle hysteresis [23]. We shall discuss the complicated character of this influence further when the Wenzel

and Cassie–Baxter wetting regimes have been introduced. At this point, we want to mention that experimental study of the impact exerted by roughness on the contact hysteresis is challenged by serious experimental difficulties. Fetzer and Ralston have recently shown that this study is sensitive to experimental technique: the sessile drop and captive bubble methods supplied different values for the advancing and receding angles [16]. It was demonstrated that the advancing and receding contact angles established on rough surfaces also depend on the size of the droplet (bubble) [13]. The aforementioned factors make the study of contact angle hysteresis on rough surfaces extremely challenging from both experimental and theoretical points of view.

3.14 Use of macroscopic contact angles for characterization of solid surfaces

Wetting measurements are probably the most commonly performed and simplest surface analysis technique. The measurement of macroscopic contact angles is carried out with inexpensive equipment, and the measurement procedure is rapid and simple; that is why contact angles are widely used for characterization of solid surfaces. For example, Chibowski et al. proposed a formula allowing calculation of γ_{SA} from the measured advancing and receding contact angles [9]. It is also important to note that wettability often correlates strongly with adhesion. At the same time, the interpretation of these measurements is far from trivial, and misunderstandings and misinterpretations in this field are regrettably abundant.

In many papers, we find the notion of the so-called "static contact angle," which describes the contact angle of the droplet simply put on the substrate. This notion is meaningless [38]. As we already saw in Section 3.2, even smooth chemically homogeneous surfaces demonstrate contact angle hysteresis. Thus, necessarily both the advancing and receding angles should be supplied for the characterization of a solid surface. Moreover, the technique used for establishment of these angles and the volumes of the droplets should be supplied, because the advancing and receding contact angles are sensitive to experimental techniques and the sizes of droplets (bubbles) used for their estimation [13, 19, 30].

The most problematic is the notion of the receding contact angle [38]. The receding contact angle depends strongly on the experimental technique used for its establishment. As demonstrated in Section 3.5, even zero contact angles are possible for droplets evaporated on polymer substrates. In this situation, it is plausible to propose using *only advancing contact angles for the characterization of solid surfaces*.

Let us take a closer look at the Young equation (2.11). The surface tensions, γ_{SA}, γ, are objective physical quantities independent of the history of droplet deposition. They can be established by using independent experimental techniques. The same is not true for the surface tension γ_{SL}. It may be phenomenologically supposed that

γ_{SL} contains all the information related to contact angle hysteresis. Thus, the advancing contact angle corresponds to the maximal value of the solid/liquid surface tension γ_{SL}^{max}:

$$\cos\theta_A = \frac{\gamma_{SA} - \gamma_{SL}^{max}}{\gamma} . \tag{3.25}$$

The advancing contact angle corresponds to the minimal work of adhesion, given by the Dupré equation:

$$W_{min} = \gamma(1 + \cos\theta_A) . \tag{3.26}$$

Equation (3.26) becomes clear from simple qualitative considerations. Indeed, the advancing contact angle corresponds to the maximal solid–liquid surface tension, γ_{SL}^{max}. Hence, the formation of the solid–liquid interface needs maximal energy, and it is energetically unfavorable; this case naturally corresponds to the minimal work of adhesion, given by the Dupré equation. It should be stressed that the advancing contact angles are the most reproducible contact angles available for the solid–liquid pair.

Additional Reading

Contact angle hysteresis observed on polymer surfaces has been discussed in much detail in Grundke et al. [46]. It was demonstrated that roughness below some threshold value (typically < 100 nm) does not usually influence contact angle hysteresis. The authors studied fluoropolymer surfaces with identical chemistry but various roughness [46]. The weak effects on contact angle hysteresis were already observable for height roughness values in the range between 40 and 50 nm. Mean height roughness values of about 160 nm had a remarkable effect on hysteresis [46]. The influence of contact angle hysteresis in physical phenomena relevant for industrial applications such as sliding drops, coffee stain phenomenon (in general evaporative self-assembly), and curtain and wire coating techniques was reviewed in Eral et al. [47]. The review of experimental techniques used for the establishment of contact angle hysteresis is supplied in Yuan and Lee [48]. Accurate modern scientific terminology related to the classification of contact angles is presented in Marmur et al. [49]. The mechanism of stick–slip motion of the triple line (presented in Section 3.3) was suggested and simulated in Li et al. [50].

Appendix 3A. A droplet on an inclined plane

As we already mentioned in Section 3.1, a droplet can be at rest on an inclined plane only because of contact angle hysteresis (Figure 3.1). The precise solution of the physical problem that deals with a droplet placed on the inclined plane is far from trivial. Remarkably, one of the first solutions of this problem was proposed by the distinguished

physicist Yakov Ilyitch Frenkel [17]. Frenkel treated the simplest approximation of this problem, i.e., considered two-dimensional droplets when the shape of the drop is approximated with the infinite cylinder (see also Section 2.3). Frenkel proposed the following sliding condition for the droplet:

$$\gamma(\cos\theta_R - \cos\theta_A) = \widetilde{m}g\sin\alpha\,, \tag{3.27}$$

where $\widetilde{m}$ is the mass of the unit length of a two-dimensional drop, and α is the critical (sliding) angle introduced in Section 3.1. Restoring historical justice calls for mentioning that Frenkel first clearly demonstrated that the Young equation is actually the *boundary condition* of the problem of wetting (see also Section 2.2). A result similar to equation (3.27) was independently reported by Macdougall and Ockrent [28]. The shape of 2D droplets is given by a catenary curve, which is not surprising; the same curve already appeared in the problem of the shape of a meniscus of a liquid wetting a fiber, also resulting from the interplay of surface tension and gravity (Section 2.11, expression (2.55)).

The problem was generalized for 3D droplets and experimentally studied by various investigators [8, 14, 18]. Furmidge proposed for the 3D droplet the following sliding condition:

$$\gamma l(\cos\theta_R - \cos\theta_A) = mg\sin\alpha\,, \tag{3.28}$$

where l is the length of the triple line contouring a droplet and m is its mass [18]. The Furmidge equation (3.28) is broadly used in experimental practice. Krasovitski and Marmur proposed writing the sliding condition in a generalized form [25]:

$$\gamma C(\cos\theta_R - \cos\theta_A) = \sin\alpha\,, \tag{3.29}$$

where C is the constant that includes gravitational acceleration, the fluid density and the geometric parameters of the drop. However, Krasovitski and Marmur demonstrated that contact angles at the upper and lower contact lines do not always simultaneously equal the receding and advancing contact angles respectively [25]. On a hydrophobic surface, the lowest contact angle (at the upper contact line, see Figure 3.16a) tends to be approximately equal to the receding contact angle, whereas the highest contact angle (at the lower contact line, Figure 3.16a) may be much lower than the advancing contact angle [25]. For hydrophilic surfaces, the opposite is true. These results cast suspicion on "the tilted plane method" for experimental establishment of contact angle hysteresis. The problem of sensitivity of contact angle hysteresis to the experimental technique used for its measurement should be emphasized once more.

The problem of the calculation of the precise shape of a droplet placed on an inclined plane is not simple either. Carre and Shanahan [8] proposed describing the shape of a droplet with the function, $z(r, \phi)$, in the polar coordinates depicted in Figure 3.16a,b:

$$z(r,\phi) \cong \frac{a^2 - r^2}{2R} + \varepsilon(r,\phi)\,, \tag{3.30}$$

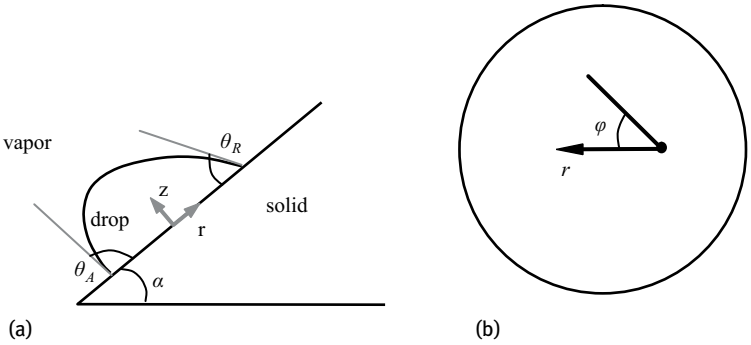

Fig. 3.16: a: Droplet on an inclined plane; b: polar coordinates used in Carre and Shanahan [8] for the calculation of the droplet's shape.

where R is the radius of curvature of the unperturbed drop, and a is its contact radius [8]. The first term corresponds to the undisturbed form, and $\varepsilon(r, \phi)$ is a perturbation caused by gravity [8]. For the function, $\varepsilon(r, \phi)$, in the nearest vicinity of the triple line, Carre and Shanahan obtained:

$$\varepsilon(r_0) \cong -\frac{\rho g a^3 \sin\alpha \cos\phi}{9\gamma}\,, \tag{3.31}$$

where ρ is the liquid density and α is the slope of the inclined plane [8].

Bullets

- A spectrum of equilibrium contact angles is possible for a certain solid/liquid pair. Maximal and minimal contact angles are called *advancing* and *receding* contact angles. The phenomenon is called *contact angle hysteresis*.
- Contact angle hysteresis is observed, even on ideal, atomically flat substrates owing to the pinning of the contact (triple) line.
- Contact angle hysteresis is clearly observed under evaporation of liquid droplets. The eventual contact angle of evaporated droplets often equals zero. Study of the evaporation of sessile droplets allows qualitative characterization of the pinning of the triple line.
- Contact angle hysteresis is due to the multiple minima of the free energy of a droplet deposited on the substrate. These minima are separated by potential barriers.
- Contact angle hysteresis is strengthened by the roughness and chemical heterogeneity of a substrate.
- Rough and chemically heterogeneous surfaces are characterized by an *apparent contact angle*.

- Contact angle hysteresis is influenced by liquid swelling and deformation of the substrate.
- Contact angle hysteresis depends on the droplet volume.
- Advancing and receding contact angles are sensitive to the experimental technique used for their establishment. Advancing contact angles are the most reproducible contact angles available for the solid–liquid pair.
- Contact angle hysteresis defines the behavior of a droplet on a tilted plane.

References

[1] M. E. Abdelsalam, P. Bartlett, N. K. Kelf, and J. Baumberg, Wetting of regularly structured gold surfaces, *Langmuir* **21** (2005), 753–1757.

[2] K. W. Bewig and W. A. Zisman, The Wetting of Gold and Platinum by water, *J. Phys. Chem*. **69** (1965), 4238–4242.

[3] E. Bormashenko, Why does the Cassie–Baxter equation apply? *Colloids & Surfaces A* **324** (2008), 47–50.

[4] E. Bormashenko, Y. Bormashenko, T. Stein, G. Whyman, and R. Pogreb, Environmental scanning electron microscopy study of the fine structure of the triple line and Cassie–Wenzel wetting transition for sessile drops deposited on rough polymer substrates, *Langmuir* **23** (2007), 4378–4382.

[5] E. Bormashenko, Y. Bormashenko, G. Whyman, R. Pogreb, A. Musin, R. Jager, and Z. Barkay, Contact angle hysteresis on polymer substrates established with various experimental techniques, its interpretation, and quantitative characterization, *Langmuir* **24** (2008), 4020–4025.

[6] E. Bormashenko, A. Musin, G. Whyman, and M. Zinigrad, Wetting transitions and depinning of the triple line, *Langmuir* **28**(7) (2012), 3460–3464.

[7] E. Bormashenko, A. Musin, and M. Zinigrad, Evaporation of droplets on strongly and weakly pinning surfaces and dynamics of the triple line, *Colloids & Surfaces A* **385** (2011), 235–240.

[8] A. Carre and M. Shanahan, Drop motion on an inclined plane and evaluation of hydrophobic treatments to glass, *J. Adhesion* **49** (1995), 177–185.

[9] E. Chibowski and R. Perea-Carpio, Problems of contact angle and solid surface free energy determination, *Advances in Colloid & Interface Sci.* **98** (2002), 245–264.

[10] E. L. Decker and S. Garoff, Contact line structure and dynamics on surfaces with contact angle hysteresis, *Langmuir* **13** (1997), 6321–6332.

[11] P. G. de Gennes, F. Brochard-Wyart, and D. Quéré, Capillarity and Wetting Phenomena, Springer, Berlin, 2003.

[12] J. Drelich, Instability of the three-phase contact region and its effect on contact angle relaxation, in: J. Drelich, J. S. Laskowski, and K. L. Mittal (eds.), Apparent and Microscopic Contact Angles, VSP, Utrecht, 2000.

[13] J. Drelich, J. D. Miller, and R. J. Good, The effect of drop (bubble) size on advancing and receding contact angles for heterogeneous and rough solid substrates as observed with sessile-drop and captive-bubble technique, J. Colloid & Interface Sci. 179 (1996), 37–50.

[14] C. Extrand and Y. Kumagai, Liquid drops on an inclined plane: The Relation between contact angles, drop shape, and retentive force, *J. Colloid & Interface Sci.* **170** (1995), 515–521.

[15] C. W. Extrand and Y. Kumagai, An experimental study of contact angle hysteresis, *J. Colloid & Interface Sci.* **191** (1997), 378–383.

[16] R. Fetzer and J. Ralston, Exploring defect height and angle on asymmetric contact line pinning, *J. Phys. Chem. C* **115** (2011), 14,907–14,913.
[17] Y. I. Frenkel, On the behavior of liquid drops on a solid surface. I. The sliding of drops, *J. Exptl. Theoret. Phys.* (USSR) **18** (1948), 659.
[18] C. G. L. Furmidge, Studies at phase interfaces. I. The sliding of liquid drops on solid surfaces and a theory for spray retention, *J. Colloid & Interface Sci.* **17** (1962), 309–324.
[19] R. J. Good and M. N. Koo, The effect of drop size on contact angle, *J. Colloid & Interface Sci. 71* (1979), 283–292.
[20] Y. Gu, Drop size dependence of contact angles of oil drops on a solid surface in water, Colloids & Surfaces A 181 (2001), 215–224.
[21] S. M. Iveson, S. Holt, and S. Biggs, Advancing contact angle of iron ores as a function of their hematite and goethite content: implications for pelletising and sintering, *Int. J. Miner. Process*. **74** (2004), 281–287.
[22] J. F. Joanny and P. G. de Gennes, A model for contact angle hysteresis, *J. Chem. Phys.* **81**(1) (1984), 552–562.
[23] R. E. Johnson and R. H. Dettre, Contact Angle Hysteresis II. Contact Angle Measurements on Rough Surfaces, in: F. M. Fowkes (ed(s).), Contact Angle, Wettability, and Adhesion, 136–144, Advances in Chemistry Series 43, American Chemical Society, Washington D. C., 1964.
[24] R. E. Johnson, R. H. Dettre, and D. A. Brandreth, Dynamic contact angles and contact angle hysteresis, J. *Colloid & Interface Sci.* **62** (1977), 205–212.
[25] B. Krasovitski and A. Marmur, Drops down the hill: theoretical study of limiting contact angles and the hysteresis range on a tilted plane, *Langmuir* **21** (2005), 3881–3885.
[26] C. N. C. Lam, R. Wu, D. Li, M. L. Hair, and A. W. Neumann, Study of the advancing and receding contact angles: liquid sorption as a cause of contact angle hysteresis, *Advances in Colloid & Interface Sci.* **96** (2002), 169–191.
[27] D. Long, A. Ajdari, L. Leibler, Static and dynamic properties of thin rubber films, *Langmuir* **12** (1996), 5221–5230.
[28] G. Macdougall and C. Ockrent, Energy relations in liquid/solid systems. I. The adhesion of liquids to solids and a new method of determining the surface tension of liquids, *Proceedings of the Royal Society of London A* **180** (1942), 151–173.
[29] A. Marmur, Contact angle hysteresis on heterogeneous smooth surfaces, J. *Colloid & Interface Sci.* **168** (1994), 40–46.
[30] A. Marmur, Contact-angle hysteresis on heterogeneous smooth surfaces: theoretical comparison of the captive bubble and drop methods, *Colloids & Surfaces A* 136 (1998), 209–215.
[31] A. Marmur, A guide to the equilibrium contact angles maze, in: K. L. Mittal (ed(s).), Contact Angle Wettability and Adhesion, 6, 3–18, Brill/VSP, Leiden, 2009.
[32] A. W. Neumann and R. J. Good, Thermodynamics of contact angles. I. Heterogeneous solid surfaces. *J. Colloid & Interface Sci*. **38** (1972), 341–358.
[33] R. Pericet-Camara, G. K. Auernhammer, K. Koynov, S. Lorenzoni, R. Raiteri, and E. Bonaccurso, Solid-supported thin elastomer films deformed by microdrops, *Soft Matter 5* (2009), 3611–3617.
[34] M. O. Robbins and J. F. Joanny, Contact angle hysteresis on random surfaces, *Europhys. Lett*. **3** (1987), 729.
[35] M. E. R. Shanahan, Simple theory of "stick-slip" wetting hysteresis, *Langmuir* **11** (1995), 1041–1043.
[36] M. E. R. Shanahan and A. Carre, Viscoelastic dissipation in wetting and adhesion phenomena, *Langmuir* **11** (1995), 1396–1402.
[37] M. E. R. Shanahan and K. Sefiane, Kinetics of triple line motion during evaporation, in: Contact Angle, Wettability and Adhesion, 6, 19–31, Brill/VSP, Leiden, 2009.

[38] M. Strobel and C. S. Lyons, An essay on contact angle measurements, *Plasma Process. Polym.* **8** (2011), 8–13.
[39] R. Tadmor, Line energy and the relation between advancing, receding and Young contact angles, *Langmuir* 20 (2004), 7659–7664.
[40] R. Tadmor, Approaches in wetting phenomena, *Soft Matter* **7** (2011), 1577–1580.
[41] R. Tadmor, P. Bahadur, A. Leh, H. E. N'guessan, R. Jaini, and L. Dang, Measurement of lateral adhesion forces at the interface between a liquid drop and a substrate, *Phys. Rev. Lett.* **103** (2009), 266101.
[42] R. Tadmor and P. S. Yadav, As-placed contact angles for sessile droplets, *J. Colloid & Interface Sci.* **317** (2008), 241–246.
[43] S. Vedantam and M. V. Panchagnula, Constitutive modeling of contact angle hysteresis, *J. Colloid & Interface Sci*. **321** (2008), 393–400.
[44] R. Wang, M. Takeda, and M. Kido, Micro pure water wettability evaluation of SUS304 steel with a tapping mode of atomic force microscope, *Scripta Materialia* **46** (2002), 83–87.
[45] V. V. Yaminsky, Hydrophobic transitions, in: J. Drelich, J. S. Laskowski, and K. L. Mittal (eds.) Apparent and microscopic contact angles, 47–93, VSP, Utrecht, 2000.

Additional Reading

[46] K. Grundke, K. Pöschel, A. Synytska, R. Frenzel, A. Drechsler M. Nitschke, A. L. Cordeiro, P. Uhlmann and P. B. Welzel, Experimental studies of contact angle hysteresis phenomena on polymer surfaces – toward the understanding and control of wettability for different applications, *Advances Colloid & Interface Sci*. **222**, (2015), 350–376.
[47] H. B. Eral, D. J. C. M. 't Mannetje, J. M. Oh, Contact angle hysteresis: a review of fundamentals and applications, *Colloid & Polymer Sci.* **291**(2) (2013), 247–260.
[48] Y. Yuan, T. R. Lee, Contact Angle and Wetting Properties, In: Bracco G., Holst B. (eds) Surface Science Techniques. Springer Series in Surface Sciences, 51. Springer, Berlin, Heidelberg, 2013.
[49] A. Marmur, C. Della Volpe, S. Siboni, A. Amirfazli and J. W. Drelich, Contact angles and wettability: towards common and accurate terminology, *Surface Innovations* **5**(1) (2017), 3–8.
[50] Q. Li, P. Zhou and H. J. Yan, Pinning–depinning mechanism of the contact line during evaporation on chemically patterned Surfaces: A Lattice Boltzmann study, *Langmuir* **32**(37), (2016), 9389–9396.

4 Dynamics of wetting

4.1 The dynamic contact angle

Previous to this chapter we have discussed only the statics of wetting. Now we consider a much more complicated situation: when the triple line moves. When the triple line moves, the dynamic contact angle, θ_D, does not equal the Young angle, as shown in Figure 4.1. It can be larger or smaller than the Young angle (Figure 4.1). The excess force pulling the triple line is given by [7]:

$$F(\theta_D) = \gamma_{SA} - \gamma_{SL} - \gamma \cos\theta_D \ . \tag{4.1}$$

The usual experimental technique allowing the study of dynamic contact angles is with use of the Wilhelmy plate described in Section 2.14, by which a substrate is pulled from or immersed in liquid [14, 22]. As we already mentioned in the previous chapter, the effect of contact angle hysteresis complicates the study of wetting, even in a static situation. The movement of the triple line introduces additional difficulties; thus, the reproducibility of the results of the measurements of dynamic contact angles becomes a challenging task [10]. We start from the theoretical analysis of dynamic wetting on ideally smooth, rigid, nonreactive surfaces.

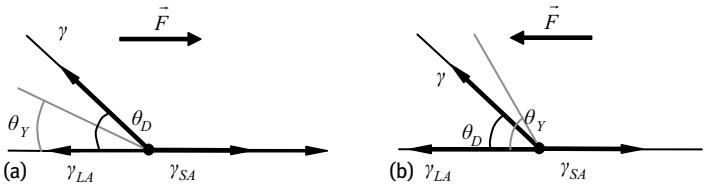

Fig. 4.1: Origin of the dynamic contact angle. a: the dynamic contact angle θ_D is larger than the Young angle θ_Y; b: the opposite situation – the dynamic contact angle θ_D is smaller than the Young angle θ_Y.

4.2 The dynamics of wetting: the approach of Voinov

Now we find ourselves in the realm of hydrodynamics. Systematic study of the problem of the dynamics of wetting has been undertaken by Voinov [23]. He studied two-dimensional noninertial motion of an incompressible liquid with a free surface along a plane solid surface, shown in Figure 4.2. The fluid motion is governed by equations:

$$\nabla p = \eta \Delta \vec{v} \ , \quad \operatorname{div} \vec{v} = 0 \tag{4.2}$$

https://doi.org/10.1515/9783110583144-004

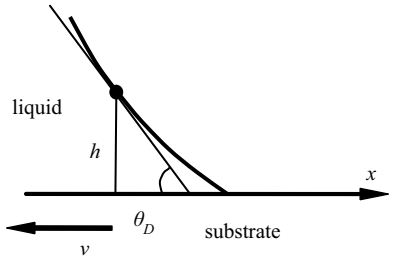

Fig. 4.2: Formation of the dynamic contact angle θ_D according to Voinov [23].

where p is the pressure, $\vec{v}$ is the velocity, and η is the viscosity. Adhesion at the solid boundary is assumed; thus, at the boundary we have:

$$v_x = -v\,, \quad v_y = 0\,. \tag{4.2a}$$

The boundary conditions at the free surface are:

$$\vec{v}\cdot\vec{n} = 0\,, \quad p_\tau = 0\,. \tag{4.2b}$$

Here, p_τ is the tangential stress. The normal stress on the free surface is determined by the capillary forces:

$$p_n = p_0 + \gamma\hat{C}\,, \tag{4.2c}$$

where p_0 is the atmospheric pressure, and $\hat{C}$ is the curvature of the surface, introduced in Section 1.5. The viscous stresses on the free surface decrease with an increase in height h above the solid surface; thus,

$$p_n = -p_0\,, \quad h \to \infty\,. \tag{4.2d}$$

Voinov also imposed the additional demand of a weak change in the dynamic contact angle, θ_D, with a height, h, above the solid surface:

$$h\left|\frac{\mathrm{d}\theta_D}{\mathrm{d}h}\right| \ll \theta_D\,. \tag{4.2e}$$

When the inertia-related contributions are neglected (and this is the case in the model proposed by Voinov) the only dimensionless number, governing the flow, is the capillary number, Ca, defined as:

$$Ca = \frac{\eta\tilde{v}}{\gamma}\,, \tag{4.3}$$

where $\tilde{v}$ is the characteristic velocity. The capillary number describes the interplay between the viscosity and surface tension-induced effects. Voinov demonstrated that the condition (4.2e) takes place when:

$$\theta_D^3 \gg 3\frac{\eta v}{\gamma} = 3Ca\,. \tag{4.4}$$

Voinov also phenomenologically introduced the angle of the free surface slope, θ_m (the microscopic contact angle, introduced in Section 2.8), at the height of the limiting scale, h_m:

$$\theta_D = \theta_m, \quad h = h_m \,. \tag{4.5}$$

Voinov noted that θ_m is unknown beforehand and should be determined during the solution of the problem [23]. The accurate mathematical solution of the hydrodynamic problem defined by equation (4.2) yielded for the dynamic contact angle:

$$\theta_D(h) = \left[\theta_m^3 + 9\frac{\eta v}{\gamma}\ln\frac{h}{h_m}\right]^{1/3} = \left[\theta_m^3 + 9Ca\ln\frac{h}{h_m}\right]^{1/3} . \tag{4.6}$$

Formula (4.6) is referred to as the Cox–Voinov law, and it is valid for $\theta_D < 3\pi/4$ [23]. Hoffmann has shown that the experimental dependence $\theta_D(Ca)$ is represented by a universal curve (corrected with a shifting factor) for a diversity of liquids [12]. A detailed discussion of the validity and applicability of the Cox–Voinov law is supplied in Bonn et al. [4]. It is seen from expression (4.6) that the slope varies logarithmically with the distance from the triple line. Thus, it is impossible to assign a unique dynamic contact angle to a triple line moving at a given speed [4]. Hence, Figure 4.1 depicts an obvious oversimplification of the actual dynamic wetting situation. It is also noteworthy that θ_D depends slightly on the cutoff length, h_m; however, it depends strongly on the microscopic angle, θ_m. For a detailed discussion of actual values of θ_m and h_m see Bonn et al. [4].

4.3 The dynamic contact angle in a situation of complete wetting

There are numerous experimental data supporting the Cox–Voinov law given by formula (4.6) for $\theta_m = 0$ [4, 12]. It means that we find ourselves in the realm of complete wetting, when the spreading parameter, Ψ, introduced in Section 2.1, is positive. In this situation, the formation of the dynamic contact angle is very different from the picture displayed in Figure 4.1. The fluid wedge is surrounded with a precursor film of a width $\hat{b}$, as shown in Figure 4.3. We are already acquainted with a similar static situation described in Section 2.6, where the drop deposited on a solid substrate is surrounded by a layer of absorbed molecules of liquids. The thickness of the precursor film equals several atomic diameters; the behavior of such thin layers is governed by the disjoining pressure, defined in Sections 2.5 and 2.6. The characteristic length $\tilde{a}$ describing the thin liquid layer is built from the Hamaker constant A (see Section 2.5) and the surface tension γ [4]:

$$\tilde{a} = \sqrt{\frac{A}{6\pi\gamma}} \,. \tag{4.7}$$

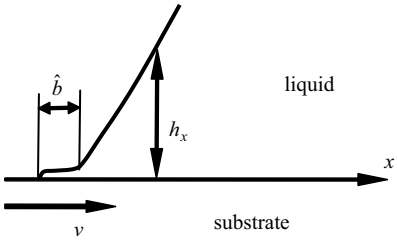

Fig. 4.3: Spreading of liquid in the situation of complete wetting. Substrate moves with a velocity v. The precursor film with a width of $\hat{b}$ is shown.

Substitution of the numerical values of parameters into expression (4.7) yields $\tilde{a} \cong 1$ Å. In equilibrium, and subject to the constraint of a fixed volume, the surface forces produce a thin film of thickness [6]

$$l = \tilde{a}\sqrt{\frac{3\gamma}{2\Psi}} \,. \tag{4.8}$$

Recall that the spreading parameter for ideally smooth surfaces equals $\Psi = \gamma_{SA} - (\gamma_{SL} + \gamma)$. The total width of the precursor film $\hat{b}$ (Figure 4.3) decreases with speed (see Bonn et al. [4]):

$$\hat{b} = \tilde{a}\sqrt{\frac{\Psi}{\gamma}} Ca^{-1} \,. \tag{4.9}$$

Hence, even for $Ca = 10^{-5}$, we obtain the estimation $\hat{b} \cong 100\,\mu\text{m}$, which is quite a macroscopic value [4]. The existence of a precursor film was observed by various groups [1, 15]. As mentioned in Bonn et al. [4] the existence of the precursor film governs the dynamics of wetting to a large extent. It should be stressed that Ψ in expression (4.9) is the *nonequilibrium spreading parameter*, which could not be expressed through the Young contact angle according to expression (2.13).

4.4 Dissipation of energy in the vicinity of the triple line

Assuming that a nonslip condition (4.2a) at the solid surface gives rise to the Huh–Scriven paradox, the dissipation of energy is logarithmically diverging. Consider a simple geometry where the liquid is at rest and the solid substrate moves with velocity v (Figure 4.4). Owing to the nonslip condition at the substrate (liquid sticks to the substrate) the fluid at the bottom moves with the constant velocity v. The dissipation of energy (per unit time and per unit length of the triple line) $\dot{W}_{\text{diss}}$ is given by [18]:

$$\dot{W}_{\text{diss}} = \eta \int_0^{\text{L}} \left(\frac{\mathrm{d}v_x}{\mathrm{d}y}\right)^2 h(x)\,\mathrm{d}x \,. \tag{4.10}$$

Considering $\mathrm{d}h/\mathrm{d}x = \theta_{\text{D}}$ and $\mathrm{d}v_x/\mathrm{d}y = v/h(x)$ yields:

$$\dot{W}_{\text{diss}} = \eta \int_0^{\text{L}} \left(\frac{v}{h}\right)^2 h \frac{\mathrm{d}h}{\theta_{\text{D}}} = \frac{\eta v^2}{\theta_{\text{D}}} \int_0^{\text{L}} \frac{\mathrm{d}h}{h} \,, \tag{4.11}$$

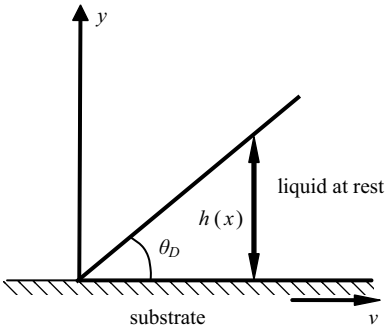

Fig. 4.4: Illustration of the Huh–Scriven paradox.

where L is an appropriate-length scale like the radius of the droplet. Integral (4.11) logarithmically diverges; thus, the rate of energy dissipation becomes infinite. Therefore, no motion of the solid in contact with the liquid is possible. This statement is known as the Huh–Scriven paradox [4, 13]. Physically plausible solving of this paradox implies introducing the cutoff length L_{cutoff}:

$$\dot{W}_{\text{diss}} = \frac{\eta v^2}{\theta_{\text{D}}} \int\limits_{L_{\text{cutoff}}}^{\text{L}} \frac{\text{d}h}{h} = \frac{\eta v^2}{\theta_{\text{D}}} \ln \frac{L}{L_{\text{cutoff}}} \,. \tag{4.12}$$

Thus, we see that purely macroscopic hydrodynamics does not work in this case, and a cutoff length L_{cutoff} based on microscopic considerations should be introduced. The lack of experimental data related to accurate determining L_{cutoff} should be mentioned [4].

4.5 Dissipation of energy and the microscopic contact angle

The analysis of energy balance in the vicinity of a moving triple line supplies important information about the microscopic contact angle θ_{m}. We denote the energy input by a moving substrate W. It is reasonable to suggest that $W = \Lambda(v)v$ (where $\Lambda(v)$ is a phenomenological parameter, which will be discussed in detail further) [4, 23]. The energy balance yields:

$$W = T\dot{S} \,. \tag{4.13}$$

Here, S is the entropy and $T\dot{S}$ corresponds to all dissipation processes occurring in the vicinity of the triple line; the temperature, T, is supposed to be constant. The viscous dissipation in the fluid equals [18]:

$$T\dot{S} = 3v^2\eta \int\limits_{L_{\text{cutoff}}}^{x} \frac{\text{d}x}{h} \,, \tag{4.14}$$

where the integration is performed from the microscopic cutoff length L_{cutoff} to the hypothetical boundary of the liquid at x [4]. The analysis of the energy balance yields [4]:

$$\theta_{\text{m}}^2 = \theta_{\text{Y}}^2 + 2\frac{\Lambda(v)}{\gamma} . \tag{4.15}$$

Equation (4.15) allows calculation of the microscopic contact angle, θ_{m}, with a known equilibrium contact angle, θ_{Y}, and the parameter of macroscopic dissipation $\Lambda(v)$. It is seen from expression (4.15) that the microscopic contact angle θ_{m} is velocity dependent [4]. In the simplest case, when $\Lambda(v) = \Lambda = \text{const}$; $W = \Lambda v$, the microscopic contact angle, θ_{m}, in the Cox–Voinov law (4.6) should be replaced by the advancing contact angle, θ_{A}, for the advancing triple line, and correspondingly by the receding contact angle, θ_{R}, for the receding triple line (see Section 3.1) [4, 23].

4.6 A microscopic approach to the displacement of the triple line

The meaning of the phenomenological parameter, Λ, appearing in equation (4.15), remains obscure, and it is desirable to obtain its relation to the microscopic parameters of a solid–liquid system. A microscopic theory of the displacement of the triple line was developed by Blake and Haynes [3]. This theory is based on the assumption of jumps of the molecules of liquid surmounting potential barriers, U. This theory resembles the general approach to activation processes developed by Eyring and Frenkel (in particular for the explanation of the viscosity of liquids) [8, 9]. It is suggested in this theory that when the triple line moves with a velocity, v, molecules jump over a potential comb of a wavelength, $\tilde{l}$, and a potential depth, U (Figure 4.5). The microscopic contact angle resulting from this approach is given by:

$$\theta_{\text{m}}^2 = \theta_{\text{Y}}^2 + \frac{2k_{\text{B}}T}{\gamma\tilde{l}^2}\,\text{arcsh}\,\frac{v\tau_0 e^{\frac{U}{k_{\text{B}}T}}}{2\tilde{l}} , \tag{4.16}$$

where τ_0 is a microscopic time for a single "jump attempt" [4]. When θ_{m} is calculated from (4.16), Λ results from equation (4.15).

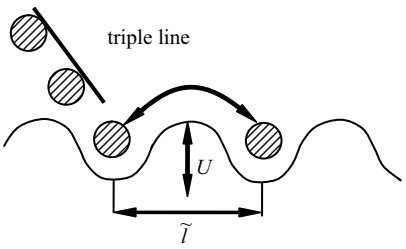

Fig. 4.5: Microscopic picture of the displacement of the triple line.

4.7 Spreading of droplets: Tanner's law

An important case of dynamic wetting is the spreading of droplets. We restrict ourselves by the following assumptions: (1) the Bond number introduced in Section 2.7, $Bo \ll 1$; thus, the effects due to gravity are negligible (in other words, the drop radius is smaller than the capillary length l_{ca}); (2) the capillary number, $Ca = \eta\tilde{v}/\gamma \ll 1$. When we speak about the spreading of droplets $\tilde{v} = \mathrm{d}a/\mathrm{d}t$, where a is the running *contact* radius of the droplet (measured from the droplet center to the triple line as shown Figure 4.6), i.e., $\tilde{v}$ is the speed of the triple line. As $Ca \ll 1$ is assumed, the liquid–air interface is not affected by viscosity (except of the region adjacent to the triple line). Once the drop has become sufficiently flat ($\mathrm{d}h/\mathrm{d}r \ll 1$; Figure 4.6), its shape is given by:

$$h(r,t) = \frac{2V}{\pi a(t)^2}\left[1 - \left(\frac{r}{a(t)}\right)^2\right]. \tag{4.17}$$

At a given volume, V, the shape of the droplet is totally determined by the dynamic contact angle, θ_D [4]. For thin droplets, $-\mathrm{d}h/\mathrm{d}r(r = a) = \tan\theta_D \cong \theta_D$. Considering (4.17) yields:

$$\theta_D = \frac{4V}{\pi a(t)^3}. \tag{4.18}$$

Thus, the dynamic contact angle, θ_D, goes to zero as the droplet spreads completely [4]. The time dependence of the contact radius of the droplet is given by:

$$a(t) = \left[\frac{10\gamma}{9B\eta}\left(\frac{4V}{\pi}\right)^3\right]^{1/10} t^n, \tag{4.19}$$

which is known as Tanner's law [21]. B is the constant discussed in Bonn et al. [4]. The power n in expression (4.19) equals 1/10 for the viscous spreading of small droplets [4, 5, 21].

Spreading of droplets governed by gravity was studied in Lopez et al. [19], and it was shown that in this case, $a(t) \cong C \cdot t^{1/8}$ (C is the constant) [19].

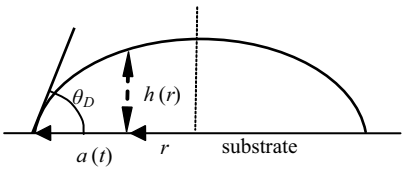

Fig. 4.6: Spreading of a droplet.

4.8 Superspreading

Superspreading is a relatively new phenomenon demonstrating a diversity of promising technological applications. It was revealed that certain trisiloxane polyoxyethy-

lene surfactants promoted rapid spreading of water on low-energy, i.e., hydrophobic surfaces, such as polyethylene or paraffin wax (see Section 1.7) [11, 27]. Wetting by surfactant solutions is much more complicated than wetting by homogeneous liquids, partly because of the time-dependent surface and interfacial tensions, and partly because the orientation of surfactant molecules adsorbed at the various interfaces in the vicinity of the triple line strongly influences the driving force for spreading given by expression (4.1) [11, 27]. Superspreading remains a hot topic in interface science, and it is not yet understood to its fullest extent.

4.9 Dynamics of the filling of capillary tubes

In Section 2.10, we obtained the Jurin law given by expression (2.46), describing the statics of capillary rise. The dynamics of water penetration into capillary tubes was studied by a number of investigators [2, 20, 24, 26]. This dynamics is driven by the interplay of capillary force, viscosity, gravity, and inertia [7]. Washburn [24] assumed that the Poiseuille flow occurs in the capillary tube, i.e.,

$$\mathrm{d}V = \frac{\sum_{\mathrm{i}} p_{\mathrm{i}}}{8\eta l}\left(r^4 + 4\tilde{\varepsilon}r^3\right)\mathrm{d}t\,, \tag{4.20}$$

where $\mathrm{d}V$ is the volume of the liquid, which in the time $\mathrm{d}t$ flows through any cross-section of the capillary, $\sum_{\mathrm{i}} p_{\mathrm{i}}$ is the total effective pressure that is acting to force the liquid along the capillary, r is the radius, and $l(t)$ is the length of the column of liquid in the capillary at the time, t, $\tilde{\varepsilon}$ is the coefficient of slip, and η is the viscosity of the liquid [24]. Washburn studied a very general case of filling a capillary tube (depicted in Figure 4.7) and obtained the following differential equation for the velocity of liquid penetration:

$$\frac{\mathrm{d}l(t)}{\mathrm{d}t} = \frac{\left[p_0 + \rho g(h - l(t)\sin\psi) + \frac{2\gamma}{r}\cos\theta\right](r^2 + 4\tilde{\varepsilon}r)}{8\eta l(t)}\,, \tag{4.21}$$

where p_0 is the atmospheric pressure and θ is the contact angle; the height h and angle ψ are shown in Figure 4.7 (see Washburn [24]). Equation (4.21) could be solved for an arbitrary ψ only numerically; however, in the case of the $\psi = 0$ corresponding

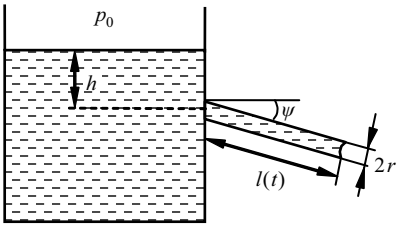

Fig. 4.7: Illustration of Washburn's law.

to filling of a horizontal capillary tube, Washburn obtained the analytical solution:

$$l^2(t) = \frac{\left[p_0 + \rho g h + \frac{2\gamma}{r}\cos\theta\right](r^2 + 4\tilde{\varepsilon}r)\,t}{4\eta}\,, \tag{4.22}$$

which is known as Washburn's law [24]. It may be noted that with capillaries open at both ends, $p_0 = 0$. When the weight of the liquid is neglected and $\tilde{\varepsilon} = 0$, we obtain a very simple law for horizontal capillaries open at both ends:

$$l^2(t) = \frac{1}{2}\frac{\gamma r\cos\theta}{\eta}t\,. \tag{4.23}$$

A more complicated solution for vertical capillaries ($\psi = \pi/2$) is supplied in Washburn [24]. Marmur extended the Washburn solution to the case when a capillary tube is connected to a liquid reservoir of a finite size [20]. Zhmud et al. discussed the filling of a capillary tube by surfactant (see Section 1.4) solutions [26].

Inertia is neglected in the Washburn model. The inertia-driven filling of capillary tubes, when a tube is connected to a vessel containing a liquid at rest, which resists sudden movements, is treated in de Gennes et al. [7]. In this case, the law governing the filling of a tube is given by:

$$l(t) = \left(\frac{2\gamma\cos\theta}{\rho r}\right)^{1/2} t\,, \tag{4.24}$$

which implies a constant velocity of filling.

4.10 The drag-out problem

Consider an infinite flat plate, which is pulled vertically, with a constant speed, v_p, from a bath of liquid with a viscosity, η, which has a horizontal free surface, and a steady state is established. What is the thickness of the film of liquid adhering to the plate at a large height above the free surface? This is the drag-out problem, which is of primary importance for industrial coating and painting problems. De Gennes et al. demonstrated that two very different situations are possible, depending on the pulling speed, v_p, as shown in Figure 4.8. These are the "meniscus regime" depicted in Figure 4.8a and the "film regime" shown in Figure 4.8b. The critical pulling speed, v_p^*, at

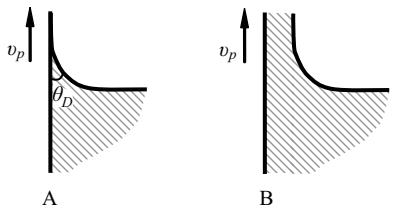

Fig. 4.8: Two regimes occurring when a vertical plate is extracted from a pool of liquid. a: $v_\mathrm{p} < v_\mathrm{p}^*$; b: $v_\mathrm{p} > v_\mathrm{p}^*$. A meniscus is impossible.

which a switch from the meniscus to film regime occurs, is given by:

$$v_{\mathrm{p}}^{*} = \frac{\gamma}{\eta 9\sqrt{3}\ln\frac{L}{L_{\mathrm{cutoff}}}}\theta_{\mathrm{Y}}^{3}\,, \tag{4.25}$$

where L_{cutoff} and L are the cutoff and scale lengths, introduced in Section 4.3. For $v_{\mathrm{p}} > v_{\mathrm{p}}^{*}$, a meniscus becomes impossible. In water for $\theta_{\mathrm{Y}} = 0.1$ and $\ln L/L_{\mathrm{cutoff}} \cong 20$, $v_{\mathrm{p}}^{*} \cong 0.2$ mm/s.

The thickness of liquid film, $\tilde{h}$, adhering to the plate, was first established in the classic work by Landau and Levich [17]. The thickness, $\tilde{h}$, results from the interplay of surface tension, gravity, and viscosity. Thus, it is reasonable to introduce the characteristic thickness scale, $\tilde{d}$, according to:

$$\tilde{d} = \left(\frac{\eta v_{\mathrm{p}}}{\rho g}\right)^{1/2}\,. \tag{4.26}$$

Landau and Levich demonstrated that for small capillary numbers, $Ca = \eta v_{\mathrm{p}}/\gamma \ll 1$, the resulting thickness of the film is given by:

$$\tilde{h} = \lambda\tilde{d}(Ca)^{1/6}\,, \tag{4.27}$$

where λ is a dimensionless constant to be extracted from the numerical solution of a canonical ordinary differential equation describing the shape of the free surface in the overlap region (Figure 4.9) [17]. The accurate solution of the drag-out problem was obtained by Wilson, for an arbitrary angle of immersion, α (Figure 4.9). Wilson carried out a matching of solutions in "fully developed", "overlap", and meniscus areas, and reported the final solution as a series:

$$\tilde{h} = \left(\frac{\eta v_{\mathrm{p}}}{\rho g}\right)^{1/2}\frac{2}{\sqrt{1-\sin\alpha}}\left[0.94581(Ca)^{1/6} - \frac{0.10685}{1-\sin\alpha}(Ca)^{1/2} + \cdots\right]\,, \tag{4.28}$$

where $\tilde{h}$ is the film thickness at infinity up the slope, that is, as $x \to \infty$ (Figure 4.9) [25]. The effects of surfactants on the drag-out problem were discussed by Krechetnikov and Homsy [16].

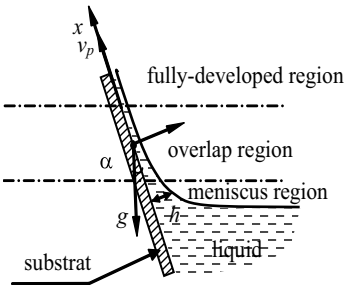

Fig. 4.9: General drag-out problem solved by Wilson [25]. $h(x)$ is the thickness of the adhered film, $\tilde{h}$ is the thickness of the adhered film in the fully developed region.

4.11 Dynamic wetting of heterogeneous surfaces

As we have already seen in Section 3.8, even the static wetting of heterogeneous surfaces is not trivial, owing to the pronounced contact angle hysteresis. Obviously, study of the dynamic wetting of chemically heterogeneous substrates is a challenging task. Johnson et al. studied dynamic wetting of various specially prepared chemically heterogeneous surfaces with the Wilhelmy balance, described in Section 2.14.1 [14]. They measured the force exerted on the heterogeneous plate and plotted it as a function of the immersion depth, as shown in Figure 4.10 (see Johnson et al. [14]). The typical hysteresis loop is recognized; thus, the notion of the "contact angle hysteresis" obtains its natural meaning. The arms of the graph correspond to advancing and receding contact angles, as shown in Figure 4.10. Johnson et al. experimentally established several rules typical of dynamic contact angle hysteresis. They found that receding dynamic angles are less sensitive to velocity than advancing ones [14]. Johnson et al. attributed this effect to a difference in the way in which the liquid interface recedes compared with the way in which it advances. When the liquid is advancing, the triple line moves in jumps. When the triple line recedes, the recession starts at one edge and moves across the plate like a zipper. Accordingly, the wetting force is more ragged for advancing than for receding.

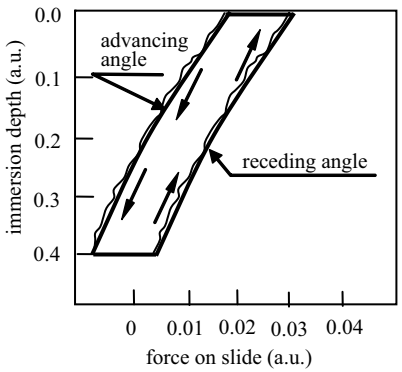

Fig. 4.10: Contact angle hysteresis loop obtained with the Wilhelmy balance by Johnson et al. [14]. Reprinted from Johnson et al. [14], with permission from Elsevier.

Johnson et al. stated that all types of hysteresis observable in nature require a large number of metastable states that are accessible to a system (see Section 3.4). These metastable states, separated by energetic barriers, are created in the discussed situation by surface heterogeneity. The smoother movement of the triple line during recession causes there to be fewer (or lower) energy barriers for receding than for advancing, and this presumably accounts for the lower dependence of receding contact angles on the triple-line velocities [14].

Additional Reading

The state-of-art of the problem of the dynamics of wetting is well-summarized in Eral et al. [28]. The numerical analysis of the "drag-out problem" is reported in Jin and Acrivos [29].

Bullets

- When the triple line moves, wetting is characterized by the dynamic contact angle, which is different from the Young angle.
- An interplay between viscosity and surface tension-related effects is described by the capillary number, $Ca = \eta\tilde{v}/\gamma$.
- The dynamic contact angle is given by the Cox–Voinov law:

$$\theta_{\mathrm{D}}(h) = \left[\theta_{\mathrm{m}}^3 + 9Ca \ln \frac{h}{h_{\mathrm{m}}}\right]^{1/3} .$$

  θ_{m} is the microscopic contact angle, which is velocity dependent and can be calculated from microscopic theory, describing the displacement of the triple line as a sequence of jumps of liquid molecules.
- In the numerous cases of dynamic wetting, the fluid wedge is surrounded by a precursor film.
- Assuming that a nonslip condition at the solid surface gives rise to the Huh–Scriven paradox, the dissipation of energy is logarithmically diverging, and "not even Hercules could sink a solid." The puzzle is resolved by introducing a cutoff length.
- When gravity is neglected and $Ca \ll 1$, spreading of droplets is governed by Tanner's law: $a(t) \cong \text{const} \cdot t^{1/10}$.
- Spreading of droplets governed by gravity occurs according to $a(t) \cong \text{const} \cdot t^{1/8}$.
- Use of trisiloxane polyoxyethylene surfactants leads to the superspreading phenomenon, i.e., spreading of a liquid on a hydrophobic surface.
- Filling of horizontal capillaries is ruled by Washborn's law: $l^2(t) = 1/2\gamma r \cos\theta/\eta t$.
- The formation of a meniscus in the drag-out problem is possible when the pulling speed is lower than the critical value given by expression (4.25).
- The thickness of a liquid film adhering to a solid plate in the drag-out problem is given by expression (4.28).

References

[1] D. Ausserre, A. M. Picard, and L. Leger, Existence and role of precursor film in spreading of polymer liquids, *Phys. Rev. Lett.* **57** (1986), 2671–2674.

[2] J. M. Bell and F. K. Cameron, The flow of liquids through capillary spaces *J. Phys. Chem.* **10** (1906), 658–674.

[3] T. D. Blake and J. M Haynes Kinetics of liquid/liquid displacement, *J. Colloid & Interface Sci.* **30** (1969), 421–423.
[4] D. Bonn, J. Eggers, J. Indekeu, J. Meunier, and E. Rolley, Wetting and Spreading, *Reviews of Modern Physics*, **81** (2009), 739–805.
[5] M. Brenner and M. Bertozzi, Spreading of droplets on a solid surface, *Phys. Rev. Lett.* **71** (1993), 593–596.
[6] P.-G. de Gennes, Wetting: statics and dynamics, *Reviews of Modern Physics* **57**, (1985), 827.
[7] P.-G. de Gennes, F. Brochard-Wyart, and D. Quéré, *Capillarity and Wetting Phenomena*, Springer, Berlin, 2003.
[8] H. J. Eyring, *The Theory of Rate Processes*, McGraw-Hill, New York, 1955.
[9] Y. I. Frenkel, *Kinetic Theory of Liquids*, Dover, New York, 1955.
[10] S. Garoff and G. D. Nadkarni, Reproducibility of contact line motion on surfaces exhibiting contact angle hysteresis, *Langmuir* **10** (1994), 1618–1623.
[11] R. Hill. Superspreading, *Current Opinion in Colloid & Interface Sci.* **3** (1998), 247–254.
[12] R. L. Hoffman, A study of the advancing interface, *J. Colloid & Interface Sci.* **50** (1975), 228–241.
[13] C. Huh and L. E. Scriven, Hydrodynamic model of steady movement of a solid/liquid/fluid contact line, *J. Colloid & Interface Sci.* **35** (1971), 85–101.
[14] R. E. Johnson, R. Dettre, and D. A. Brandreth, Dynamic contact angles and contact angle hysteresis, *J. Colloid & Interface Sci.* **62** (1977), 205–212.
[15] H. P. Kavehpour, B. Ovryn, and G. H. McKinley, Microscopic and macroscopic structure of the precursor layer in spreading viscous drops, *Phys. Rev. Lett.* **91** (2003), 196104.
[16] R. Krechetnikov and G. M. Homsy, Surfactant effects in the Landau–Levich problem *J. Fluid Mech.* **559** (2006), 429–450.
[17] L. Landau and B. Levich, Dragging of a liquid by a moving plate, *Acta Physicochim. (USSR)* **17** (1942), 42–54.
[18] L. Landau and E. Lifshitz, *Fluid Mechanics*, 2nd edn.; Butterworth-Heinemann, Oxford, UK, 1987.
[19] J. Lopez, C. A. Miller, and E. Ruckenstein, Spreading kinetics of liquid drops on solids, *J. Colloid & Interface Sci.* **56** (1971), 460–468.
[20] A. Marmur, Penetration of a small drop into a capillary, *J. Colloid & Interface Sci.* **122** (1988), 209–219.
[21] L. H. Tanner, The spreading of silicon oil drops on horizontal surfaces, *J. Phys. D*, **12** (1979), 1473–1484.
[22] O. N. Tretinnikov and Y. Ikada, Dynamic wetting and contact angle hysteresis of polymer surfaces studied with the modified Wilhelmy balance method, *Langmuir* **10** (1994), 1606–1614.
[23] O. V. Voinov, Hydrodynamics of wetting, *Fluid Dynamics* **11** (1976), 714–721.
[24] E. W. Washburn, The dynamics of capillary flow, *Physical Rev.* **17** (1921), 273–283.
[25] S. D. R. Wilson, The drag-out problem in film coating theory, *J. Engg. Math.* **16** (1982), 209–221.
[26] B. V. Zhmud, F. Tiberg, and K. Hallstensson, Dynamics of capillary rise, *J. Colloid & Interface Sci.* **228** (2000), 263–269.
[27] S. Zhu, W. G. Miller, L. E. Scriven, and H. T. Davis, Superspreading of water-silicone surfactant on hydrophobic surfaces, *Colloids & Surfaces A* **90** (1994), 63–78.

Additional Reading

[28] H. B. Eral, D. J. C. M. 't Mannetje, and J. M. Oh, Contact angle hysteresis: a review of fundamentals and applications, *Colloid & Polymer Sci.* **291**(2) (2013), 247–260.
[29] B. Jin and A. Acrivos, The drag-out problem in film coating, *Physics of Fluids* **17**, (2005), 103603.

5 Wetting of rough and chemically heterogeneous surfaces: the Wenzel and Cassie Models

5.1 General remarks

In this chapter, we develop basic models describing the wetting of rough and chemically heterogeneous surfaces, i.e., the Wenzel and Cassie models. Recall that wetting of rough or chemically heterogeneous surfaces is characterized by the *apparent contact angle*, introduced in Section 3.8. The Cassie and Wenzel models predict the apparent contact angle, which is an essentially macroscopic parameter. This fact limits the field of validity of these models: they work when the characteristic size of a droplet is much larger than that of the surface heterogeneity or roughness. The use of the Wenzel and Cassie equations needs a certain measure of care; numerous misinterpretations of these models are found in the literature. We discuss the applicability of these basic models in detail. In our treatment, we intensively exploit the technique of transversality conditions of the variational problem of wetting, developed in Chapter 2.

5.2 The Wenzel model

The Wenzel model, introduced in 1936, deals with the wetting of rough, chemically homogeneous surfaces and implies total penetration of a liquid into the surface grooves, as shown in Figure 5.1. When the spreading parameter $\Psi < 0$ (see Section 2.1), a droplet forms a cap resting on the substrate with an apparent contact angle, θ^*. If the axisymmetric droplet is exposed to an external field, $U(x, h)$, the free energy of G could be written as:

$$G(h, h') = \int_o^a \left[2\pi\gamma x\sqrt{1 + h'^2} + 2\pi x(\gamma_{SL} - \gamma_{SA})\widetilde{r} + U(x, h) \right] \mathrm{d}x \,, \tag{5.1}$$

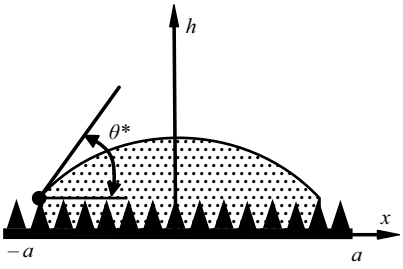

Fig. 5.1: Wenzel wetting of a chemically homogeneous rough surface: the liquid completely wets the grooves.

https://doi.org/10.1515/9783110583144-005

where $h(x, y)$ is the local height of the liquid surface above the point (x, y) of the substrate, $U(x, h(x))$ is the linear density of interaction of the droplet with the external field with the dimension of J/m, a is the contact radius, and the integral is extended over the substrate area (see Section 2.2). Equation (5.1) is very similar to equation (2.4), the only difference being parameter $\tilde{r}$, which is the roughness ratio of the wet area, or in other words, the ratio of the real surface in contact with liquid to its projection onto the horizontal plane. Parameter $\tilde{r}$ describes the increase in the wetted surface due to roughness and obviously $\tilde{r} > 1$ takes place.

We also suppose that the volume of a droplet is constant:

$$V = \int_o^a 2\pi x h \, \mathrm{d}x = \text{const} \, . \tag{5.2}$$

Equations (5.1) and (5.2) reduce the problem to the minimization of the functional:

$$G(h, h') = \int_0^a \widetilde{G}(h, h', x) \, \mathrm{d}x \, , \tag{5.3}$$

where

$$\widetilde{G}(h, h', x) = 2\pi\gamma x\sqrt{1 + h'^2} + 2\pi x(\gamma_{SL} - \gamma_{SA})\tilde{r} + U(x, h) + 2\pi\lambda x h \, , \tag{5.4}$$

where λ is the Lagrange multiplier to be deduced from equation (5.2).

We suppose that the boundary (the triple line) of the droplet is free to slip along the x-axis and we solve the variational problem with free endpoints [4]. This assumption allows use of the conditions of transversality of the variational problem, as described in detail in Chapter 2 (see Section 2.2 and Appendix 2A). Already familiar to us is the transversality condition at the endpoint a, which yields:

$$(\widetilde{G} - h' G'_{h'})_{x=a} = 0 \, , \tag{5.5}$$

where $\widetilde{G}'_{h'}$ denotes the h' derivative of $\widetilde{G}$. Substitution of formula (5.4) into the transversality condition (5.5), and taking into account $h(a) = 0$, $U(x = a, h = 0) = 0$ supplies:

$$\left(\gamma\sqrt{1 + h'^2} + \tilde{r}(\gamma_{SL} - \gamma_{SA}) - \frac{\gamma h'^2}{\sqrt{1 + h'^2}}\right)_{x=a} = 0 \, . \tag{5.6}$$

Simple transformations yield:

$$\left(\frac{1}{\sqrt{1 + h'^2}}\right)_{x=a} = \tilde{r}\frac{\gamma_{SA} - \gamma_{SL}}{\gamma} \, . \tag{5.7}$$

Taking into account $h'(x = a) = -\tan\theta^*$, and $\gamma_{SA} - \gamma_{SL}/\gamma = \cos\theta_Y$, where θ^* and θ_Y are the apparent and the Young contact angles, correspondingly yields:

$$\cos\theta^* = \tilde{r}\cos\theta_Y \, . \tag{5.8}$$

Formula (5.8) presents the famous *Wenzel equation* [31]. Three important conclusions follow from equation (5.8):

- Inherently smooth hydrophilic surfaces ($\theta_Y < \pi/2$) are more hydrophilic when riffled: $\theta^* < \theta_Y$ due to the fact that $\tilde{r} > 1$.
- For the same reason, inherently hydrophobic flat surfaces ($\theta_Y > \pi/2$) are more hydrophobic when grooved: $\theta^* > \theta_Y$.
- The Wenzel angle given by equation (5.8) is *independent of the droplet shape and external field U* under very general assumptions about U, i.e., $U = U(x, h(x))$.

The simpler thermodynamic groundings of the Wenzel equation have been proposed (see Bico et al. and Good [2, 19]), but the insensitivity of the Wenzel angle to external fields is demonstrated in an elegant way only with the use of the variational principles [4]. The Wenzel equation can be easily understood from the following intuitive considerations: the cosine of the apparent contact angle in the situation of the Wenzel-like wetting could be written as:

$$\cos\theta^* = \frac{\hat{G}^*_{SA} - \hat{G}^*_{SL}}{\gamma},$$

where $\hat{G}^*_{SA}$ and $\hat{G}^*_{SL}$ are the specific surface energies at the solid–air and solid–liquid rough interfaces (see Section 2.1).

The specific surface energies are $\hat{G}^*_{SA} = \tilde{r}\hat{G}_{SA} = \tilde{r}\gamma_{SA}$, $\hat{G}^*_{SL} = \tilde{r}\hat{G}_{SA} = \tilde{r}\gamma_{SL}$, when the difference between specific surface energies and surface tensions is neglected (see Section 1.6). Thus,

$$\cos\theta^* = \frac{\tilde{r}\gamma_{SA} - \tilde{r}\gamma_{SL}}{\gamma} = \tilde{r}\frac{\gamma_{SA} - \gamma_{SL}}{\gamma} = \tilde{r}\cos\theta\,.$$

It is also seen that in the limiting case of $\cos\theta^* = -1$, we have $\hat{G}^*_{SA} - \hat{G}^*_{SL} = -\gamma$; hence, the spreading parameter $\Psi = \hat{G}^*_{SA} - (\hat{G}^*_{SL} + \hat{G}^*_{LA}) = \hat{G}^*_{SA} - (\hat{G}^*_{SL} + \gamma) = -2\gamma$, and the situation of complete dewetting, depicted in Figure 2.1c, takes place (see Section 2.1).

5.3 Wenzel wetting of chemically homogeneous curved rough surfaces

Consider a 2D wetting problem where a cylindrical drop extended uniformly in the y direction is deposited on a chemically homogeneous curved rough surface [6] (Figure 5.2 depicts the cross-section of such a drop). We consider the liquid drop to be symmetrical about z-axis deposited on the curved solid substrate described by the given function $f(x)$ and exposed to some external field that is also symmetrical about the z-axis. The interaction of the droplet with the field gives rise to the linear energy density $U(x, h(x))$, as it was shown in the previous section. The free energy of the droplet is supplied by:

$$G(h, h') = \int_{-a}^{a} \left[\gamma\sqrt{1 + h'_x} + \tilde{r}(\gamma_{SL} - \gamma_{SA})\sqrt{1 + f'_x} + U(x, h(x))\right] \mathrm{d}x\,, \tag{5.9}$$

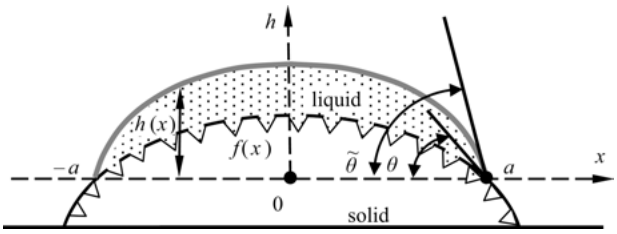

Fig. 5.2: Wenzel wetting of a chemically homogeneous curved rough surface.

where $h(x)$ is the local height of the liquid surface above the point x of the substrate (the profile of the droplet $h(x)$ is assumed to be a single-valued and even function). The condition (2.15) of the constant area S also has to be taken into account:

$$S = \int_{-a}^{a} [h(x) - f(x)]\,\mathrm{d}x = \text{const}\,. \tag{5.10}$$

Note that this is equivalent to the constant volume requirement in the case of cylindrical "drops" (extended in the y direction; h is independent of y).

Equations (5.9) and (5.10) reduce the problem to minimization of the functional:

$$G(h, h') = \int_{-a}^{a} \widetilde{G}(h, h', x)\,\mathrm{d}x\,, \tag{5.11}$$

$$\widetilde{G}(h, h', x) = \gamma\sqrt{1 + h'^2} + \tilde{r}(\gamma_{\mathrm{SL}} - \gamma_{\mathrm{SA}})\sqrt{1 + f'^2} + U(x, h) + \lambda(h - f)\,, \tag{5.12}$$

where λ is the Lagrange multiplier to be deduced from equation (5.10). Now, we perform transformations identical to those described in Section 2.3, i.e., we suggest that the endpoints of the drop $x = \pm a$ are not fixed and are free to move along the line $f(x)$. Without the loss of generality, we suggest that the curve $f(x)$ and the entire problem are symmetrical around the vertical axis. Thus, the transversality condition in this case obtains the form [18]:

$$\left[\widetilde{G} + G'_{h'}(f' - h')\right]_{x=a} = 0\,, \tag{5.13}$$

where $\widetilde{G}'_{h'}$ denotes the h' derivative of $\widetilde{G}$. Substitution of formula (5.12) into transversality condition (5.13), and considering $h(a) = f(a)$, $U(a, h(a)) = 0$ gives rise to:

$$\left[\gamma\sqrt{1 + h'^2} + \tilde{r}(\gamma_{\mathrm{SL}} - \gamma_{\mathrm{SA}})\sqrt{1 + f'^2} + \frac{\gamma h'(f' - h')}{\sqrt{1 + h'^2}}\right]_{x=a} = 0\,. \tag{5.14}$$

Simple transformations akin to those presented in the Sections 2.3 and 5.2 yield:

$$\cos(\tilde{\theta} - \theta) = \tilde{r}\frac{\gamma_{\mathrm{SA}} - \gamma_{\mathrm{SL}}}{\gamma}\,, \tag{5.15}$$

where $h'(x = a) = -\tan\widetilde{\theta}$, where $\widetilde{\theta}$ is the slope of the liquid–air interface at $x = a$; and $f'(x = a) = -\tan\theta$, where $\tan\theta$ is the slope of the solid substrate in $x = a$ (the grooves are small). It is reasonable to redefine the apparent contact angle as $\theta^* = \widetilde{\theta} - \theta$; thus, equation (5.15) may be rewritten as:

$$\cos\theta^* = \overline{r}\cos\theta_{\mathrm{Y}}\,, \tag{5.16}$$

where θ_{Y} is the Young contact angle established on the flat surface and given by the well-known Young equation, $\cos\theta_{\mathrm{Y}} = \gamma_{\mathrm{SA}} - \gamma_{\mathrm{SL}}/\gamma$. Formulae (5.15) and (5.16) supply the Wenzel equation generalized for curved surfaces.

Three-dimensional rough homogeneous axially symmetrical surfaces are treated in a similar way. The free energy functional G supplying the free energy of the droplet assumes the form $G(h, h') = \int_0^a \widetilde{G}(h, h', x)\,\mathrm{d}x$, where:

$$\widetilde{G}(h, h', x) = 2\pi\gamma x\sqrt{1 + h'^2} + 2\pi x\sqrt{1 + f'^2}\overline{r}(\gamma_{\mathrm{SL}} - \gamma_{\mathrm{SA}}) + U(x, h) + 2\pi\lambda x(h - f) \tag{5.17}$$

(λ is the Lagrange multiplier). We leave to the reader to carry out the useful exercise of the substitution of formula (5.17) into the transversality condition (5.13) and derivation of the modified Wenzel equations (5.15) and (5.16).

5.4 The Cassie–Baxter wetting model

The Cassie–Baxter wetting model introduced in Cassie and Cassie and Baxter [11, 12] deals with the wetting of *flat chemically heterogeneous* surfaces. Suppose that the surface under the drop is flat, but consists of n sorts of materials randomly distributed over the substrate, as shown in Figure 5.3. This corresponds to the assumptions of the Cassie–Baxter wetting model [11, 12]. Each material is characterized by its own surface tension coefficients, $\gamma_{i,\mathrm{SL}}$ and $\gamma_{i,\mathrm{SA}}$, and by the fraction in the substrate surface. The free energy of an axisymmetric drop of a radius a exposed to an external field $U(x, h)$ is given by the following expression (analogous to expression (5.1)):

$$G(h, h') = \int_o^a \left[2\pi\gamma x\sqrt{1 + h'^2} + 2\pi x\sum_{i=1}^{n} f_{\mathrm{i}}(\gamma_{i,\mathrm{SL}} - \gamma_{i,\mathrm{SA}}) + U(x, h)\right]\mathrm{d}x\,. \tag{5.18}$$

Condition (5.2) of the constant volume introduces the Lagrange multiplier λ. Analogous to the above treatment we obtain for $\widetilde{G}$,

$$\widetilde{G}(h, h', x) = 2\pi\gamma x\sqrt{1 + h'^2} + 2\pi x\sum_{i=1}^{n} f_{\mathrm{i}}(\gamma_{i,\mathrm{SL}} - \gamma_{i,\mathrm{SA}}) + U(x, h) + 2\pi\lambda xh\,. \tag{5.19}$$

Substitution of expression (5.19) into the transversality condition (5.5) and transformations akin to (5.6) and (5.7) yield the famous Cassie–Baxter equation:

$$\cos\theta^* = \frac{\sum_{i=1}^{n} f_{\mathrm{i}}(\gamma_{i,\mathrm{SA}} - \gamma_{i,\mathrm{SL}})}{\gamma}\,, \tag{5.20}$$

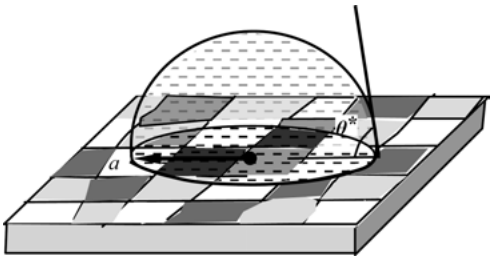

Fig. 5.3: Cassie–Baxter wetting of flat, chemically heterogeneous surfaces (various gray-scale colors correspond to different chemical species).

predicting the so-called Cassie apparent contact angle θ^* on flat chemically heterogeneous surfaces. It is demonstrated that the Cassie apparent contact angles are also insensitive to external fields [4]. When the substrate consists of two kinds of species, the Cassie–Baxter equation obtains the form:

$$\cos\theta^* = f_1 \cos\theta_1 + f_2 \cos\theta_2 \,, \tag{5.21}$$

which is widespread in the scientific literature dealing with the wetting of heterogeneous surfaces [14, 15]. It is noteworthy that Cassie and Baxter based the equation (5.21) on semiqualitative considerations. More rigorous derivation of the Cassie–Baxter equation exploiting the principle of virtual works can be found in Bico et al. and de Gennes et al. [2, 14]. Our general approach demonstrates explicitly that the Cassie–Baxter apparent contact angle is insensitive to external fields of a very general form, i.e., $U = U(x, h(x))$.

5.5 The Israelachvili and Gee criticism of the Cassie–Baxter model

Israelachvili and Gee demonstrated a simple and elegant derivation of the Cassie–Baxter equation based on the Young–Dupré equation (Section 2.12) supplying the energy of the adhesion of a droplet to the solid heterogeneous substrate: $W_{\mathrm{ad}} = \gamma(1 + \cos\theta^*)$, where θ^* is the apparent contact angle. Consider a substrate built from two different homogeneous species, characterized by the Young contact angles, θ_1 and θ_2. For these homogeneous surfaces, the energies of adhesion could be written as:

$$W_{\mathrm{ad1}} = \gamma(1 + \cos\theta_1); \quad W_{\mathrm{ad2}} = \gamma(1 + \cos\theta_2) \,. \tag{5.22}$$

For the heterogeneous surface we have:

$$W_{\mathrm{ad}} = \gamma(1 + \cos\theta^*) = f_1 W_{\mathrm{ad1}} + f_2 W_{\mathrm{ad2}} \,, \tag{5.23}$$

where f_1 and f_2 are the fractional areas of the patches. Substitution of expression (5.22) into (5.23) immediately gives rise to the Cassie–Baxter equation (5.21) [20]. Israelachvili and Gee noted that the derivation latently implied that the surface is composed of well-separated domains of either type 1 or type 2; thus, the mean adhesion

energy is averaged according to equation (5.23). However, if the chemical heterogeneity is of atomic or molecular dimensions, then from theories of intermolecular forces, it is clear that it is not the cohesion energy that should be averaged, but rather the polarizabilities or dipole moments (see Section 1.2, formulae (1.2)–(1.4)) [20]. The appropriate averaging yielded the following equation:

$$(1 + \cos\theta^*)^2 = f_1(1 + \cos\theta_1)^2 + f_2(1 + \cos\theta_2)^2 \,. \tag{5.24}$$

Israelachvili and Gee noted that the derivation of equation (5.24) was based on rather crude assumptions, and for more rigorous conclusions, specific intermolecular forces appropriate to the system should be considered [20]. In spite of this criticism, equation (5.21) – based on even more crude assumptions – is broadly used by investigators for predicting apparent contact angles on chemically heterogeneous surfaces. It should be mentioned that it is difficult to experimentally establish the advantage of equation (5.24) over (5.21) for predicting apparent contact angles owing to the very high contact angle hysteresis inherent to chemically heterogeneous surfaces. Actually, we always obtain a broad spectrum of measured contact angles (see Section 3.8); thus, the precise value of θ^* remains unknown. However, the crude, traditional Cassie–Baxter equation (5.21) describes the wetting of flat heterogeneous surfaces in a qualitatively true way.

5.6 Cassie–Baxter wetting in a situation where a droplet partially sits on air

The peculiar form of the Cassie–Baxter equation given by equation (5.21) was successfully used to explain the phenomenon of superhydrophobicity, which is discussed in detail in the next chapter. Jumping ahead, we admit that in the superhydrophobic situation, a droplet is partially supported by solid substrate and partially by air cushions, as shown in Figure 5.4. Consider a situation where the mixed surface comprises solid surface and air pockets, with the contact angles θ_Y (which is the Young angle of the solid substrate) and π respectively. We denote by f_s and $1 - f_S$ relative fractions of solid and air respectively. Thus, we deduce from (5.21):

$$\cos\theta^* = -1 + f_S(\cos\theta_Y + 1) \,. \tag{5.25}$$

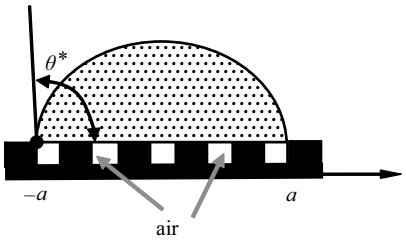

Fig. 5.4: The particular case of Cassie wetting: a droplet is partially supported by solid and partially by air cushions.

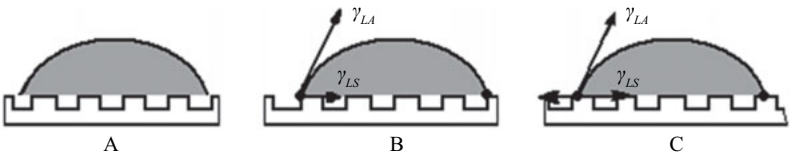

Fig. 5.5: Cassie wetting in the situation when a droplet is partially supported by air pockets: equilibrium in situations A and B is impossible.

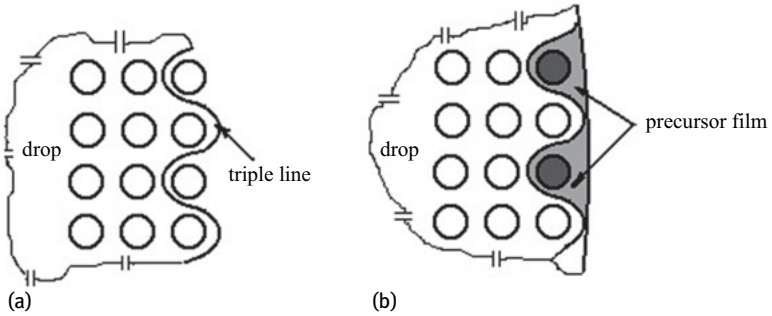

Fig. 5.6: a: a triple line winds around the surface heterogeneities; this scenario is impossible owing to the excess energy arising from a triple line bending; b: a precursor film smooths the effect of the meandering triple line.

Formula (5.25) predicts the apparent contact angle in the situation where a droplet sits partially on solid and partially on air, and it was shown experimentally that it works for a diversity of porous substrates [8]. It is noteworthy that switching from equation (5.21) to equation (5.25) is not straightforward, because the triple (three phase) line could not be at rest on pores [3]. When a droplet is supported by air pockets, the equilibrium of the triple line becomes possible only for where it is sitting on solid islands, as shown in Figure 5.5. Equilibrium in states A and B is impossible. The drop can sit on the air pocket, but the triple line cannot [3]. Thus, a straightforward application of the variational principles or the principle of virtual works is at least problematic for a derivation of equation (5.25). It could be supposed that the triple line meanders, as shown in Figure 5.6a; however, such meandering gives rise to the excess free energy of the droplet related to the line tension and the elasticity of the triple line effects (see Sections 2.4 and 3.10.1).

Hence, the relevant question is: how did the Cassie–Baxter model succeed in predicting the apparent contact angle at various rough surfaces? The reasonable explanation for the success of the Cassie–Baxter formula (5.25), may perhaps be related to considering the fine structure of the triple line discussed in Section 3.10.3 and illustrated in Figure 3.13 (see also Additional Reading to this Chapter). Actually, the drop is surrounded by a thin precursor film, such as those depicted in Figures 3.13, 5.6, and 5.7. The precursor film (depicted in Figure 5.6a as a shadowed area adjacent to the drop

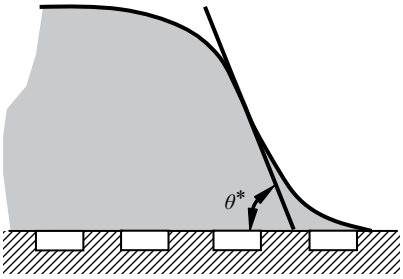

Fig. 5.7: The fine structure of the triple line. θ^* is an apparent contact angle.

boundary) diminishes the energy excess connected with the triple line bending (see also Figure 5.7 illustrating the effect schematically).

The environmental scanning electron microscope image displayed in Figure 3.13 shows that the precursor film smooths away local windings of the triple line [3]. The physical behavior of the precursor film is governed by long-range intermolecular forces acting between molecules of the substrate and liquid, discussed in Section 2.5. It should also be stressed that only the substrate area adjacent to the triple line and located under the precursor film exerts an influence on the apparent contact angle, as is discussed further in detail later. The apparent contact angle θ^* in this case needs redefinition, discussed in Section 2.6 and illustrated in Figures 2.7 and 5.7. It should be defined as an angle between the horizontal axis and the tangent to the droplet cap profile at the point where it touches the precursor film.

5.7 The Cassie–Baxter wetting of curved surfaces

Consider a curved surface consisting of n sorts of materials randomly distributed over the substrate (Figure 5.8). As in Section 5.4, we assume that every material is characterized by its own surface tension coefficients, $\gamma_{i,\mathrm{SL}}$ and $\gamma_{i,\mathrm{SA}}$, and by the fraction f_i in the substrate surface, $\sum_{i=1}^{n} f_\mathrm{i} = 1$. Akin to formulae (5.17) and (5.19), we have for $\widetilde{G}$:

$$\widetilde{G} = \gamma\sqrt{1+h'^2} + \left(\sqrt{1+f'^2}\right)\sum_{i=1}^{n} f_\mathrm{i}(\gamma_{i,\mathrm{SL}} - \gamma_{i,\mathrm{SA}}) + U(x,h) + \lambda(h-f)\,. \tag{5.26}$$

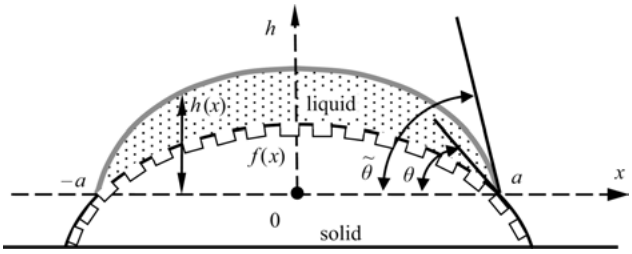

Fig. 5.8: Cassie-like wetting of a curved surface.

Substitution of formula (5.26) into transversality condition (5.13), and considering $h(a) = f(a)$, $U(a, h(a)) = 0$ gives rise to the corrected Cassie–Baxter apparent contact angle $\theta^* = \widetilde{\theta} - \theta$:

$$\cos\theta^* = \cos(\widetilde{\theta} - \theta) = \frac{\sum_{i=1}^{n} f_i(\gamma_{i,\mathrm{SA}} - \gamma_{i,\mathrm{SL}})}{\gamma} . \tag{5.27}$$

There is no need to note that the apparent contact angle $\theta^* = \widetilde{\theta} - \theta$ is insensitive to external fields, satisfying the demands defined above.

5.8 Cassie–Baxter impregnating wetting

There exists one more possibility of the heterogeneous wetting: this is the so-called Cassie–Baxter impregnating wetting state first introduced in Erbil [15] and well explained in de Gennes et al. [14]. In this case liquid penetrates into the grooves of the solid and the drop finds itself on a substrate viewed as a patchwork of solid and liquid (solid "islands" ahead of the drop are dry, as shown in Figure 5.9). This wetting state should be distinguished from the Wenzel wetting illustrated in Figure 5.1. When the Wenzel wetting occurs, the *solid outside of the triple line is dry*, whereas in the Cassie–Baxter impregnating situation, it is partially wetted by liquid as shown in Figure 5.9. The Cassie–Baxter equation (5.21) can be applied to the mixed surface depicted in Figure 5.9, with contact angles θ_Y and zero respectively. We then derive for the apparent contact angle θ^*:

$$\cos\theta^* = 1 - f_S + f_S\cos\theta_Y . \tag{5.28}$$

We denote by f_s and $1 - f_S$ the relative fractions of the solid and liquid phases underneath the droplet [14, 15]. Equation (5.28) may be obtained from the first variational principles (presented in Section 5.4) for the composite surface comprising two species characterized by the Young angles of θ_Y and zero. As demonstrated in de Gennes et al. and Erbil [14, 15], the Cassie–Baxter impregnating wetting is possible when the Young angle satisfies equation (5.29):

$$\cos\theta_Y > \frac{1 - f_s}{\widetilde{r} - f_s} . \tag{5.29}$$

Equation (5.29) defines an angle θ_c so that when $\theta_Y < \theta_c$, a liquid film impregnates the texture [14, 15]. The existence of the Cassie–Baxter impregnating state has recently

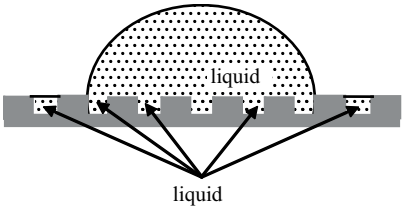

Fig. 5.9: The Cassie–Baxter impregnating wetting state.

been demonstrated experimentally [9, 10]. The Cassie–Baxter impregnating state corresponds to the apparent contact angle θ^* that is lowest for a certain solid–liquid pair when compared with that predicted by the Wenzel (equation (5.8)) and the Cassie–Baxter air trapping (equation (5.25)) wetting regimes.

The Cassie–Baxter impregnating state becomes important in view of wetting transitions on rough surfaces discussed further in Chapter 7.

5.9 The importance of the area adjacent to the triple line in the wetting of rough and chemically heterogeneous surfaces

In 2007, Gao and McCarthy initiated a stormy scientific discussion with their paper provocatively titled "How Wenzel and Cassie were wrong?," followed in 2009 by the paper "An attempt to correct the faulty intuition perpetuated by the Wenzel and Cassie "Laws" [16, 17]. They put forward the following question: what will the apparent contact angle be in the situation presented in Figure 5.10, when a drop of a radius a is deposited on a flat surface comprising a spot of radius b that is smaller than the radius of the droplet? The substrate and the spot are made from different materials possessing various surface energies. The question is: will this spot affect the contact angle? On the one hand, the surface is chemically heterogeneous and it seems that the spot influences the contact angle; on the other hand, the intuition relating the Young equation to the equilibrium of forces acting on the triple line suggests that the contact angle might "feel" only the areas adjacent to the triple line, and the central spot might have no impact on the contact angle. The question may be generalized: is the wetting of a composite surface a 1D or 2D affair? We shall see the importance of this question in Chapter 7, which is devoted to wetting transitions. Or, in other words: is the apparent contact angle governed by the entire surface underneath a drop (2D scenario), or it is dictated by the area adjacent to the triple (three-phase) line (1D scenario)? The problem was cleared up in a series of papers [5, 25, 26, 28, 29].

Consider a liquid drop of a radius a deposited on a two-component composite flat surface including a round spot of a radius b (i.e., chemical heterogeneity) in the axisymmetric way depicted in Figure 5.10. The free energy of the drop is given by equation (5.30):

$$G = \int_0^a \left[2\pi\gamma x\sqrt{1+h'^2} + U(h,x)\right] \mathrm{d}x + 2\pi \int_b^a (\gamma_{\mathrm{SL}}^1 - \gamma_{\mathrm{SA}}^1) x \,\mathrm{d}x + \pi b^2 (\gamma_{\mathrm{SL}}^2 - \gamma_{\mathrm{SA}}^2)\,, \quad (5.30)$$

where $U(h, x)$ describes the external field, superscripts 1 and 2 are related to the substrate and spot respectively (Figure 5.10), and the profile of the droplet $h(x)$ is assumed to be a single-value and even function. It has to be stressed that the endpoints are free to move along the x-axis, whereas the radius of spot b is fixed. Thus, it is clear that the second term in equation (5.30) is a variable, whereas the third term is constant

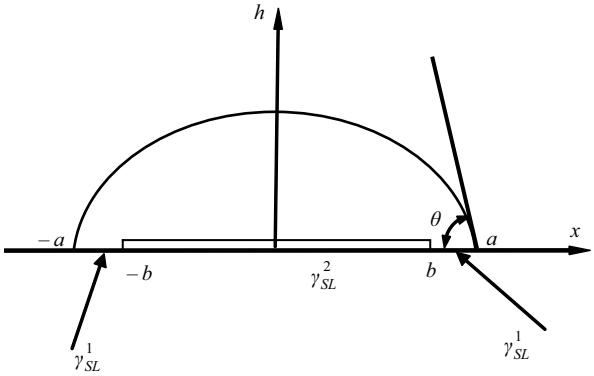

Fig. 5.10: A drop of a radius a deposited axisymmetrically on a composite surface, comprising a "spot" with a radius b.

and could be omitted or redefined. The constant energy has no physical manifestation; only energy changes are important. Without loss of generality, we can shift the zero level of the free energy of the droplet, and the free energy could be redefined as follows:

$$\begin{aligned}\overline{G} &= \int_0^a \left[2\pi y x\sqrt{1+h'^2} + U(h,x)\right] \mathrm{d}x + 2\pi \int_b^a (\gamma_{\mathrm{SL}}^1 - \gamma_{\mathrm{SA}}^1) x \,\mathrm{d}x + \pi b^2 (\gamma_{\mathrm{SL}}^1 - \gamma_{\mathrm{SA}}^1) \\ &= \int_0^a \left[2\pi y x\sqrt{1+(h')^2} + U(h,x) + 2\pi(\gamma_{\mathrm{SL}}^1 - \gamma_{\mathrm{SA}}^1) x \,\mathrm{d}x\right] . \end{aligned} \tag{5.31}$$

It is clear that the free energy variation of the droplet deposited on the composite substrate equals the variation of free energy of the droplet deposited on the homogeneous substrate; however, equation (5.31) is much more convenient for mathematical treatment, and it allows the immediate application of transversality conditions. Equation (5.31) and the condition of the contact volume of the droplet given by equation (5.2) reduce the problem to minimization of the functional $\overline{G} = \int_0^a \widetilde{G}(h, h', x)\,\mathrm{d}x$, where

$$\widetilde{G}(h, h', x) = 2\pi y x\sqrt{1+h'^2} + 2\pi(\gamma_{\mathrm{SL}}^1 - \gamma_{\mathrm{SA}}^1)x + U(h,x) + 2\pi\lambda x h \,, \tag{5.32}$$

where λ is the Lagrange multiplier to be calculated from equation (5.2). Substitution of formula (5.32) into transversality condition (5.5), taking into account $h(a) = 0$, $U(a, h(a)) = 0$, and $h'(x = a) = -\tan\theta$, where $\tan\theta$ is the slope of the liquid–air interface at $x = a$, gives rise to the well-known Young equation:

$$\cos\theta = \frac{\gamma_{\mathrm{SA}}^1 - \gamma_{\mathrm{SL}}^1}{\gamma} \,. \tag{5.33}$$

It is clear that the spot has no influence on the contact angle, and therefore a discrepancy with the force-based approach is avoided. The external field $U = U(h, x)$ does

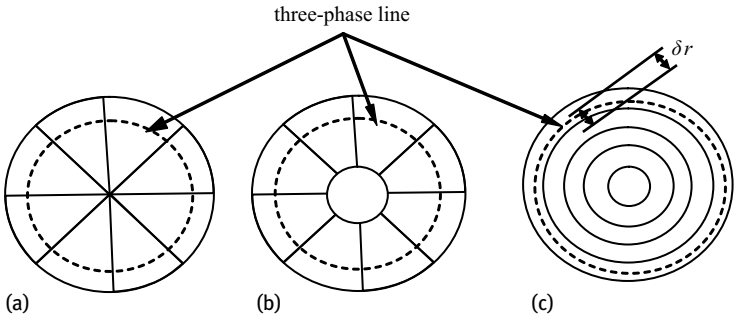

Fig. 5.11: Composite Cassie-like surfaces of different kinds.

not exert influence on the contact angle either. Now, the most delicate point has to be considered. All our treatment is valid when $\delta x \ll a - b$; namely, the boundary is far from the spot, and it can be moved freely. The question is: what is the precise meaning of the expression "far from the spot"? From the physical point of view, it means that the macroscopic approach is valid when a three-phase line is displaced; namely, $a - b \geq 100\,\text{nm}$. When this condition is fulfilled, particles located on the triple line do not "feel" the spot, i.e., the influence of van der Waals forces is negligible (see Sections 1.2, 2.5). It should be stressed that the apparent contact angle is essentially a macroscopic notion; hence, our entire discussion assumes the macroscopic approach.

Now consider more complicated composite Cassie-like surfaces, such as those depicted in Figure 5.11, when a solid substrate comprises two species of solids characterized by various γ_{SL}. It is important to note that there is no general approach to the Cassie-like wetting. It has already been well understood by Johnson and Dettre that Figures 5.11a and c demonstrate very different kinds of surface heterogeneities [21]. When a droplet is deposited axisymmetrically onto a composite surface, depicted in Figure 5.11a, the 2D scenario of wetting occurs independently of the heterogeneity scale. The three-phase line, when displaced, covers both species of solids, and the transversality conditions for the appropriate variational problem yield the well-known Cassie–Baxter equation (5.21). It should be stressed that, again, only the area adjacent to the triple line governs the apparent contact angle. If the Cassie-like surface includes the central spot (depicted in Figure 5.11b), and this spot is spaced far from the triple line, it has no influence on the apparent contact angle. It should be mentioned that for the surfaces displayed in Figures 5.11a and b the surface and linear fractions (as measured along the three-phase line) occupied by the species coincide.

The situation on the composite surface depicted in Figure 5.11c is much more complicated. Inner and outer stripes located far from the three-phase line do not exert an impact on the apparent contact angle. What about the stripes close to the triple line? If the characteristic scale $\delta r \gg 100\,\text{nm}$ (Figure 5.11c), the Cassie–Baxter equation fails, because the displacement of the boundary in the variational problem covers only one

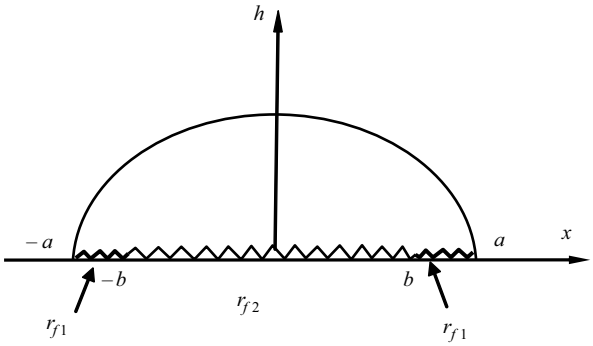

Fig. 5.12: Wenzel-like wetting of the composite substrate.

kind of species, which dictates the apparent contact angle. In this case, everything depends on the initial radius of the drop. If $\delta r \sim 100\,\text{nm}$ or less, the displacement of the boundary covers both kinds of solid species, and equation (5.21) does work; i.e., a 2D scenario of wetting takes place. It could be recognized that the linear fraction of species is irrelevant in this case.

Wenzel-like wetting is analyzed in a similar way. Figure 5.12 depicts a drop deposited on a composite surface characterized by variable roughness; the roughness of the central spot with radius b equals $\tilde{r}_{f_2}$, whereas the roughness of the area adjacent to the triple line equals $\tilde{r}_{f_1}$ (Figure 5.12). The free energy of the drop is given by:

$$G = \int_0^a \left[2\pi\gamma x\sqrt{1+h'^2} + U(h,x)\right] \mathrm{d}x + 2\pi\tilde{r}_{f_1}\int_b^a (\gamma_{\mathrm{SL}}-\gamma_{\mathrm{SA}})x\,\mathrm{d}x + \tilde{r}_{f_2}\pi b^2(\gamma_{\mathrm{SL}}-\gamma_{\mathrm{SA}}). \quad (5.34)$$

The last term in formula 5.34 is constant, and transformations akin to those leading to expression (5.31) yield:

$$\overline{G} = \int_0^a \left[2\pi\gamma x\sqrt{1+h'^2} + U(h,x) + 2\pi\tilde{r}_{f_1}(\gamma_{\mathrm{SL}}-\gamma_{\mathrm{SA}})x\,\mathrm{d}x\right]. \quad (5.35)$$

The conservation of volume given by equation (5.2) yields $\widetilde{G}$ defined according to formula (5.36):

$$\widetilde{G}(h,h',x) = 2\pi\gamma\sqrt{1+h'^2} + 2\pi\tilde{r}_{f_1}(\gamma_{\mathrm{SL}}-\gamma_{\mathrm{SA}})x + U(h,x) + 2\pi\lambda xh\,. \quad (5.36)$$

Substitution of equation (5.36) into the transversality condition (5.5), taking into account $h(a) = 0$, $U(a, h(a)) = 0$, and $h'(x = a) = -\tan\theta^*$, supplies:

$$\cos\theta^* = \tilde{r}_{f_1}\frac{\gamma_{\mathrm{SA}}-\gamma_{\mathrm{SL}}}{\gamma} = \tilde{r}_{f_1}\cos\theta\,. \quad (5.37)$$

Again, when $a - b \geq 100\,\text{nm}$, only the roughness in the area adjacent to the triple line dictates the apparent contact angles.

5.10 Wetting of gradient surfaces

Now we apply the technique developed in the previous sections to the analysis of so-called "gradient" surfaces possessing a continuous gradient of wettability [13]. Such surfaces are of great interest in view of their applications in microfluidics devices [13, 29]. For the sake of simplicity, we treat a 2D wetting problem where a cylindrical drop is under discussion (the cross-section of the drop is presented in Figure 5.13). When the surface is "gradient," the surface tensions are already not constant, but $\gamma_{SL} = \gamma_{SL}(x)$; $\gamma_{SA} = \gamma_{SA}(x)$ take place. Thus, the free energy per unit length of the cylindrical drop could be written as:

$$G(h, h') = \int_{-a}^{a} \left[\gamma\sqrt{1 + h'^2} + \gamma_{SL}(x) - \gamma_{SA}(x) + U(h)\right] \mathrm{d}x \,. \tag{5.38}$$

Condition (5.39) of a constant area S also has to be taken into account:

$$S = \int_{-a}^{a} h(x)\,\mathrm{d}x = \text{const}\,, \tag{5.39}$$

which is equivalent to the constant volume requirement in the case of cylindrical "drops." Equations (5.38) and (5.39) reduce the problem to minimization of the functional $G = \int_{-a}^{a} \widetilde{G}(h, h')\,\mathrm{d}x$, where:

$$\widetilde{G} = \gamma\sqrt{1 + h'^2} + \gamma_{SL}(x) - \gamma_{SA}(x) + U(h) + \lambda h\,, \tag{5.40}$$

where λ is the Lagrange multiplier to be deduced from equation (5.39). Transversality condition (5.5) at the endpoint a, taking into account $h(a) = 0$, $U(h = 0) = 0$ gives rise to

$$\cos\theta = \frac{\gamma_{SA}(a) - \gamma_{SL}(a)}{\gamma}\,. \tag{5.41a}$$

We conclude that, as could be expected, only the values of surface tensions at the endpoints govern the contact angle θ [5]. Consider now the simplest situation, when

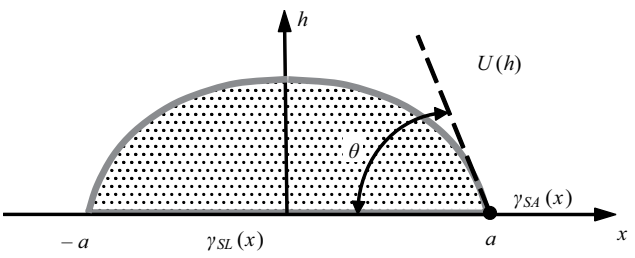

Fig. 5.13: Cross-section of a cylindrical drop deposited on a gradient surface.

the x-dependencies of interfacial tensions are linear; namely, assume:

$$\gamma_{SA}(x) = \gamma_{SA}^0 + \alpha x\,; \quad \alpha = \text{const}\,; \quad [\alpha] = \text{N/m}^2 \quad \text{and}$$
$$\gamma_{SL}(x) = \gamma_{SL}^0 + \beta x\,; \quad \beta = \text{const}\,; \quad [\beta] = \text{N/m}^2\,,$$

where: $\gamma_{SA}^0 = \gamma_{SA}(x = 0)$; $\gamma_{SL}^0 = \gamma_{SL}(x = 0)$. In this case equation (5.41a) is reduced to equation (5.41b):

$$\cos\theta - \cos\theta_0 = \frac{a}{\gamma}(\alpha - \beta)\,, \tag{5.41b}$$

where: $\cos\theta_0 = (\gamma_{SA}^0 - \gamma_{SL}^0)/\gamma$.

5.11 The mixed wetting state

As it always takes place in nature, the pure Wenzel and Cassie wetting regimes introduced in the previous sections rarely occur. More abundant is a so-called mixed wetting state, depicted schematically in Figure 5.14, introduced in Miwa et al. [27], and discussed in much detail in Marmur [24]. In this situation, the droplet is supported partially by air and partially by *a rough chemically homogeneous solid surface*. In such a case, the free energy of the droplet is given by:

$$G = \int_0^a \left[\gamma 2\pi x\sqrt{1 + h'^2} + 2\pi x\,(\gamma_{SL} - \gamma_{SA})\,\tilde{r} f_S + 2\pi x\gamma(1 - f_S) + U(h, x)\right] \mathrm{d}x\,, \tag{5.42}$$

where f_S is the fraction of the solid surface that is wetted by the liquid, and $\tilde{r}$ is the *roughness ratio of the wet area*. Consideration of a constant volume of the droplet and exploitation of the already familiar mathematical tool of transversality conditions (see Sections 5.2 and 5.4) yield for the apparent contact angle:

$$\cos\theta^* = \tilde{r} f_S \cos\theta_Y + f_S - 1\,. \tag{5.43}$$

Obviously for $\tilde{r} = 1$, we return to the usual Cassie air-trapping equation (5.25). Equation (5.43) was derived in Miwa et al. [27] and analyzed in Marmur [24], and is extremely useful for understanding the phenomenon of superhydrophobicity, which is to be discussed in detail in the next chapter.

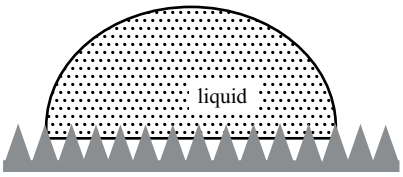

Fig. 5.14: The mixed wetting state.

5.12 Considering the line tension

At first glance, it would appear that considering the line tension Γ (introduced and discussed in Section 2.4) is essential only for very small droplets. It was shown in Section 2.4 that the characteristic scale at which line tension-related effects are important equals approximately 100 nm [1, 23, 30]. Thus, it seems that for large droplets with a characteristic size of 0.01–1 mm, at which point the notion of the apparent contact angle may be introduced (see Section 5.1), the effects due to line tension are negligible. However, in the case of rough surfaces, the actual situation is more complicated owing to the "effect of internal triple lines" introduced in Wong and Ho [32] and illustrated in Figure 5.15. This figure depicts a droplet deposited on a substrate built of conical posts, and shows the "external" and "internal" triple lines. In this most general case, where an axially symmetrical droplet of a contact radius a is deposited on a rough, chemically homogeneous surface and exerted to the external potential $U(h, x)$, its free energy G is given by:

$$G = \int_0^a \left[\gamma 2\pi x \sqrt{1 + h'^2} + 2\pi x \left(\gamma_{SL} - \gamma_{SA}\right) \tilde{r} f_S + 2\pi x \gamma (1 - f_S) + 2\pi \Gamma + 2\pi x \Gamma \xi + U(h, x) \right] \mathrm{d}x \tag{5.44}$$

where ξ is the perimeter of the triple line per unit area of the substrate under the droplet (with the dimension of m^{-1}). In equation (5.44), $\int_0^a 2\pi\Gamma \,\mathrm{d}x$ represents the energy of the external triple line surrounding the droplet, and $\int_0^a 2\pi x \Gamma \xi \,\mathrm{d}x$ is the energy of the internal triple lines (Figure 5.15). Considering a constant volume of the droplet and transversality condition (5.5) yields a general equation describing static wetting of rough chemically homogeneous surfaces:

$$\cos\theta^* = \tilde{r} f_S \cos\theta + f_S - 1 - \frac{\Gamma}{\gamma}\left(\xi + \frac{1}{a}\right) . \tag{5.45}$$

It could be recognized that equation (5.45) includes all equations describing the wetting of rough chemically homogenous surfaces [7]. Indeed, when $\tilde{r} = 1$ and the effects related to the line tension, Γ, are negligible, we return to the traditional Cassie–Baxter "air trapping" equation (5.25). In the case when $\tilde{r} \neq 1$, but the effects related to the line tension, Γ, are negligible, we obtain the modified Cassie–Baxter equation (5.43), introduced by Miwa et al. and Marmur [24, 27]. In the situation when $\tilde{r} = 1$ and the effects related to the external perimeter of the droplet are negligible, i.e., $\xi \gg 1/a$, we have the equation proposed recently by Wong and Ho in [32]:

$$\cos\theta^* = f_S \cos\theta + f_S - 1 - \frac{\Gamma\xi}{\gamma} . \tag{5.46}$$

The experimental situation described by equation (5.46) is exemplified by Figure 5.16, where the droplet sits on square posts with an area of $c \times c$; the distance between posts is b. In this simple case, parameter ξ equals $4c/(c + b)^2$ (the perimeters of the

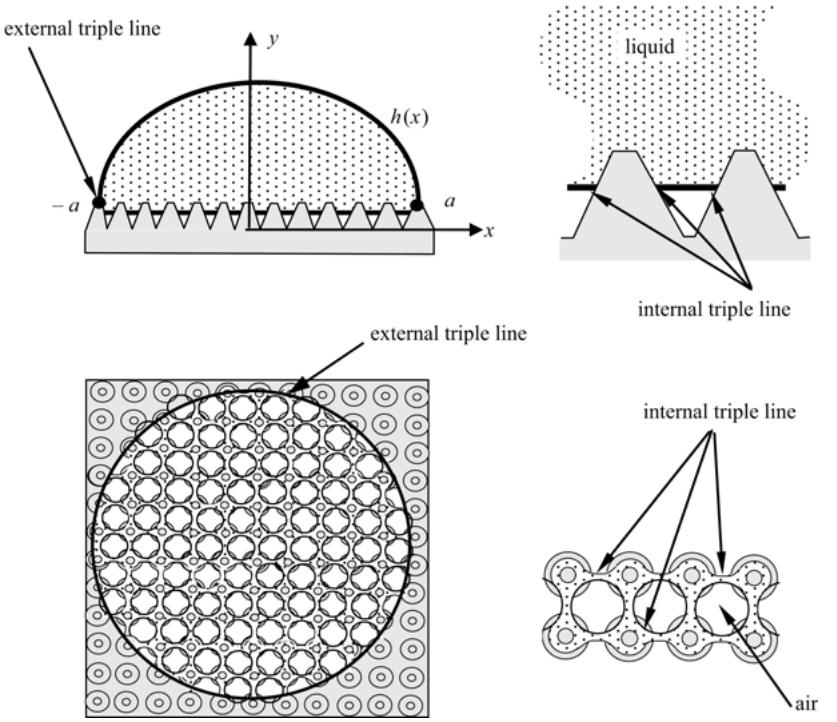

Fig. 5.15: Wetting of a substrate built of conical posts. The external and internal triple lines are shown. Reprinted from Bormashenko [7], with permission from Elsevier.

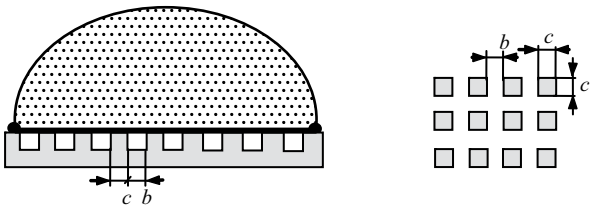

Fig. 5.16: Cassie wetting in the situation where a droplet sits on square posts, $c \times c$. The perimeters of the posts form internal triple lines.

posts form internal triple lines). For nanostructures $c \sim b \sim 10^{-9}$ m, $\xi \sim 10^{9}$ m^{-1}, and it is seen from equation (5.46) that the effect of the internal-line tension is feasible for reasonable values of line tension reported in Amirfazli and Neumann, Marmur, and Pompe et al. [1, 23, 30] and discussed in Section 2.4. The true value of the line tension remains highly disputable; hence, its effect on the apparent contact angles on rough surfaces also remains obscure. Wong and Ho suggested that equation (5.46) successfully explains the extremely high apparent contact angles observed on nano-

scaled surfaces [32]. The calculation of ξ for more complicated topographies of the relief was carried out in Wong and Ho [32].

Assuming $\xi \ll 1/a$ (the effects related to internal triple lines are negligible) in equation (5.45), we obtain the natural extension of the Neumann–Boruvka equation (see Section 2.4, equation (2.24)) for rough surfaces:

$$\cos\theta^* = \bar{r} f_S \cos\theta + f_S - 1 - \frac{\Gamma}{\gamma a} . \tag{5.47}$$

In the case where $f_S = 1$ and the effects related to the line tension, Γ, are negligible, we obtain the well-known Wenzel equation (5.8). Thus, we see that equation (5.45) includes all particular cases related to the wetting of rough, chemically homogeneous surfaces [7]. It is seen that the apparent contact angles predicted by equation (5.45) are *independent of external fields*. The validity of equation (5.46) was checked with atomic force microscopic imaging and molecular dynamics simulations in Włoch et al. [33], and it turned out that the influence of the line tension on the apparent contact angles was weak.

Appendix 5A. Alternative derivation of the Young, Cassie, and Wenzel equations

We derived the Young (2.11), Wenzel (5.16), and Cassie–Baxter (5.20) equations within the general framework of the transversality conditions of the appropriate variational problem. It is instructive to supply the alternative derivation of these basic equations based on straightforward thermodynamic arguments. Consider a drop of the radius a deposited on an ideally flat surface. If θ denotes the contact angle, we have the volume V and surface S of the drop expressed as:

$$V = \frac{\pi R^3}{3}(1-\cos\theta)^2(2+\cos\theta) = \frac{\pi R^3}{3\sin^3\theta}(1-\cos\theta)^2(2+\cos\theta) , \tag{5.48}$$

$$S = 2\pi R^2(1-\cos\theta) = \frac{2\pi R^2}{1+\cos\theta} , \tag{5.49}$$

where R is the radius of the droplet to be distinguished from the contact radius a (Figure 5.17); obviously $a = R\sin\theta$. For the sake of simplicity, we assume that the liquid–air interface is spherical (gravity is neglected). The Gibbs free surface energy of the drop is expressed by equation (5.50) (within an additive constant):

$$G = \gamma S + \pi a^2(\gamma_{SL} - \gamma_{SA}) = \gamma S - \pi R^2 \Theta \sin^2\theta , \tag{5.50}$$

where γ, γ_{SL}, γ_{SA} are the interfacial tensions and S is the spherical liquid–air interface area. Having in mind further derivation of the Wenzel and Cassie–Baxter equations, we have introduced here the constant Θ, which in the special case of flat homogeneous substrates is defined as:

$$\Theta = \gamma_{SA} - \gamma_{SL} . \tag{5.51}$$

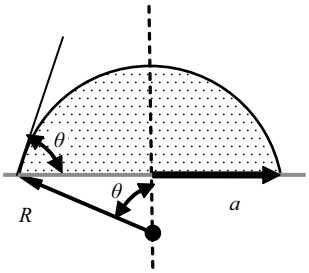

Fig. 5.17: Scheme illustrating the interrelation between the radius of the droplet R and the contact radius a.

The general form of the dependence in the right-hand part of equation (5.50) remains true in many other cases of physical interest. Now we make the main assumption of our treatment: namely, we assume a constant volume for the drop, V=const. Substitution of formulae (5.48) and (5.49) into equation (5.50), and considering (5.51) yields:

$$G = \left[\frac{9\pi V^2}{(1-\cos\theta)(2+\cos\theta)^2}\right]^{1/3} (2\gamma - \Theta(1+\cos\theta)) \ . \tag{5.52}$$

Now G is a function of *only one* independent variable θ, which is the contact angle. The straightforward differentiation gives:

$$\frac{\mathrm{d}G}{\mathrm{d}\theta} = \left[\frac{9V^2\pi}{(1-\cos\theta)^4(2+\cos\theta)^5}\right]^{\frac{1}{3}} 2(\Theta - \gamma\cos\theta)\sin\theta \ . \tag{5.53}$$

It is clear that $\mathrm{d}G/\mathrm{d}\theta(\theta = \theta_\mathrm{Y}) = 0$ is fulfilled when $\Theta = \gamma\cos\theta_\mathrm{Y}$, or, in other words,

$$\cos\theta_\mathrm{Y} = \frac{\gamma_{\mathrm{SA}} - \gamma_{\mathrm{Sl}}}{\gamma} \ .$$

Thus, the well-known Young equation (2.11) for the equilibrium contact angle on flat homogeneous surfaces is obtained.

Now consider Wenzel-like wetting of a rough surface (Figure 5.1) characterized by the roughness $\tilde{r} > 1$ (see Section 5.2). This means that the area of liquid–solid interface is equal to $\pi a^2\tilde{r}$, and we have for the free surface energy G equation (5.50) with Θ defined as $\Theta = \tilde{r}(\gamma_{\mathrm{SA}} - \gamma_{\mathrm{SL}})$. This immediately yields the well-known Wenzel equation for the equilibrium apparent contact angle θ^*, i.e.,

$$\cos\theta^* = \frac{\Theta}{\gamma} = \tilde{r}\frac{\gamma_{\mathrm{SA}} - \gamma_{\mathrm{Sl}}}{\gamma} = \tilde{r}\cos\theta_\mathrm{Y}$$

(compare with equation (5.16)).

Now consider the Cassie–Baxter wetting of a flat chemically heterogeneous surface. Analogous to the above treatment, we simply define:

$$\Theta = \sum_{i=1}^{n} f_\mathrm{i}(\gamma_{i,\mathrm{SA}} - \gamma_{i,\mathrm{SL}}) \ ;$$

for designations, see Section 5.4. The mathematical procedure akin to equation (5.52) and (5.53) supplies the Cassie–Baxter apparent contact angle:

$$\cos\theta^* = \frac{\Theta}{\gamma} = \frac{\sum_{i=1}^{n} f_i(\gamma_{i,\mathrm{SA}} - \gamma_{i,\mathrm{SL}})}{\gamma} .$$

Additional Reading: scaling law governing the fine structure of the triple line

As discussed in Section 3.10.3 and Section 5.6 and depicted in Figures 3.13 and 5.6, the three-phase line is not ideally smooth but meanders, even on flat surfaces. It is mentioned in Section 3.10.3 that the fine structure of the triple line obeys the scaling law, discussed in detail in Bormashenko et al. [34], namely $\tilde{b}(L) \sim L^{\hat{\alpha}}$, where $\tilde{b}$ is the root-mean-square width of the three-phase line, L is its length, and $\hat{\alpha}$ is the scaling exponent. It was demonstrated that the same is also true (with $\hat{\alpha} \cong 0.5$) for the Cassie and Wenzel regimes for very different solid–liquid pairs [34]. Moreover, the same scaling law (with $\hat{\alpha} \cong 0.7$) governs the roughness of the swash edge line [35].

Bullets

- Wetting of rough or chemically heterogeneous surfaces is described by the apparent contact angle, which may be introduced when the characteristic size of a droplet is much larger than that of the surface heterogeneity or roughness.
- Wetting of rough, chemically homogeneous surfaces is described by the Wenzel equation. Surface roughness always magnifies the underlying wetting properties.
- Wetting of flat, chemically heterogeneous surfaces is described by the Cassie–Baxter equation.
- The Cassie–Baxter model may be extended to a situation where a droplet traps air, i.e., it is supported partially by a solid and partially by air.
- One more wetting regime is possible, i.e., the Cassie–Baxter impregnating state, when a drop is deposited on a substrate comprising a patchwork of solid and liquid, where solid "islands" ahead of the drop are dry.
- The mixed wetting regime corresponds to the situation where a droplet is supported by a rough solid surface and air.
- The line tension effects may be important for the prediction of apparent contact angles for nano-rough surfaces due to "internal triple lines."
- The area adjacent to the triple line is of primary importance for predicting apparent contact angles.
- The apparent contact angles, predicted by the Wenzel and Cassie–Baxter models, are independent of external fields, volume, and shape of droplets.

References

[1] A. Amirfazli and A. W. Neumann, Status of the three-phase line tension, *Adv. Colloid & Interface Sci.* **110** (2004), 121–141.

[2] J. Bico, U. Thiele, and D. Quéré, Wetting of textured surfaces, *Colloids and Surfaces A* **206** (2002), 41–46.

[3] E. Bormashenko, Why does the Cassie–Baxter equation apply? *Colloids & Surfaces A* **324** (2008), 47–50.

[4] E. Bormashenko, Young, Boruvka–Neumann, Wenzel and Cassie–Baxter equations as the transversality conditions for the variational problem of wetting, *Colloids and Surfaces A* **345** (2009), 163–165.

[5] E. Bormashenko, A variational approach to wetting of composite surfaces: is wetting of composite surfaces a one-dimensional or two-dimensional phenomenon? *Langmuir* **25** (2009), 10,451–10,454

[6] E. Bormashenko, Wetting of flat and rough curved surfaces, *Journal of Physical Chemistry C*, **113** (2009) 17,275–17,277.

[7] E. Bormashenko, General equation describing wetting of rough surfaces, *J. Colloid & Interface Sci.* **360** (2011), 317–319.

[8] E. Bormashenko, Y. Bormashenko, G. Whyman, R. Pogreb, and O. Stanevsky, Micrometrically scaled textured metallic hydrophobic interfaces validate the Cassie–Baxter wetting hypothesis, *J. Colloid & Interface Sci.* **302** (2006), 308–311.

[9] E. Bormashenko, R. Pogreb, T. Stein, G. Whyman, M. Erlich, A. Musin, V. Machavariani, and D. Aurbach, Characterization of rough surfaces with vibrated drops, *Phys. Chem. Chem. Phys.* **10** (2008), 4056–4061.

[10] E. Bormashenko, R. Pogreb, G. Whyman, S. Balter, and D. Aurbach, Wetting transitions on post-built and porous reliefs, *J. Adhesion Sci. & Technology* **26** (2012), 1169–1180.

[11] A. B. D. Cassie, Contact angles, *Discuss. Faraday Soc.* **3** (1948), 11–16.

[12] A. B. D. Cassie and S. Baxter, Wettablity of porous surfaces, *Trans. Faraday Soc.* **40** (1944), 546–551.

[13] S. K. Daniel, M. K. Chaudhury, Rectified motion of liquid drops on gradient surfaces induced by vibration, *Langmuir* **18** (2002), 3404–3407.

[14] P. G. de Gennes, F. Brochard-Wyart, and D. Quéré, *Capillarity and Wetting Phenomena*, Springer, Berlin, 2003.

[15] H. Y. Erbil, *Surface Chemistry of Solid and Liquid Interfaces*, Blackwell, Oxford, 2006.

[16] L. Gao and T. J. McCarthy, How Wenzel and Cassie were wrong? *Langmuir* **23** (2007), 3762–3765.

[17] L. Gao and T. J. McCarthy, An attempt to correct the faulty intuition perpetuated by the Wenzel and Cassie "Laws", *Langmuir* **25** (2009), 7249–7255.

[18] I. M. Gelfand and S. V. Fomin, *Calculus of Variations*, Dover, 2000.

[19] R. J. Good, A Thermodynamic derivation of Wenzel's modification of Young's equation for contact angles; together with a theory of hysteresis, *J. Am. Chem. Soc.* **74** (1952), 5041–5042.

[20] J. N. Israelachvili and M. L. Gee, Contact angles on chemically heterogeneous surfaces, *Langmuir* **5** (1989), 288–289.

[21] R. E. Johnson and R. H. Dettre, Contact angle hysteresis. III. Study of an idealized heterogeneous surface, *J. Phys. Chemistry* **68** (1964), 1744–1750.

[22] G. McHale, Cassie and Wenzel: Were they really so wrong? *Langmuir* **23** (2007), 8200–8205.

[23] A. Marmur, Line tension and the intrinsic contact angle in solid-liquid-fluid systems, *J. Colloid & Interface Sci.* **186** (1997), 462–466.

[24] A. Marmur, Wetting on hydrophobic rough surfaces: To be heterogeneous or not to be? *Langmuir* **19** (2003), 8343–8348.
[25] A. Marmur, When Wenzel and Cassie are right: reconciling local and global considerations *Langmuir* **25** (2009), 1277–1281.
[26] A. J. B. Milne and A. Amirfazli, The Cassie equation: How it is meant to be used, *Advances in Colloid & Interface Sci.* **170** (2012), 48–55.
[27] M. Miwa, A. Nakajima, A. Fujishima, K. Hashimoto, and T. Watanabe, Effects of the surface roughness on sliding angles of water droplets on superhydrophobic surfaces, *Langmuir* **16** (2000), 5754–5760.
[28] M. Nosonovsky, On the range of applicability of the Wenzel and Cassie equations, *Langmuir* **23** (2007), 9919–9920.
[29] M. V. Panchagnula and S. Vedantam, Comment on How Wenzel and Cassie were wrong, *Langmuir* **23** (2007), 13,242–13,242.
[30] T. Pompe, A. Fery, and S. Herminghaus, Measurement of contact line tension by analysis of the three-phase boundary with nanometer resolution, in: J. Drelich, J. S. Laskowski, and K. L. Mittal (eds), *Apparent and Microscopic Contact Angles*, 3–12, VSP, Utrecht, 2000.
[31] R. N. Wenzel, Resistance of solid surfaces to wetting by water, *Ind. Eng. Chem*. **28** (1936), 988–994.
[32] T.-S. Wong and C.-M. Ho, Dependence of macroscopic wetting on nanoscopic surface textures, *Langmuir* **25** (2009), 12,851–12,854.
[33] J. Włoch, A. P. Terzyk, M. Wiśniewski, and P. Kowalczyk, Nanoscale water contact angle on Polytetrafluoroethylene surfaces characterized by molecular dynamics–atomic force microscopy imaging, *Langmuir* **34** (2018), 4526–4534.

Additional Reading

[34] E. Bormashenko, A. Musin, G. Whyman, Z. Barkay, and M. Zinigrad, On universality of scaling law describing roughness of triple line, *Eur. Phys. J. E* **38** (2015), 2–11.
[35] E. Bormashenko, A. Musin, and R. Grynyov, Scaling law governing the roughness of the swash edge line, *Scientific Reports* **4** (2015), 6243.

6 Superhydrophobicity, superhydrophilicity, and the rose petal effect

6.1 Superhydrophobicity

The phenomenon of superhydrophobicity was revealed in 1997 when W. Barthlott and C. Neinhuis studied the wetting properties of a number of plants and stated that the "interdependence between surface roughness, reduced particle adhesion and water repellency is the keystone in the self-cleaning mechanism of many biological surfaces" [1]. They discovered the extreme water repellency and unusual self-cleaning properties of the "sacred lotus" (*Nelumbo nucifera*) and coined the notion of the "lotus effect," which is now one of the most studied phenomena in surface science. Afterward, the group led by W. Barthlott studied a diversity of plants and revealed a deep correlation among the surface roughness of plants, their surface composition, and their wetting properties (varying from superhydrophobicity to superhydrophilicity) [17, 30].

The amazing diversity of the surface reliefs of plants observed in nature was reviewed in Barthlott et al. [17]. They noted that plants are coated by a protective outer membrane coverage, or *cuticle*. This cuticle is a composite material built up by a network of polymer *cutin* and waxes [17]. One of the most important properties of this cuticle is *hydrophobicity*, which prevents the desiccation of the interior plant cells [17, 30].

It is noteworthy that the cuticle demonstrates only moderate inherent hydrophobicity (or even *hydrophilicity* for certain plants such as the famous lotus [8]), whereas the rough surface of the plant may be extremely water-repellent.

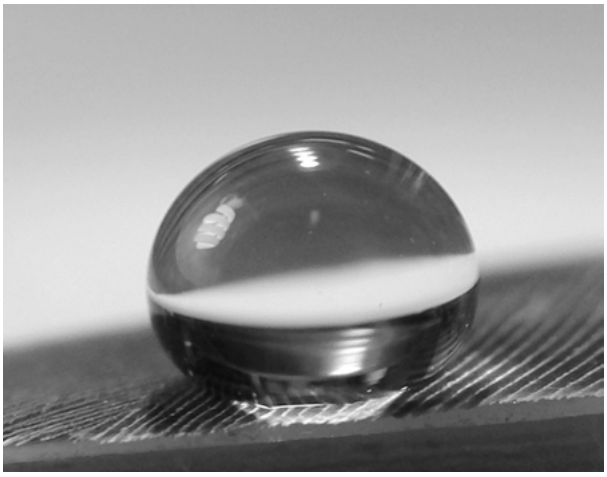

Fig. 6.1: A 50-µl water droplet deposited on a pigeon feather. The pronounced superhydrophobicity of the feather is clearly seen.

https://doi.org/10.1515/9783110583144-006

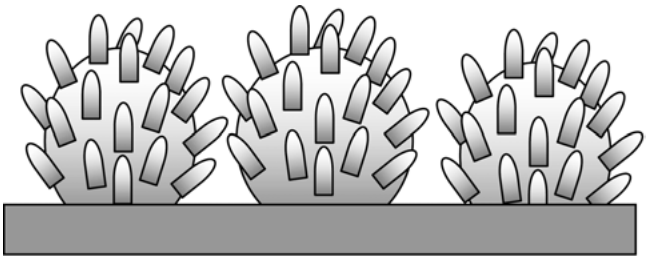

Fig. 6.2: Typical hierarchical reliefs inherent to lotus-like surfaces.

Barthlott et al. also clearly understood that the micro- and nanostructures of the plants' surfaces define their eventual wetting properties, in accordance with the Cassie–Baxter and Wenzel models (discussed in detail in the previous chapter). As Barthlott et al. reported the extreme water repellency of the lotus, similar phenomena were reported for a diversity of biological objects: water strider legs, as well as bird and butterfly wings (shown in Figure 6.1) [3, 10, 26, 31]. It is noteworthy that the keratin constituting bird wings is also inherently *hydrophilic* [3]. Barthlott et al. also drew the attention of investigators to the *hierarchical reliefs* inherent in plants characterized by superhydrophobicity, such as depicted in Figure 6.2. The interrelation between the hierarchical topography of surfaces and their water repellency is discussed in detail below.

6.2 Superhydrophobicity and the Cassie–Baxter wetting regime

In this chapter, we deal with the wetting of micro- or nanorough surfaces. The wetting of these surfaces is characterized by an *apparent contact angle*, introduced in Sections 3.8 and 5.1. The surfaces characterized by an apparent contact angle larger than 150° are referred to as superhydrophobic [22, 24]. It should be immediately emphasized that high apparent contact angles observed on a surface are not sufficient to refer to it as superhydrophobic. True superhydrophobicity should be distinguished from the pseudosuperhydrophobicity inherent to surfaces exhibiting the "rose petal effect," to be discussed later. The pseudosuperhydrophobic surfaces are characterized by large apparent contact angles accompanied by high contact angle hysteresis, which was discussed in great detail in Chapter 3. In contrast, truly superhydrophobic surfaces are characterized by large apparent contact angles and low contact angle hysteresis resulting in a low value of a sliding angle: a water drop rolls along such a surface even when it is tilted at a small angle. Truly superhydrophobic surfaces are also *self-cleaning*, as rolling water drops wash off contaminations and particles such as dust or dirt, as shown schematically in Figure 6.3 [17, 22, 24, 30]. Actually, the surface should satisfy one more demand to be referred to as superhydrophobic: the Cassie–Baxter

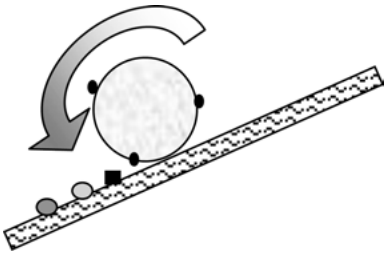

Fig. 6.3: Rolling downward on the superhydrophobic surface; the droplet entrains contaminants.

wetting regime on this surface should be stable. The stability of the Cassie–Baxter wetting regime is important for preventing the Cassie–Wenzel wetting transitions (to be discussed in Chapter 7).

The Cassie–Baxter equation (5.25), developed for the air trapping situation where the droplet is partially supported by air cushions (Figure 5.4), supplies the natural explanation for the phenomenon of superhydrophobicity. Indeed, the apparent contact angle θ^* in this situation given by $\cos\theta^* = -1 + f_S(\cos\theta_Y + 1)$ ultimately approaching π when the relative fraction of the solid f_s approaches zero (see Section 5.1). This corresponds to complete dewetting, discussed in Section 2.1 and illustrated by Figure 2.1c. Note that the apparent contact angle also approaches π when the Young angle tends toward π. However, this situation is practically unachievable, because the most hydrophobic polymer, polytetrafluoroethylene (Teflon) demonstrates an advancing angle smaller than 120°, and this angle is always larger than the Young angle [13]. Hence, it is seen from the Cassie–Baxter equation that the apparent contact angles could be increased by decreasing the relative fraction of the solid surface underneath a droplet. However, there exists a more elegant way to manufacture surfaces characterized by ultimately high apparent contact angles: producing hierarchical reliefs, and this is the situation observed in natural objects such as lotus leaves (to be discussed in the next section).

Note that the Wenzel equation (5.8) also predicts high apparent contact angles approaching π for inherently hydrophobic surfaces ($\theta_Y > \pi/2$), when $\tilde{r}\cos\theta_Y$ is close to -1. However, the Wenzel-like wetting, depicted in Figure 5.1, is characterized by high contact angle hysteresis, whereas superhydrophobicity accompanied by self-cleaning calls for the contact angle hysteresis to be as low as possible.

6.3 Wetting of hierarchical reliefs: approach of Herminghaus

Herminghaus developed a very general approach to the wetting of hierarchical reliefs, based on the concept of the effective surface tension of a rough solid–liquid interface γ_{SL}^{eff}. It is reasonable to suggest phenomenologically that this surface tension is increased compared with that of the flat solid surface, γ_{SL}, owing to the roughness. Herminghaus treated indented surfaces; however, his approach is valid for bumpy

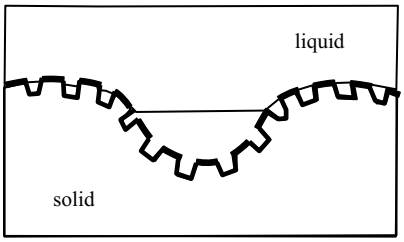

Fig. 6.4: Scheme of the wetting of a hierarchical relief.

surfaces as well. The effective surface tension of a rough surface with a single-scale roughness is given by:

$$\gamma_{SL1}^{eff} \cong (1 - f_L)\gamma_{SL} + f_L(\gamma + g_0\gamma_{SA}) , \tag{6.1}$$

where f_L is the fraction of free liquid surfaces suspended over the indentations of the relief, $g_0 \geq 1$ is the geometrical factor describing the total surface area of the indentation, γ_{SA} is the surface tension of the flat solid surface–air interface, and the subscript 1 in γ_{SL1}^{eff} denotes the single-scale type of the roughness. It is seen from equation (6.1) that an indented interface has a larger effective surface tension than a flat one. This warrants the apparent contact angle, θ_1, which is larger than θ_Y inherent to the flat surface, but does not explain the exceptionally large apparent contact angles observed on many biological objects discussed in Section 6.1. To explain the extreme apparent contact angles, Herminghaus analyzed hierarchical reliefs, such as those depicted in Figure 6.4. For such a double-scaled relief, the effective surface tension is given by:

$$\gamma_{SL2}^{eff} \cong (1 - f_{L1})\gamma_{SL1} + f_{L1}(\gamma + g_1\gamma_{SA}(1 + (g_0 - 1)f_L)) . \tag{6.2}$$

For hierarchically indented substrates, Herminghaus deduced the following recursion relation:

$$\cos\theta_{n+1} = (1 - f_{Ln})\cos\theta_n - f_{Ln} , \tag{6.3}$$

where n denotes the number of the generation of the indentation hierarchy. A larger n corresponds to a larger length scale. According to equation (6.3), $\cos\theta_{n+1} - \cos\theta_n = -f_{Ln}(1 + \cos\theta_n) < 0$, so that the sequence represented by equation (6.3) is monotonic. Herminghaus stressed that θ_0 corresponding to θ_Y must only be finite, but need not exceed $\pi/2$ to obtain high resulting apparent contact angles on hierarchical surfaces. Herminghaus also considered fractal surfaces and estimated the Hausdorff dimension of such surfaces. Generally, the model proposed by Herminghaus successfully explained high apparent contact angles observed on a diversity of biological objects.

6.4 Wetting of hierarchical structures: a simple example

Herminghaus discussed a very general situation of wetting of fractal hierarchical structures [14]. Actually, both natural and artificial superhydrophobic surfaces are

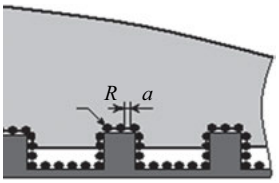

Fig. 6.5: Simple example of the wetting of a hierarchical relief.

usually built from twin-scale surfaces, such as those shown in Figure 6.2. Thus, a simple example demonstrating the advantages of hierarchical reliefs is useful. Consider the surface of the form, depicted in Figure 6.5, roughly modeling the real one reported in Bormashenko et al. [5] and textured on two scales, with the air trapped in rectangular "large" channels and "small" pockets between small balls of a radius R. Air is trapped between the liquid drop and the rough surface. Let w be the fraction of the large channels' liquid–air interface in the underlying substrate surface; let v be the similar fraction of the small pockets' cross-section; and let $\widetilde{g}(\theta_Y)$ be the geometric factor that is the ratio between the balls' surfaces under the liquid drop and their projection onto the substrate. When a drop of liquid moves in all directions over a distance $\mathrm{d}x$, the apparent surface under the drop increases by $l\,\mathrm{d}x$, where l is the length of the intersection line of the three interfaces. From this surface, a new liquid–vapor interface $wl\,\mathrm{d}x$ appears over the large channels (remember that their fraction is w). This type of interface of an area $v(1-w)l\,\mathrm{d}x$ also appears over small pockets on the remaining surface $(1-w)l\,\mathrm{d}x$ (Figure 6.5). The remainder of the horizontal projection onto the substrate $l\,\mathrm{d}x - wl\,\mathrm{d}x - v(1-w)l\,\mathrm{d}x = (1-v)(1-w)l\,\mathrm{d}x$ is in contact with the liquid.

But the liquid–solid interface is not a plane, unlike the vapor–liquid one; therefore, the geometrical factor $\widetilde{g}$ should be taken into account, and the area of this interface equals $\widetilde{g}(1-v)(1-w)l\,\mathrm{d}x$. Exactly the same area of solid–vapor interface disappears. After multiplying each surface by the corresponding surface tension coefficient, the variation of the energy per unit area is obtained as:

$$\mathrm{d}G = (w + v(1-w))\gamma + \widetilde{g}(1-v)(1-w)(\gamma_{SL} - \gamma_{SA}) + \gamma\cos\theta^* \,. \tag{6.4}$$

The latter term accounts for the increase in the upper liquid–air interface of the drop. From the minimum condition $\mathrm{d}G = 0$, we get on account of (6.4):

$$\cos\theta^* = (1-w)(\widetilde{g}(1-v)\cos\theta_Y - v) - w \,. \tag{6.5}$$

From simple trigonometry considerations:

$$v = 1 - \frac{2\pi R^2 \sin^2\theta_Y}{\sqrt{3}(2R+a)^2}\,; \quad \widetilde{g} = \frac{1}{\sin^2\theta_Y/2}\,,$$

where R is the radius of the balls constituting the smaller scale, and a is the shortest distance between their surfaces (Figure 6.5). For the convex balls' profile and an

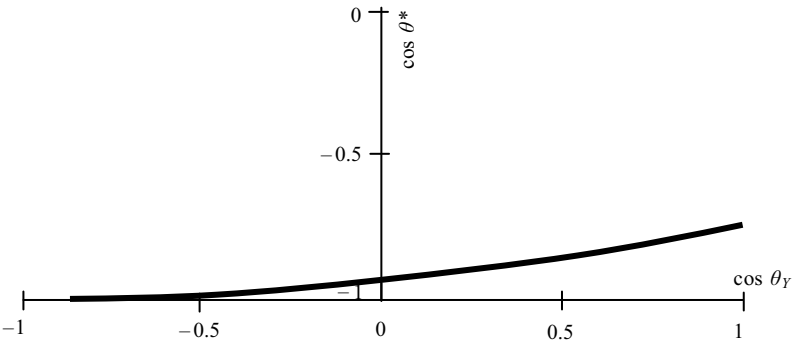

Fig. 6.6: Dependence of the apparent contact angle θ^* on the local one θ_Y, given by equation (6.5).

acute contact angle, θ_Y, the equilibrium of a liquid–air interface is possible if the latter descends below the equatorial plane of the spherical balls. The dependence of the apparent contact angle θ^* on the Young contact angle θ_Y for a certain hierarchical topography such as that depicted in Figure 6.5 was studied in Bormashenko et al. [5]. It should be stressed that this dependence, given by equation (6.5) and illustrated by Figure 6.6, is very weak. This prediction was verified experimentally with hierarchical reliefs based on polyvinylidene fluoride ($\theta_Y = 80^\circ$) and micrometrically scaled chromium balls ($\theta_Y = 30^\circ$) [5]. The Young angles varied drastically, but the apparent contact angles as experimentally established were close: $\theta^*_{PVDF} = 153^\circ$; $\theta^*_{chromium} = 141^\circ$ (see Bormashenko et al. [5]). This fact opens the way to the manufacturing of superhydrophobic surfaces based on inherently hydrophilic materials such as metals [5, 6, 16, 25]. It should also be mentioned that the surfaces of natural superhydrophobic objects, such as lotus leaves and bird wings, are built from hydrophilic or moderately hydrophobic tissues such as *cutin* and *keratin* [3, 17]. We conclude that hierarchical topography is crucial for constituting high apparent contact angles, and allow high apparent contact angles for surfaces built with inherently hydrophilic materials.

A variety of sophisticated technologies have been applied for manufacturing hierarchical micro- and nanoscaled superhydrophobic surfaces. For a review of these techniques, the reader should refer to Carre and Mittal, Ma and Hill, Nosonovsky and Bormashenko, and Roach et al. [7, 20, 22, 24].

6.5 Superoleophobicity

The design and manufacture of surfaces repelling organic oils is an important technological task. At the same time, it is an extremely challenging goal, because organic oils possess surface tensions significantly lower than that of water (see Table 1.1, Chapter 1). Thus, typical superhydrophobic surfaces demonstrate the Wenzel "sticky"

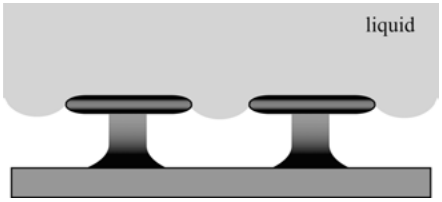

Fig. 6.7: "Hoodoo-like" elements supplying the surface with superoleophobic properties [27, 28].

wetting when an oil drop is put onto them. Several groups succeeded in solving this problem and reported oil-repellent surfaces [27, 28]. These surfaces comprise "hoodoo-like" elements, as depicted in Figure 6.7 [27, 28]. It should be mentioned that the physical mechanism of observed superoleophobicity remains obscure and calls for theoretical insights.

Aizenberg et al. proposed a witty approach to manufacturing superoleophobic surfaces, inspired by the *Nepenthes* pitcher plant, exploiting an intermediary liquid filling the grooves constituting a microrelief in the biological tissue [29]. Well-matched solid and liquid surface energies, combined with microtextural roughness, create a highly stable wetting state resulting in superoleophobicity [21, 29]. Aizenberg et al. applied perfluorinated fluids epoxy-resin and Teflon-based nanostructured reliefs to manufacture superoleophobic surfaces [29].

6.6 The rose petal effect

It was already mentioned in Section 6.2 that high apparent contact angles are necessary but not sufficient for true superhydrophobicity accompanied by self-cleaning properties of a surface. Jiang et al. reported that rose petal surfaces demonstrate high contact angles accompanied by extremely high contact angle hysteresis [11]. The surface of the rose petal is built from hierarchically riffled "micro-bumps" resembling those of lotus leaves [11]. At the same time, the wetting of rose petals is very different from that of lotus leaves. The apparent angles of droplets placed on a rose petal are high, but the droplets are simultaneously in a "sticky" wetting state; they do not roll [11]. Jiang et al. called this phenomenon the "rose petal effect" [11].

Later, very similar wetting behavior was revealed on surfaces built from *lycopodium* particles, shown in Figure 6.8 [4]. Lycopodium particles, which are spores of the plant *Lycopodium clavatum*, are microscopically scaled porous balls with an external diameter of 20–30 μm, and they are characterized by a pronounced hierarchical structure. Lycopodium particles comprise pores with a characteristic size of 3–5 μm, clearly recognized in Figure 6.8. Thus, according to the approach developed in Sections 6.3 and 6.4, these particles are expected to exemplify strong superhydrophobicity. Indeed, surfaces built from these particles demonstrate apparent contact angles as high as 150° (see Bormashenko et al. [4]). However, droplets deposited on these surfaces did not slide when the surface was tilted; moreover, they

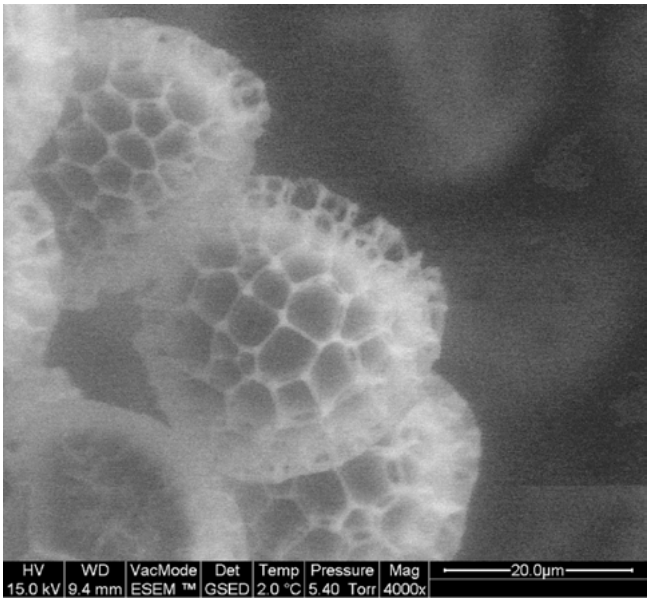

Fig. 6.8: Scanning electron microscopy image of lycopodium particles. The scale bar is 20 µm.

Fig. 6.9: A 10-µl droplet deposited on a surface built of lycopodium particles.

were steadily attached even when the surface was turned upside down, as depicted in Figure 6.9. Artificial surfaces demonstrating the "rose petal effect" have been also reported [23].

The natural explanation for the "rose petal effect" is supplied by the Wenzel model (see Section 5.2). Inherently hydrophobic flat surfaces may demonstrate apparent contact angles approaching π when rough. Wenzel wetting is characterized by high contact angle hysteresis; thus, the experimental situation depicted in Figure 6.9 becomes possible. However, the Wenzel model does not explain the existence of the "rose petal effect" for inherently hydrophilic surfaces. Bhushan and Nosonovsky demonstrated that wetting of hierarchical reliefs may be of a complicated nature, resulting in the "rose petal effect," as shown in Figure 6.10 [2]. Various wetting modes are possible for hierarchical reliefs: it is possible for a liquid to fill the larger grooves, whereas small-scale grooves are not wetted and trap air, as shown in Figure 6.10a. The inverse situation is also possible, in which small-scale grooves are wetted and large-scale ones

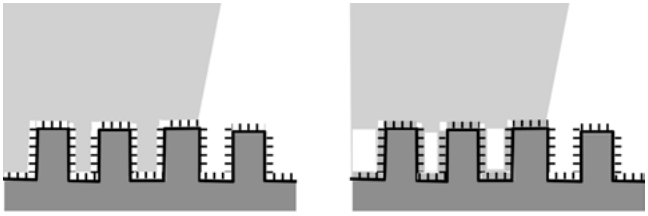

Fig. 6.10: Scheme of various wetting scenarios possible on a hierarchical relief [2].

form air cushions (Figure 6.10b). According to Bhushan and Nosonovsky [2], the larger structure controls the contact angle hysteresis, whereas the smaller (usually nanometric) scale is responsible for high contact angles [2, 4]. Thus, the relief depicted in Figure 6.10a demonstrates high contact angles attended by high contact angle hysteresis. This hypothesis reasonably explains the "rose petal effect." However, it is clearly seen that a broad variety of wetting modes is possible on hierarchical surfaces, opening the way to a diversity of technological applications of hierarchically rough surfaces.

6.7 Superhydrophilicity

As mentioned in Section 2.1, when the spreading parameter $\Psi = G^*_{SA} - (G^*_{SL} + G_{LA}) > 0$, the total wetting shown in Figure 2.1b is predicted. Metals and ceramics possessing high specific surface energies G^*_{SA} (see Section 1.7) are expected to be completely wetted. However, as shown in Section 3.3, even well-polished and thoroughly cleaned metallic surfaces rarely demonstrate complete wetting, because of the phenomenon of the pinning of the triple line, resulting in high contact hysteresis. The second fact affecting the spreading of liquids on these surfaces is the existence of thin layers of absorbed molecules of liquid, as discussed in detail in Section 2.6. Thus, manufacturing of surfaces demonstrating complete wetting turns out to be a challenging task.

It is also noteworthy that even the definition of superhydrophilicity remains controversial [9]. Drelich et al. defined superhydrophilic surfaces, as well as coatings, as rough (and sometimes porous) surfaces (coatings) of materials with a greater affinity to water than to nonpolar air. Water spreads completely on these rough surfaces [9]. The authors stressed that flat and smooth surfaces of hydrophilic materials, on which water spreads completely, do not belong to this category (even if hydrophilicity results from photoinduced or other cleaning) [9].

The Wenzel model (see Section 5.2) supplies the natural explanation for the complete spreading of liquids on rough, inherently hydrophilic surfaces. Various experimental techniques involving ZnO, SiO_2, and TiO_2 micro- and nanoparticles were applied successfully to manufacture superhydrophilic surfaces [12, 15, 18, 19]. Main applications of the effect of superhydrophilicity include the manufacture of antifogging surfaces and bioimplants [9].

Additional Reading

A review of the state of art of the phenomenon of superhydrophobicity and its industrial applications is supplied in Samaha et al. [32]. The recently revealed "underwater superoleophobicity," when oil droplets submerged in water demonstrate high apparent contact angles, is discussed in Li et al. [33].

Bullets

- Superhydrophobic (or "lotus-like") surfaces are characterized by high apparent contact angles, low contact angle hysteresis, and high stability of the Cassie air-trapping ("fakir") wetting state. When a superhydrophobic surface is tilted, a droplet slides from it easily.
- Superhydrophobic surfaces are usually hierarchical; they possess several topography scales. The hierarchy of scales increases the apparent contact angle in the Cassie wetting mode. The modified Cassie equation should be used for predicting apparent contact angles on hierarchical reliefs.
- Superhydrophobic surfaces may be built from inherently hydrophilic materials.
- When a drop of oil deposited on a surface demonstrates a high apparent contact angle, the surface is called superoleophobic.
- High apparent contact angles may be accompanied by high contact angle hysteresis. This situation is called the "rose petal effect." The "rose petal effect" may occur on hierarchical reliefs when large-scale grooves are filled by liquid, whereas small-scale details of the relief remain unwetted and trap air.
- When water spreads completely on a rough or porous surface, the surface is called superhydrophilic.

References

[1] W. Barthlott and C. Neinhuis, Purity of the sacred lotus, or escape from contamination in biological surfaces, *Planta* **202** (1997), 1–8.

[2] B. Bhushan and M. Nosonovsky, The rose petal effect and the modes of superhydrophobicity, *Philosophical Transactions of the Royal Society A* **368** (2010), 4713–4728.

[3] E. Bormashenko, Y. Bormashenko, T. Stein, and G. Whyman, Why do pigeon feathers repel water? Hydrophobicity of pennae, Cassie–Baxter wetting hypothesis and Cassie–Wenzel capillarity-induced wetting transition, *J. of Colloid & Interface Sci.* **311** (2007), 212–216.

[4] E. Bormashenko, T. Stein, R. Pogreb, and D. Aurbach, "Petal effect" on surfaces based on lycopodium: high stick surfaces demonstrating high apparent contact angles, *J. Phys. Chem. C* **113** (2009), 5568–5572.

[5] E. Bormashenko, T. Stein, G. Whyman, R. Pogreb, S. Sutobsky, Y. Danoch, Y. Shoham, Y. Bormashenko, B. Sorokov, and D. Aurbach, Superhydrophobic metallic surfaces and their wetting properties, *J. Adhesion Sci. & Technology*, **22** (2008), 379–385.

[6] E. Bormashenko, T. Stein, G. Whyman, Y. Bormashenko, and R. Pogreb, Wetting properties of the multiscaled nanostructured polymer and metallic superhydrophobic surfaces, *Langmuir* **22** (2006), 9982–9985.
[7] A. Carre, K. L. Mittal (eds.), *Superhydrophobic surfaces*, VSP, Leiden Boston, 2009.
[8] Y.-T. Cheng and D. E. Rodak, Is the lotus leaf superhydrophobic, *Applied Phys. Lett.* **86** (2005), 144101.
[9] J. Drelich, E. Chibowski, D. D. Meng, and K. Terpilowski, Hydrophilic and superhydrophilic surfaces and materials, *Soft Matter* **7** (2011), 9804–9828.
[10] X.-Q. Feng, X. Gao, Z. Wu, L. Jiang, and Q.-S. Zheng, Superior water repellency of water strider legs with hierarchical structures: experiments and analysis, *Langmuir* **23** (2007), 4892–4896.
[11] L. Feng, Y. Zhang, J. Xi, Y. Zhu, N. Wang, F. Xia, and L. Jiang, Petal effect: A superhydrophobic state with high adhesive force, *Langmuir*, 2008, **24**, 4114–4119.
[12] S. Ganjoo, R. Azimirad, O. Akhavan, and A. Z. Moshfegh, Persistent superhydrophilicity of sol–gel derived nanoporous silica thin films, *J. Phys. D: Appl. Phys.* **42** (2009), 025302.
[13] R. J. Good and M. N. Koo, The effect of drop size on contact angle, *J. Colloid & Interface Sci.* **71** (1979), 283–292.
[14] S. Herminghaus, Roughness-induced non-wetting, *Europhys. Lett.* **52** (2000), 165–170.
[15] Y. Horiuchi, K. Mori, N. Nishiyama, and H. Yamashita, Preparation of superhydrophilic mesoporous silica thin films containing single-site photocatalyst (Ti, V, Cr, Mo, and W oxide moieties), *Chem. Lett.* **7**, (2008), 748–749.
[16] A.-M. Kietzig, S. G. Hatzikiriakos, and P. Englezos, Patterned superhydrophobic metallic surfaces, *Langmuir* **25** (2009), 4821–4827.
[17] K. Koch, B. Bhushan, and W. Barthlott, Multifunctional surface structures of plants: an inspiration for biomimetics, *Progress in Materials Sci.* **54** (2009) 137–178.
[18] H. Liu, L. Feng, J. Zhai, L. Jiang, and D. B. Zhu, Reversible wettability of a chemical vapor deposition prepared ZnO film between superhydrophobicity and superhydrophilicity, *Langmuir* **20** (2004), 5659–5661.
[19] X. M. Liu and J. H. He, Superhydrophilic and antireflective properties of silica nanoparticle coatings fabricated via layer-by-layer assembly and postcalcination, *J. Phys. Chem. C* **113** (2009), 148–152.
[20] M. Ma and R. M. Hill, Superhydrophobic surfaces, *Current Opinion in Colloid & Interface Sci.* **11** (2006), 193–202.
[21] M. Nosonovsky, Materials Science: slippery when wetted, *Nature* **477** (2011), 412–413.
[22] M. Nosonovsky and E. Bormashenko, Lotus effect: superhydrophobicity and self-cleaning, in: E. A. Favret and N. O. Fuentes (eds.), *Functional properties of bio-inspired surfaces*, 43–78, World Scientific, 2009.
[23] Y. M. Park, M. Gang, Y. H. Seo, and B. H. Kim, Artificial petal surface based on hierarchical micro- and nanostructures, *Thin Solid Films* **520** (2011), 362–367.
[24] P. Roach, N. J. Shirtcliffe, and M. I. Newton, Progress in superhydrophobic surface development, *Soft Matter* **4** (2008), 224–240.
[25] N. J. Shirtcliffe, G. McHale, M. I. Newton, and C. C. Perry, Wetting and wetting transitions on copper-based super-hydrophobic surfaces, *Langmuir* **21** (2005), 937–943.
[26] T. Sun, L. Feng, X. Gao, and L. Jiang, Bioinspired surfaces with special wettability, *Acc. Chem. Res.* **38** (2005), 644–652.
[27] A. Tuteja, W. Choi, M. Ma, J. M. Mabry, S. A. Mazzella, G. C. Rutledge, G. H. McKinley, and R. E. Cohen, Designing superoleophobic surfaces, *Science* **318** (2007), 1618–1622.
[28] A. Tuteja, W. Choi, G. H. McKinley, R. E. Cohen, and M. F. Rubner, Design parameters for superhydrophobicity and superoleophobicity, *MRS Bulletin* **33** (2008), 752–758.

[29] T.-S. Wong, S. H. Kang, S. K. Y. Tang, E. J. Smythe, B. D. Hatton, A. Grinthal, and J. Aizenberg, Bioinspired self-repairing slippery surfaces with pressure-stable omniphobicity, *Nature* **477** (2011), 443–447.
[30] Y. Y. Yan, N. Gao, and W. Barthlott, Mimicking natural superhydrophobic surfaces and grasping the wetting process: a review on recent progress in preparing superhydrophobic surfaces, *Advances in Colloid & Interface Sci.* **169** (2011), 80–105.
[31] Y. Zheng, X. Gao, and L. Jiang, Directional adhesion of superhydrophobic butterfly wings, *Soft Matter* **3** (2007), 178–182.

Additional Reading

[32] M. A. Samaha, H. V. Tafreshi, and M. Gad-el-Hak, Superhydrophobic surfaces: from the lotus leaf to the submarine, *Comptes Rendus Mécanique* **340**, (2012), 18–34.
[33] J. Li, D. Li, Y. Yang, J. Li, F. Zha, and Z. Lei, A prewetting induced underwater superoleophobic or underoil (super) hydrophobic waste potato residue-coated mesh for selective efficient oil/water separation, *Green Chem.* **18**, (2016), 541–549.

7 Wetting transitions on rough surfaces

7.1 General remarks

We already discussed wetting transitions occurring on flat surfaces, which are temperature-induced transitions from partial wetting to complete wetting. This kind of transition is seen macroscopically as a jump of the contact angle from a certain finite value to zero (see Section 2.13). Wetting transitions taking place on rough surfaces are also attended by a change in an apparent contact angle. External factors such as pressure, vibrations or bouncing may promote a Cassie–Wenzel transition, accompanied by filling of the surface grooves with liquid, resulting in a change of the apparent contact angle. Obviously, the physical mechanisms of wetting transitions on flat versus rough surfaces are very different, and these transitions should be clearly distinguished.

As was shown in Section 3.8, when a droplet is deposited on a flat, chemically heterogeneous surface, its free energy demonstrates multiple minima separated by energetic barriers. These minima correspond to metastable states observable on the surface, characterized by various equilibrium apparent contact angles. The situation becomes even more complicated on rough surfaces, but generally the concept remains the same: a diversity of metastable states is possible for a droplet corresponding to a variety of equilibrium apparent contact angles (Figure 7.1). Passing from one metastable wetting state to another requires the energetic barrier to be surmounted. The origin of this barrier is discussed in this chapter in detail. The design of reliefs characterized by high barriers separating the Cassie and Wenzel states is crucial for manufacturing "truly superhydrophobic," self-cleaning surfaces. Thus, the considerations supplied in this chapter are of highly practical importance.

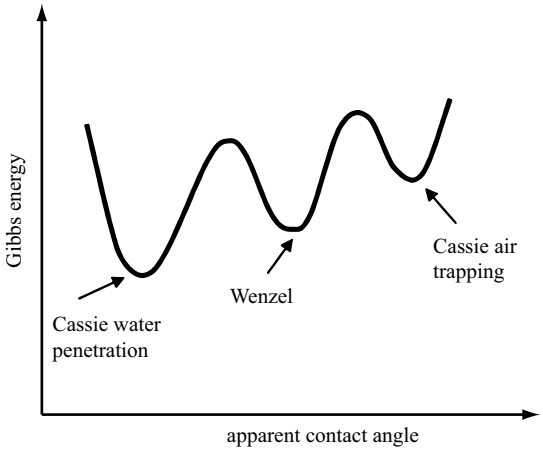

Fig. 7.1: Sketch of multiple minima of the Gibbs energy of a droplet deposited on a rough surface.

https://doi.org/10.1515/9783110583144-007

7.2 Wetting transitions on rough surfaces: experimental data

Consider the situation where a droplet deposited on a rough (not necessarily superhydrophobic) surface is in the Cassie air trapping wetting state (see Section 5.6). External factors imposed on a droplet may switch the wetting regime, and then the liquid fills the pores or grooves constituting the relief, i.e., promotes the wetting transitions. Wetting transitions were observed under various experimental techniques utilizing a diversity of factors: gravity [42], pressure [25], bouncing of droplets [4, 21, 22, 24, 30], evaporation of droplets [20, 27, 28], electric field in the electrowetting experiments [1, 2], and vibration of droplets [5, 7, 10, 12–15]. An interesting experimental technique allowing the study of an air layer responsible for the formation of the Cassie state was reported recently [37]. A superhydrophobic surface exposed to hydrostatic water pressure was irradiated by a laser beam. The jump in the reflectivity of the laser beam indicated the occurrence of a wetting transition. Reflection interference contrast microscopy was used for the study of the air–water interface on textured polydimethylsiloxane (PDMS) surfaces [28]. Environmental scanning electron microscopy (ESEM) technique was used successfully for the study of wetting transitions during microdroplet evaporation [30]. As was already discussed (see Section 3.10.3), ESEM imaging is extremely useful for visualization of the triple line.

It should be mentioned that various experimental methods used for the investigation of wetting transitions supplied the near values for the pressure necessary for the Cassie–Wenzel transition, which is on the order of magnitude of 100–300 Pa for 10-μl droplets deposited on micrometrically scaled rough surfaces [7, 10, 12, 14, 15, 25]. It is noteworthy that the Cassie air trapping wetting regime observed on natural objects (birds' wings) was much more stable compared with that of artificial surfaces [10]. This observation still calls for explanation. Single and two-stage pathways of wetting transitions were observed, including the Cassie (air-trapping)–Wenzel–Cassie (impregnating), Wenzel–Cassie (impregnating), and Cassie (air-trapping)–Cassie (impregnating) transitions (see Sections 5.2, 5.6, and 5.8) [10]. The lowest energy state usually corresponds to the Cassie impregnating wetting regime. A vibration-induced Cassie (air-trapping)–Cassie (impregnating) transition observed on PDMS substrate is illustrated in Figure 7.2.

Fig. 7.2: Wetting transitions observed by vibration of a 15-μl water drop deposited on a micrometrically rough polydimethylsiloxane surface. a: the initial Cassie state; a: the Cassie impregnating state induced by vibrations.

7.3 Time-scaling of wetting transitions

The mechanisms of wetting transitions on rough surfaces are not simple and involve a variety of factors; the design of a unified "umbrella" covering all factors is a challenging task. Let us start from time-scaling arguments. As already mentioned, wetting transitions were observed under evaporation, pressing, vibration, and bouncing of droplets [1, 2, 4, 5, 7, 10, 12–15, 20–22, 24, 25, 27, 28, 30, 42].

(a) *Pressuring droplets*. When a droplet deposited on a rough surface is exposed to external pressure, the characteristic time of the pressure change, τ, should be introduced. Pressuring a droplet causes a subsequent change in the apparent contact angle with the same characteristic time (owing to the phenomenon of contact angle hysteresis) [25]. This time, τ, has to be compared with the time of transitions, τ_{tr}. Actually, τ_{tr} is the time necessary for filling the texture with liquid, which definitely depends on the topography of the relief. As was established for microscopically scaled reliefs usually used for the study of wetting transitions, $\tau_{tr} \approx 2 \cdot 10^{-2}$ s [28]. Two experimental situations are possible, the first of which is a "quick" transition occurring when $\tau \gg \tau_{tr}$. In this case, the transition takes place under a constant apparent contact angle. The second case corresponds to slow transitions, when $\tau_{tr} \gtrsim \tau$, and the change of the apparent contact angle in the course of transition should be taken into account.

(b) *Evaporation of droplets*. The characteristic time of evaporation of a 10-µl droplet equals dozens of minutes, which is much larger than the characteristic time of transitions τ_{tr}. Thus, the transition occurring under evaporation of a droplet is a "quick" one.

(c) *Droplets are vibrated with a frequency, ν*. If the contact line is pinned under vibration, both the contact angle and the pressure in the drop vary with a characteristic time, $\tau \approx 1/\nu$. For the reported value of $\nu = 36$ Hz (see Bormashenko et al. [7, 14, 15]), $\tau \approx 10^{-2}$ s, and it is seen that $\tau \approx \tau_{tr}$. This is a most complicated situation, and the mechanism of the wetting transition is explained by lateral displacement of the three-phase (triple) line. The apparent contact angle changes in the course of transition.

(d) *Bouncing of droplets*. When droplets fall on a solid substrate, the characteristic time of the pressure and contact angle equilibration, τ, equals the so-called contact time. It was shown that τ is independent of the velocity of the bouncing droplet and depends strongly on its radius R [35]. It was also demonstrated that for droplets with a radius in the range 0.1–10 mm, τ varies from 0.5 to 100 ms [35]. Thus, it could be concluded that for bouncing droplets, various interrelations between τ and τ_{tr} are possible.

7.4 Origin of the barrier separating the Cassie and Wenzel wetting states: the case of hydrophobic surfaces

7.4.1 The composite wetting state

As mentioned in Section 7.1, the Cassie air trapping wetting state corresponds to the highest of multiple minima of Gibbs energy of a droplet deposited on a rough surface (with biological and hierarchical surfaces being exceptions). Thus, for the wetting transition, the energy barrier must be surmounted [3, 19, 31]. It was supposed that this energy barrier corresponds to the surface energy variation between the Cassie state and a hypothetical *composite* state, with the almost complete filling of surface asperities by water, as shown in Figure 7.3, keeping the liquid–air interface under the droplet and the contact angle constant. In contrast to the equilibrium mixed wetting state, shown in Figure 5.14 and discussed in Section 5.11, the composite state is unstable for hydrophobic surfaces and corresponds to an energy maximum (transition state). For the simple topography depicted in Figure 7.4, the energy barrier could be calculated as follows (see Bormashenko et al. [11]):

$$W_{\mathrm{tr}} = 2\pi a^2 \frac{h}{\tilde{l}}(\gamma_{\mathrm{SL}} - \gamma_{\mathrm{SA}}) = -2\pi a^2 \frac{h}{\tilde{l}}\gamma\cos\theta_{\mathrm{Y}}\,, \tag{7.1}$$

where h and $\tilde{l}$ are the geometric parameters of the relief, shown in Figure 7.4, and a is the radius of the contact area. The numerical estimation of the energetic barrier according to formula (7.1), with the parameters $\tilde{l} = h = 20\,\mu\mathrm{m}$, $a = 1\,\mathrm{mm}$, $\theta_{\mathrm{Y}} = 105^\circ$ (corresponding to low density polyethylene, LDPE), and $\gamma = 72\,\mathrm{mJ}\cdot\mathrm{m}^{-2}$ gives a value of $W_{\mathrm{tr}} = 120\,\mathrm{nJ}$. For $\theta_{\mathrm{Y}} = 114^\circ$ (corresponding to polytetrafluoroethylene), equation (7.1) yields $W_{\mathrm{tr}} = 180\,\mathrm{nJ}$. It should be stressed that according to equation (7.1), the energy barrier scales as $W_{\mathrm{tr}} \sim a^2$. The validity of this assumption is discussed below.

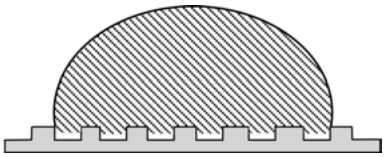

Fig. 7.3: The composite wetting state.

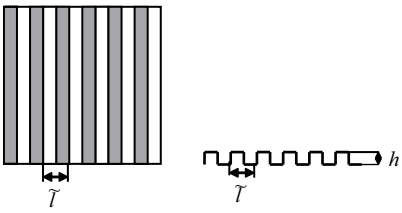

Fig. 7.4: Geometric parameters of the model relief used for the calculation of a Cassie–Wenzel transition energy barrier.

The energetic barrier is extremely large compared with thermal fluctuations

$$\frac{W_{\mathrm{tr}}}{k_{\mathrm{B}}T} \approx \left(\frac{a}{d_{\mathrm{m}}}\right)^2 \gg 1 \,,$$

where d_{m} is an atomic scale [19]. At the same time, W_{tr} is much less than the energy of evaporation of the droplet, $Q \approx (4/3)\pi R^3 \tilde{\lambda}$, where $\tilde{\lambda}$ is the volumetric heat of water evaporation ($\tilde{\lambda} = 2 \cdot 10^9\ \mathrm{J/m^3}$). For a 3-μl droplet with the radius $R \approx 1$ mm, it yields $Q \approx 10$ J; hence, $k_{\mathrm{B}}T \ll W_{\mathrm{tr}} \ll Q$. Actually, this interrelation between characteristic energies is what makes wetting transitions possible. If that were not the case, a droplet exposed to external stimuli might evaporate before the wetting transition [40]. It is instructive to estimate the radius at which $W_{\mathrm{tr}} \approx Q$. Equating W_{tr} given by equation (7.1) to Q yields $R \approx -(3/2)\gamma \cos\theta_{\mathrm{Y}}/\tilde{\lambda} \approx 5 \cdot 10^{-11}$ m. This means that wetting transitions are possible for any volume of a droplet. It is noteworthy that the ratio $\gamma/\tilde{\lambda}$ is practically the same for all liquids, and it is of the order of magnitude of molecular size d_{m} (see Section 1.2 and Bormashenko [6]). Hence, wetting transitions are possible for any liquid in any volume.

Now consider the situation depicted in Figure 7.5, describing a hierarchical relief built of posts possessing rough side facets. Obviously, these side facets increase the energetic barrier separating the Cassie and Wenzel states, owing to the increase in the hydrophobic surface to be wetted. If the additional-scale roughness of the side surface equals r_{s}, the energetic barrier to be surpassed by the droplet is given by:

$$W_{\mathrm{tr}} = -2r_{\mathrm{s}}\pi a^2 \gamma \frac{h}{\tilde{l}} \cos\theta_{\mathrm{Y}} \,. \tag{7.2}$$

It should be stressed that equation (7.2) implies Wenzel wetting of side surfaces of pillars when the roughness, r_{s} (defined as the ratio of the wetted surface to the projection area of a substrate), satisfies the inequality:

$$1 < r_{\mathrm{s}} < -\frac{1}{\cos\theta_{\mathrm{Y}}} \,.$$

As a result, the theoretical limit in the above example is $W_{tr,\max} = 2r_{\mathrm{s}}\pi a^2 \gamma h/\tilde{l}$, which increases the barrier estimation about 2.5 times for the above-mentioned angle of Teflon, $\theta_{\mathrm{Y}} = 114°$. We come to a very important conclusion: the hierarchical roughness of side surfaces of posts, constituting the relief, makes the Cassie air trapping

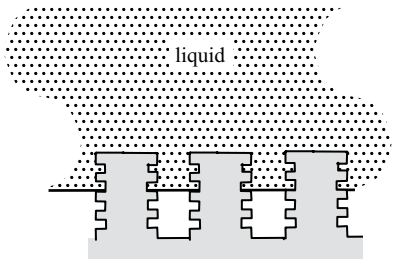

Fig. 7.5: Pillars possessing rough side facets.

state more stable. Nosonovsky and Bhushan demonstrated that curved hierarchical reliefs also provide stable equilibrium positions for the triple line [29].

7.4.2 Energy barriers and Cassie, Wenzel, and Young contact angles

It is well established experimentally that wetting transitions are usually irreversible. This conveys the suggestion that some general reasons for such irreversibility exist. It turns out that a variety of wetting states, in addition to transitions between them, may be described on the same mathematical basis that gives the possibility of elucidating their features that are independent of peculiarities of a particular substrate. Starting with the spherical model for the droplet shape, it can be shown that the surface-energy dependence, $G(\theta)$, on the (nonequilibrium) apparent contact angle, θ, looks like (see Whyman et al. [40, 41]):

$$G_{\mathrm{i}}(\cos\theta) = \left[\frac{9\pi V^2}{(1-\cos\theta)(2+\cos\theta)^2}\right]^{1/3} \gamma\,(2-\cos\theta_{\mathrm{i}}(1+\cos\theta))\ , \tag{7.3}$$

and its minimum G_{0i} is expressed as:

$$G_{0i} = \gamma[9\pi V^2(1-\cos\theta_{\mathrm{i}})^2(2+\cos\theta_{\mathrm{i}})]^{1/3}\ , \tag{7.4}$$

where V is the droplet volume and θ_{i} is the equilibrium apparent contact angle of a given wetting state. In particular, equation (7.4) supplies equilibrium energies in the Cassie (i = C) and Wenzel (i = W) states or in the wetting state on flat surfaces (i = Y, Young's angle $\theta_{\mathrm{i}} = \theta_{\mathrm{Y}}$) with the corresponding angles in equations (5.25), (5.8), and (2.11) respectively. Moreover, for a definite mechanism of transition, equations (7.3) and (7.4) supply the energies of the transition state (i = trans). For *hydrophobic* materials and orthogonal reliefs, it can be shown that the energy in the transition state is also expressed by expressions (7.3) and (7.4), with $\cos\theta_{\mathrm{trans}}$ given by (see Whyman and Bormashenko [40]):

$$\cos\theta_{\mathrm{trans}} = \cos\theta_{\mathrm{W}} + \cos\theta_{\mathrm{C}} - \cos\theta_{\mathrm{Y}}\ . \tag{7.5}$$

The mentioned mechanism of the Cassie–Wenzel transition is described as wetting the side surfaces of a hydrophobic relief accompanied by an energy increase [3]. A transition (composite) state corresponds to the almost complete filling of relief asperities. A transition barrier is overcome when liquid touches their bottoms, and the high-energy liquid–air interface under the droplet disappears.

Equations (7.3)–(7.5) enable the energy barrier of transition to be calculated by using the measured or calculated values of contact angles in the wetting states, without entering geometrical details of a substrate relief. In this way, for example, the results of the barrier calculation reported in Barbieri et al. [3] can be reproduced [40].

As mentioned in Section 7.3, wetting transitions may proceed quickly or slowly. Accordingly, two types of wetting transitions may proceed in principle: *adiabatic transitions* with a fixed value of the contact angle, and *slow nonadiabatic transitions* when a droplet has time to relax and the contact angle changes in the course of liquid penetration into depressions (or going out from them). Both these types of energy barriers can be calculated on the basis of the presented model, e.g., for the transition from the Cassie state to the Wenzel one, as:

$$W_{\mathrm{ad}} = G_{\mathrm{trans}}(\cos\theta_{\mathrm{C}}) - G_{0\mathrm{C}}\,, \quad W_{\mathrm{nonad}} = G_{0\mathrm{trans}} - G_{0\mathrm{C}}\,. \tag{7.6}$$

The irreversibility of wetting transitions is seen from peculiarities of the dependence given by expression (7.4) of the equilibrium surface energies on the equilibrium apparent contact angles (Figure 7.6). The function $G_{0i}(\cos\theta_{\mathrm{i}})$ is a monotonically decreasing one, with a weak dependence for low values of $\cos\theta_{\mathrm{i}}$ (~ -1) and a strong dependence on higher values. Furthermore, as can be proven, $\cos\theta_{\mathrm{trans}} < \cos\theta_{\mathrm{C}}$, and $\cos\theta_{\mathrm{trans}} < \cos\theta_{\mathrm{W}}$, i.e., $\cos\theta_{\mathrm{trans}}$ is located out of the interval between $\cos\theta_{\mathrm{C}}$ and $\cos\theta_{\mathrm{W}}$, closer to the lower limit. Consequently, the energy barrier is very asymmetrical, low from the side of the metastable (higher-energy) state and high from the side of the stable state, as shown in Figure 7.7. Calculations of real transition barriers based on expressions (7.4)–(7.6) give a difference of almost one order of magnitude [40]. Taking into account exponential (Arrhenius-type) dependence of the transition probability on the barrier height shows that a reverse transition is impossible. Remember that the arguments supplied in this paragraph are valid for inherently hydrophobic surfaces.

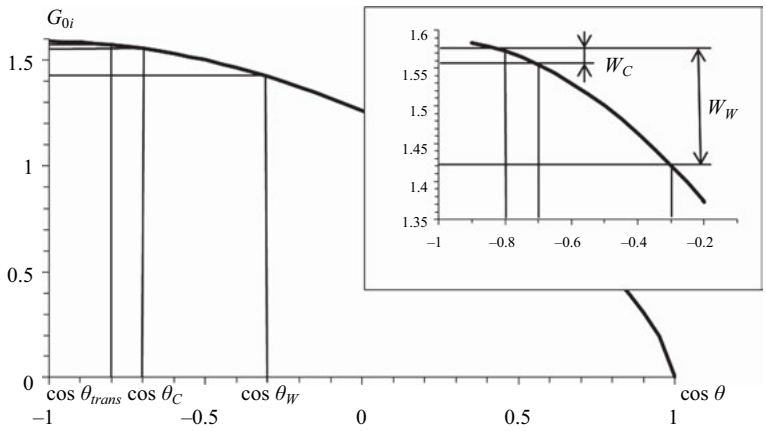

Fig. 7.6: Dependence (equation (7.3)) of the equilibrium surface energy (in units of $\gamma(9\pi V^2)^{1/3}$) on the equilibrium apparent contact angle and barriers of wetting transitions. Numerical values of apparent contact angles are 107.4° (Wenzel), 134.4° (Cassie), and 101.5° (Young). The transition state angle calculated in Whyman and Bormashenko [40] is 143.1°. The heights of the highly asymmetrical energy barrier for a water droplet of a volume of 3 µl are: from the side of the (metastable) Cassie state $W_{\mathrm{C}} = 8$ nJ, and from the side of the (stable) Wenzel state $W_{\mathrm{W}} = 70$ nJ.

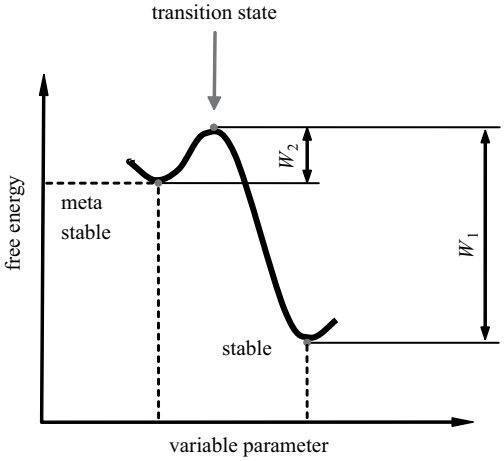

Fig. 7.7: Sketch illustrating the irreversibility of wetting transitions. W_1 is the energetic barrier from the side of the stable state, W_2 is the energetic barrier from the side of the metastable state, $\Delta W_1 \gg \Delta W_2$.

The origin of the energetic barrier for inherently *hydrophilic* surfaces is of a different nature and is discussed later.

7.5 Critical pressure necessary for wetting transition

As always in physics, both "energetic" and "force"-based approaches to the problem of wetting transitions on rough surfaces are possible. Now we develop the force (pressure)-based approach to the problem. Consider a single-scale pillar-based biomimetic surface, similar to that studied by Yoshimitsu with a pillar width b, and a groove width c [42]. Analysis of the balance of forces at the air–liquid interface, at which equilibrium is still possible, yields for the critical pressure p_c (see Zheng et al. [43]):

$$p_c > -\frac{\gamma f_s \cos\theta_Y}{(1-f_s)\lambda}\,, \tag{7.7}$$

where $\lambda = A/L$, A and L are the pillar cross-sectional area and perimeter respectively, and f_s is the fraction of the projection area that is wet (see Section 5.6).

As an application of equation (7.7) with $\theta = 114^\circ$ (Teflon), $b = 50\,\mu\text{m}$, $c = 100\,\mu\text{m}$, and $f_s = 1/9$, we obtain $p_c = 296\,\text{Pa}$, in excellent agreement with the experimental results [42, 43]. Recalling that the dynamic pressure of rain droplets may be as high as 10^4–10^5 Pa, which is much larger than $p_c \approx 300\,\text{Pa}$, we conclude that creating biomimetic reliefs with very high critical pressure is of practical importance [43]. The concept of critical pressure leads to the conclusion that reducing the microstructural scales (e.g., the pillars' diameters and spacing) is the most efficient measure for enlarging the critical pressure [28, 43].

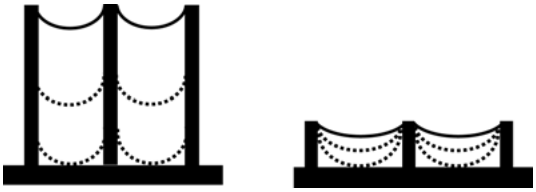

Fig. 7.8: Vertical "de-pinning" and "sag" types of wetting transitions.

Two different scenarios of wetting transitions are possible for pillar-based surfaces, as depicted in Figure 7.8. If the hanging liquid surface is such that it cannot remain pinned at the pillar tops, then it proceeds down the pillars and eventually wets the surface. Lack of pinning occurs if the contact angle formed by the liquid–air interface is greater than the maximum contact angle available for the specific liquid–pillar system [24, 26, 32]. This is the vertical de-pinning mechanism of the wetting transition. Even when a liquid–air interface can remain pinned at the pillar tops, transition to the Wenzel state is possible. This happens if the curved liquid–air interface is such that it touches the bottom of the roughness groove; this is the so-called "sag" transition [32].

7.6 Wetting transitions and de-pinning of the triple line; the dimension of a wetting transition

Not only vertical but also horizontal de-pinning of the triple line leading to a wetting transition is possible, as shown in Figure 7.9. Figure 7.9a depicts a wetting transition under a pinned triple line, whereas Figure 7.9b demonstrates the transition under a horizontally de-pinned triple line. Wetting transitions accompanied by the de-pinning of the triple line were observed under vibration and bouncing of droplets [7, 10, 12–15, 21, 22]. In this case, it is necessary not only to fill hydrophobic grooves of the surface (this gives rise to the potential barrier W_1, separating the Cassie and Wenzel states, dealt with in Section 7.4.1), but also to displace the triple line horizontally, as shown in Figure 7.9b. For the sake of simplicity, we suggest that this displacement might occur on a smooth horizontal portion of the relief.

Obviously, the mechanical work should be performed for such a displacement, giving rise to the additional energetic barrier W_2 (the units of both W_1 and W_2 are J, and they are related to the entire droplet, when $W_1 = S\widetilde{W}_1$, $W_2 = \overline{p}\widetilde{W}_2$, where S and $\overline{p}$ are area underneath the droplet filled by water and the perimeter of the triple line respectively, with the dimensions $[\widetilde{W}_1] = \mathrm{J/m^2}$, $[\widetilde{W}_2] = \mathrm{J/m}$). Hence, the resulting energetic barrier to be surmounted for the Cassie–Wenzel transitions equals:

$$W_{\mathrm{tr}} = W_1 + W_2 \,. \tag{7.8}$$

It could be supposed that $W_2 \ll W_1$, but we demonstrate that the situation is more complicated, and the interrelation between W_1 and W_2 depends on the topography of

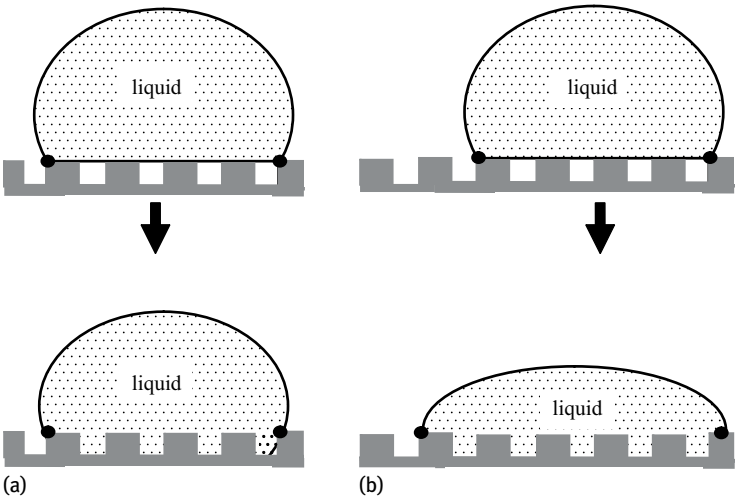

Fig. 7.9: Scheme of two scenarios of wetting transitions.

the relief [9]. The potential barrier W_2 originates from the intermolecular interactions between molecules of the liquid and the solid. Thus, calculation of W_2 is a challenging task. However, it *can* be measured, as demonstrated in Section 3.4. Study of the stick–slip motion of the triple line of evaporated droplets yielded for the energetic barrier related to the unit length of the triple line $\widetilde{W}_2 = W_2/2\pi a \cong 10^{-6}$ J/m (a is the radius of the contact area; see Section 3.4).

Now compare $W_2 = \overline{p}\widetilde{W}_2$ with W_1, i.e., the energy barrier originating from the filling of hydrophobic pores (grooves). The simple model of posts is used with dimensions of $b \times b \times h$ separated by grooves with a width b (Figure 7.10). The energy barrier W_1 equals the maximal change in surface energy when the liquid wets the walls of the posts, but does not yet touch the substrate bottom (Figure 7.10). The change in the surface energy when one "cell" is filled with liquid is:

$$\Delta W_{\text{cell}} = 4bh(\gamma_{\text{SL}} - \gamma_{\text{SA}}) = -4bh\gamma\cos\theta_{\text{Y}}\,, \tag{7.9}$$

where γ_{SL} and γ_{SA} are the surface tensions at the solid–liquid and solid–air interfaces respectively.

Now we have to answer a very important question: how many cells must be filled by the liquid to observe wetting transitions? The answer to this question dictates the *dimension of a wetting transition.* As shown in Section 5.9,the apparent contact angle is controlled by the area adjacent to the triple line. Thus, to observe wetting transitions, it is sufficient to fill "cells" located in the vicinity of the triple line. In this case, we observe the 1D scenario of a wetting transition (Figure 7.11a) [7]. The existence of a 1D mechanism for wetting transitions has been demonstrated experimentally in Bahadur and Garimella, and Bormashenko et al. [2, 7, 10, 12, 14, 15]. The 2D scenario requires

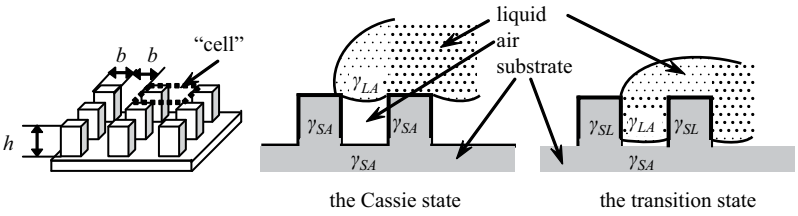

Fig. 7.10: Scheme illustrating the filling of grooves with liquid for the Cassie–Wenzel transition state. The transition state is immediately before the Wenzel (complete wetting) state. Adapted with permission from Bormashenko et al. [9]. Copyright 2012 American Chemical Society.

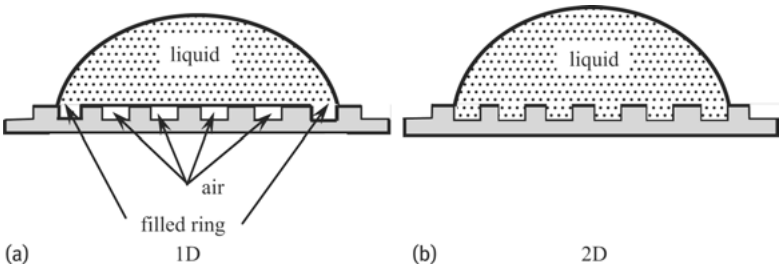

Fig. 7.11: Scheme illustrating a: 1D; b: 2D (B) scenarios of wetting transitions.

all the pores underneath the droplet to be filled (Figure 7.11b). Both possibilities are considered.

When only pores adjacent to the triple line (the circle in Figure 7.11a) are filled with liquid ("1D" transition), the number of "cells" to be filled is $N_1 = 2\pi a/2b = \pi a/b$. Therefore, the surface-energy change per droplet is expressed as:

$$W_1^{1D} = 4bh_{1D}(\gamma_{SL} - \gamma_{SA})N_1 = -4\pi h_{1D} a\gamma \cos\theta_Y \,. \tag{7.10}$$

If the whole surface beneath the droplet is filled ("2D" transition), the number of "cells" to be filled by liquid is $N_2 = \pi a^2/4b^2$, and:

$$W_1^{2D} = 4bh_{2D}(\gamma_{SL} - \gamma_{SA})N_2 = \frac{-\pi h_{2D} a^2 \gamma \cos\theta_Y}{b} \,. \tag{7.11}$$

Let us calculate the height of posts for which the surface component of the barrier W_1^{1D} is equal to the de-pinning energy of the triple line $W_1^{1D} = -4\pi h_{1D} a\gamma \cos\theta_Y = \pi a\widetilde{W}_2$. Assuming $\widetilde{W}_2 \approx 10^{-6}$ J/m, $\gamma = 72 \cdot 10^{-3}$ J/m^2, and $\cos\theta_Y = -0.34$, the following is obtained:

$$h_{1D} = -\frac{\widetilde{W}_2}{4\gamma \cos\theta_Y} \approx 10\,\mu\text{m} \,. \tag{7.12}$$

Similarly, for the 2D mechanism, $W_1^{2D} = -\pi h_{2D}\, a^2 \gamma \cos\theta_Y/b = \pi a\widetilde{W}_2$, and assuming $b \sim 10^{-5}$ m, $a \sim 10^{-3}$ m, we get:

$$h_{2D} = -\frac{\widetilde{W}_2 b}{a\gamma \cos\theta_Y} \approx 0.04\,\mu\text{m} \,. \tag{7.13}$$

It could be recognized that when only the pores nearest to the triple line are filled in the course of the wetting transition, the energy of filling pores and the energy of the triple line de-pinning are comparable at quite a reasonable post height: $h_{1D} \sim 10\,\mu m$, which is typical for superhydrophobic surfaces. Thus, in this case, the energy necessary for de-pinning of the triple line on a smooth portion of the relief is at least not negligible.

When $h \gg h_{1D}$, the energy barrier separating the Cassie and Wenzel state is determined by the energy of filling the pores (grooves); if $h \ll h_{1D}$, it is governed by the energy of de-pinning the triple line. The low value (equation (7.13)) of h_{2D} obtained for the 2D scenario shows that in this case, wetting transitions are governed by the filling of pores, not by the de-pinning of the triple line (if microstructured substrates are considered) [9].

It should be stressed that the pinning of the triple line is responsible for a variety of wetting phenomena observed on rough surfaces. In particular, owing to the effect of pinning, *the Cassie apparent contact angle is not the maximal* possible one observable on a rough surface [17]. A droplet that traps air in the Cassie wetting state could be inflated, and the advancing apparent contact angle becomes larger than the Cassie one [17]. De-pinning of the triple line was observed directly with the use of reflection interference contrast microscopy [28].

7.7 The experimental evidence for the 1D scenario of wetting transitions

The experiments carried out with vibrated drops deposited on porous substrates supported the 1D scenario of wetting transitions [7, 10, 12, 14, 15]. It has been established that the transition occurs when the condition $F_c = \text{const}$ is fulfilled, where F_c is the critical force acting on the unit length of the triple line, and the transition is caused by de-pinning of the triple line [7, 10, 12, 14, 15]. The critical value of the de-pinning force has been established experimentally for various microscopically structured surfaces as $F_c \approx 200\text{–}350\,mN \cdot m^{-1}$ [10]. The energy barrier W_{tr}^{1D} to be surmounted for the elementary displacement of the triple line δr could be estimated as:

$$W_{tr}^{1D} \approx 2\pi a F_c \delta r\,, \tag{7.14}$$

which scales as the contact radius a [11]. This scaling law corresponds to the results obtained with vibrated drops, but contradicts the scaling law given by expressions (7.1) and (7.2). The potential barrier calculated according to expression (7.14) for a drop with a contact radius of $a \approx 1\,mm$ deposited on the LDPE relief ($F_c \approx 350\,mN \cdot m^{-1}$, the elementary displacement $\delta r \approx \tilde{l}/2 \sim 10^{-5}\,m$) equals $W_{tr}^{1D} \approx 20\,nJ$, smaller than the value predicted by formula (7.1), but still much larger than thermal fluctuations (see Section 7.4.1 and Bormashenko [7]).

The electrowetting experiments (see Chapter 8 for an explanation of the phenomenon of electrowetting) also supported the 1D mechanism of transitions [2]. In contrast, it was suggested that the Cassie–Wenzel transition occurs via a nucleation mechanism

starting from the drop center [18]. A lack of trustworthy experimental data in the field should be stressed.

7.8 Wetting transitions on hydrophilic surfaces

Pronounced Cassie wetting accompanied by high apparent contact angles and low contact angle hysteresis has also been observed on inherently hydrophilic (metallic) surfaces [16, 23, 36].

It is easily seen that neither the "energy-rooted" equation (7.1) nor the "force-based" equation (7.7) explains the existence of Cassie wetting on inherently hydrophilic surfaces. Indeed, W_{tr} and p_c calculated according to equations (7.10) and (7.7) are negative for $\theta_Y < \pi/2$, which makes air trapping impossible on hydrophilic surfaces. Hence, the alternative physical reasoning explaining experimentally observed high apparent contact angles should be involved. Recall that the equilibrium contact angle θ_Y of superhydrophobic natural tissues, constituting lotus leaves and birds' wings, is acute (see Section 6.1). Moreover, birds' wings, which are built from inherently hydrophilic *keratin*, demonstrate extremely stable Cassie wetting [10]. Hence, new insights explaining pronounced Cassie wetting of hydrophilic materials are necessary.

7.8.1 Cassie wetting of inherently hydrophilic surfaces: criteria for gas entrapping

To explain the roughness-induced superhydrophobicity of inherently hydrophilic materials, it was supposed that air is entrapped by cavities constituting the topography of the surface [8, 33, 39]. The simple mechanism of "geometrical" trapping could be explained as follows: consider a hydrophilic surface ($\theta_A < \pi/2$, θ_A is the advancing contact angle, see Chapter 3) comprising pores, as depicted in Figure 7.12. It is seen that air trapping is possible only if $\theta_A > \varphi_0$, where φ_0 is the angle between the tangent at the highest point of the pattern and the horizontal symmetry axis is O_1O. Indeed, when the liquid level is descending, the actual angle θ grows (Figure 7.12), and if the condition $\theta_A > \varphi_0$ is violated, the equilibrium $\theta = \theta_A$ is impossible [8]. The phenomenon of contact angle hysteresis makes the variation of θ possible (see Chapter 3).

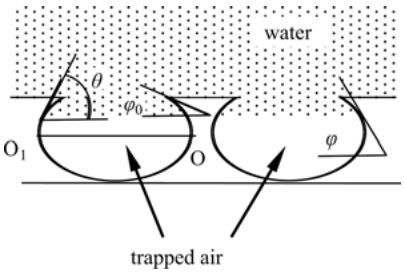

Fig. 7.12: Geometrical air trapping on hydrophilic reliefs.

In the equilibrium position, small fluctuations of the contact angle lead to the appearance of curvature on the plane air–water interface, which is energetically unfavorable. Below the central plane O–O_1, where $\theta > \pi/2$, the equilibrium is impossible in the case of $\theta_A < \pi/2$. Fluctuations of θ can lead to the curved air–liquid interface touching the pore bottom near its center, followed by filling the pore and the consequent collapse of the Cassie air trapping wetting regime. The effects of the compressibility of trapped air on wetting transitions on hydrophilic surfaces have also been considered by Patankar [33].

7.8.2 Origin of the energetic barrier separating Cassie and Wenzel wetting regimes on hydrophilic surfaces

What is the physical origin of the potential barrier separating Cassie and Wenzel states on hydrophilic surfaces? When the pore is hydrophilic it is energetically favorable to a liquid to wet it. But when a liquid fills a pore, as presented in Figure 7.12, the area of the liquid–air interface grows as this interface is descending. The increase in the energy of the liquid–air interface may overcompensate for the decrease in free energy due to the wetting of the hydrophilic walls of a pore; this gives rise to the energetic barrier separating the Cassie and Wenzel states.

To perform a quantitative analysis, consider a spherical model of the cavity, as drawn in Figure 7.13. The surface energy G of the cavity filled by liquid is expressed as:

$$G = 2\pi r^2 \gamma \cos\theta_Y (\cos\phi - \cos\phi_0) + \gamma\pi r^2 \sin^2\phi \,, \tag{7.15}$$

where the first and second terms are the energies of the liquid–solid and liquid–air interfaces respectively, and r is the cavity radius. The energy maximum corresponds to $\phi = \theta_Y$. Note that a central angle, ϕ which defines the liquid lEvel, is simultaneously a current contact angle. Thus, the energetic barrier per cavity, w, from the side of the Cassie state ($\phi = \phi_0$) is (under condition $\theta_Y > \phi_0$):

$$w = \gamma\pi r^2 (\cos\phi_0 - \cos\theta_Y)^2 \tag{7.16}$$

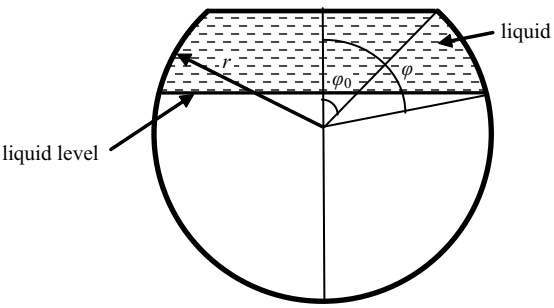

Fig. 7.13: Formation of a transition state in a spherical cavity.

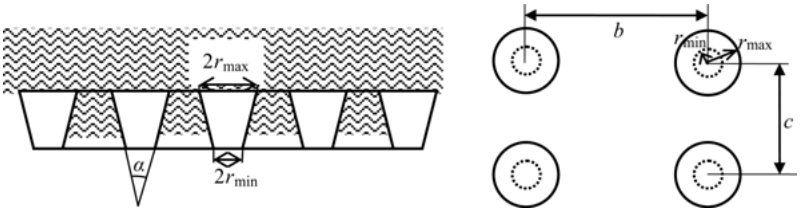

Fig. 7.14: Transition state for a hydrophilic relief of overturned truncated cones. b and c are the parameters of a rectangular two-dimensional lattice. The radius of the upper cone base is r_{max} and that of the bottom base is r_{min}; the opening angle of the cone is α.

The counterpart of w in equation (7.16) per one droplet can roughly be evaluated as $W \sim \pi r^2 \gamma N$, where $N \sim S/4r^2$ is the number of unit cells in the liquid–substrate interface area S for a plane quadratic close-packed lattice with a lattice constant $2r$. Thus, for a droplet with a contact radius $a \sim 1$ mm the upper limit is $W \sim \pi S\gamma/4 \sim 10^2$ nJ, which is of the same order of magnitude as the barrier inherent to microscopically scaled hydrophobic surfaces, as shown in Section 7.4.1.

The energy difference between the Cassie state and the Wenzel one ($\varphi = \pi$), given by:

$$G_C - G_W = \gamma\pi r^2(1 + \cos\phi_0)(1 - \cos\phi_0 + 2\cos\theta_Y) \tag{7.17}$$

is always positive for hydrophilic material. Consequently, the Cassie state is energetically unfavorable in this case, but it may be stabilized by a high energy barrier separating the Cassie and Wenzel wetting states.

Thus, the Cassie–Wenzel transition proceeds here in the following way. In the initial Cassie state, the cavity is completely filled by air. The spontaneous liquid penetration into the cavity does not take place because of the energy increase (under the condition $\theta_Y > \phi_0$; for the sake of simplicity, contact angle hysteresis is neglected). When some external factor (pressure, etc.) promotes liquid penetration into the cavity, the energy attains its maximum when the contact angle reaches the Young value $\phi = \theta_Y$. After that, liquid spontaneously fills the cavity with a large energy gain.

Another hydrophilic relief stabilizing the Cassie state, which presents a system of overturned truncated cones, is shown in Figure 7.14. The energy of varying interfaces is expressed as (per unit lattice cell):

$$G = \gamma(bc - \pi x^2) - \frac{\pi(r_{max}^2 - x^2)}{\sin(\alpha/2)}\gamma\cos\theta_Y\,, \tag{7.18}$$

where x is the current cone radius at the liquid level, r_{max} is the radius of the upper base of the cone, and α is the opening angle of the cone. The first and second terms correspond to the liquid–air and liquid–solid interfaces respectively. The energy increases monotonically as x decreases, and reaches its maximum at the minimal cone radius $x = r_{min}$. From equation (7.18), the barrier of the Cassie–Wenzel transition is:

$$\omega = \pi\left(r_{max}^2 - r_{min}^2\right)\gamma\,[1 - \cos\theta_Y/\sin(\alpha/2)]\,, \tag{7.19}$$

whereas the energy difference of the equilibrium Cassie and Wenzel states is determined independently as:

$$G_C - G_W = \gamma \left[(bc - \pi r_{max}^2)(1 + \cos\theta_Y) + \pi(r_{max}^2 - r_{min}^2)\cos\theta_Y \left(\frac{1}{\sin(\alpha/2)} + 1 \right) \right] . \tag{7.20}$$

The barrier exists, i.e., $w > 0$, if the opening angle, α, of the cones is sufficiently large:

$$\pi/2 - \alpha/2 < \theta_Y , \tag{7.21}$$

which simply means that the actual local contact angle, which equals $\pi/2 - \alpha/2$, must be less than the Young angle (Figure 7.14). This is possible because of the phenomenon of contact angle hysteresis. The minimal value of equation (7.20) corresponds to the minimal product bc, which is equal to $4r_{max}^2$ (from geometrical reasoning: $b = c = 2r_{max}$, Figure 7.14). As $4 > \pi$, it follows from equation (7.20) that the Cassie state is metastable ($G_C > G_W$), but the maximal possible energy barrier from the Cassie state side is higher here than that in the case of spherical cavities:

$$\omega_{max} = \pi r_{max}^2 \gamma (1 - \cos\theta_Y) \tag{7.22}$$

(compare equations (7.22) and (7.16)).

The Cassie–Wenzel transition for the present relief proceeds in a similar way to the preceding case with one difference: the energy maximum is reached just before the liquid touches the bottoms of the relief, not at an intermediate liquid level, as with the relief of the spherical cavities.

It should be mentioned that the proposed mechanism of wetting transitions remains valid for hydrophobic surfaces (see Section 7.4.1). This means that the energy increase, due to the growth of the liquid–air interface in the course of liquid penetration into pores or grooves constituting the relief, enhances the total energy barrier separating the Cassie and Wenzel states. It is reasonable to suggest that the energetic barrier arising from the rapid increase in the liquid–air interface explains the superoleophobicity of the "hoodoo-like" surfaces discussed in Section 6.5 and depicted in Figure 6.7.

7.8.3 Surfaces built of ensembles of balls

An instructive example is presented by a surface built of a system of balls resembling the lotus surface [16]. The surface energy of the model system, shown in Figure 7.15 is given by:

$$G = \gamma bc - \pi r^2 \gamma [\sin^2\phi + 2(1 - \cos\phi)\cos\theta_Y] \tag{7.23}$$

which has a local minimum at $\phi = \pi - \theta_Y$. This means that the Cassie state is characterized here by the liquid penetration below the balls' equators (and, in the case of a moderate hydrophilicity, close to them) [42]. The maximal value of the energy in

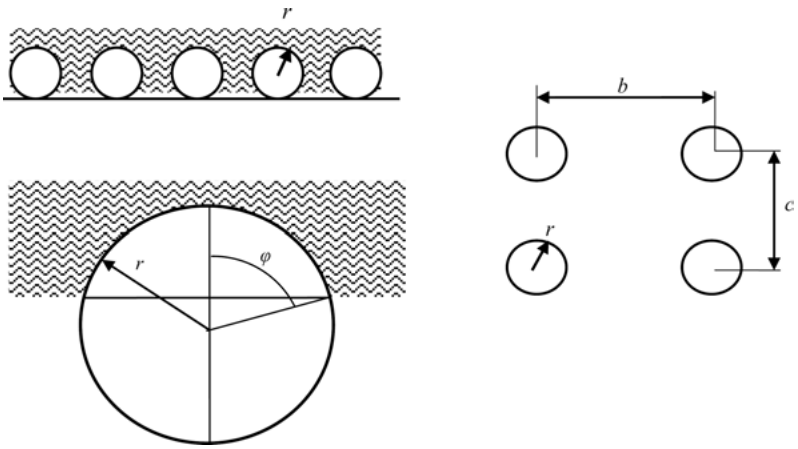

Fig. 7.15: Transition state for a relief comprising balls; b and c are the parameters of a rectangular two-dimensional lattice.

equation (7.23) is attained for $\phi = \pi$, i.e., when liquid completely fills the cavities (but does not touch the relief bottoms). Thus, the barrier is:

$$\omega = \pi r^2 \gamma (1 - \cos\theta_Y)^2 \,. \tag{7.24}$$

The difference between the energies of the Cassie and Wenzel states is:

$$G_C - G_W = \gamma bc(1 + \cos\theta_Y) - \pi r^2 \gamma (1 - \cos\theta_Y)^2 \,. \tag{7.25}$$

The Cassie state is thermodynamically favorable when:

$$G_C < G_W \,, \tag{7.26}$$

or in other words

$$\tan^2 \frac{\theta_Y}{2} > \frac{bc}{4\pi r^2} \left[1 + \sqrt{1 + \frac{8\pi r^2}{bc}} \right] \,. \tag{7.27}$$

For the close-packed quadratic lattice $b = c = 2r$, correspondingly

$$\theta_Y > 94.7^\circ \,. \tag{7.28}$$

This is in accordance with the general conclusion that on hydrophilic surfaces the Cassie state is thermodynamically unfavorable. For the discussed relief, the stability of this state may be due a weak hydrophobicity according to equation (7.28)) or due to the energy barrier given by expression (7.24) separating the Cassie and Wenzel states. The barrier given by expression (7.24) is maximal for $\theta_Y = \pi$; however, the largest known Young angle is 114°, registered for polytetrafluoroethylene. It is also seen that the barrier becomes sufficiently large starting from angles close to $\pi/2$. This explains

the pronounced superhydrophobicity of reliefs based on nanoscaled polyvinylidene-fluoride balls ($\theta_Y = 85^\circ$) and, perhaps, that of the lotus leaves as well [16].

The order of magnitude of the barrier W_{tr} for a droplet with a contact area S may be evaluated as $W_{tr} = \gamma\pi r^2 N$, where $N = S/(bc) \sim S/4r^2$ is the number of unit cells in the area S. Thus, for a droplet of a 1-mm contact radius the barrier $W_{tr} \sim S\gamma\pi/4 \approx 200$ nJ is close to the barriers calculated in Sections 7.4.1 and 7.8.2.

The question is: what is the quantitative parameter describing the stability of the "fakir" state? Is it w, related to filling a single pore? Or is it perhaps W_{tr}, related to the entire droplet? It could be seen that the energy barrier W_{tr} is of the order of magnitude of γS, and that it is independent of the microtopography of the hydrophilic relief. However, the final results for the unit–cell barrier, w, given by expressions (7.16), (7.22), and (7.24), differ for various topographies and depend on the geometric parameters of a relief. The answer depends on the 1D or 2D scenario of the transition discussed in Sections 7.6 and 7.7 and illustrated in Figure 7.11. If a transition occurs according to the 1D scenario, depicted in Figure 7.11a, the surface unit cell-related barrier, w, defines the stability of the Cassie wetting. If wetting transitions imply simultaneous filling of all pores (the 2D scenario, shown in Figure 7.11b), then W_{tr}, related to a whole droplet, adequately describes the stability of the "fakir" wetting. Of course, the time scaling and pressure-related arguments developed in Sections 7.3 and 7.5 should be considered as well.

7.9 Mechanisms of wetting transitions: the dynamics

The experimental data related to the dynamics of wetting transitions are scanty [28, 34, 38]. The characteristic time of a Cassie–Wenzel transition (i.e., the time necessary for filling microscopically scaled grooves) was established by reflection interference contrast microscopy as less than 20 ms [28]. The dynamics of wetting transitions for droplets placed on polymer micrometer-sized square pillars was studied by optical microscopy in combination with high-speed imaging [34]. Two regimes of droplet front displacement were observed: zipping and nonzipping. In the zipping regime, the front velocity in one direction (to advance to the next row of pillars) is much smaller than the velocity in the other direction (liquid filling up one row of micropillars). The topography of the surface (pillar height and gap size between pillars) and water contact angle were varied. It was established that the velocity of the wetting front increases with increasing gap size, decreasing pillar height, or decreasing contact angle [34]. A velocity of the wetting front as high as 1.5 m/s was registered [34]. Balancing interfacial energy contributions with viscous dissipation yielded universal equations for the zipping and transition dynamics [34]. It should be stressed that the eventual stage of the transition is not necessarily the Wenzel state; it may be the Cassie impregnating state, discussed in Section 5.8.

To conclude, we state that in spite of intensive theoretical and experimental efforts expended for the study of wetting transitions, the physical mechanisms of these phenomena remain unclear, and new physical insights are necessary to clarify these mechanisms.

Additional Reading

As mentioned in Section 7.4.2 the Cassie–Wenzel wetting transitions are regarded as irreversible. However the existence of a "mono-stable" region in the phase space of surface chemistry and roughness, where transitions from Cassie to (impaled) Wenzel states became spontaneously reversible, was demonstrated experimentally in Li et al. [44]. This result is of primary importance for the development of superhydrophobic and superoleophobic materials.

Bullets

- An abrupt change in an apparent contact angle observed on a rough surface is called a "wetting transition."
- Wetting transitions on rough surfaces may be promoted by bouncing, evaporation, pressing or the vibration of droplets.
- Various pathways of wetting transitions are possible, including the Cassie (air trapping)–Wenzel, and the Cassie (air trapping)–Cassie impregnating states.
- Time-scaling arguments are important for understanding wetting transitions: "quick" and "slow" transitions are possible.
- An energy barrier separates the Cassie and Wenzel wetting states on both hydrophobic and hydrophilic surfaces; however, the physical origin of these barriers on hydrophobic versus hydrophilic surfaces is different.
- The energy barrier separating the Cassie and Wenzel wetting states on hydrophobic surfaces is due to energy growth when hydrophobic grooves of the surfaces are wetted by liquid.
- On hydrophilic surfaces, the energy barrier arises from the increase in the liquid–air interface when the pore is filled.
- The energy barrier is extremely large compared with thermal fluctuations, and is much less than the evaporation energy of the droplet.
- 1D (only pores adjacent to the triple line) and 2D scenarios of wetting transitions on rough surfaces are possible.

References

[1] V. Bahadur and S. V. Garimella, Electrowetting-based control of droplet transition and morphology on artificially microstructured surfaces, *Langmuir* **24** (2008), 8338–8345.

[2] V. Bahadur and S. V. Garimella, 1D Preventing the Cassie–Wenzel Transition Using Surfaces with Noncommunicating Roughness Elements. *Langmuir* **25** (2009), 4815–4820.

[3] L. Barbieri, E. Wagner, and P. Hoffmann, Water wetting transition parameters of perfluorinated substrates with periodically distributed flat-top microscale obstacles, *Langmuir* **23** (2007), 1723–1734.

[4] D. Bartolo, F. Bouamrirene, E. Verneuil, A. Buguin, B. Silberzan, and S. Moulinet, Bouncing of sticky droplets: Impalement transitions on superhydrophobic micropatterned surfaces, *Europhys. Lett*. **74** (2006), 299–305.

[5] J. B. Boreyko and C.-H. Chen, Restoring superhydrophobicity of Lotus leaves with vibration-induced dewetting, *Phys. Rev. Lett.* **103** (2009), 174502.

[6] E. Bormashenko, Why are the values of the surface tension of most organic liquids similar? *Am. J. Phys*. **78** (2010), 1309–1311.

[7] E. Bormashenko, Wetting transitions on biomimetic surfaces, *Philosophical Transactions of the Royal Society A* **365** (2010), 4695–4711.

[8] E. Bormashenko, Y. Bormashenko, G. Whyman, R. Pogreb, and O. Stanevsky, Micrometrically scaled textured metallic hydrophobic interfaces validate the Cassie–Baxter wetting hypothesis, *J. Colloid & Interface Sci.* **302** (2006), 308–311.

[9] E. Bormashenko, A. Musin, G. Whyman, and M. Zinigrad, Wetting transitions and depinning of the triple line, *Langmuir* **28** (2012), 3460–3464.

[10] E. Bormashenko, R. Pogreb, T. Stein, G. Whyman, M. Erlich, A. Musin, V. Machavariani, and D. Aurbach, Characterization of rough surfaces with vibrated drops, *Phys. Chem. Chem. Phys.* **27** (2008), 4056–4060.

[11] E. Bormashenko, R. Pogreb, and G. Whyman, Comment on: Water wetting transition parameters of perfluorinated substrates with periodically distributed flat-top microscale obstacles *Langmuir* **25** (2009), 13,694–13,695.

[12] E. Bormashenko, R. Pogreb, G. Whyman, S. Balter, and D. Aurbach, Wetting transitions on post-built and porous reliefs, *J. Adhesion Sci. & Technology* **26** (2012), 1169–1180.

[13] E. Bormashenko, R. Pogreb, G. Whyman, and M. Erlich, Vibration-induced Cassie–Wenzel wetting transition on rough surfaces, *Appl. Phys. Lett.* **90** (2007), 201917.

[14] E. Bormashenko, R. Pogreb, G. Whyman, and M. Erlich, Cassie–Wenzel wetting transition in vibrating drops deposited on rough surfaces: Is dynamic Cassie–Wenzel wetting transition a 2D or 1D affair? *Langmuir* **23** (2007), 6501–6503.

[15] E. Bormashenko, R. Pogreb, G. Whyman, and M. Erlich, Resonance Cassie–Wenzel wetting transition for horizontally vibrated drops deposited on a rough surface, *Langmuir* **23** (2007), 12,217–12,221.

[16] E. Bormashenko, T. Stein, G. Whyman, Y. Bormashenko, and R. Pogreb, Wetting properties of the multiscaled nanostructured polymer and metallic superhydrophobic surfaces, *Langmuir* **22** (2006), 9982–9985.

[17] B. He, J. Lee, and N. A. Patankar, Contact angle hysteresis on rough hydrophobic surfaces, *Colloids and Surfaces A* **248** (2004), 101–104.

[18] C. Ishino and K. Okumura, Nucleation scenarios for wetting transition on textured surfaces: The effect of contact angle hysteresis. *Europhys. Lett.* **76** (2006), 464–470.

[19] C. Ishino, K. Okumura, D. Quéré, Wetting transitions on rough surfaces, *Europhys. Lett*. **68** (2004), 419–425.

[20] Y. C. Jung and B. Bhushan, Wetting transition of water droplets on superhydrophobic patterned surfaces, *Scripta Materialia* **57**, (2007), 1057–1060.
[21] Y. C. Jung and B. Bhushan, Dynamic effects of bouncing water droplets on superhydrophobic surfaces, *Langmuir* **24** (2008), 6262–6269.
[22] Y. C. Jung and B. Bhushan Dynamic effects induced transition of droplets on biomimetic superhydrophobic surfaces, *Langmuir* **25** (2009), 9208–9218.
[23] A.-M. Kietzig, S. G. Hatzikiriakos, and P. Englezos, Patterned superhydrophobic metallic surfaces, *Langmuir* **25** (2009), 4821–4827.
[24] D. H. Kwon and S. J. Lee, Impact and wetting behaviors of impinging microdroplets on superhydrophobic textured surfaces, *Appl. Phys. Lett*. **100** (2012), 171601.
[25] A. Lafuma and D. Quéré, Superhydrophobic states, *Nature Materials* **2** (2003), 457–460.
[26] B. Liu and F. Lange, Pressure induced transition between superhydrophobic states: Configuration diagrams and effects of surface feature size, *J. Colloid & Interface Sci*. **298** (2006), 899–909.
[27] G. McHale, S. Aqil, N. J. Shirtcliffe, G. M. I. Newton, and H. Y. Erbil, Analysis of droplet evaporation on a superhydrophobic surface, *Langmuir* **21** (2005), 11,053–11,060.
[28] S. Moulinet and D. Bartolo, Life and death of a fakir droplet: Impalement transitions on superhydrophobic surfaces, *European Phys. J. E* **24** (2007), 251–260.
[29] M. Nosonovsky and B. Bhushan, Hierarchical roughness makes superhydrophobic states stable, *Microelectronic Engineering* **84** (2007), 382–386.
[30] M. Nosonovsky and B. Bhushan, Patterned nonadhesive surfaces: superhydrophobicity and wetting regime transitions, *Langmuir* **24** (2008), 1525–1533.
[31] N. A. Patankar, Transition between superhydrophobic states on rough surfaces, *Langmuir* **20** (2004), 7097–7102.
[32] N. A. Patankar, Consolidation of Hydrophobic Transition Criteria by Using an Approximate Energy Minimization Approach, *Langmuir* **26** (2010), 8941–8945
[33] N. A. Patankar, Hydrophobicity of surfaces with cavities: making hydrophobic substrates from hydrophilic materials? *J. Adhes. Sci. & Technol*. **23** (2009), 413–433.
[34] A. M. Peters, C. Pirat, M. Sbragaglia, B. M. Borkent, M. Wessling, D. Lohse, and R. G. H. Lammertink, Cassie–Baxter to Wenzel state wetting transition: Scaling of the front velocity, *Eur. Phys. J.* **29** (2009), 391–397.
[35] D. Richard, C. Clanet, and D. Quéré, Contacting time of a bouncing droplet, *Nature* **417** (2002), 811–812.
[36] A. Safaee, D. K. Sarkar, and M. Farzaneh, Superhydrophobic properties of silver-coated films on copper surface by galvanic exchange reaction, *Appl. Surf. Sci*. **254** (2008), 2493–2498.
[37] M. Sakai, T. Yanagisawa, A. Nakajima, Y. Kameshima, and K. Okada, Effect of surface structure on the sustainability of an air layer on superhydrophobic coatings in a water–ethanol mixture. *Langmuir* **25** (2009), 13–16.
[38] M. Sbragaglia, A. M. Peters, C. Pirat, B. M. Borkent, R. G. H. Lammertink, M. Wessling, and D. Lohse, Spontaneous breakdown of superhydrophobicity, *Phys. Rev. Lett*. **99** (2007), 156001.43.
[39] J. Wang and D. Chen, Criteria for entrapped gas under a drop on an ultrahydrophobic surface, *Langmuir* **24** (2008), 10,174–10,180.
[40] G. Whyman and E. Bormashenko, Wetting transitions on rough substrates: general considerations, *J. Adhes. Sci. & Technol*. **26** (2012), 207–220.
[41] G. Whyman, E. Bormashenko, and T. Stein, The rigorous derivation of Young, Cassie–Baxter and Wenzel equations and the analysis of the contact angle hysteresis phenomenon. *Chemical Physics Letters* **450** (2008), 355–359.

[42] Z. Yoshimitsu, A. Nakajima, T. Watanabe, and K. Hashimoto, Effects of surface structure on the hydrophobicity and sliding behavior of water droplets, *Langmuir* **18** (2002), 5818–5822.
[43] Q.-S. Zheng, Y. Yu, and Z.-H. Zhao, Effects of hydraulic pressure on the stability and transition of wetting modes of superhydrophobic surfaces, *Langmuir* **21** (2005), 12,207–12,212.

Additional Reading

[44] Y. Li, D. Quéré, C. Lv, and Q. Zheng, Monostable superrepellent materials, *PNAS* **114**(13) (2017) 3387–3392.

8 Electrowetting and wetting in the presence of external fields

8.1 General remarks

We have demonstrated that equilibrium contact angles are independent of external fields when all interfacial tensions are independent of these fields. This is true for flat and rough, chemically homogeneous and heterogeneous surfaces (see Sections 2.2, 5.2, and 5.4). The statement likewise stands for curved surfaces (see Sections 2.3, 5.3, and 5.7). Even considering line tension, this general statement remains valid (see Sections 2.4 and 5.12).

However, in principle it is possible for interfacial tensions to be field-dependent. The impact of these dependencies on apparent contact angles is dealt with in this chapter.

8.2 Electrowetting

The most important possibility for controlling interfacial tension with external fields occurs under electrowetting. Lippmann revealed that interfacial tension of a mercury/water system changes as one applies a voltage $\hat{U}$ to mercury [3, 6]. Since then, similar phenomena were revealed for various solid surface/electrolyte systems [8]. From a practical point of view, it is important that water or aqueous solutions can be used as the electrolyte [10]. A typical scheme of an electrowetting experiment is given in Figure 8.1. When an aqueous electrolyte contacts a solid surface a double electrical layer (shown in Figure 8.1) is formed [1]. The double layer works as a capacitor; thus, the effective energy of the solid/liquid interface may be written as:

$$\gamma_{SL} = \gamma_{SL}^{0} - \frac{1}{2}\tilde{C}\hat{U}^2 \,, \tag{8.1}$$

where γ_{SL}^{0} represents the solid–liquid interface tension at zero voltage, $\tilde{C}$ is the specific capacitance of the double layer $[\tilde{C}] = \Phi/m^2$, and $\hat{U}$ is the voltage. Substitution of expression (8.1) into the Young formula, $\cos\theta = (\gamma_{SA} - \gamma_{SL})/\gamma$, yields for the elec-

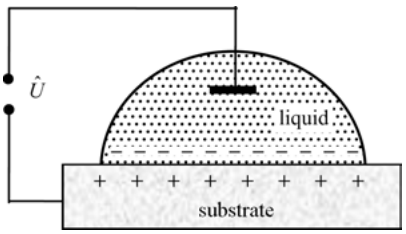

Fig. 8.1: Typical scheme of an electrowetting experiment.

https://doi.org/10.1515/9783110583144-008

trowetting a contact angle θ_{el}:

$$\cos\theta_{el} = \frac{\gamma_{SA} - \gamma^0_{SL} + \frac{\tilde{C}\hat{U}^2}{2}}{\gamma} = \cos\theta_Y - \frac{1}{2\gamma}\tilde{C}\hat{U}^2 \,. \tag{8.2a}$$

Formula (8.2) is the well-known Lippmann formula predicting the dependence of the contact angle on applied voltage.

When the capacitance of the double layer is heterogeneous (in other words we have a gradient surface addressed in Section 5.10; of course, not only surface tensions but the specific capacity of the double layer may be heterogeneous) we easily obtain the modified Lippmann equation. Consider the axisymmetric situation, when $C = C(r)$ takes place, where C is the capacitance of the double layer ($[C] = \Phi$). In this case we derive:

$$\cos\theta_{el} = cos\theta_Y - \frac{\hat{U}^2}{4\pi a\gamma}\left(\frac{\partial C}{\partial r}\right)_{r=a} \,, \tag{8.2b}$$

where a is the radius of the contact line (Figure 8.1). It is seen from equation (8.2b) that the gradient of the capacity of the double layer governs the apparent contact angle of the electrowetting (compare with equations (5.41a) and (5.41b)); thus, illustrating the principle of locality: equilibrium contact angles are dictated by physical events occurring in the vicinity of the triple (three-phase) line.

8.3 Wetting in the presence of external fields: a general case

Consider the general situation, where interfacial tensions depend on external fields [5, 9]. Consider the most general case treated in Section 5.12, where a droplet is placed on a rough surface and the mixed wetting regime depicted in Figure 5.15 occurs. We also suggest that the effects related to the line tension (see Section 2.4) are not negligible. All interfacial tensions (with the exception of line tension) are assumed to be field-dependent for the sake of generality. We assume that the interfacial tensions could be expressed as explicit functions of the coordinates (the frame of the axis, shown in Figure 5.15, is used):

$$\gamma = \gamma(x, y) \,, \quad \gamma_{SL} = \gamma_{SL}(x, y) \,, \quad \gamma_{SA} = \gamma_{SA}(x, y) \,. \tag{8.3}$$

The types of these functions are governed by the spatial distribution of the external field and are also supposed to be known. The free energy G of the axially symmetrical droplet with a contact radius a exposed to the axially symmetrical field $U(h, x)$ is given by:

$$G = \int_0^a \Big[\gamma(x,h)2\pi x\sqrt{1+h'^2} + 2\pi x\left(\gamma_{SL}(x,0) - \gamma_{SA}(x,0)\right)\tilde{r}f_S + 2\pi x\gamma(x,0)(1-f_S) + 2\pi\Gamma + 2\pi x\Gamma\xi + U(h,x)\Big]\,\mathrm{d}x \,, \tag{8.4}$$

where f_S is the fraction of the solid surface that is wetted by the liquid, $\tilde{r}$ is the dimensionless roughness ratio of the wetted area, and ξ is the perimeter of the triple line per unit area of the substrate under the droplet (with the dimension of m^{-1}; see Section 5.12). Considering a constant volume for the droplet and the transversality condition at the endpoints a, $-a$ given by equation (5.5) yield the general equation predicting an apparent contact angle, θ^*, in the presence of external fields (for details see Bormashenko [2])

$$\cos\theta^* = \frac{\gamma_{SA}(a,0) - \gamma_{SL}(a,0)}{\gamma(a,0)}\tilde{r}f_S + f_S - 1 - \frac{\Gamma}{\gamma(a,0)}\left(\xi + \frac{1}{a}\right). \tag{8.5}$$

It can be recognized that only the values of interfacial tensions at the endpoints (in other words at the triple line) govern the contact angle. It is also noteworthy that the apparent contact angle, θ^*, does not *explicitly* depend on the linear density of the external field $U(h,x)$; however, the external field dictates the types of $\gamma = \gamma(x,0)$, $\gamma_{SL} = \gamma_{SL}(x,0)$, and $\gamma_{SA} = \gamma_{SA}(x,0)$. Now let us discuss special cases of wetting. When the substrate is flat ($\tilde{r} = 1, f_S = 1$) and the effects related to line tension are negligible, we obtain:

$$\cos\theta^* = \frac{\gamma_{SA}(a,0) - \gamma_{SL}(a,0)}{\gamma(a,0)}. \tag{8.6}$$

When γ, $\gamma_{SA} = \text{const}$, $\gamma_{SL} = \gamma_{SL}^0 - C\hat{U}^2/2$ and we return to the well-known equation of electrowetting (equation (8.2) derived in the previous section).

When $\tilde{r} = 1$, and the effects related to the line tension are negligible, we obtain a modified Cassie–Baxter equation (see for comparison equation (5.25)) considering the field dependencies of the interfacial tensions:

$$\cos\theta^* = \frac{\gamma_{SA}(a,0) - \gamma_{Sl}(a,0)}{\gamma(a,0)}f_S + f_S - 1. \tag{8.7}$$

When $f_S = 1$, and the effects related to the line tension are negligible, we obtain a modified Wenzel equation (compare with equation (5.16))

$$\cos\theta^* = \frac{\gamma_{SA}(a,0) - \gamma_{Sl}(a,0)}{\gamma(a,0)}\tilde{r}. \tag{8.8}$$

When the effects related to the line tension are negligible, and so-called mixed wetting occurs, $\tilde{r} \neq 1$, then we obtain a modified Miwa–Marmur equation (compare with equation (5.43)):

$$\cos\theta^* = \frac{\gamma_{SA}(a,0) - \gamma_{Sl}(a,0)}{\gamma(a,0)}\tilde{r}f_S + f_S - 1. \tag{8.9}$$

We already became acquainted with the fact that as seen from equations (8.5) to (8.9) only the area adjacent to a triple line exerts an influence on the apparent contact angle. Apparent contact angles are governed by interfacial tensions at the triple line and by the geometrical parameters of defects f_S, ξ, $\tilde{r}$ located in the vicinity of the three-phase (triple) line (see Section 5.9).

The phenomenon of electrowetting was exposed to intensive investigation in the past decade owing to its numerous promising applications: from "lab-on-a-chip" devices to adjustable lenses and new kinds of electronic displays [7]. Krupenkin et al. demonstrated electrical control of the wetting behavior of liquids on nanostructured surfaces, which spans the entire possible range from superhydrophobic behavior to nearly complete wetting [4].

Additional Reading

The review of the state of the art in the field of electrowetting is supplied in Chen and Bonaccurso [11]. Electrowetting of gradient surfaces has been addressed in Bormashenko and Gendelman [12].

Bullets

- The contact angle of a droplet depends on the applied voltage due to the electric field dependence of interfacial tensions.
- When an aqueous electrolyte contacts a solid surface, a double electrical layer is formed. The double layer works as a capacitor.
- The dependence of the contact angle on the applied voltage is given by the Lippmann formula, which could be generalized for rough surfaces.
- When the specific capacity of the double layer is heterogeneous, the apparent contact angle of electrowetting depends on the derivative of the specific capacity, calculated at the triple line.

References

[1] A. W. Adamson and A. P. Gast, *Physical Chemistry of Surfaces*, 5th edn., Wiley Interscience Publishers, New York, 1990.
[2] E. Bormashenko, Contact angles of sessile droplets deposited on rough and flat surfaces in the presence of external fields, *Math. Model. Nat. Phenom.* **7**(4) (2012), 1–5.
[3] P. G. de Gennes, F. Brochard-Wyart, and D. Quéré, *Capillarity and Wetting Phenomena*, Springer, Berlin, 2003.
[4] T. N. Krupenkin, J. A. Taylor, T. M. Schneider, and S. Yang, From rolling ball to complete wetting: the dynamic tuning of liquids on nanostructured surfaces, *Langmuir* **20** (2004), 3824–3827.
[5] L. Liggieri, A. Sanfeld, and A. Steinchenbad, Effects of magnetic and electric fields on surface tension of liquids, *Physica A* **206** (1994), 299–331.
[6] G. Lippmann, Bemerkungen über einige neuere electrocapillare Versuche, *Wied. Ann.* **11** (1880), 316–324.
[7] F. Mugele and J.-C. Baret, Electrowetting: from basics to applications, *J. Phys.: Condens. Matter* **17** (2005), R705–R774.

[8] A. Quinn, R. Sedev, and J. Ralston, Contact angle saturation in electrowetting, *J. Phys. Chem. B*, **109** (2005), 6268–6275.
[9] B. Shapiro, H. Moon, R. L. Garrell, and C. J. Kim, Equilibrium behavior of sessile drops under surface tension, applied external fields, and material variations, *J. Appl. Physics* **93** (2003), 5794–5811.
[10] H. J. J. Verheijen and M. W. J. Prins, Reversible electrowetting and trapping of charge: model and experiments, *Langmuir* **15** (1999), 6616–6620.

Additional Reading

[11] L. Chen and E. Bonaccurso, Electrowetting – From statics to dynamics, *Adv. Colloid & Interface Sci.* **210** (2014), 2–12.
[12] E. Bormashenko and O. Gendelman, A generalized electrowetting equation: its derivation and consequences, *Chem. Phys. Lett.* **599** (2014), 139–141.

9 Nonstick droplets

9.1 General remarks

We already discussed nonadhesive droplets in Sections 6.1 and 6.2 when we discussed the effect of superhydrophobicity. Recall that the possibility of obtaining nonstick droplets is limited by the fact that the maximal possible contact angle registered on Teflon is less than 120°. Thus, nonstick wetting was created by decreasing the liquid–solid contact area, accompanied by supporting a droplet with air cushions. There exist at least two additional pathways for preparing highly mobile droplets: Leidenfrost droplets and liquid marbles.

9.2 Leidenfrost droplets

More than 250 years ago, the German physician Johann Gottlob Leidenfrost published a treatise in which he described the remarkable behavior of liquid drops on a very hot plate, such as water on steel at 300 °C. The Leidenfrost effect is a phenomenon in which a liquid, in close contact with a mass significantly hotter than the liquid's boiling point, produces an insulating vapor layer that keeps that liquid from boiling rapidly. Leidenfrost drops are very mobile (the slightest slope makes them drift). The Leidenfrost effect was first systematically studied by Gottfried et al. [23, 24]. Their research was followed recently by several groups of investigators [5, 16, 25, 27].

Let us start by establishing scaling laws interrelating the geometrical parameters of a levitating drop. These parameters are the radius of a drop R, and the radius of the contact area a (Figure 9.1). The shape of the Leidenfrost droplet results from an interplay of gravity and surface tension. Hence, two ranges of drop radii are possible, i.e., $R < l_{ca} = \sqrt{\gamma/\rho g}$ and $R > l_{ca}$, where l_{ca} is the capillary length introduced in Section 2.7, and ρ and γ are the density and surface tension of the liquid respectively. When $R < l_{ca}$, the drop is nearly spherical, except at the bottom where it is flattened. In this case, if the center mass of a drop is lowered by a quantity, δ, the difference

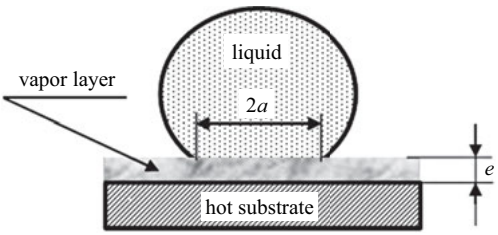

Fig. 9.1: Scheme explaining the Leidenfrost effect: the drop is supported by the vapor layer.

https://doi.org/10.1515/9783110583144-009

in energy can be written dimensionally as $\Delta G \approx \gamma\delta^2 - \rho g R^3 \delta$. Minimization of this expression and considering the geometric Hertz relation, $a \approx \sqrt{\delta R}$, yield (see Biance et al. and Mahadevan and Pomeau [5, 28]):

$$a \approx \frac{R^2}{l_{ca}} . \tag{9.1}$$

For large levitating droplets ($R > l_{ca}$) (the so-called "puddles" discussed in Section 2.7), the scaling law $a \sim R$ was proposed in Biance et al. [5]. The equilibrium thickness of the puddle derived in Section 2.7 is given by expression (2.43), i.e., $h = 2l_{ca} \sin\theta_Y/2$. The maximal thickness of the levitating puddle corresponding to the situation of total nonwetting (see Figure 2.1c) $\theta_Y = \pi$ is given by $h_{max} = 2l_{ca}$. This formula was successfully checked experimentally in Biance et al. [5].

Now let us discuss the origin and thickness of the vapor layer separating the Leidenfrost droplet and the substrate. The heat supplied to the droplet per unit time is proportional to the area, πa^2 (Figure 9.1). The rate of evaporation is given by:

$$\frac{dm}{dt} = \frac{\kappa}{\hat{\lambda}} \frac{\Delta T}{e} \pi a^2 \tag{9.2}$$

where κ is the thermal conductivity ($[\kappa] = \mathrm{kg \cdot m \cdot s^{-3} \cdot K^{-1}}$), $\hat{\lambda}$ is the specific mass latent heat of evaporation ($[\hat{\lambda}] = m^2 \cdot s^{-2}$), e is the thickness of the vapor layer (Figure 9.1), and ΔT is the difference between the plate temperature and the boiling temperature of the liquid. Integrating the radial Poiseuille flow of vapor outside the supporting layer carried out in Biance et al. [5] yielded:

$$\frac{dm}{dt} = \rho_v \frac{2\pi e^3}{3\eta_v} \Delta p , \tag{9.3}$$

where ρ_v and η_v are the vapor density and viscosity respectively, and Δp is the pressure imposed by the drop. In a permanent regime, the mass of vapor films remains constant. Thus, we can deduce from equations (9.2) and (9.3) the expression for the film thickness, e. For large droplets (puddles) $a \sim R$ and the pressure acting on the vapor layer equals $\rho g h_{max} = 2\rho g l_{ca}$. This yields (see Biance et al. [5]):

$$e = \left(\frac{3\kappa \Delta T \eta_v}{4\hat{\lambda}\rho_v \rho g l_{ca}} \right)^{\frac{1}{4}} R^{\frac{1}{2}} , \tag{9.4}$$

For small droplets, the situation is more complicated. As was demonstrated (see expression (9.1)), $a \approx R^2/l_{ca}$; $\Delta p \approx 2\gamma/R$. Thus, the dependence $e \sim R^{5/4}$ is expected. But for small drops, the vapor layer plays a minor role in the evaporation process, as its flat (lower) surface area scales as R^4 (see expression (9.1)). Hence, the temperature gradient should be of the order of $\Delta T/R$, and evaporation takes place over the spherical (upper) drop surface, which scales as R^2. This gives for the rate of evaporation:

$$\frac{dm}{dt} \approx \frac{\kappa}{\hat{\lambda}} \frac{\Delta T}{R} R^2 . \tag{9.5}$$

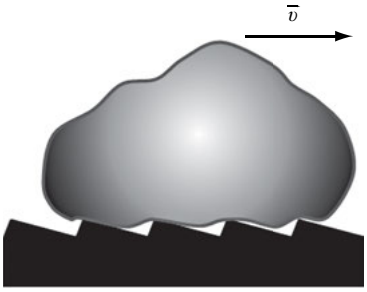

Fig. 9.2: Self-propelling Leidenfrost droplets deposited on an asymmetrical ratchet-like surface [25, 27].

Combining expressions (9.5) and (9.3) yields:

$$e = \left(\frac{\kappa \Delta T \eta_v \rho g}{\hat{\lambda} \rho_v \gamma^2} \right)^{\frac{1}{3}} R^{\frac{4}{3}} . \tag{9.6}$$

Scaling laws (9.4) and (9.6) coincide well with the experimental findings [5]. The typical thickness of the insulating vapor layer, e, is of the order 10–100 μm [5].

An interest in Leidenfrost droplets was strengthened by a recent experimental finding: these droplets demonstrate self-propelling when deposited on asymmetrical ratchet-like surfaces, shown in Figure 9.2 [25, 27]. The teeth of the ratchet have typically millimetric lengths and heights of 150 μm. Leidenfrost drops on these ratchets accelerate and reach a constant velocity of 5–15 cm/s. The physical mechanism of self-propelling is discussed in Lagubeau et al. [25].

9.3 Liquid marbles

9.3.1 What are liquid marbles?

Liquid marbles, which are nonstick droplets coated with nano- or micrometrically scaled particles, were introduced in the pioneering works of Quéré et al. [3, 4, 21]. Liquid marbles demonstrate extremely low friction when rolling on solid substrates [3, 4, 21]. Typical liquid marbles are depicted in Figure 9.3. Liquid marbles are also found naturally; for example, aphids convert honeydew droplets into marbles [30]. Liquid marbles can be obtained by mixing a hydrophobic powder in water or by rolling drops on a solid substrate covered with a layer of powder, as depicted in Figure 9.4.

Both hydrophobic and hydrophilic particles can be used for wrapping droplets. Aussillous and Quéré demonstrated that for both the scenarios of marble formation shown in Figure 9.4, i.e., a particle coming from either air (Figure 9.4a) or liquid (Figure 9.4b), the surface energy ΔG of the liquid/particle/air system decreases. When the smooth spherical particle comes from air, the energy gain is given by (see Dandan and Erbil [18]):

$$\Delta G_1 = -\pi R^2 \gamma (1 + \cos \theta_Y)^2 . \tag{9.7}$$

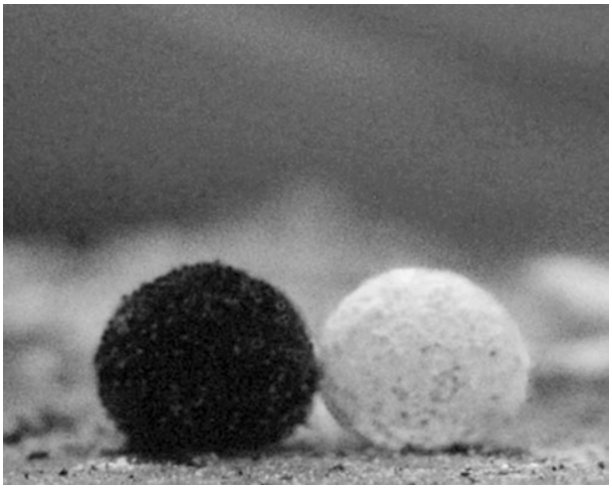

Fig. 9.3: Typical 20-µl liquid marbles. The black marble is coated with carbon black, the white marble is coated with Teflon particles.

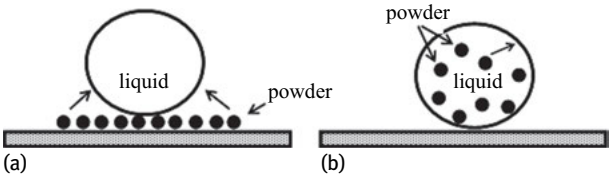

Fig. 9.4: Two possible scenarios of marble formation. a: the powder particle comes from air; b: the powder particle comes from liquid (under stirring).

For the particle coming out of liquid, we have:

$$\Delta G_2 = -\pi R^2 \gamma (1 - \cos\theta_Y)^2 \,, \tag{9.8}$$

where θ_Y is the Young angle inherent to the particle/liquid/air system, γ is the surface tension at the liquid/vapor interface, and R is the radius of the particle. In both cases, a particle lowers its energy by sticking to the interface regardless of the contact angle [18]. Marbles coated with strongly hydrophobic particles ($\theta_Y > 90°$) such as polytetrafluoroethylene, and marbles coated with hydrophilic graphite and carbon black ($\theta_Y < 90°$), have both been reported [34, 35].

A variety of liquids were converted into liquid marbles, including water and water solutions, glycerol, organic and ionic liquids [3, 4, 6, 7, 12, 18, 20, 21, 30, 36]. Janus marbles, composed of two hemispheres coated with different powders (such as depicted in Figure 9.5), were reported [6]. Composite marbles comprising diiodomethane and water and coated in a common shell, were also demonstrated [10].

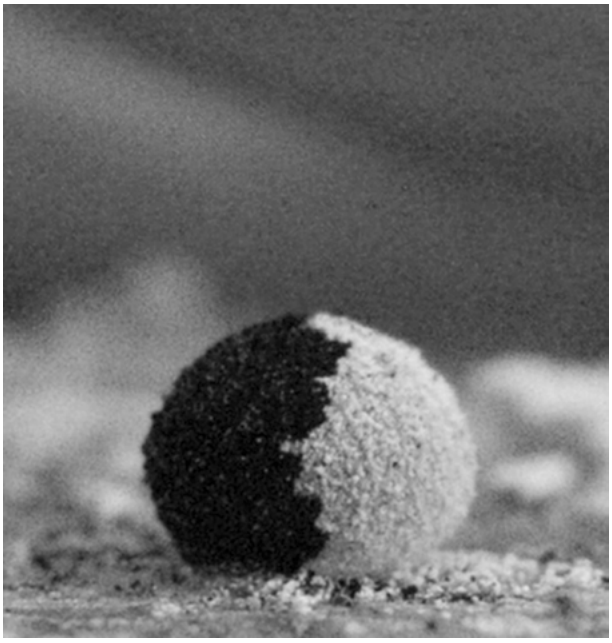

Fig. 9.5: Forty-microliter water Janus marble coated with carbon black and Teflon.

9.3.2 Liquid marble–support interface

Liquid marbles are separated from their solid or liquid support by "air pockets" in a way similar to that of the Leidenfrost drops discussed above. Similar air pocket separation of droplets from a substrate occurs under "lotus-like" wetting of rough surfaces, which were dealt with in Sections 6.1 and 6.2. The existence of an air layer separating marbles from liquid and solid supports has been evidenced experimentally. Liquid marbles containing NaOH water solutions floated on an alcoholic solution of phenolphthalein with no chemical reaction [8]. Likewise, no chemical reaction was observed during the sliding of liquid marbles, consisting of NaOH water solutions, on polymer substrates coated with phenolphthalein [8]. Air pockets trapped by liquid marbles promote their nonstick properties.

9.3.3 Liquid marble–vapor interface

The liquid marble–vapor interface was studied using optical microscopy, confocal microscopy, and environmental scanning electron microscopy (ESEM) [4, 15, 29, 34]. It was demonstrated that various powders wrapping the marbles do not form a uniform shell. It is noteworthy that the powder shell constituting a marble is permeable for gases. ESEM imaging demonstrated that solid particles are separated by micro-

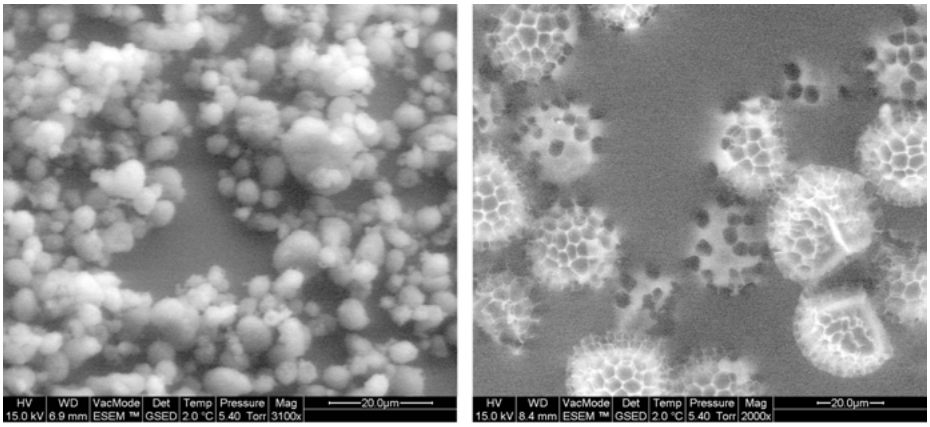

Fig. 9.6: Environmental scanning electron microscopy images of the surface of liquid marbles are depicted. a: liquid marble coated with polyvinylidene fluoride powder is shown. Scale bar is 20 µm. b: liquid marble coated with lycopodium is shown. Scale bar is 20 µm. Water clearings are clearly seen on both images.

scaled water clearings, as shown in Figure 9.6. The kinetics of evaporation of liquid marbles coated with polytetrafluoroethylene (PTFE) and graphite has also been reported [18, 35]. It was suggested that colloidal particles coating marbles may form relatively large (~ 10–50 µm) aggregates which trap air, making the Cassie–Baxter wetting possible at the aggregate/liquid interface, thus increasing the apparent contact angle and resembling the natural marbles produced by aphids [12, 30]. Cassie–Baxter wetting could also be expected when marbles are coated with micro-scaled lycopodium particles, characterized by a well-developed surface (see Section 6.6 and Figures 6.8, 9.6).

9.3.4 Effective surface tension of liquid marbles

One of the most intriguing questions is: what is the effective surface tension γ_{eff} of liquid marbles? Several independent experimental techniques were applied for the establishment of the effective surface tension of liquid marbles: 1) the puddle height method, 2) analysis of marble shape, 3) vibration of marbles, 4) the method of capillary rise, and 5) the Wilhelmy plate method.

1. The puddle height method is based on a formula supplying the maximal height of a liquid puddle, written now as $h_{\max} = 2l_{\text{ca}} = 2\sqrt{\gamma_{\text{eff}}/\rho g}$ (see Sections 2.7 and 9.2). This immediately yields for the effective surface tension:

$$\gamma_{\text{eff}} = \frac{\rho g h_{\max}^2}{4} \,. \tag{9.9}$$

2. The effective surface tension of marbles could be established by the analysis of the marble shape. The precise shape of the marble could be calculated only numerically [4]. However, it was demonstrated that the shape of a marble deformed by gravity is described satisfactorily as an oblate spheroid (see Section 2.7). Fitting of the calculated and measured geometrical parameters allowed the establishment of the effective surface tension of marbles [14].
3. Measurement of the resonance frequencies of vibrated marbles also allowed the establishment of their effective surface tension (see Section 2.14.4 and Bombashenko et al. [14]).
4. Arbatan and Shen introduced a capillary tube directly into a marble coated in PTFE and deduced the effective surface tension from the capillary rise (see Section 2.10) [2].
5. Arbatan and Shen in parallel established the effective surface tension of PTFE-coated marbles exploiting the Wilhelmy plate method (see Section 2.14.1) [2]. The measurements demonstrated that the effective surface tension is independent of the size of PTFE particles coating the marble, and that it is close to that of pure water [2].

Effective surface tensions in the range $45-75\,\mathrm{mJ/m^2}$ were reported for water-based liquid marbles coated in various particles [2, 4, 14]. It should be mentioned that experimental data related to the effective surface tension of liquid marbles are scarce, and extensive experimental activity devoted to the problem is called for.

The current experimental situation is complicated, because the physical properties of surfaces stabilized with solid particles depend on the density and nature of their covering. Such surfaces behave as two-dimensional elastic *solids* (and not liquids) when compressed [32]. The stretching modulus and bending stiffness of such surfaces were reported recently [32]. Future experimental activity in the field considering the impact exerted by the physical nature and density of the solid covering on the surface properties of marbles is necessary to clarify the situation.

9.3.5 Scaling laws governing the shape of liquid marbles

As was already mentioned in Section 9.2, the shape of nonstick droplets is dictated by the interplay of gravity and effective surface tension. For large marbles ($R > l_{ca}$), the scaling law relating the contact radius a to the radius of the marble R was proposed in the form $a \approx R^{3/2} l_{ca}^{-1/2}$, whereas for small marbles ($R < l_{ca}$), the scaling law is $a \approx R^2 l_{ca}^{-1}$ (compare with expression (9.1)). The aforementioned scaling laws have been validated experimentally for marbles coated in both hydrophobic and hydrophilic powders [3, 12].

9.3.6 Properties of liquid marbles: the dynamics

Very few works have treated the complicated dynamics of liquid marbles [7, 28, 31, 33]. It was shown that liquid marbles moving down a tilted substrate are rolling and not sliding [7, 28, 33]. The dynamics of marbles is expectedly governed by a Reynolds number, $Re = \rho v R/\eta$, representing inertia versus viscosity (ρ and η are the density and viscosity respectively, v is the characteristic velocity), by a so-called capillary number, $Ca = \eta v/\gamma$, representing viscous forces versus surface tension (see Section 4.2), and by a Weber number, $We = \rho v^2 R/\gamma$, representing inertial effects versus surface tension. It was shown that for 10-μl water-based marbles rolling with a velocity of $v \approx 0.1$ m/s, Ca is much smaller than unity, whereas for the glycerol-based marbles of the same volume and velocity, it is close to unity [7, 33]. Thus, it is clear that for rolling water marbles, the viscous dissipation is negligible compared with that related to the disconnection of the contact line of the marble, whereas for glycerol ones, the viscous dissipation plays a decisive role in slowing a marble. Glycerol liquid marbles rolling downhill move with a center mass velocity, v_{cm}, governed by the scaling law:

$$v_{\mathrm{cm}} \approx \frac{\gamma}{\eta}\frac{l_{\mathrm{ca}}}{R}\sin\alpha\,, \tag{9.10}$$

where α is the inclination angle, and R is the radius of the marble. This result looks rather paradoxical and counterintuitive: the small marbles descend faster than the large ones [21, 28, 33]. However, this amazing prediction has been validated experimentally [3, 33]. It was also demonstrated that the stopping distance, l_{stop}, for glycerol marbles rolling on the horizontal substrate is estimated as:

$$l_{\mathrm{stop}} \cong \frac{7}{15}\frac{\rho v_{\mathrm{cm0}} R^5}{\eta a^3} \tag{9.11}$$

where v_{cm0} is the initial center mass velocity of a droplet, and a is the contact radius of the marble [7]. In contrast to glycerol marbles, the principal dissipation mechanism for water marbles can be attributed to the disconnection of the contact line [7, 33]. As mentioned in Bormashenko et al. [11], this kind of friction is a one-dimensional (1D) phenomenon (the force is proportional to the perimeter of the contact line).

It is noteworthy that both mechanisms of friction, i.e., viscous dissipation and disconnection of the triple line are nonAmontonian [7]. Recall that Amontons' laws of friction imply that: (1) the force of friction is directly proportional to the applied load, (2) the force of friction is independent of the apparent area of contact, and (3) kinetic friction is independent of the sliding velocity. Obviously, Amontons' laws are irrelevant with respect to liquid marbles. The friction of liquid marbles is dependent on velocity and contact perimeter [7, 28, 33].

In spite of the fact that liquid marbles roll and do not slide, it would be wrong to describe the moving droplet as being similar to a common rigid rotating ball – it is worthwhile mentioning that such a "ball" cannot just be at rest on an inclined surface.

A liquid marble can not only be at rest on an inclined substrate, but it moves laterally on such surfaces [7]. Deformation of liquid marbles is discussed in de Gennes et al. [21]. It was shown that under rotation, the marble can deform into a disk, and even a peanut [3, 21]. It was demonstrated that the shape of a rotating marble is governed by the balance of inertia (the rotating force being responsible for distorting the marble) and capillarity (tending to preserve a spherical shape). Hence, the shape of rotating marbles is dictated by the Weber number [3, 21].

Planchette et al. studied the impact of liquid marbles with solid substrates [31]. Three regimes of impact were revealed: nonbouncing, bouncing, and rupture of the surface coverage, which prevents the droplet from integer bouncing, occurring at a critical droplet extension [31]. Planchette et al. has shown that when $Re \gg 1$, a droplet extension scales as $\sqrt{We}$, similar to bare droplets [19, 31]. The intriguing open question is: what is the effective dynamic surface tension of moving and bouncing liquid marbles?

9.3.7 Actuation of liquid marbles with electric and magnetic fields

Liquid marbles are of interest in view of their micro-fluidics applications. Various groups have demonstrated that liquid marbles could be actuated with electric and magnetic fields [2, 14, 15, 32, 34, 35]. Consider the electrical actuation of liquid marbles. As was demonstrated in Section 2.9, a dielectric droplet is distorted by an electric field. Thus, it may be expected that droplets deposited on superhydrophobic surfaces, as well as liquid marbles, show similar behavior when exposed to an electric field; surprisingly, the behavior of droplets versus marbles in the electric field is essentially different.

As was shown in Section 2.9, the dependence of eccentricity on the value of the applied electric field is linear for droplets deposited on superhydrophobic surfaces. Somewhat unexpectedly, the dependence of the marble eccentricity on the value of the applied electric field turned out to be nonlinear, and it is described by a rather complicated function [13]. The following explanation for this discrepancy was proposed in Bormashenko et al. [13]: droplets contacting a solid substrate form an electric double layer within the contact area (see Section 8.2). At the same time, liquid marbles are disconnected from the solid substrate and possess zero dipole moment in the absence of an external electric field [13]. This, perhaps, explains the very different behavior of liquid marbles versus droplets exposed to an electric field [13].

Electrical actuation of composite marbles comprising diiodomethane and water and coated by a common shell, was reported recently [10]. The water drop climbed onto the diiodomethane drop when the composite marble was exposed to an electric field [10]. For an explanation of the effect, see Bormashenko et al. [10].

Now let us discuss the possibility of actuating liquid marbles with a magnetic field. The simplest method is to introduce and disperse ferromagnetic particles in

the liquid bulk [11]. It was shown that 20-µl marbles containing γ-modification of Fe_2O_3 nanoparticles could be accelerated by a magnetic field of 0.5 T to a velocity of 25 cm/s [11]. A more elegant and sophisticated method of magnetic actuation of liquid marbles was demonstrated by Lin et al. [37]. They synthesized highly hydrophobic Fe_3O_4 nanoparticles by coprecipitation of Fe(II) and Fe(III) salts in an ethanol–water solution with ammonia in the presence of fluorinated alkyl silane, which hydrolyzed in solution to form a low-free-energy coating on the Fe_3O_4 nanoparticles [37]. Liquid marbles were then coated with these hydrophobic Fe_3O_4 nanoparticles. Thus, the possibility of opening and closing marbles (making a hole in a coating) reversibly with a magnetic field was shown [37].

Janus marbles coated partially with dielectric particles (Teflon) and partially with semiconductor (carbon black) particles, depicted in Figure 9.5, could be rotated with an electric field [9].

9.3.8 Applications of liquid marbles

Liquid marbles, because of their small dimensions, provide optimal conditions for miniaturized chemical processes [36]. Such processes have many advantages related to the reduced use of chemical reagents and solvents, precisely controlled reaction conditions and a greatly shortened reaction time [36]. Highly hydrophobic particles (reported in Xue et al. [36]) allowed manufacturing of marbles with low surface tension organic liquids such as ethanol and toluene. The permeability of the powder shell coating liquid marbles has allowed their application for gas sensing [34]. Arbatan et al. demonstrated the use of liquid marbles as micro-bioreactors, for blood typing [1]. Only a few seconds of gentle shaking of the marble containing the blood and antibody mixture was enough to initiate the hemagglutination reaction [1].

9.4 Nonstick drops bouncing in a fluid bath

One of the most fascinating manifestations of nonstick droplets are noncoalescing droplets bouncing against a *liquid* surface. Couder et al. demonstrated that a drop of silicon oil bouncing vertically in an oscillating bath filled with the same oil remains stable for any time span [17]. The effect is due to the stable thin air film separating a bouncing drop from the oscillating bath [17]. Couder et al. showed that the coalescence is inhibited when the acceleration is higher than a certain threshold value, and that this value grows as a squared frequency of the vibration. The authors explained this scaling by balancing the gravity, the inertial forces, and the lubrication force exerted on the droplet by the squeezed air layer [17]. For a more comprehensive treatment of this phenomenon, see Gilet et al. [22].

Additional Reading

Liquid marbles demonstrate not only "liquid" but also "elastic" properties; namely, they do not coalesce when they collide, and restore their shape after deformation. Elastic properties of liquid marbles were addressed in Asare-Asher et al. and Whyman and Bormashenko [38, 39]. Floating liquid marbles (such as depicted in Figure 9.7) filled with aqueous solutions of volatile compounds, such as alcohols and camphor, demonstrated prolonged self-propelled motion, driven by Marangoni flows, as reported in Wong et al. and Bormashenko et al. [40, 41].

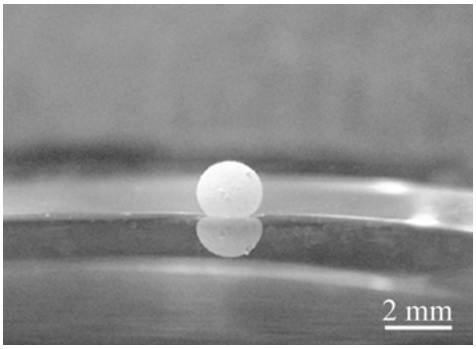

Fig. 9.7: Ten-microliter liquid marble coated with the Teflon powder and supported by water is depicted.

Bullets

- The "Leidenfrost effect" is observed when a droplet is deposited on a very hot support. The rapid evaporation of a droplet gives rise to an insulating vapor layer, allowing levitation of the droplet.
- The typical thickness of the insulating vapor layer, e, is of the order 10–100 μm.
- A self-propelling effect was observed for Leidenfrost droplets deposited on asymmetrical ratchet-like surfaces.
- Liquid marbles are nonstick droplets wrapped in micro- or nanometrically scaled particles. The marbles are separated from their solid or liquid support by air pockets.
- The powder shell coating of liquid marbles is permeable for gases.
- Effective surface tensions in the range 45–75 mJ/m^2 were reported for water-based liquid marbles coated with various particles.
- NonAmontonian friction is inherent to liquid marbles.
- Liquid marbles could be actuated with electric and magnetic fields.

References

[1] T. Arbatan, L. Li, J. Tian, and W. Shen, Liquid marbles as micro-bioreactors for rapid blood typing, *Adv. Healthcare Mater.* **1** (2012), 80–83.

[2] T. Arbatan and W. Shen, Measurement of the surface tension of liquid marbles *Langmuir* **27** (2011), 12,923–12,929.

[3] P. Aussillous and D. Quéré, Liquid marbles, *Nature* **411** (2001), 924–927.

[4] P. Aussillous and D. Quéré, Properties of liquid marbles, *Proceedings of the Royal Society A* **462** (2006), 973–999.

[5] A.-L. Biance, C. Clanet, and D. Quéré, Leidenfrost drops, *Physics of Fluids* **15** (2003), 1632–1637.

[6] B. P. Binks and R. Murakami, Phase inversion of particle-stabilized materials from foams to dry water, *Nature Materials* **5** (2006), 865–868.

[7] E. Bormashenko, Y. Bormashenko, and O. Gendelman, On the nature of the friction between nonstick droplets and solid substrates, *Langmuir* **26** (2010), 12,479–12,482.

[8] E. Bormashenko, Y. Bormashenko, A. Musin, and Z. Barkay, On the mechanism of floating and sliding of liquid marbles, *Chem. Phys. Chem.* **10** (2009), 654–656.

[9] E. Bormashenko, Y. Bormashenko, R. Pogreb, and O. Gendelman, Janus Droplets: Liquid Marbles Coated with Dielectric/Semiconductor Particles, *Langmuir* **27** (2011), 7–10.

[10] E. Bormashenko, R. Pogreb, R. Balter, O. Gendelman, and D. Aurbach, Composite nonstick droplets and their actuation with electric field, *Appl. Phys. Lett.* **100** (2012), 151601.

[11] E. Bormashenko, R. Pogreb, Y. Bormashenko, A. Musin, and T. Stein, New investigations on ferrofluidics: ferrofluidic marbles and magnetic-field-driven drops on superhydrophobic surfaces, *Langmuir* **24** (2008), 12,119–12,122.

[12] E. Bormashenko, R. Pogreb, A. Musin, R. Balter, G. Whyman, and D. Aurbach, Interfacial and conductive properties of liquid marbles coated with carbon black, *Powder Technology* **203** (2010), 529–533.

[13] E. Bormashenko, R. Pogreb, T. Stein, G. Whyman, M. Schiffer, and D. Aurbach, Electrically deformable liquid marbles, *J. Adhesion Sci. Technol.* **25** (2011), 1371–1377.

[14] E. Bormashenko, R. Pogreb, G. Whyman, and A. Musin, Surface tension of liquid marbles, *Colloids & Surfaces A* **351** (2009), 78–82.

[15] E. Bormashenko, R. Pogreb, G. Whyman, A. Musin, Y. Bormashenko, and Z. Barkay, Shape, vibrations, and effective surface tension of water marbles, *Langmuir* **25** (2009), 1893–1896.

[16] S. Chandra and S. D. Aziz, Leidenfrost evaporation of liquid droplets, *J. Heat Transfer* **116** (1994), 999–1006.

[17] Y. Couder, E. Fort, C.-H. Gautier, and A. Boudaoud, From bouncing to floating: noncoalescence of drops on a fluid bath, *Phys. Rev. Lett.* **94** (2005), 177801.

[18] M. Dandan and H. Y. Erbil, Evaporation rate of graphite liquid marbles: comparison with water droplets, *Langmuir* **25** (2009), 8362–8367.

[19] J. Eggers, M. A. Fontelos, C. Josserand, and S. Zaleski, Drop dynamics after impact on a solid wall: theory and simulations, *Physics of Fluids* **22** (2010), 062101.

[20] L. Gao and T. J. McCarthy, Ionic liquid marbles, *Langmuir* **23** (2007), 10,445–10,447.

[21] P. G. de Gennes, F. Brochard-Wyart, and D. Quéré, *Capillarity and Wetting Phenomena*, Springer, Berlin, 2003.

[22] T. Gilet, D. Terwagne, N. Vandewalle, and S. Dorbolo, Dynamics of a bouncing droplet onto a vertically vibrated interface, *Phys. Rev. Lett.* **100** (2008), 167802.

[23] B. S. Gottfried and K. J. Bell, Film boiling of spheroidal droplets. Leidenfrost phenomenon, *Ind. Eng. Chem. Fundamen.* **5** (1966), 561–568.

[24] B. S. Gottfried, C. J. Lee, and K. J. Bell, The Leidenfrost phenomenon: film boiling of liquid droplets on a flat plate, *Int. J. Heat & Mass Transfer* **9** (1966), 1167–1188.
[25] G. Lagubeau, M. Le Merrer, C. Clanet, and D. Quéré, Leidenfrost on a ratchet, *Nature Physics* **7** (2011), 395–398.
[26] J. G. Leidenfrost, *De Aquae Communis Nonnullis Qualitatibus Tractatus*, Duisburg, 1756.
[27] H. Linke, B. J. Alemán, L. D. Melling, M. J. Taormina, M. J. Francis, C. C. Dow-Hygelund, V. Narayanan, V. R. P. Taylor, and A. Stout, Self-propelled Leidenfrost droplets, *Phys. Rev. Lett.* **96** (2006), 154502.
[28] L. Mahadevan and Y. Pomeau, Rolling droplets, *Physics of Fluids* **11** (1999), 2449–2453.
[29] T. H. Nguyen, K. P. Hapgood, and W. Shen, Observation of the liquid marble morphology using confocal microscopy, *Chemical Engineering J.* **162** (2010), 396–405.
[30] N. Pike, D. Richard, W. Foster, and L. Mahadevan, How aphids lose their marbles, *Proceedings of the Royal Society B* **269** (2002), 1211–1215.
[31] C. Planchette, A. L. Biance, and E. Lorenceau, Transition of liquid marble impacts onto solid surfaces, *Europhysics Lett.* **97** (2012), 14003.
[32] C. Planchette, E. Lorenceau, and A.-L. Biance, Surface wave on a particle raft, *Soft Matter* **8** (2012), 2444–2451.
[33] D. Richard and D. Quéré, Viscous drops rolling on a tilted non-wettable solid, *Europhysics Letters* **48** (1999), 286–291.
[34] J. Tian, T. Arbatan, X. Li, and W. Shen, Liquid marble for gas sensing, *Chemical Communications* **46** (2010), 4734–4736.
[35] A. Tosun and H. Y. Erbil, Evaporation rate of PTFE liquid marbles, *Appl. Surf. Sci.* **256** (2009), 1278–1283.
[36] Y. Xue, H. Wang, Y. Zhao, L. Dai, L. Feng, X., and T. Lin, Magnetic liquid marbles: a "precise" miniature reactor, *Advanced Materials* **22** (2010), 4814–4818.
[37] Y. Zhao, J. Fang, H. Wang, X. Wang, and T. Lin, Magnetic liquid marbles: manipulation of liquid droplets using highly hydrophobic Fe_3O_4 nanoparticles, *Advanced Materials* **22** (2010), 707–710.

Additional Reading

[38] S. Asare-Asher, J. N. Connor and R. Sedev, Elasticity of liquid marbles, *J. Colloid & Interface Sci.* **449** (2015), 341–346.
[39] G. Whyman and E. Bormashenko, Interpretation of elasticity of liquid marbles, *J. Colloid & Interface Sci.* **457** (2015), 148–151.
[40] C. Y. H. Wong, M. Adda-Bedia, and D. Vella, Non-wetting drops at liquid interfaces: from liquid marbles to Leidenfrost drops, *Soft Matter* **13** (2017), 5250–5260.
[41] E. Bormashenko, Y. Bormashenko, R. Grynyov, H. Aharoni, G. Whyman, and B. P. Binks, Self-Propulsion of liquid marbles: Leidenfrost-like levitation driven by Marangoni flow, *J. Phys. Chem. C* **119**(18) (2015), 9910–9915.

10 Wetting of lubricated surfaces

10.1 General remarks

Until now, we have considered wetting phenomena taking place on dry, solid surfaces. Now we discuss the wetting of lubricated solid surfaces, which is rich in its physical content. Capillarity-inspired effects occurring on flat [1, 4, 6, 7, 9–11, 15, 16] and rough [2, 5, 8, 12–15] lubricated solid surfaces should be distinguished. The wetting of rough, oil-infused surfaces is of great interest for the development of highly stable superhydrophobic and ice-phobic surfaces [5]. Indeed, the wetting transitions addressed in Chapter 7 become impossible on these surfaces [5].

10.2 Capillarity-inspired effects on wet (lubricated), flat, solid surfaces

10.2.1 The effect of wettability on the tribology of ideal lubricated surfaces

Wetting effects influence the tribology properties of lubricated surfaces. The microhydrodynamics of silicon wafers lubricated with water and oil was studied in Daniel et al. [5]. Recall that silicon wafers are regarded as atomically flat rigid substrates, and are considered very close to ideal surfaces (see Sections 2.2 and 3.2). In addition, by means of chemical treatments, silicon can easily be made hydrophilic or hydrophobic [6]. The hydrodynamic interactions of a ball on a flat arrangement as a model of single asperity contact has been investigated [6]. It was shown that for water and for oil, Newtonian friction is valid even for a liquid film with a thickness in the lower nanometer range, as established for surfaces demonstrating low contact angles [6]. In the case of surfaces demonstrating high contact angles, the Newtonian friction law breaks down [6].

10.2.2 Impact of droplets: collision with wet, flat substrates

Now consider the collision of droplets with a pre-wetted substrate [4, 9, 15, 16]. The character of the impact depends on the Weber dimensionless number, representing inertial effects versus surface tension (as introduced in Section 9.3.6) and the Ohnesorge number, defined as:

$$Oh = \frac{\eta}{(\rho\gamma D)^{1/2}} = \frac{\sqrt{We}}{Re}\ , \tag{10.1}$$

https://doi.org/10.1515/9783110583144-010

where γ, ρ, η, and D are the surface tension, density, viscosity, and initial diameter of the impinging droplet respectively. The Ohnesorge number, supplied by equation (10.1), relates the viscous forces to inertial and surface tension forces. However, the Ohnesorge number is not an independent value; as is seen from equation (10.1), it is expressed via the Reynolds and Weber numbers (see Section 9.3.6). The number and choice of dimensionless numbers necessary for an adequate description of physical problems is dictated by the Buckingham theorem (which is also called the "π-theorem," see Bormashenko and Buckingham [1, 3]).

Generally, two main regimes of droplet spreading are possible, mentioned in Cossali et al. [4] as "splashing" and "deposition." The term "splashing" is usually used to indicate the formation of secondary drops (droplets) after the impact of the impinging drop; and the term "deposition" indicates an impact without the production of secondary droplets, forming a liquid crown [4, 15, 16]. Cossali et al. [4] empirically established the threshold at which a switch from deposition to splash spreading takes place, which is given by equation (10.2):

$$Oh^{-0.4}We = 2100 + 5888\delta^{1.44}\,, \tag{10.2}$$

where $\delta = h/D$ is the dimensional droplet thickness, and h is the thickness of a liquid film wetting a solid substrate.

Bouncing on a pre-wetted surface occurs under the successive impact of droplets on the solid substrate [10]. The normal impact of successive mono-disperse ethanol drops (with an initial diameter $D \sim 70$–$340\,\mu$m and an impact velocity v_{imp} up to 30 m/s) on a solid surface was studied experimentally in by Yarin and Weiss [16]. Following the first impact, the wall was permanently covered by a thin liquid film with a thickness on the order of h; let f be the frequency of the impacts and f^{-1} the characteristic time of one impact [16]. For $f \approx 10^4\ \text{s}^{-1}$ and kinematic viscosity, $\tilde{\nu}_{\text{kin}} \approx 10^{-6}\ \text{m}^2/\text{s}$, the values of h were in the range 20–50 μm, typically with $\delta \cong 1/6$. The film thickness was sufficiently large relative to the mean surface roughness (1 or 16 μm). The experiments revealed the two aforementioned characteristic flow patterns on the surface, namely "deposition" and "splashing" [4, 15, 16]. The experimental threshold velocity for drop splashing in a droplets train of frequency f has been established by Yarin and Weiss [16] as:

$$v_{\text{splash}} = 18\left(\frac{\gamma}{\rho}\right)^{1/4}\tilde{\nu}_{\text{kin}}^{1/8}f^{3/8}\,. \tag{10.3}$$

10.3 Wetting of impregnated (infused), solid, rough substrates

When liquid wets a rough surface infused by another liquid, different wetting regimes are possible, as discussed in Smith et al. [13] and depicted in Figure 10.1. Consider a high surface energy droplet (say, water) placed on a low surface energy (say, silicone oil) infused micro-porous surface. The oil may spread over and "cloak" the water drop-

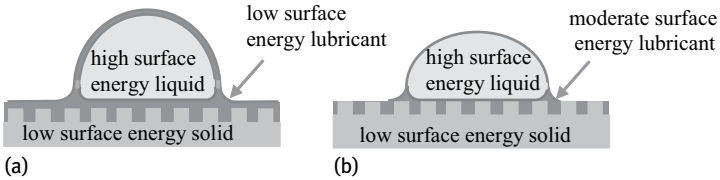

Fig. 10.1: Main wetting regimes inherent for the wetting of oil-infused rough surfaces. a: high surface energy liquid (water) is completely coated in a thin layer of low surface energy oil (silicone oil). The condition $\Psi > 0$ takes place. b: The drop of high surface energy liquid remains uncoated ($\Psi < 0$).

let (Figure 10.1a) [9, 13]). This is important because cloaking can cause the progressive loss of impregnated oil through entrainment in the water droplets as they are shed from the surface. The criterion for coating ("cloaking") is given by equation (10.4):

$$\Psi = \gamma_{wa} - (\gamma_{wo} + \gamma_{oa}) > 0\,, \tag{10.4}$$

where Ψ is the spreading coefficient, introduced in Section 2.1, and γ_{wa}, γ_{wo}, and γ_{oa} are the surface tensions at the water–air, water–oil, and oil–air interfaces respectively [8, 13]. In the situation where $\Psi < 0$, the wetting regime depicted in Figure 10.1b takes place. Then, as shown in Smith et al. [13], there are three distinct three-phase contact lines at the perimeter of the drop that confine the wetting ridge: the oil–water–air contact line, the oil–solid–air contact line outside the drop, and the oil–solid–water contact line underneath the drop. When the demand $\Psi < 0$ is fulfilled, 12 stable "wetting configurations" are possible (as listed in Smith et al. [13]), depending on the location of the wetting ridge (introduced in Section 3.11). These wetting configurations not only govern the contact line pinning (discussed in Sections 3.2 and 3.3) that controls the droplets initial resistance to movement, but they also govern the level of viscous dissipation and hence their sliding velocity once the droplets begin to move [13]. In contrast, none of these contact lines exists when equation (10.4) takes place, and the high surface energy liquid is coated by the low surface energy lubricant, as shown in Figure 10.1a.

Visualization of both coated and noncoated wetting regimes was carried out using laser scanning confocal microscopy by Vollmer et al. [12]. These authors showed that for droplets put on oil-infused tilted surfaces, the receding and advancing of the rim of a drop are fundamentally different processes. Drops recede through well-defined de-pinning events, whereas for the advancing contact line, no critical contact angle exists. The drop–lubricant interface gradually bends downward until it touches the top face of the foremost protrusion. The high apparent contact angles, the small width of the contact area, the low interfacial tension, and the increased effective mass of the drop result in easy sliding of the drop [12].

10.4 Impact of water droplets on oil-infused surfaces

Bouncing water droplets on silicone oil-infused polymer honeycomb surfaces were addressed in Multanen et al. [8]. The authors considered the impact of water droplets on cold-plasma-treated and nontreated silicone-oil-infused surfaces [8]. Cold plasma treatment of oil-infused surfaces switches the quasi-elastic bouncing to a two-stage spreading. At the first stage, spreading is governed by the square-root time dependence of the contact radius; whereas at the final stage, the kinetics of spreading conforms to the Tanner-like law, discussed in Section 4.7. Water droplets placed on the pristine silicone-oil infused surfaces are eventually coated with the silicone oil; in contrast, water droplets spread on the plasma-treated oil remained uncoated, because of the increase in the specific energy of the silicon oil induced by the plasma treatment, followed by a consequent change in the spreading parameter (see equation (10.4) and Multanen et al. [8]).

10.5 Electrowetting of lubricated surfaces

Electrowetting of lubricated surfaces is of special interest to engineers, because it allows diminishing of the voltage $\hat{U}$ necessary for actuating a droplet. Indeed, when a droplet is placed on an impregnated (infused) solid surface, the triple line is de-pinned (as discussed in Section 10.3), which facilitates its displacement under the applied voltage. Consider the wetting regime depicted in Figure 10.1a, where oil completely coats a droplet (say, a water droplet). Minimization of the free energy of a droplet, G, performed in Bormashenko et al. [2], yields the value of the apparent contact angle, θ^*, and the following dependence on the applied voltage, $\hat{U}$:

$$\cos\theta^* = \frac{\gamma_{oa} - \gamma^*_{ow}(\hat{U})}{\gamma_{oa} + \gamma^0_{ow} + \Omega(e)}\,, \tag{10.5}$$

where, γ^0_{ow} is the initial (i.e., corresponding to the zero voltage) surface tension at the oil–air interface, $\gamma^*_{ow}(\hat{U})$ is the voltage-dependent surface tension at the oil–water interface (see Section 8.2), and $\Omega(e)$ is the term resulting from disjoining pressure, $\Pi(e)$, namely, $\Pi(e) = -\mathrm{d}\Omega/\mathrm{d}e$, where e is the thickness of the oil layer coating a droplet (see Section 2.5 and Figure 10.1a). It is plausible to suggest that the change in the oil–water interface tension due to the voltage $\hat{U}$ is described by equation (10.6) (similar to that suggested in Section 8.2):

$$\gamma^*_{ow}\left(\hat{U}\right) = \gamma^0_{ow} - \frac{\tilde{C}\hat{U}^2}{2}\,, \tag{10.6}$$

where $\tilde{C}$ is the specific capacity of the double layer formed at the oil–water interface. Thus, the contact angle for electrowetting of lubricated surfaces is given by an equa-

tion similar to the Lippmann formula, supplied in Section 8.2:

$$\cos\theta^* = \cos\theta + \frac{\alpha\hat{U}^2}{2} \tag{10.7a}$$

$$\alpha = \frac{\tilde{C}}{\gamma_{oa} + \gamma_{ow}^0 + \Omega(e)} \tag{10.7b}$$

Bullets

- Wettability influences the tribology properties of ideal lubricated surfaces. Ideal solid surfaces (Si wafers) demonstrating low contact angles are characterized by Newton-like viscosity friction, whereas for the ideal surfaces showing high contact angles the Newton friction breaks down.
- When water droplets impact a pre-wetted ideal surface, two main spreading scenarios are possible: spreading (deposition) and splashing. See the excellent review supplied by Yarin [15].
- When water droplets are placed on oil-infused rough surfaces, two main wetting regimes occur: namely, the droplets are coated ("cloaked") with oil, or they keep their surfaces uncoated. The wetting regime depends on the sign of the spreading parameter.
- Receding and advancing of the rim of a drop are fundamentally different processes for droplets placed on oil-infused tilted surfaces.
- Electrowetting of water droplets placed on silicone-oil-infused honeycomb surfaces provide the relatively low voltage values necessary for the electrical actuation of droplets.

References

[1] E. Bormashenko, *Physics of wetting: phenomena and applications of liquids on surfaces*, Ch. 7, 10, De Gruyter, Berlin, 2017.
[2] E. Bormashenko, R. Pogreb, Y. Bormashenko, H. Aharoni, E. Shulzinger, R. Grinev, D. Rozenma, and Z. Rozenman, Progress in low voltage reversible electrowetting with lubricated polymer honeycomb substrates, *RSC Adv.* **5**, (2015), 32,491–32,496.
[3] E. Buckingham, The principle of similitude, *Nature* 1915**, 96** (2406), 396–397.
[4] G. E. Cossali, A. Coghe, and M. Marengo, The impact of a single drop on a wetted solid surface, *Exper. Fluids* **22**(6), (1997), 463–472.
[5] D. Daniel, J. V. I. Timonen, R. Li, S. J. Velling, and Joanna Aizenberg, Oleoplaning droplets on lubricated surfaces, *Nature Physics* **13** (2017), 1020–1026.
[6] W. Hild, A. Opitz, J. A. Schaefer, and M. Scherge, The effect of wetting on the microhydrodynamics of surfaces lubricated with water and oil, *Wear* **254** (2003), 871–875.
[7] Z. Levin and P. V. Hobbs, Splashing of water drops on solid and wetted surfaces: hydrodynamics and charge separation, *Phil. Transact. Royal Society London A* **269**(1200) (1971), 555–585.

[8] V. Multanen, G. Whyman, E. Shulzinger, V. Valtsifer, and E. Bormashenko, Plasma treatment of silicone oil-infused surfaces switches impact of water droplets from bouncing to Tanner-like spreading, *Colloids & Surfaces A* **538** (2018), 133–139.
[9] R. Rioboo, C. Bauthier, J. Cont, M. Voue, and J. De Coninck, Experimental investigation of splash and crown formation during single drop impact on wetted surfaces, *Exp. Fluids* **35** (2003), 648–652.
[10] V. Roisman, B. Prunet-Foch, C. Tropea, and M. Vignes-Adler, Multiple drop impact onto a dry solid substrate, *J. Colloid & Interface Sci.* **256**, (2002), 396–410.
[11] I. V. Roisman and C. Tropea, Impact of a drop onto a wetted wall: description of crown formation and propagation, *J. Fluid Mech.* **472**, (2002), 373–397.
[12] F. Schellenberger, J. Xie, N. Encinas, A. Hardy, M. Klapper, P. Papadopoulos, H.-J. Butt, and D. Vollmer, Direct observation of drops on slippery lubricant-infused surfaces, *Soft Matter* **11** (2015), 7617–7626.
[13] J. D. Smith, R. Dhiman, S. Anand, E. Reza-Garduno, R. E. Cohen, G. H. McKinley, and K. K. Varanasi, Droplet mobility on lubricant-impregnated surfaces, *Soft Matter* **6** (2013), 1772–1780.
[14] T.-S. Wong, S. H. Kang, S. K. Y. Tang, E. J. Smythe, B. D. Hatton, A. Grinthal, and J. Aizenberg, Bioinspired self-repairing slippery surfaces with pressure-stable omniphobicity, *Nature*, **477** (2011), 443–447.
[15] A. L. Yarin, Drop impact dynamics: splashing, spreading, receding, bouncing, *Annual Rev. Fluid Mech*. **38** (2006), 159–192.
[16] A. L. Yarin and Weiss D. Impact of drops on solid surfaces: self-similar capillary waves, and splashing as a new type of kinematic discontinuity, *J. Fluid Mech*. **283** (1995), 141–173.

11 Reactive wetting

11.1 General remarks

In this chapter we consider reactive systems, in which an extensive chemical reaction and the formation of a new solid compound takes place at a spreading liquid–reactive substrate interface [1–7]. For example, during soldering on a copper substrate the process will always result in the formation of intermetallics of Sn and Cu [5]. Similarly, in the reactive metal penetration technique for producing the novel composites, a molten metal wets, penetrates, and reacts with either a dense or a porous ceramic preform, converting it into a metal–ceramic composite. A broad diversity of processes, such as diffusion, chemical reaction, and fluxing (and their possible combinations) are involved in reactive wetting; hence, the quantitative analysis of this process remains challenging and attractive to investigators.

11.2 Kinetics of reactive wetting

Five stages are identified in a reactive wetting event: (1) an initial rapid spreading, (2) an initial quasi-equilibrium, (3) an interfacial front advancing, (4) no advancing but a continuous decrease in drop height, and (5) a final wetting equilibrium [5]. The rapid spreading stage is similar to nonreactive wetting, and the contact angle at this stage may be predicted by the modified Young's equation. Let us explain this qualitatively. In reactive metal/ceramic or metal/metal systems, the time needed to reach a steady contact angle is often several orders of magnitude longer than that inherent for nonreactive systems [6]. Therefore, in the reactive wetting systems the apparent dynamic contact angle is not controlled by the interplay of viscous resistance and surface tension (as occurs in the Voinov model, addressed in Section 4.2), but by the surface tension and interfacial reaction themselves. Assume that the solid–liquid interface tension is given by equation (11.1), as suggested in Aksay et al. [1]:

$$\gamma_{SL} = \gamma_{SL}^{0} + \Delta G_r \,, \tag{11.1}$$

where γ_{SL}^{0} is the specific surface energy of the pristine solid–liquid interface, and ΔG_r is the change in Gibbs energy released per unit area by the reaction in the "immediate vicinity of the solid/liquid interface" [1]. In this case, the spreading parameter defined in Chapter 2 by equation (2.1) should be introduced as follows:

$$\Psi_{rw} = \gamma_{SA} - \left(\gamma_{SL}^{0} + \gamma + \Delta G_r\right) \,, \tag{11.2}$$

where γ, γ_{SL}^{0} and γ_{SA} are the specific surface energies of pristine liquid–air, solid–liquid, and solid–air interfaces respectively. The situation where $\Psi_{rw} > 0$ takes place corresponds to the complete wetting regime (see Chapters 2, 10) when the eventual

https://doi.org/10.1515/9783110583144-011

contact angle equals zero, as demonstrated in Section 2.1. In the situation where $\Psi_{rw} < 0$, we observe the partial reactive (dissolution) wetting regime, in which the finite, nonzero resulting contact angle of reactive wetting is expected. It is immediately recognized that the spreading parameter of reactive wetting is time-dependent (in other words, it depends on the kinetics of the occurring chemical reaction). This makes the problem of reactive wetting challenging.

Substituting equation (11.1) into the expression of the total free energy of the droplet, given by equation (2.4) and involving the transversality conditions of the variational problem of wetting (as discussed in detail in Section 2.2), immediately yields the reactive wetting Young-like equation:

$$\cos\theta_{rw} = \cos\theta_0 - \frac{\Delta G_r}{\gamma} \tag{11.3a}$$

$$\cos\theta_0 = \frac{\gamma_{SA} - \gamma_{SL}^0}{\gamma}, \tag{11.3b}$$

where γ_{SA} is the solid/air interfacial tension and θ_{rw} is the apparent contact angle of reactive wetting [2, 5].

In Sections 3.2–3.4, and 5.9 we already mentioned the dominating role of the triple (three-phase) line in constituting apparent contact angles. This role becomes even more pronounced for reactive wetting systems, because the spreading liquid has direct access to the solid at the triple line; the reaction rate at this particular line is two to three orders of magnitude higher than the reaction rate at the interface far from the triple line, where the reaction occurs by slow diffusion through a solid layer [6].

Generally, two limiting cases can be defined, depending on the rate of the chemical reaction at the triple line compared with the rate of diffusion of reactive solute from the drop bulk to the triple line (or of a soluble reaction product from the triple line to the drop bulk). In the first limit case, chemical kinetics at the triple line are rate-limiting because diffusion within the droplet is comparatively rapid. In this case the spreading process is shown to be linear, i.e., $R(t) \sim t$ [6]. This result is obviously far from that predicted by Tanner's law for viscous spreading of small droplets, as discussed in Section 4.7. The linear kinetics of spreading was also reported by Taitelbaum et al. [7], in which the effect of temperature on the dynamics and geometry of a mercury droplet ($\sim 150\,\mu m$) spreading on a silver substrate (4000 Å) was studied. Moreover, the spreading process was linear, $R(t) \sim t$, for all temperatures [7]. Taitelbaum et al. also addressed the scaling law governing the roughness of the triple line under reactive wetting [7], which was discussed in Section 3.10.3. The value of the scaling exponent was established as $\hat{\alpha} \cong 0.8$.

The second limiting case of reactive wetting occurs when we have diffusion-limited spreading. This wetting regime occurs when local reaction rates are comparatively high and the rate of the lateral growth of the reaction product at the triple line is limited by the diffusive supply of reactant from the drop bulk to the triple line [6]. In this case, the time-dependent wetting is expected [6].

As of today, no theoretical models have been developed to describe the complete reactive wetting phenomenon [5]. Only empirical relations are used, in which best fit equations are suggested for the experimental results [5].

Bullets

- Reactive wetting takes place when extensive chemical reaction and the formation of a new solid compound takes place at a spreading liquid–reactive substrate interface.
- The processes occurring in the vicinity of the triple line are crucial for constituting the regime and apparent contact angles of reactive wetting.
- The reactive wetting Young-like equation considering the reaction-inspired change in the Gibbs energy of a droplet/solid system was suggested.
- In the case when chemical kinetics at the triple line are rate-limiting, the spreading process is linear, i.e., $R(t) \sim t$.

References

[1] I. A. Aksay, C. E. Hoge, and J. A. Pask, Wetting under chemical equilibrium and nonequilibrium conditions, *J. Phys. Chem*. **78**(12) (1974), 1178–1183.
[2] N. Eustathopoulos, Dynamics of wetting in reactive metal/ceramic systems, *Acta Materialia* **46** (1998), 2319–2327.
[3] P. de Gennes, F. Brochard-Wyart, and D. Quéré, *Capillarity and Wetting Phenomena*, Springer, Berlin, 2003.
[4] M. Harel and H. Taitelbaum, Effect of temperature on the dynamics and geometry of reactive-wetting interfaces around room temperature, *Phys. Rev. E* **96** (2017), 062801.
[5] G. Kumar and K. N. Prabhu, Review of non-reactive and reactive wetting of liquids on surfaces, *Adv. Colloid & Interface Sci*. **133** (2007), 61–89.
[6] K. Landry and N. Eustathopoulos, Dynamics of wetting in reactive metal/ceramic systems: linear spreading, *Acta Materialia* **44**(10) (1996), 3923–3932.
[7] L. Yin, B. T. Murray, Sh. Su, Y. Sun, Y. Efraim, H. Taitelbaum, and T. J. Singler, Reactive wetting in metal–metal systems, *J. Physics: Condensed Matter* **21**(46) (2009), 464130.

Index

https://doi.org/10.1515/9783110583144-012

De Gruyter Studies in Mathematical Physics

Volume 49
Invariant Differential Operators. Volume 2: Supersymmetry
Vladimir K. Dobrev
ISBN 978-3-11-052663-9, e-ISBN (PDF) 978-3-11-052749-0,
e-ISBN (EPUB) 978-3-11-052669-1

Volume 48
Dynamical Systems and Geometric Mechanics. An Introduction
Jared Maruskin
ISBN 978-3-11-059729-5, e-ISBN (PDF) 978-3-11-059780-6,
e-ISBN (EPUB) 978-3-11-059803-2

Volume 47
Elementary Particle Theory: Volume 3: Relativistic Quantum Dynamics, 2018
Eugene Stefanovich
ISBN 978-3-11-049090-9, e-ISBN (PDF) 978-3-11-049322-1,
e-ISBN (EPUB) 978-3-11-049139-5

Volume 46
Elementary Particle Theory: Volume 2: Quantum Electrodynamics, 2018
Eugene Stefanovich
ISBN 978-3-11-049089-3, e-ISBN (PDF) 978-3-11-049320-7,
e-ISBN (EPUB) 978-3-11-049143-2

Volume 45
Elementary Particle Theory: Volume 1: Quantum Mechanics, 2018
Eugene Stefanovich
ISBN 978-3-11-049088-6, e-ISBN (PDF) 978-3-11-049213-2,
e-ISBN (EPUB) 978-3-11-049103-6

Volume 44
Collective Effects in Condensed Matter Physics, 2018
Vladimir V. Kiselev
ISBN 978-3-11-058509-4, e-ISBN (PDF) 978-3-11-058618-3,
e-ISBN (EPUB) 978-3-11-058513-1